The Variability of Warm Absorbers in Active Galactic Nuclei

by

Robert R. Gibson

Submitted to the Department of Physics
in partial fulfillment of the requirements for the degree of

Doctor of Philosophy

at the

MASSACHUSETTS INSTITUTE OF TECHNOLOGY

September 2006

Author ....
Department of Physics
July 31, 2006

Certified by ....
Claude R. Canizares
Associate Provost
Bruno Rossi Professor of Experimental Physics
Thesis Supervisor

Accepted by ....
Thomas Greytak
Professor of Physics
Associate Department Head for Education

The Variability of Warm Absorbers in Active Galactic Nuclei

by

Robert R. Gibson

Submitted to the Department of Physics
on July 31, 2006, in partial fulfillment of the
requirements for the degree of
Doctor of Philosophy

Abstract

This thesis presents three studies of warm (photoionized) absorber variability in Active Galactic Nuclei (AGN) using high-resolution X-ray spectra provided by the *Chandra* High Energy Transmission Grating (HETG). The first study is a single observation of the AGN MR 2251-178, which is known to have a highly variable warm absorber (WA). We find an unusually thin effective hydrogen column density along the line of sight compared to previous observations. Strong line emission without corresponding absorption indicates significant WA geometric structure. Strong absorption features in the spectrum are evidence of a highly-ionized, high-velocity outflow, which could be carrying a large amount of mass and energy out of the AGN.

In the second study, we search for absorption lines variability in the well-studied WA of MCG -6-30-15. We find a significant anti-correlation over time between at least two ions, with suggestions of additional time variation in other ions. At least one line, the $1s-2p$ resonance line of Mg XII, varies as a function of 2-10 keV continuum luminosity. Luminosity-driven ionization changes alone are insufficient to explain the observed variation. Either multiple factors influence line strength on observable time scales, or the line of sight to the central source varies over time through a structured absorber.

In the third study, we survey spectra from the HETG data archive. We model the normalized excess variance (NEV) spectrum of a varying WA and find that it does not explain high-energy (>2 keV) spectral variation, nor does it generally fit NEV spectra at lower energies (<2 keV). We also search through each spectrum at high resolution ($\Delta\lambda = 0.01$ Å) for bins which vary more than expected due to normal Poissonian fluctuations. We find some evidence for such variation in the aggregate sample, though not in AGN individually.

Our results show that WA structure is more complicated than pictured in contemporary models. Future high-resolution spectroscopic variability studies are certainly warranted. AGN models should eventually consider the effects of WA structure and the influence of continuum variation on the WA.

Thesis Supervisor: Claude R. Canizares
Title: Associate Provost
Bruno Rossi Professor of Experimental Physics

Acknowledgments

I would like to thank all the people who have contributed to my growth as a graduate student at MIT and, particularly, to the ideas and analysis presented in this thesis. My advisor, Claude Canizares, has given me a good deal of analytical input, advice, support, and a healthy distaste for the passive voice. Herman Marshall has also contributed many hours of advice and explanation of statistical methods. I will be saving all his long, descriptive emails for future reference.

I appreciate the input, feedback, and support of Julia Lee and Andy Young, who collaborated on the papers which comprise Chapters 4 and 5 of this thesis. Thanks also to the HETG team at MIT for their general assistance, and especially for their support of the HETG instrument. John Houck and John Davis provided the ISIS/S-Lang software environment which I have used for almost all the data analysis in this thesis, as well as for homework problems and other miscellaneous projects. Dave Huenemoerder developed the AGLC tools which I used for data analysis described in Chapters 5 and 6. I would also like to thank Deepto Chakrabarty and Max Tegmark who, as members of my thesis committee, contributed their time, thoughts, and practical advice which will apply to future projects.

I would like to thank family and friends who have added a great deal to my enjoyment of graduate school. I was very honored by the number of non-scientists who expressed interest in my thesis studies. I found statements like this one to be very gratifying: "I tremendously enjoyed observing his thesis [defense], although I understood almost nothing that was said."

My wife, Ann, has contributed more to this process than I can express. Some of her contributions have been wonderful "intangibles." She has also made very concrete contributions, ranging from editorial input to scientific critique. We will always look back fondly to our first date, when she asked, "So what can we gain from your research?" Today, as I write, is the "due date" for her to give birth to our first child. As we wait for the labor process to begin (soon, hopefully!), I realize that I can finally answer her question. Studying far-distant galaxies can certainly enhance our knowledge about the origin and structure of the universe. But I would be most happy if studies such as these can (in some way) contribute to showing young people like little Ross that the world is an amazing, fascinating place, an ideal home for people like us.

Contents

List of Figures

List of Tables

Preface

Some galaxies emit large amounts of energy from their central regions. The energy output may be highly variable, and can not be attributed purely to star formation or other stellar processes. The central region of such a galaxy is called an Active Galactic Nucleus (AGN).

In the standard "unification" model, a supermassive black hole (SMBH) resides at the heart of the AGN. The SMBH may have the mass of millions or even billions of suns. An AGN core emits large amounts of energy across the electromagnetic spectrum. It is believed that an accretion disk and perhaps the base of an outflowing jet (if present) are primary sources of the emitted energy, but the exact mechanisms of energy generation are not well-understood.

Recent studies have shown that AGN interact with and influence their immediate surroundings on galactic and extra-galactic scales. AGN influence (or are strongly influenced by) the galaxy formation process, and AGN activity strongly influences the energetics of galaxy clusters. If we want to understand the physics of galaxies and galaxy clusters, we need to understand the physics of AGN.

AGN can be very bright in X-rays, and the X-ray spectra of many AGN are absorbed by the lines and photoionization edges of ions in an intrinsic "warm absorber." Recent studies have used high-resolution X-ray spectroscopy to analyze in detail the absorber imprint on time-integrated spectra. A few studies have searched for variation in the absorber, typically by splitting the observation into a small number of time segments based on continuum flux. The results of these studies have been mixed.

Variability studies can potentially reveal a great deal of information about the physics of warm absorbers and their AGN hosts. For example, measuring ionization time scales can indicate absorber densities, which can in turn constrain the absorber location. In this thesis, we search for and characterize absorber variability in recent high-resolution X-ray spectroscopy of AGN.

We first present an introduction to WAs and AGN in general (Chapter 1) and a discussion of the physics of WAs (Chapter 2). We then present a history of variability studies in AGN spectroscopy, a summary of recent issues in WA studies, and a description of two well-studied WAs (Chapter 3). The remainder of the thesis consists of three studies we have performed to study absorber variability. In the first study, we examine the time-integrated spectrum of MR 2251-178, which is known to have a highly variable WA (Chapter 4). In the second study, we search in detail for variations in individual lines in the WA of MCG -6-30-15 (Chapter 5). In the third study, we search for signatures of WA variation over observable time scales in AGN spectra in the *Chandra* HETG archive (Chapter 6). Finally, we conclude with a discussion of our results applied to current WA unification models and discuss the feasibility of variability studies in future X-ray missions (Chapter 7).

Chapter 1

Introduction

AGN are large (perhaps hundreds of parsecs across), bright (with some emitting 10^{47} erg s^{-1} or more in X-rays alone), and ubiquitous in the universe. The Sloan Digital Sky Survey (SDSS) Data Release 4 (DR4) contains optical spectra of 64,000 bright AGN (Adelman-McCarthy, J. K. et al. 2006). Yet despite the size and luminosity of AGN, after decades of multiwavelength observations we are still not sure that even our general models of their structure are completely accurate. This is unfortunate, because AGN physics is believed to strongly influence host galaxies and clusters, and therefore understanding AGN is very important to understanding the large-scale structure of the universe.

Many factors complicate observing campaigns. AGN are believed to be driven by energy released during accretion onto a central supermassive black hole with gravitational radii GM_{BH}/c^2 of 10^{11} to 10^{15} cm. Even modern, high-resolution telescopes are incapable of resolving the regions where the high-energy processes occur that power AGN. Emission from the central region in the ultraviolet (UV) or X-rays is obscured by dust in the AGN, in the AGN's host galaxy, and in our Galaxy. AGN also seem to be rule-breakers; generalized statements about them are frequently contradicted by at least a handful of exceptional cases.[1]

In this chapter, we provide a brief introduction to AGN. We present "unification models" which attribute AGN diversity to the observed orientation of a few simple components (§1.1). Then we briefly present several current issues in AGN studies which indicate that AGN are influencing their environments on very large scales (§1.2). Finally, we present an introduction to the research program of this thesis (§1.3).

1.1 Unification Models of AGN

The original AGN unification model (which we will call "UM_O"), in which the diversity in observed traits is attributed to different orientations of AGN with respect to our line of sight, is commonly attributed to the spectropolarimetric study of the nearby Seyfert 2 NGC 1068 by Antonucci and Miller (1985).[2] In that well-known study, the authors observed that the continuum polarization fraction of NGC 1068 is about 16%, independent

---

[1] This also leads us to conclude that at least a handful of AGN are *not* rule-breakers. If we only knew which AGN they are!

[2] Robert Antonucci notes in a later review article (Antonucci 1993) that several previous researchers, of which he was unaware, had suggested ideas related to the unification model of Antonucci and Miller (1985). The model of Antonucci and Miller (1985) is one prominent link in a chain of evolving unification models extending from the 1970's to the present.

of wavelength. Broad permitted lines characteristic of Seyfert 1 AGN were evident in the polarized flux, while the unpolarized flux showed the narrow lines of a Seyfert 2. The direction of polarization (required to be perpendicular to the photons' last direction of travel before scattering) suggested that the photons left the nucleus in a polar direction before being scattered. In the polarized spectrum, the ratio of Hβ line luminosity to soft X-ray luminosity was consistent with that typically measured for Seyfert 1's, strengthening the conclusion that the polarized flux was a scattered reflection of a Seyfert 1 continuum. This further indicated that X-rays were being scattered just as the optical continuum was, so that the scattering cross-section was wavelength-independent. Electrons were therefore favored over dust to be the scattering material. Finally, some method of obscuration was required so that the Seyfert 1 continuum would not be directly observed in Seyfert 2's. This obscuration has become known as "the torus" due to its presumed azimuthal geometry. Figure 1-1 shows an artist's image of an AGN following the UM_0.

The unification model of Antonucci and Miller (1985), modified slightly over time, uses a small number of AGN components (SMBH, accretion disk, broad line region (BLR), narrow line region (NLR), obscuring torus, and a relativistic jet) to describe in general terms the wide variety of AGN observations. It has survived for two decades and become widely accepted. It fits well with current studies of phenomena, such as the X-ray background (Triester and Urry 2005), that are unrelated to the original data it was used to explain. Yet much work remains to be done before we have a comprehensive, quantitative model of AGN.

Modern studies of AGN are showing that AGN are much more complex than the simple picture of the UM_0. For example, Urry (2004) points out that radio AGN are classified by the observer's orientation with respect to the jet axis which is likely, but not certainly, the same as the torus axis of symmetry. Although we have general estimates of the radial distance of structural components from the central source, we know very little about the physics of the individual components. In some cases, we do not understand broad components of AGN spectra. For example, we do not know the origin of the "soft excess" sometimes seen at X-ray energies below 2 keV. The UM_0 is a static picture; it does not tell us how AGN form, how they feed, how they interact with their host galaxies, or how they interact with the extra-galactic environment. Alternative unification models have even been constructed which have different structural components, such as the disk wind model of Elvis (2000), which does not require an obscuring torus.

The UM_0 is therefore a powerful first step along the path to understanding AGN, but much more study and modeling is clearly needed. In this thesis, we will be focusing on the warm absorber (WA), a photoionized X-ray absorber detected in about half of all AGN (Reynolds 1997; George et al. 1998). Recent high-resolution spectroscopy has revealed (in some cases) complicated X-ray line absorption of Seyfert 1 continua. The WA is typically believed to reside within about 10 pc of the nucleus, and perhaps much closer. Radial flow velocities can be measured in spectroscopic data, giving us the ability (in theory) to map out absorber structure. Analysis of ionization stages, column densities, etc., can tell us about the physical conditions of the absorbing material. Thus an increased understanding of the WA can potentially advance our understanding of the gas structure and dynamics of AGN.

AGN studies are complicated by a "chicken and the egg" problem. On the one hand, we are unable to observe AGN as well as we would like due to time constraints, obscuration, resolution limitations, etc. On the other hand, it has been difficult to build testable models that are much more complex than the UM_0. Without testable predictions from detailed models, it is difficult to interpret the complex data we have. But modeling efforts need more constraints from unambiguous data measurements to advance.

Large amounts of spectroscopic data exist, particularly at lower spectral resolutions insufficient to distinguish absorption lines. Many models have been proposed to explain at least localized features of AGN. In a few cases, researchers have begun to combine diverse data – particularly variability studies – to constrain or elucidate models of specific components of an AGN. This is the case with X-ray continuum emission models, which are inspired by power spectra (e.g., Uttley and McHardy 2001) or Fe Kα line structure and variability (Miniutti and Fabian 2004).

In many cases, modeling attempts are hindered by the fact that the data cannot distinguish between competing models. The X-ray soft excess, for example, is often described as black body radiation or simply fit phenomonologically as a low-energy power law component. Some researchers have proposed a model in which emission lines produced by reflection of the continuum off the accretion disk are relativistically blurred to produce the excess (e.g., Crummy et al. 2006). But in at least several cases, it is not even clear that a soft excess is present. An apparent excess in soft X-rays may be the result of miscalculating the complicated aborption modifying the higher-energy power-law continuum. In other cases, an apparent detection of photoionized absorber edges may be due to an inaccurate description of the (assumed) shape of the underlying continuum.

Given these current constraints on AGN studies, in this thesis we look for a way forward by considering a phenomenon which has received a small amount of previous attention: short time-scale absorber variability. The underlying physics of photoionized, absorbing plasmas is very well understood, at least for optically thin absorbers. Recent *Chandra* spectroscopy of well-studied variable AGN such as MR 2251-178 and MCG -6-30-15 provides an excellent platform for variability studies. The X-ray WA has the potential to be an important discriminator of AGN models. Its location and structure is handled differently in the various models, as we will describe below. WAs seem to be a promising candidate for study, given that WA atomic physics is well-understood; we have access to high-resolution, spectroscopic data of several AGN with strong WAs; and WAs play an important role in AGN models.

We have selected two candidate models which have received some attention in the recent literature – the "evaporating torus" model and the "accelerating disk wind" model – for consideration in our study. These models modify the UM_0 to incorporate a WA.

1.1.1 An Evaporating Torus

In Figure 1-2, we show a plot of temperature T against an ionization parameter

$$\Xi \equiv \frac{\xi}{4\pi ckT}, \tag{1.1}$$

where c is the speed of light, k is the Boltzmann constant, and ξ is the ionization parameter $\xi \equiv L_{ion}/nr^2$ in terms of the 13.6 eV - 13.6 keV ionizing luminosity L_{ion}, the particle number density n, and the absorber distance r from the continuum source. Since L_{ion}/c is assumed proportional to the ionizing radiation pressure and nkT is the ideal gas pressure of the absorber, the ionization parameter Ξ is typically used when pressure balance is being considered.

Photoionization models will be described in general in another chapter. For now, we simply state that photoionization models calculate the equilibrium properties of a photoionized gas, where "equilibrium" is defined as the unique state for a given ionization level ξ for which the heating and cooling processes are balanced. Under this constraint, the electron temperature T is a monotonically increasing function of the ionization parameter ξ.

In the plot of T vs. Ξ of Figure 1-2, the solid line shows the equilibrium states of the gas. The temperature T is, in general, not uniquely determined by Ξ. Krolik et al. (1981) pointed out that this plot has interesting thermodynamic properties. Heating processes are dominated by photoionization (releasing energetic electrons into the gas) and Compton scattering. The heating processes are proportional to the electron density, n_e. If the heating and cooling rates are, respectively, $n_e\Gamma$ and Λ, then the total cooling rate of the gas is

$$\mathcal{L} = \Lambda - n_e\Gamma. \tag{1.2}$$

The ratio n_e/n approaches a constant (≈ 1) at ionization levels required for X-ray spectral lines to be visible, so we will assume $n_e \approx n$ for this discussion. Writing Ξ in terms of the ionizing flux assumed to be $F_{ion} = L_{ion}/4\pi r^2$,

$$\Xi \equiv \frac{F_{ion}}{nkTc} \tag{1.3}$$

and substituting for $n(\approx n_e)$ in equation (1.2), we find that at equilibrium (where $\mathcal{L} = 0$),

$$\Xi = \frac{\Lambda F_{ion}}{ckT\Gamma}. \tag{1.4}$$

Now suppose we fix a value of Ξ. Then $T \propto \Lambda/\Gamma$. Generally, the heating processes included in Γ are independent (to first order) of T. On the other hand, cooling processes are very dependent on temperature. If T is perturbed at fixed Ξ (corresponding to movement on a vertical line in Figure 1-2), the process will return to equilibrium if $d\Lambda/dT > 0$. Otherwise, temperature perturbations will increase. Krolik et al. (1981) pointed out that the cooling curves (Λ vs. T) are such that temperature perturbations (at fixed Ξ) are stable when $d\Xi/dT > 0$ and unstable when $d\Xi/dT < 0$. Thus the central region of the S-curve of Figure 1-2 is unstable to such perturbations. Equilibrated gas at critical values of Ξ where $T(\Xi)$ is multivalued can exist in multiple phases, and some equilibrium states are unstable.[3]

In further studies (Krolik and Kriss 2001; Krolik 2002), Krolik and Kriss argued that the specific types of perturbations required to exploit this instability occur naturally in AGN in cases where the flow time scales are long. Consider a photoionized absorber in contact with a cool reservoir of gas. The absorber may in fact be "boiling" off the gas due to radiation heating from the continuum source. The tendency of the evaporating absorber to heat up will be opposed by the increased pressure due to additional absorbing material evaporating off the reservoir. Conversely, if the absorber started cooling below Ξ_c, the evaporated material would condense back onto the reservoir and decrease the pressure, raising Ξ_c.

---

[3] To see this without actually calculating cooling rates, consider the following argument. The $T(\Xi)$ curve is monotonic for many ionizing continuum shapes. It only "bends backward" into an S-curve for certain continua, such as when hard X-rays are strong. In a monotonic case, we would naturally expect that cooling dominates heating above the curve, and *vice versa* below. If we deform the continuum slowly so that the $T(\Xi)$ curve bends into an S-curve, we find that cooling dominates to the left of the curve, and heating to the right. (Since the curve is by definition the set of points where heating and cooling are equal, we do not expect the sign of $\mathcal{L}$ to change except on the curve.) Then vertical upward excursions from the curve result in increased cooling where $dT/d\Xi > 0$ and increased heating where $dT/d\Xi < 0$.

In this scenario, the WA is therefore identified with the material expected to be evaporating from the obscuring torus. This material may also become the polar scattering region in the UM_0 which scatters Seyfert 1 emission into sight for a Seyfert 2 nucleus. Consequently, the WA is placed at a distance of 1-10 pc from the central source, based on rough estimates of the torus location. The inner edge of the torus has been estimated to be around 1 pc in order to provide a stable balance between the inflow of matter through the torus to the nucleus and the outflow of material ablated from torus clouds by nuclear radiation (Krolik and Begelman 1988). In order to effectively obscure BLR emission lines, the torus must also be larger than the BLR, typically estimated to be on the order of 10^{17} cm based on ionization levels. The instability of the gas along much of the equilibrium curve may naturally explain the diversity of ionization stages seen in X-ray (and UV) absorbers.

We note that, to our knowledge, these models have not been thoroughly tested with numerical hydrodynamical codes. We hope to pursue such a modeling study in future work. The task is complicated by the fact that the radiating source is varying on short time scales, and the structure of the absorber will certainly be important.

1.1.2 An Accelerating Disk Wind

Evaporating torus models (§1.1.1) apply physical arguments about photoionized gas to generally explain features observed in the UV and X-rays with a minimal number of unification model components. The disk wind model of Elvis (2000) follows a slightly different approach. It began as a qualitative attempt to describe a wide array of observed features in AGN spectra, again with a minimal number of components. As it evolves, it is becoming more quantitative, even incorporating the $T(\Xi)$ physics of Krolik et al. (1981).

In this model, absorption and emission features in the optical, UV, and X-rays are produced in a wind flowing out from the accretion disk. The wind leaves the disk vertically, but each parcel of matter has a Keplerian angular velocity inherited from the disk. At some height above the disk, the wind angles outwards to about 60° from the polar axis and *accelerates* radially. At this stage, the flow obstructs about 6-12° in angular extent. The wind as a whole is shaped like a funnel with a cylindrical base. Figure 1.3 shows the outflow structure along with proposed outflow velocities. The figure also shows the angles which are required to describe the components of the flow in order to produce the correct proportion of AGN types.

Viewed along the pole, we look down the throat of the funnel and see no absorption. If we look directly into the accelerating wind, we see a Broad Absorption Line (BAL) AGN, which shows broad outflowing optical absorption lines from 2000 up to perhaps 60,000 km s^{-1} (Krolik 1999). The absorption in BAL AGN typically begins at some minimum "detachment" velocity, corresponding to whatever velocity the accelerating wind had reached at when it bent into a radial direction. Narrow-line absorbers, such as those seen in the X-ray WA's, arise from a line of sight through the vertical part of the wind, where it leaves the disk. The angular extent of the wind segments is chosen empirically to match the observed fraction of AGN of each type.

The wind is warm enough to contain line-emitting clouds. In fact, the wind confines the clouds, keeping them from evaporating or expanding too rapidly. If the clouds move along with the wind, they are not subject to shear forces that would otherwise destroy them. These clouds, at a wide range of velocities along the line of sight due to rotation around the polar axis and outflow velocities in the wind, emit photons that we detect as broad emission lines. The wind is layered, so that higher-ionization lines are emitted from clouds closer to the source, while clouds farther out are screened by the wind and can exist at lower ionization levels.

The flow itself, while required by observed column densities to be rather thin along lines of sight roughly perpendicular to the flow, is posited to be sufficiently voluminous overall to scatter continuum photons into our lines of sight. This would account for the approximately 10% polarization fractions seen in spectra such as that of NGC 1068. It would also likely produce the reflection spectrum believed to be responsible for the "Compton hump" and Fe Kα line seen in X-rays (e.g., Ross and Fabian 2005; Ross et al. 1999).

In a conference presentation in 2003 (Elvis 2003), Martin Elvis added several arguments in favor of the disk wind model, generally based on the fact that the model was consistent with characteristics of individual AGN observations. In particular, he referred to an analysis of the NGC 3783 X-ray spectrum by Krongold et al. (2003), who found two separate WA components in the spectrum that both lay on stable parts of the $T(\Xi)$ curve and were in pressure equilibrium. Elvis suggested that, if these WAs are related to BAL clouds in a confining medium, the clouds would survive longer if they were flowing along with the confining medium. He also offered a mechanism that could explain how such a wind could be launched from an accretion disk with such a narrow radial footprint.

The disk wind model has been used to explain data that are apparently inconsistent with the UM_0. Risaliti et al. (2002) collected X-ray observations of 25 galaxies defined as Seyfert 2's based on X-ray spectra. They found that these galaxies showed significant column density variation on time scales of years. The result was not confined to a small subset of the sample; in fact, only 3 of the 25 galaxies were consistent with having a constant column density N_H. The variation did not appear to be correlated with flux, making ionization an unlikely cause of the variation. In no case did N_H drop below a few $\times 10^{21}$ cm^{-2}, so it did not appear that galaxies were changing character from Seyfert 2's to Seyfert 1's. Assuming the absorption variation was due to spherical clouds crossing the line of sight at Keplerian velocities, Risaliti et al. (2002) determined that at least the shorter time scale variations must be due to material within about 10^{17} cm of the center, much closer than the obscuring torus. Further arguments suggested that the variable obscuring material must cover a significant fraction of the solid angle if it alone were responsible for obscuring Seyfert 2's. These considerations naturally led them to propose a unification model related to the disk wind model. In this model, the obscuring torus is unnecessary, though they did require a second absorbing system at 5-10 pc distances to allow for longer time scale variability.

1.1.3 Comments on Models

The evaporating torus model (§1.1.1) and the accelerating disk wind model (§1.1.2) are perhaps the two most commonly discussed current models for AGN absorbers. There are other models, such as the thermally launched wind used by Chelouche and Netzer (2005) to fit the complicated absorption line spectrum of NGC 3783. In this thesis, we will address only the torus and disk wind models. They have benefited from the scrutiny of the research community for some time now, and have received the most treatment in the literature.

The two models have a lot in common. They agree on the general structure of the UM_0, with the exception that the accelerating wind model allows for the torus to be replaced by the disk wind. Even in that case, an additional, large-scale absorber may be required (Risaliti et al. 2002). They refer to the same underlying physics, in that the $T(\Xi)$ relation somehow constrains a multiphase medium to produce diversity in the WA. In both cases, the absorber is launched from a reservoir (itself a component of the UM_0) which supplies material for the flow.

Given these similarities, and the fact that detailed radiation-hydrodynamic simulations have not been performed that could identify physical problems with the models, it is rather difficult to distinguish between the two models given our current data. Nonetheless, there are differences which are, at least in principle, observable. We list a few of them here.

1. The principal difference between the two models is one of physical scale. For all but the largest SMBH's in AGN, the WA portion of the disk wind should lie within 1 pc of the central source. For smaller SMBHs with a mass about 10^7 $M_\odot$, the WA would be located about 10^{15} cm from the center. The torus is believed to be "parsec-scale" or larger (§1.1.1), in which case the WA would be located 1000 times farther out.

2. There are also important differences in absorber size. The evaporating region of the torus should presumably be a much larger volume than the thin wind launched from the accretion disk.

3. There are differences with regard to the relative locations of components of the nucleus. For example, if the WA is near the disk, it may be sensitive to the continuum emission geometry. If continuum emission occurs in outer disk regions, it would not pass through the WA.

4. The models may be discriminated by launching mechanisms. Detailed calculations and simulations have yet to be performed to enable such discrimination, but it is conceivable that certain configurations can be ruled out. For example, it may not be possible to launch a sufficiently (radially) thin wind from the disk, or it may be difficult to boil enough material off the torus with an ionizing continuum.

5. Independent of the exact physics of launching mechanisms, we would expect the WA in each model to be dependent on the launching entity. If the accretion disk changes significantly, we would expect a disk wind to vary. The torus presumably varies structurally on much longer time scales.

6. The existence of the torus is a distinguishing feature. If the torus were found not to exist, this would obviously be a problem for the evaporating torus model. Significant variations in obscuration generally attributed to the torus (such as those claimed in Risaliti et al. (2002)), may be difficult to describe in the UM_0.

7. In principle, gas density could be a discriminating factor, as claimed by Risaliti et al. (2002). Detailed hydrodynamic simulations of the physical characteristics of the gas are needed for unification models to determine a range of predicted gas densities.

Because the models have not been thoroughly characterized analytically or numerically, many of the most powerful discriminators between them are geometric. This has led us to consider time-varying properties of the absorbing material with the goal of gaining insights about the absorber structure. It may be that such insights can help to constrain AGN unification models.

1.2 Large-Scale Influence of AGN

The processes that occur in active galaxies are extremely energetic and apparently long-lived, and we might therefore expect AGN to be significant contributors to physics on galactic, inter-galactic, and even cosmological scales. The spectacular jets of galaxies such as Cygnus A, shown in Figure 1.3, demonstrate that small-scale (by galactic standards) AGN processes can have a dramatic effect on the surrounding environment, out to at least 100 kpc. Recent studies are indicating that AGN have an even bigger impact on their surroundings than we had previously believed. Although such studies are not topics of research in this thesis, we introduce a few of them very briefly here in order to demonstrate that understanding gas dynamics in the center of an AGN can inform research on much larger scales.

1.2.1 Cooling Flows and Cluster Heating

X-ray observations of galaxy clusters have revealed large volumes of hot, X-ray emitting plasma in the intra-cluster medium (ICM). Given a physically-derived model of the cooling processes of hot gas, the observed X-ray count rates could be de-projected to constrain the gas pressure and temperature in terms of the observed (projected) flux. The equation of hydrostatic equilibrium adds another constraint, and if the gravitational potential and pressure at a single radius are specified, one may determine the temperature and electron density at all radii from the center of the cluster. Once the temperature and electron density are known, the cooling rate can be used to determine a cooling time scale and, given the X-ray luminosity, a mass cooling rate. This procedure is summarized by White et al. (1997), who used *Einstein Observatory* imaging data to calculate cooling rates for a survey sample of galaxies. A review of cooling flow physics in this era of study was written by Fabian (1994).

Chandra allows for higher-resolution spectroscopic studies of these "cooling flows" in clusters. McNamara et al. (2000a) used the ACIS-I instrument to study the X-ray emitting gas in the Hydra A cluster. The spectroscopic information available at each CCD pixel allowed them to fit a thermal plasma model (MEKAL[4]) at each point to obtain density and temperature values at each point. They found that the gas temperature did decrease near the center of the cluster, but that the cooling mass rate is 34 $M_{\odot}$ yr^{-1}, only about 10% of what had previously been calculated.

Spectroscopic studies performed on other clusters returned similar results: the amount of cooling mass is much less than previously predicted (e.g., McNamara et al. 2000b). This conclusion is in agreement with star forming rates measured to be much lower than expected if large amounts of gas were cooling into the central galaxy. Apparently either the cooling mass is "missing," or the cooling process is somehow being inhibited. The theoretical overestimation (or the experimental under-observation) of the material cooling rate was confirmed by Peterson et al. (2003). These researchers used *XMM-Newton* spectroscopy of 14 galaxy clusters to show that despite the presence of material which had cooled slightly from the ambient medium, the clusters did not contain large amounts of material at the cooler temperatures required by the cooling flow model.

Even as the cooling flow problem was being discovered, a possible solution was offered. High-resolution X-ray images of clusters such as the Perseus cluster surrounding NGC 1275 (Fabian et al. 2000) revealed large cavities in the gas. These cavities became known as "ghost bubbles," because they did not appear to contain radio emission, in contrast with typical jet lobes. The bubbles are not necessarily aligned with the radio jet axis, and may not be spherical in shape. Figure 1-5 shows a 170 ks ACIS-S image of the Perseus cluster.

---

[4] The Mewe Kaastra Liedahl (MEKAL) model is described in XSPEC manuals available online at `http://heasarc.gsfc.nasa.gov/`.

A large, non-spherical cavity is evident to the northwest (top right). Its flattened shape has been compared to the cap of a rising "mushroom cloud."

It is tempting to think that ghost cavities are remants of AGN jet activity some time ago. The jet heated the gas in the bubble, and the bubble floated upward (outward). As the bubble "rises" in the cluster, it expands and does mechanical work on the surrounding gas. Intermittent AGN activity has been shown to produce acoustic waves which can dissipate on time scales shorter than the cluster cooling time, heating the cluster "gently," i.e., without shocking the intra-cluster medium (e.g., Ruszkowski et al. 2004).

1.2.2 The AGN Mass Budget: Feeding and Outflows

Assuming the AGN converts accreted mass to luminosity at a rate $0.1\dot{M}c^2$, a bolometric luminosity of 10^{45} erg s^{-1} requires a "modest" mass accretion rate of about 0.2 $M_\odot$ yr^{-1}. Bright AGN can be a few orders of magnitude more luminous. Thus a moderately bright AGN can in principle be fueled with a fraction of the total gas in a disk galaxy. It is more difficult to understand how the gas dissipates angular momentum on its journey from the host galaxy disk into the heart of the AGN. A hierarchy of mechanisms may in fact be required (Krolik 1999).

Using near infrared (NIR) images and CO maps of four low luminosity AGN (LLAGN), García-Burillo et al. (2005) find an added complexity: the net torques are actually positive inside about 200 pc, indicating that no material at all should be flowing into the AGN in these galaxies. AGN activity may be regulated by the formation of bar structures in the galactic disk. The bar structures are transient, and their self-destruction may allow gas in the bar region to flow into the nucleus.

Other studies have suggested that AGN activity may be due to gas movement triggered by galactic collisions. Some studies (e.g., Bahcall et al. 1997) have indicated that AGN tend to live in denser cosmic neighborhoods than normal galaxies. However, other studies have suggested that AGN activity is not correlated with large-scale galaxy density (Carter et al. 2001; Miller et al. 2003).

As if the question of AGN feeding were not complicated enough, some recent studies have shown that the amount of material *coming out* of AGN is also difficult to understand. Several X-ray observations of AGN have shown evidence for highly-ionized, high-velocity outflows. While typical WA velocities are a few hundred km s^{-1}, these outflows have been measured at a few percent to a few tens of percent of the speed of light. Their ionization levels are typically extremely high; they are detected by broad, asymmetric features attributed to FeXXVI.

Because the velocities involved are so extreme, there is some ambiguity in the line identifications. In at least a few cases, they appear more like narrow edge-shaped features than Gaussian lines. Chartas et al. (2002) rejected the hypothesis that the broad feature in APM 08279+5255 was an edge, as we did for MR 2251-178 (Gibson et al. 2005). In at least one case, the claim of a high-velocity outflow (Pounds et al. 2003b) has been disputed based on a re-analysis of the data (Kaspi 2004). Nonetheless, in most cases, it is difficult to produce an alternative explanation for the features attributed to these outflows.

Making general assumptions about the outflow geometry, researchers often find that they exhibit rather extreme characteristics. For example, we estimated that the outflow in MR 2251-178 carried off a few $\times(10^2 - 10^3)f_{cov}$ $M_\odot$ yr^{-1}! Unless the fraction f_{cov} of the solid angle occupied by the outflow is small, this is a large fraction of the accretion budget. The kinetic energy outflow is similarly large in comparison to the AGN luminosity. It is unlikely that f_{cov} is too small, or else we would be extremely lucky to see these features. It may be that the outflows have been misidentified, although alternate explanations for the absorption features in the spectra are problematic. Finally, it may be that the absorber geometry is sufficiently complex that the geometric arguments used to estimate the outflowing mass and energy rates are invalid.

1.2.3 The $M_{BH} - \sigma$ Relation

In the last 20 years, it has become possible to measure SMBH masses reasonably well using techniques such as reverberation mapping (e.g., Peterson 1993). In a few cases, very accurate measurements of the SMBH mass, M_{BH}, can be made. This has been done, for example, using direct observations of stellar orbits in the Milky Way (e.g., Schödel et al. 2002; Genzel et al. 2003; Ghez et al. 2005) or high-resolution measurements of water maser activity in galaxies such as NGC 4258 (Greenhill et al. 1995). It has been previously observed that SMBH masses correlate with the luminosity of the host bulge or elliptical galaxy (Kormendy and Richstone 1995).

In August, 2000, two letters were published in the Astrophysical Journal claiming a correlation between M_{BH} and the velocity dispersion σ in the host galaxy bulge or ellipse (Ferrarese and Merritt 2000; Gebhardt et al. 2000). The studies differed slightly on specifics; Ferrarese and Merritt (2000) claimed $M_{BH} \propto \sigma^{4.8}$ (based on a sample of 12 galaxies) while Gebhardt et al. (2000) claimed $M_{BH} \propto \sigma^{3.8}$ (based on a sample of 26 galaxies). A follow-up study by Tremaine et al. (2002) found $M_{BH} \propto \sigma^{4.0}$ (based on a sample of 31 galaxies), agreeing with the latter study (within error).

While SMBH's are large and massive, their mass, size, and range of gravitational influence are all relatively small compared to their host galaxies. Thus it is surprising that SMBH properties should have much influence on properties outside the AGN. In the last few years, several models have been proposed to explain the relation between SMBH's and host bulges. This is an ongoing process. A successful model may tell us much about the formation of AGN and their host galaxies.

There are many models explaining the $M_{BH} - \sigma$ relation in current literature. Some models are driven by pre-conditions in the nuclear region which evolve into the SMBH and bulge (e.g., Adams et al. 2003). Other models consider "feedback mechanisms" by which energy or momentum are fed back from an accreting (and hence growing) SMBH to regulate the evolution of the galactic potential and bulge region (e.g., Begelman and Nath 2005). Numerical simulations of galaxy collisions have also demonstrated that AGN activity triggered by the collision can feed material back into the host galaxy, quenching AGN activity and regulating bulge properties (Di Matteo et al. 2005). AGN activity may also trigger star formation in host galaxies, which could explain why galaxies with AGN activity appear bluer than inactive galaxies of similar type (e.g., Sánchez et al. 2004).

1.2.4 The X-Ray Background

The X-ray background (XRB) was first discovered by Giacconi et al. (1962) in data collected from a rocket searching for X-rays scattered from the Moon. Various causes have been suggested for the XRB, including bremsstrahlung radiation from hot Galactic gas. Over the years, it has been spatially resolved to an increasing degree in various wavebands with observing instruments such as *Einstein* (Maccacaro et al. 1991), *ROSAT* (Hasinger et al. 1998), and *ASCA* (Ueda et al. 1998). With each observation, the challenge has been to resolve enough discrete sources to account for the XRB flux levels of a few tens of keV cm^{-2} s^{-1} sr^{-1}. Such observations require long exposure times to detect faint sources. Combining the observed spectra of resolved sources has until recently resulted in a mean spectrum that does not accurately represent the XRB spectral shape.

Deep observations with recent high-resolution instruments have resolved a large fraction of the XRB. Mushotzky et al. (2000) reported that they resolved 75% of the hard (2-10 keV) XRB as well as most of the soft (0.5-2 keV) XRB using the *Chandra* ACIS-S instrument. They found that the majority of contributors to the XRB were AGN, and that the mean hard X-ray spectrum did in fact match the XRB. Giacconi et al. (2001) found a significantly lower number of hard source counts per deg^2 than Mushotzky et al. (2000) in the *Chandra* Deep Field South (CDF-S), but still concluded that 60-80% of the hard XRB and 80% of the soft XRB was resolved in their data.

Some controversy remains, however. Using a deep (700 ks) *XMM-Newton* observation, Worsley et al. (2004) claim that only about 50% of the hard XRB above about 7 keV has been resolved into detected sources. Studies above the approximately 10 keV practical upper limit on X-ray spectroscopy of modern satellites would also be informative. AGN are expected to contribute strongly to this region of the spectrum as well, particularly because the spectral peak at about 30 keV matches well with predictions of Compton reflection components to AGN spectra. But this is relatively uncharted territory. Although much of the controversy about the XRB has been resolved, even recent studies indicate that there is more work to be done.

Now that we know the XRB is dominated by AGN (at least in energy ranges we have measured), measurements of the XRB are being used to constrain unification models. One example is a study by Triester and Urry (2005), who verify that the standard AGN unification model, $\mathrm{UM_0}$, is consistent with and can explain the shape and intensity of the XRB. This is particularly interesting considering that some unknown majority fraction of AGN are Seyfert 2's, i.e., oriented so that most of their luminosity is radiated out of our line of sight. These obscured AGN contribute to the XRB, but are not easily detected by our telescopes (in soft X-rays, at least). Triester and Urry (2005) verify that the $\mathrm{UM_0}$ does not even require redshift-evolution or luminosity variation to explain the XRB, though these may be real effects.

1.2.5 The Influence of AGN

In this section, we have briefly presented several cases drawn from recent studies of AGN that demonstrate the influence of AGN on their large-scale surroundings. SMBHs are not small objects, but it is quite remarkable that they may strongly and directly influence physics on 100 kpc scales – more than ten orders of magnitude larger than their gravitational radii! AGN influence is not confined to jet activity, but can apparently be attributed to a diversity of processes which impact the cosmos on multiple size scales. AGN appear to be tightly coupled to their host galaxies by unknown mechanisms, regulating bulge and ellipse dynamics, feeding on gas and dust, and expelling it into the intergalactic medium (IGM). They are powerful emitters of UV and X-ray radiation, and in fact dominate the XRB spectrum.

1.3 Program of This Thesis

This introductory chapter has demonstrated that AGN are complicated astrophysical entities with far-reaching influence. Although they are traditionally described in the straightforward terms of the standard unification model UM_0, most attempts to model their structure in greater detail are controversial. Comprehensive models that explain AGN components with detailed physical calculations or simulations have yet to be developed. The individual components of AGN have been modeled in some detail and with some promise, though a consensus on these models has yet to be reached. The matter is complicated by the fact that high-signal, high-resolution spectroscopic data of AGN is difficult to obtain. Analyses of such data can not currently distinguish between competing theories of the physics of AGN components, though significant constraints have certainly been applied to models.

In this thesis, we focus on one AGN component that is frequently detected in X-ray data: the WA. Studies have shown that the WA is present in about half of AGN (Reynolds 1997; George et al. 1998) and can be highly variable (e.g., Halpern 1984). Deep *Chandra* observations of strong WAs exist for well-studied galaxies such as MCG -6-30-15 and NGC 3783, and several lower-exposure observations of AGN with WAs are available in the *Chandra* archive. As we have shown in this chapter, while the WA is believed to reside in the AGN, there is sufficient controversy about its location and structure to make it an interesting topic of study. Variability in the WA can also reveal physical processes and constraints that are not evident in time-integrated spectroscopy.

This thesis is organized as follows. In Chapter 2, we present a physical introduction to WAs, including a discussion of their general spectroscopic characteristics and the physics that goes into modeling photoionized absorbers. In Chapter 3, we present a literature history of studies of WAs and topics strongly associated with WAs, such as the UV absorber. Chapters 4 through 6 describe the research we have conducted for this thesis in the context of current studies. Chapter 4 is an analysis of the time-integrated HETG spectrum of MR 2251-178, the first AGN for which a WA was proposed. Chapter 5 presents our study of absorption line variability in MCG -6-30-15, along with a discussion physical models of the WA in relation to our WA variability study of MCG -6-30-15. Chapter 6 presents results from a brief survey of the *Chandra* HETG database in which we search for evidence of absorber (and emitter) variablity in a sample of AGN spectra. Finally, in Chapter 7 we present our conclusions from these studies in light of current research and models.

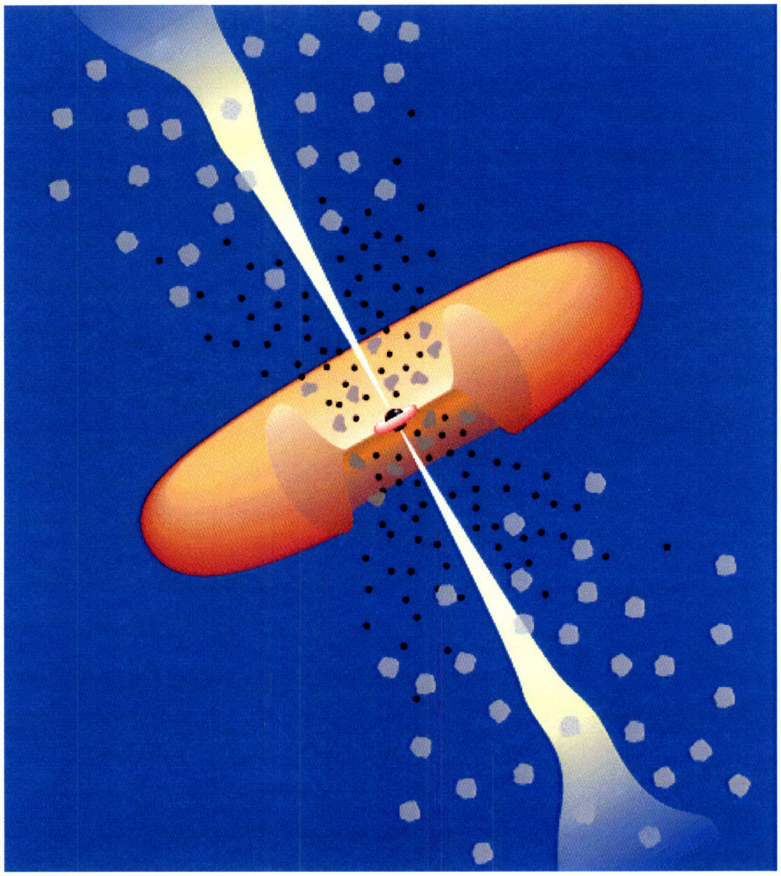

Figure 1-1: An AGN in the standard unification model. At the center, a SMBH is encircled by an accretion disk. At larger scales, the torus obscures the central region from some angles of view. Line-emitting clouds are part of an absorbing outflow. The central region produces a powerful, relatively narrow jet. From M. Urry's web page, with permission. Copyright ASP, reprinted with permission of the authors.

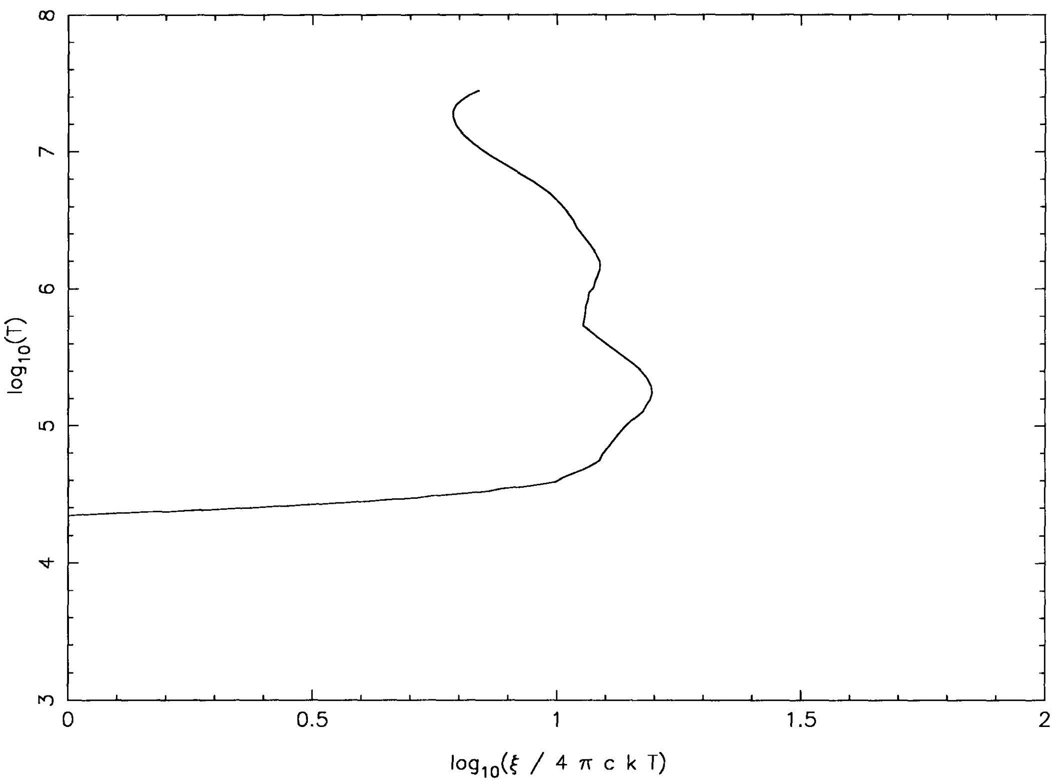

Figure 1-2: Plot of $\log_{10}$(temperature) vs. $\log_{10}(\Xi \equiv \xi/4\pi ckT)$. The data were produced using an XSTAR model applied to the broken power law ionizing continuum estimated for MR 2251-178 and described in Gibson et al. (2005).

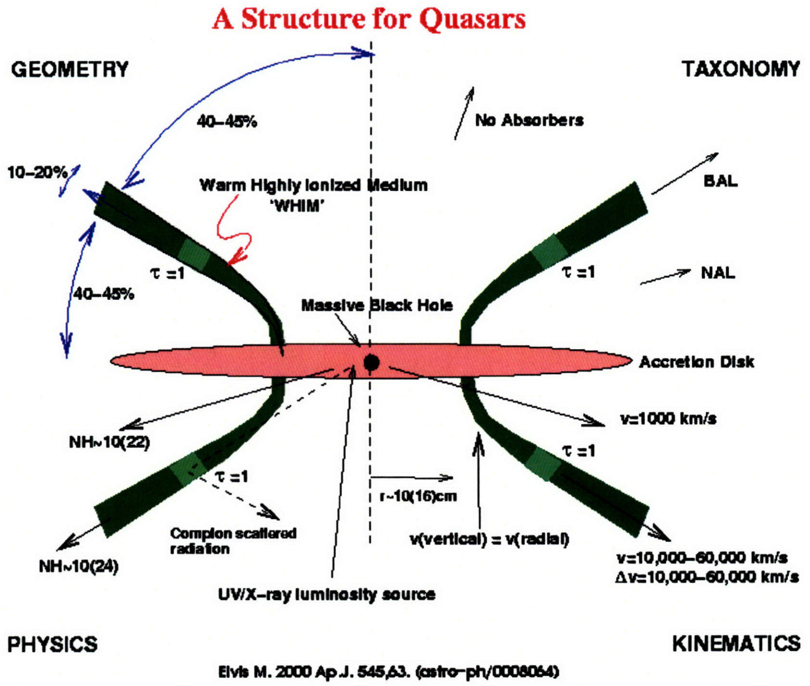

Figure 1-3: The outflow model of Elvis (2000), described in §1.1.2. This figure was obtained from Martin Elvis' web site and used with his permission.

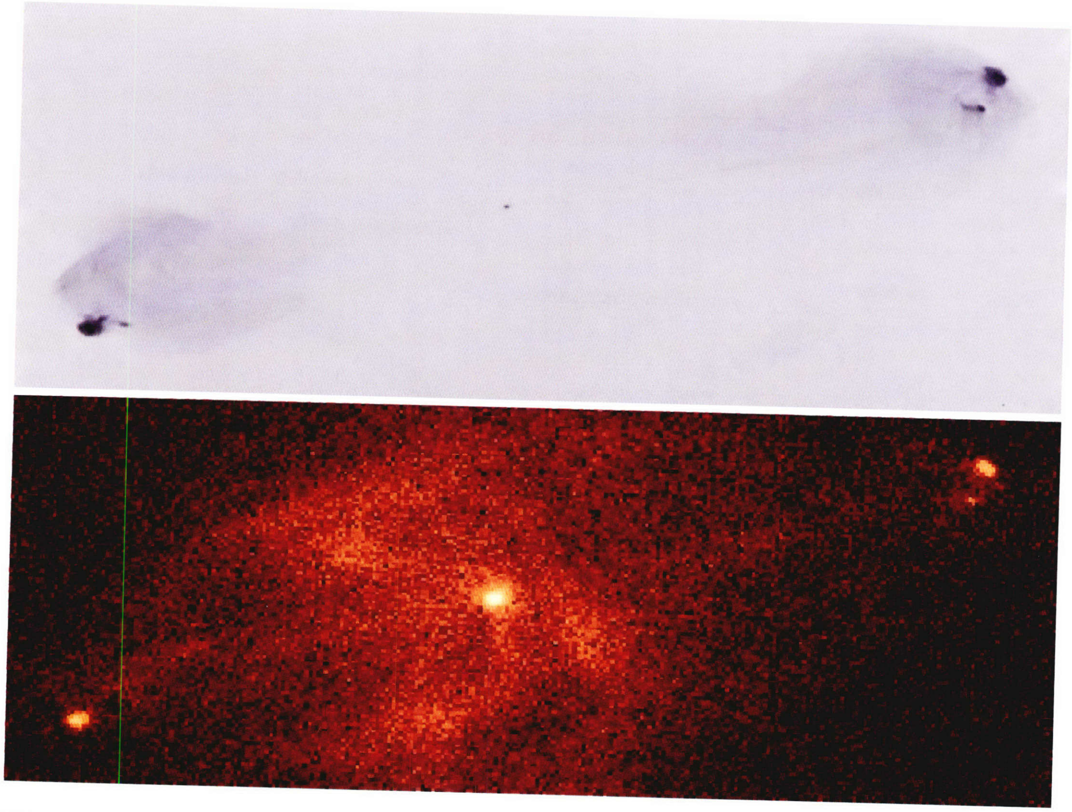

Figure 1-4: On the top: a 5 GHz VLA observation of Cygnus A with 0.4″ resolution. The data were published in Perley et al. (1984). This image was obtained from the NED database. On the bottom: a 35 ks ACIS-S image from the *Chandra* data archive, obsid number 00360. At a luminosity distance of about 220 Mpc, each 0.5″ ACIS-S pixel is about 2 kpc; the entire image is about 150 kpc from left (east) to right (west).

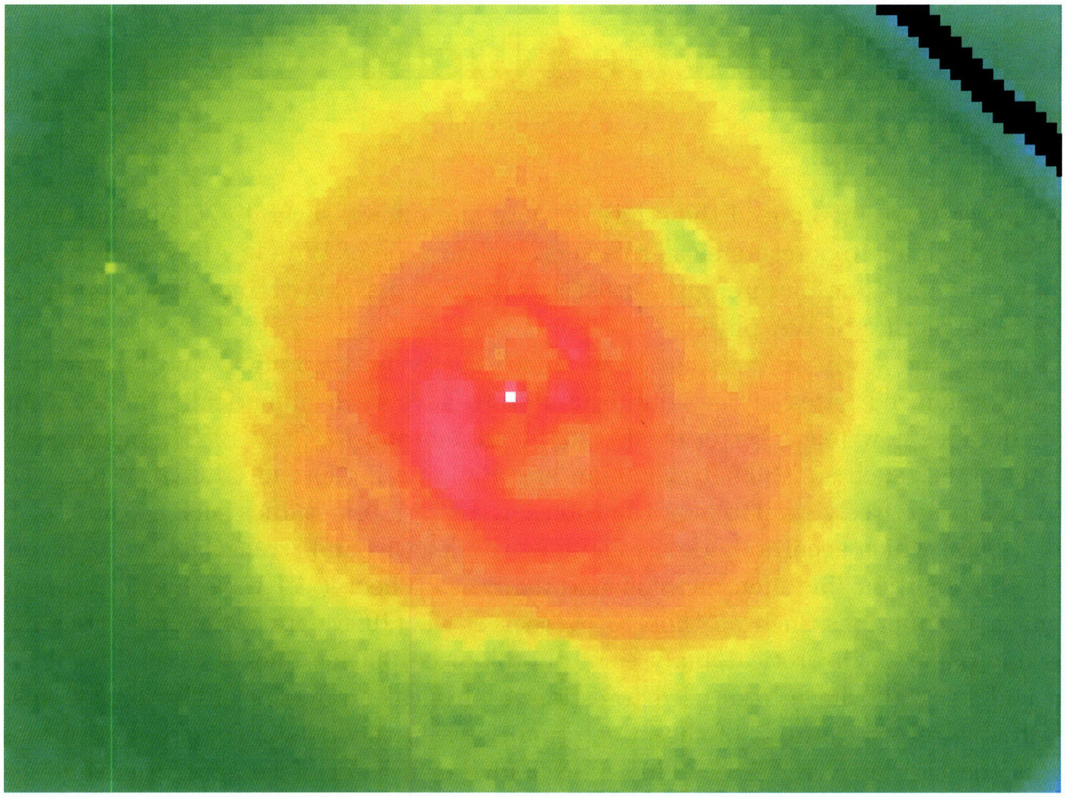

Figure 1-5: A 170 ks ACIS-S image of Abell 426, the cluster surrounding NGC 1275. This image was taken from the *Chandra* data archive, obsid number 04952. The diagonal stripes are artifacts of the CCD imager. A feature which is apparently a "flattened bubble," like the head of a mushroom cloud, is visible to the northwest (top right). At an angular diameter distance of about 70 Mpc, the figure is about 150 kpc from left to right.

Chapter 2

The Physics of Warm Absorbers in Active Galactic Nuclei

In Chapter 1, we introduced the study of WAs and offered several explanations for why it has been difficult to determine the role and configuration of WAs in AGN. This would seem to paint a depressing picture; given existing observational constraints, how can we hope to get a clear picture of WA physics?

In fact, the study of WAs has been aided greatly by theoretical and laboratory studies. Photoionized gases in the equilibrium state have been numerically modeled for over three decades now (e.g., Tarter et al. 1969; Kallman and McCray 1982), and several competing models such as XSTAR (Kallman and Bautista 2001) and CLOUDY (e.g., Ferland et al. 1998) are freely available on the Internet. Laboratory studies such as those of Brown et al. (2002) which accurately determine line wavelengths and strengths have been valuable for high-resolution line identification and analysis. Theoretical wavelength and oscillator strength calculations such as those of Verner et al. (1996) are commonly cited in spectroscopy papers. Theoretical analyses of photoionized plasma lines such as that of Porquet and Dubau (2000) have been used to estimate physical properties of the ionized gas. One remarkable recent example of the interaction between theorists and astrophysical observation is the case of NGC 3783. This AGN had shown a set of Fe absorption line features that were nearly at rest, several hundred km s^{-1} redshifted from the rest of the absorbing outflow. A large number of lines were found to be at rest, and it was considered unlikely that their theoretical wavelengths could all be off by a similar amount. Yet a recent study by Gu et al. (2005) (included in this thesis) found that theoretical calculations had indeed underestimated the wavelengths of relevant Fe ion lines consistently. Their new calculations brought the Fe absorber to the same velocity as the rest of the outflow.

We have constructed a set of XSTAR (Kallman and Bautista 2001) transmission models of WA absorption for illustrative purposes. The underlying continuum is assumed to be a broken power law approximating the measured continuum of MR 2251-178. For a complete description of the continuum used, see Gibson et al. (2005). In Figure 2-1, we show the effect of varying the absorber column density N_H for a fixed ionization parameter $\xi = 10$ erg cm s^{-1}. In Figure 2-2, we show the effect of varying ξ for a fixed column density $N_H = 10^{23}$ cm^{-2}.

The absorption edges in the example of Figure 2-1 are predominantly neutral, while only small hints of He-like ion shells are present in absorption. At higher ξ, as seen in Figure 2-2, neutral shells give way to ionized shells. At $\xi = 100$ in this example, He-like ions such as

O VII and Ne IX produce strong edges. At $\xi = 1000$, the He-like ions have been largely destroyed except at the high atomic numbers of silicon, sulphur, etc. H-like ion edges now dominate, particularly the edge of O VIII.

Increasing or decreasing ξ scales the normalization of the (UV and X-ray) ionizing continuum, but the shape of the ionizing continuum also determines the ionization state. Therefore, it is not possible to compare values of ξ calculated for different continua except in a very approximate sense. Continuum shape has a large effect on the ionization stages present at a given value of ξ. For example, a broken power law with an enhanced UV intensity over a single power law continuum will tend to ionize L and M shells to higher levels for a given ξ. However, it will be less effective at K shell ionization. The end result is that He-like ions will be present at lower ξ and over a wider range of ξ for a UV-enhanced continuum.

Figure 2-3 shows a sample plot of ionization fractions vs. ξ for the element magnesium. The He-like ion is particularly prominent in this figure because the continuum used in the XSTAR model has an enhanced UV continuum over the X-ray, and because He-like ions have high ionization potentials compared to ions with more electrons[1]. The He- and H-like stages are important over a wide range of ξ typically seen in AGN.

Other definitions of an ionization parameter have been used by photoionization models. Perhaps the most common form is

$$U = \int \frac{L_\nu / h\nu}{4\pi n r^2 c} d\nu, \tag{2.1}$$

where L_ν is the luminosity density per frequency ν. U is a measure of the ionizing photon number flux at radius r. It can be related to ξ by:

$$\xi = U \frac{L_{ion} hc}{D_L^2 \int f_\nu / \nu d\nu}, \tag{2.2}$$

where f_ν is the source flux density (e.g., Blustin et al. 2004). The ionization parameter U is useful for calculations that require counting photons; the parameter ξ is easier to calculate. Both require an assumed shape for the ionizing continuum.

2.1 Constructing a WA Model

Detailed X-ray photoionization models for a uniform cloud irradiated by a point source were first produced by Tarter et al. (1969) and Tarter and Salpeter (1969). They calculated ion fractions as a function of ξ and used them to calculate effective edge absorption cross sections. They also considered radiative transfer effects in order to estimate the emitted radiation from a multi-zone cloud. In order to calculate ionization balances and gas temperature as a function of ξ, they employed the following algorithm.

1. For a given value of ξ, guess a value of the electron temperature T_e.
2. Compute equilibrium ionization balances for the assumed T_e.
3. Derive heating and cooling rates from the predicted ionization levels and assumed T_e.

---

[1] It requires much more energy to remove electrons from the inner orbital shell than from other shells, of course, so He-like ions are not as easy to ionize as, say, Li-like ions for a given continuum. A continuum with a strong UV component can ionize Li-like ions, but X-rays are needed to ionize He-like ions of Mg.

4. Equilibrium is found when heating and cooling rates are equal.
5. If heating and cooling rates are not equal, raise or lower the guess T_e appropriately and repeat the procedure.

Modern photoionization codes use essentially the same procedure to find equilibrium states for a single-zone absorber.

Using some of the papers which were foundations of the algorithms in XSTAR, such as Halpern and Grindlay (1980), Krolik et al. (1981), and Kallman and McCray (1982), we have constructed our own model of a single-zone photoionized plasma as part of a study into the processes involved in WA physics. Because existing photoionization codes (e.g., XSTAR) can create these models in a much more rigorous and complete fashion, we have not carried this work beyond the stage of achieving rough agreement with XSTAR models. In particular, we have not implemented the important Augér processes, which can involve transitions between ions more than one level apart, making a simple treatment of ionization balance impossible. We have listed pseudocode here describing the main procedures in our simple, single-zone photoionization model to illustrate the complex physics involved. The algorithms involved are not all easily found in the foundational papers, so this description will useful for future reference.

2.1.1 Determining Ionization Balance

`Photoionization Rate:` $PIR \equiv \int 4\pi J(\nu)\sigma(\nu)d\nu$
`Collisional Ionization Rate:` $CIR \equiv n_e C(T_e)$
`Radiative Recombination Rate:` $RR \equiv n_e \alpha_{rr}(T_e)$
`Dielectronic Recombination Rate:` $DR \equiv n_e \alpha_{dr}(T_e)$
`Require: (PIR + CIR) / (RR + DR) = 1`

For a given value of T_e, calculate these rates and iterate with different assumed values of n_e until the combined ionization and recombination rates balance. This gives an approximate ionization balance and hence n_e corresponding to T_e.

Here $J(\nu)$ is the mean ionizing intensity in erg cm^{-2} sec at frequency ν, σ is the ionization cross section, n_e is the electron number density, $C(T_e)$ is the collisional ionization coefficient as a function of the electron temperature T_e, α_{rr} is the radiative recombination coefficient, and α_{dr} is the dielectronic recombination coefficient. Functional forms for the cross section and the various coefficients can be found in the literature indexed at a website managed by Dima Verner: `http://www.pa.uky.edu/ṽerner/atom.html`.

We note that the algorithm given here does not account for coupling between ionization stages more than one level apart, as can occur when Augér processes are considered.

2.1.2 Determining T_e for Given ξ

Given a value of ξ, choose an (educated) estimate of T_e. Then calculate the electron heating and cooling rates as follows. Keep guessing values of T_e until an equilibrium condition is reached in which the net heating and net cooling are equal. In what follows, J_ϵ is $dJ/d\epsilon$, where ϵ is photon energy. Heating and cooling rates are given in erg cm^{-3} s^{-1}.

Photoionization Heating

Photoionization heats the electron gas by ejecting energetic electrons from atoms into the gas.

`Photoionization Heating Rate =` $n_i \int_{\nu_{th}}^{\infty} 4\pi J_\epsilon \left(1 - \frac{\nu_{th}}{\nu}\right) \sigma_i(\nu) h d\nu$

Here n_i is the number density of the ion with cross section σ_i, ν_{th} is the ionization cross section threshhold energy and h is Planck's constant.

Bremsstrahlung Cooling

Bremsstrahlung cools the electron gas by converting electron energy into radiation, which is assumed to escape from the gas in an optically thin model.

`Bremsstrahlung Cooling Rate =` $1.42 \times 10^{-27} \sqrt{T_e} z_i^2 n_e n_i$

Here z_i is the ion charge.

Recombination Cooling

Recombination (radiative and dielectronic) cools the electron gas by removing energetic electrons. It is assumed (somewhat inaccurately) that each recombining electron gives up $3/2 k_B T_e$ of energy. Kallman and McCray (1982) roughly estimate that dielectronic recombination releases a photon with energy approximately equal to that of the lowest resonance line of the recombining ion, but if we assume that photon escapes the thin absorber there is no need to account for it.

`Recombination Cooling Rate =` $n_i n_e \frac{3}{2} k_B T_e (\alpha_{rr} + \alpha_{dr})$

Here k_B is Boltzmann's constant.

Collisional Excitation Cooling

Electrons colliding with atoms can excite electrons which then emit photons as they decay to ground. The photons are assumed to escape the single-zone gas, effectively transferring energy away from the electron gas.

This is a complicated calculation. We have used the approximation of Kato (1976) Equation (3) along with the line list of Verner et al. (1996).

Compton Heating and Cooling

Compton processes include heating by photons scattering off the electrons (including the Klein-Nishina correction to lowest order) as well as cooling by hot electrons transferring energy to photons.

`Net Compton Heating =` $\frac{\sigma_T}{m_e c^2} n_e \left(\int \left(\epsilon - \frac{21}{5} \frac{\epsilon^2}{m_e c^2} \right) J_\epsilon d\epsilon - 4 k_B T_e \int J_\epsilon d\epsilon \right)$

Here σ_T is the Thomson cross section, m_e is the electron mass, and c is the speed of light.

2.2 Additional Complexity

The photoionization model described in §2.1 is obviously a complex calculation heavily dependent on atomic data and theoretical descriptions of processes such as Compton scattering. Such models are generally believed to be appropriate descriptions of WA physics. However, there are several qualifications that should be kept in mind when using these models. We briefly describe them in this section.

Photoionization models assume that the gas is in an equilibrium state where heating and cooling processes are balanced. It is assumed that heating and cooling time scales are short enough that equilibrium can be maintained as the physical properties of the gas change. If the gas is able to change its physical structure faster than it can equilibrate, for example, typical photoionization models will not apply. AGN X-ray continua frequently vary in both shape and amplitude on very short time scales, and absorbing structures could be thicker than a few light seconds, so continuum variation could easily result in a non-equilibrium state. Due to such issues, we believe that time-varying photoionization models (which also account for WA structure) should also be developed and studied.

Existing photoionization models assume that the absorber is optically thin. This is evident from the form of the ionization parameter $\xi \propto L_{ion}/r^2$, which assumes that dilution of the ionizing continuum is solely geometric. In reality, the continuum will scatter backwards and in non-radial directions. Some continuum transfer can be handled assuming a simple geometry (e.g., spherical or slab) for the absorber, but more realistic absorber geometries cannot be treated by current codes. Emission line photons will also tend to scatter and be re-absorbed due to the high optical depth in lines. Codes such as XSTAR calculate a probability that a line photon emitted inside the absorber will escape the absorber. This probability is used to determine an emission spectrum and continuum evolution in line wavelength regions.

Line radiation from lower electron levels is treatable with sufficient computing power. Codes construct a matrix of all treated level transition rates and solve that matrix to determine an equilibrium condition. Only a finite number of electron levels can be treated this way. Ions have an infinite number of electron levels which cannot be handled directly. Codes commonly group the upper electron levels into "superlevels," which represent an infinite sum of upper levels. Given that a large number of lower levels can be treated with existing codes, this is probably not a bad approximation.

2.3 The Typical Warm Absorber

Observations have found that WAs can generally be found in complex configurations. The X-ray and UV absorbers naturally exhibit different ionization levels. Even the X-ray WA alone can contain lines from several different levels of ionization. For example, the WA of NGC 3783 (Kaspi et al. 2002) shows lines from FeXXV, NeIX, and NVI. No single ionization stage can produce significant ionization fractions of these three ions. It is common to see absorption lines from H- and He-like Ne, Mg, and Si. (These lines lie in the region of maximal *Chandra* MEG response.) Lines from O, S, Fe, and even Ca may also be present. Other lines may be detected, such as the inner-shell lines described in Behar and Netzer (2002).

Absorbers may also be detected by the combined effect of photoionization edges from all the ions present in the absorber. Unlike lines, these edges leave a broadband imprint (typically) in a soft X-ray spectrum. Several studies with *XMM-Newton* have claimed to find edge structures from multiple absorbers, such as for MR 2251-178 (Kaspi et al. 2004). The edges are typically smeared together and complicated by resonance structure, so even with high resolution, it is difficult to distinguish edge features from individual ions.

Absorption systems can frequently be found at multiple velocity shifts. A typical outflow velocity is several hundred km s^{-1}. These lower velocity outflows may be accompanied by higher velocity outflows such as ones at -1300 km s^{-1} in NGC 3783 (Kaspi et al. 2002), or -2000 km s^{-1} in MCG -6-30-15 (Sako et al. 2003; Young et al. 2005). A handful of sources have also shown evidence for highly-ionized, high-velocity outflows. These absorbing outflows, if real, are frequently detected as FeXXVI lines with "edge-like" shapes flowing outward at about 5-40% of the speed of light. Some example galaxies for which such outflows have been detected are PG 1115+080 (Chartas et al. 2003), APM 08279+5255 (Chartas et al. 2002), and MR 2251-178 (Gibson et al. 2005).

Blustin et al. (2004) have compiled a set of WA measurements from 14 AGN which have been recently observed. They find equivalent hydrogen column densities generally in the range of $21 \leq \log_{10}(N_H) \leq 22$ for Type 1 AGN, with a few instances at higher N_H. Values of ξ are widely distributed in the range $0 \leq \log_{10}(\xi) \leq 3$ with two outliers $\log_{10}(\xi) = 3.4, 3.7$ in highly-ionized, high-velocity outflow systems.

2.4 Analytical Models of WA's

In some cases, we can directly measure absorber characteristics, such as ionization level. In other cases, we can analytically derive absorber characteristics with a high degree of confidence in the result. For cases where estimates must be made, researchers have developed a set of analytical approximations used to measure WA characteristics based on observable quantities. We emphasize that these are approximations, frequently based on assumptions of spherical geometry and homogeneity which we know to be untrue. Many of these approximations have been tabulated by Krolik (1999) and Blustin et al. (2004). In this section, we list some estimates of WA properties which may be calculated from observable quantities.

2.4.1 Column Density

The column density of a specific ion is simply defined as

$$N_i \equiv \int_{r_0}^{r_1} n_i(r)dr, \tag{2.3}$$

where $n_i(r)$ is the ion number density at radius r, and the absorber extends from r_0 to r_1 along the line of sight. In general, the density is a complicated function of radius, even when the absorber is not strongly clumped. Given that the absorber thickness Δr is believed to be much smaller than its distant from the continuum source, the approximation $N_i = \langle n_i \rangle \Delta r$ is frequently used, assuming some average density $\langle n_i \rangle$. Column densities are frequently expressed in terms of the "equivalent hydrogen density," N_H, which is calculated by using the sum of the densities for neutral and ionized hydrogen. Converting between an individual ion column density and N_H requires assuming elemental abundances for the given ion, which are usually assumed to be the same as solar abundances (e.g, Anders and Grevesse 1989). N_H is therefore the number of neutral or ionized hydrogen atoms expected to be intersected by a radial beam of area 1 cm^2.

There are two commonly used methods of calculating N_H. The first method is to fit a spectrum with a model of a photoionized absorber. Such a model fit actually measures individual ion column densities by fitting absorption lines and also the overall combined shape of photoionization edges. N_H is therefore dependent on the fit value of ξ and also assumed element abundances.

N_H can also be determined analytically from a measurement of the equivalent width (EW) of a single line. Assuming the intrinsic line shape is Gaussian, and assuming a line velocity dispersion (which can be measured directly if the line is resolved), the EW can be uniquely associated with an ionic column density (Spitzer 1978). This works best on the "linear part of the curve of growth," where the EW is proportional to the column density. For larger column densities, absorbing atoms begin to radially screen each other, so that the EW nearly "flattens" as a function of column density. Unfortunately, many *Chandra* line measurements fall in this "flat part of the curve of growth" where lines do not respond as sensitively to column density. Still, ionic column densities are in principle calculable from measured data. As with the model-fitting method, an ionization fraction and elemental abundance must be assumed to convert from an ion column density to N_H.

2.4.2 Temperature

Thermal effects in an absorber at temperature T made of particles of mass m produce a Gaussian line of full width at half maximum (FWHM) 2.35σ, where $\sigma = \sqrt{kT/m}$. For typical temperatures of photoionized plasmas, these velocity dispersions are relatively low. At $T = 10^5$, $\sigma \approx 30$ km s^{-1}. This is well below the typical resolution of the *Chandra* HETG. Nonetheless, observers often detect resolved lines in HETG spectra, with widths well over 100 km s^{-1}. These lines are apparently not broadened by purely thermal effects.

Temperatures can be estimated in one of two ways. Firstly, photoionization models require (through the assumptions used to generate them) a single temperature for each value of the ionization parameter ξ. (The ionization parameter Ξ is different from ξ and may take multiple values of T.) Thus, under the assumption of equilibrium, determining the ionization level is equivalent to determining a gas temperature. Secondly, plasma diagnostics on He-like emission line triplets may be used as described in Porquet and Dubau (2000) to constrain temperatures (and densities) in the absorbing and emitting material. This requires both a good measurement of the triplet line profiles (which is difficult for AGN) and the assumption that emitting and absorbing material are in the same physical state (which is probably unreasonable for AGN). The process is described in more detail in §2.4.4.

Temperatures may be measured directly using other methods, but these methods are not commonly successful for X-ray observations. Ionized gases emit bremsstrahlung spectra characteristic of the gas temperature, but these have not been isolated in AGN spectra. Electrons recombining into the high number of upper levels in an ion will produce "radiative recombination continuum" (RRC) features in an X-ray spectrum which can be used to measure the electron temperature (e.g., Ogle et al. 2003; Liedahl 1999).

2.4.3 Time Scales

Although observing constraints make it difficult to obtain good measurements of variability data, such measurements can be very useful for determining properties of the photoionized material. We describe here a few important time scales important for photoionized gas.

Ionization Time Scale

For highly-ionized material, ionization levels are primarily driven by photoionization (PI) rates in and out, collisional ionization (CI) rates in and out, and radiative recombination rates (RR) in and out. The rate dn_i/dt of number density change of a particular ion i is the sum of these rates. We estimate the ionization time scale as

$$\tau_{ion}(\xi, n) \equiv \frac{n_i}{|dn_i/dt|} \tag{2.4}$$

$$= \frac{n_i}{|PI_{in} - PI_{out} + CI_{in} - CI_{out} + RR_{in} - RR_{out}|}, \tag{2.5}$$

where ξ is the ionization parameter, n is the total gas number density, n_i is the number density of the ion in question, and t is time.

This calculation seems straightforward, but there is a catch. Single-zone photoionization models calculate ionization balances and gas temperatures under the assumption of equilibrium, so that the denominator of equation (2.5) will be zero. The definition of the ionization time scale is an artificial estimate that becomes singular in the case of equilibrium. (In equilibrium, the ionization levels do not change, so the time scale is infinite.) To solve this problem, researchers typically perturb the gas characteristics from equilibrium slightly and estimate time scales from a sample of these near-equilibrium states. Krolik (2002) notes that photoionization and radiative recombination terms typically dominate the equation, so rough estimates can actually be computed rather simply. Depending on the ionizing continuum and especially the gas density, these times can vary widely.

Flow Time Scale

The flow time scale is an estimate of how much time is required to see significant changes in the gas due to radial velocity v_r. It depends on the gas radius r:

$$\tau_{flow} \equiv r/v_r. \tag{2.6}$$

A flow at $r = 10^{17}$ cm moving at 1000 km s^{-1} has a flow time scale of 10^9 sec, or about 30 years. If the flow time scale can be measured, it can be used to estimate the WA location and therefore discriminate between unification models.

Cooling Time Scale

The cooling time scale is the the time over which a gas at temperature T can lose significant amounts of heat, allowing it to cool to the equilibrium temperature. It is given in terms of the electron density n_e and the cooling rate Λ as:

$$\tau_{cool} \equiv \frac{3k_BT}{n_e\Lambda}. \tag{2.7}$$

In practice, Λ depends on the state of the gas.

Gas cools very efficiently through line emission. When gas is not highly ionized, the cooling time scale can be shorter than the ionization time scale. At high ionization levels, the situation is reversed (Krolik 1999).

2.4.4 Number Density

There are several methods of estimating the number density of ionized material. Each has its own limitations, and some are very rough approximations. As a result, the number density of WAs remains unknown.

Ionization Time Scales

Ionization time scales, described in §2.4.3, depend sensitively on the number density of the ionized material. Recombination and collisional processes depend on the square of the density, while photoionization involves one factor of particle density and one factor of the photon density. Detections of variation on a certain time scale allow for lower limits on the number density; at lower densities, the material wouldn't be able to respond to ionization changes coherently in the measured time.

"Triplet" Ratios

With high-resolution X-ray spectroscopy, it has become possible to measure "triplet" emission lines from $n = 2$ to $n = 1$ transitions of He-like ions. There are actually four lines in the triplet, but higher resolutions are required to distinguish two of them. The lines are: resonance ($^1P_1 \rightarrow ^1 S_0$), intercombination ($^3P_2, ^3 P_1 \rightarrow ^1 S_0$), and forbidden ($^3S_1 \rightarrow ^3 S_0$). The $^3S_1$ state is metastable; spontaneous transitions to ground are "forbidden," which merely means they occur more slowly than "allowed" transitions. In a dense gas, collisional excitation $^3S_1 \rightarrow {}^3P_{0-2}$ can easily occur before a spontanous decay. In an ionized gas, the $^1P_1$ and $^3P_{0-2}$ levels are populated by radiative cascades driven by recombination and collisional excitation processes, which are temperature-dependent.

Important information can be obtained from two population ratios which can be measured for the emitting material by comparing the appropriate triplet line strengths. The first ratio is a temperature diagnostic. The combined intercombination and forbidden line strength removes any density dependence in the $^3S_1 \rightarrow {}^3P_{0-2}$ transition. Compared to the resonance line strength, this ratio gives an estimate of the emitting gas temperature which controls how important collisional excitation processes (which preferentially populate the $^1P_1$ level) are. The ratio of forbidden line to intercombination line strengths is an indication of how quickly collisional processes are depleting the $^3S_1$ level by exciting electrons to $^3P_{0-2}$. This is an indicatore of the electron density.

Detailed calculations of these line ratios as a function of temperature and density have been performed by Porquet and Dubau (2000). In practice, using these diagnostics is complicated by our inability to measure all the triplet lines due to an insufficient number of photons or due to confusion with other atomic processes in the line region. The resonance line frequently shows up in absorption, making it difficult to know how many photons were originally present in emission.

Ionization Parameter

The ionization parameter $\xi = L_{ion}/nr^2$ can be used to estimate the number density n if an independent measure of the radius r from the continuum source is available. This is not typically the case, unfortunately. The use of this method is also subject to the caveats for modeling photoionized gases described in Chapter 1. For a continuum emitter with ionizing luminosity $L_{ion} = 10^{44}$ ergs s^{-1} and a gas at distance $r = 10^{18}$ cm with $\xi = 100$, we estimate $n = 10^6$ cm^{-3}. If we use a smaller radius $r = 10^{16}$ cm, we find $n = 10^{10}$ cm^{-3}.

Column Density

We discussed methods of determining the absorber column density in §2.4.1. The particle density can be estimated by $n = N_{WA}\Delta r$, where N_{WA} is the WA column density (for all particles) and Δr is the extent of the WA along the line of sight. This approximation is rather unreliable, as absorbers are actually found to be highly structured along the line of sight, and it is in any case difficult to determine Δr, though a rough approximation is frequently used that $\Delta r \approx r$.

2.4.5 Mass and Energy Outflow Rates

Mass outflow rates may be estimated assuming the outflow is a section of a sphere subtending $\Omega/4\pi$ sr which expands at constant ionization parameter ξ (i.e., the number density $n \propto r^{-2}$).

$$\begin{aligned} \dot{M} &= 4\pi r^2 v n \frac{m_p}{0.7}\frac{\Omega}{4\pi} && (2.8) \\ &\approx \frac{4\pi L_{ion} v}{\xi}\frac{m_p}{0.7}\frac{\Omega}{4\pi}, && (2.9) \end{aligned}$$

where m_p is the proton mass, the ratio $m_p/0.7$ is the approximate mass per particle of a gas with solar abundances, and v is the outflow velocity. The kinetic energy outflow is then $1/2\dot{M}v^2$.

In several cases, it appears that WA mass outflows are comparable to or larger than the accretion rates, although the kinetic energy outflows are comparatively small (Blustin et al. 2004).

2.4.6 Launching Radius

If a blob of material starting at rest is accelerated by radiation pressure in the gravitational field of the central black hole (BH), we may estimate the blob velocity v according to an energy balance equation. The change in kinetic energy of the absorbing blob is equal to the change in (gravitational) potential energy plus the amount of energy imparted to the absorber through momentum transfer from the radiation.

The energy imparted is the integral of the radiation force over the distance traveled. For Thomson scattering of a continuum with luminosity L, a blob of material at radius r covering solid angle $\Omega/4\pi$ receives energy

$$E = \int_{r_1}^{r_2} \frac{L\sigma_T}{4\pi r^2 c}\frac{\Omega}{4\pi}dr, \qquad (2.10)$$

where σ_T is the Thomson scattering cross section. Simulations have shown that photon scattering in atomic line regions is more effective at transferring energy than Thomson scattering for material which is not highly ionized. Previous studies have estimated the ratio of energy transfer from line scattering compared to Thomson scattering, allowing for an estimation of the total energy imparted from scattering (e.g., Arav et al. 1994; Laor and Brandt 2002).

Chartas et al. (2002) used an energy balance equation (with some mathematical approximations) to estimate the launching radius of a high-velocity wind in the quasar APM 08729+5255. Assuming the wind was launched from a radius of 2×10^{17} cm, Chartas et al. (2002) concluded that the high-velocity wind detected in their spectrum reached terminal velocity rapidly and thus was very near the launching point (or else it would have recombined to lower ionization levels as it moved rapidly outward). If a terminal velocity can be estimated, the energy balance equation can also be used to estimate the launching radius.

2.4.7 Solid Angle

Sometimes referred to as the "covering fraction" or the "global covering fraction," this is a measure of the solid angle subtended by the WA, from the point of view of the central source. This can be estimated by comparing the emission line strength to absorption line strength for a single line (in the case of a P-Signi profile) or for a pair of lines with predictable atomic properties. This sort of calculation is not frequently performed because of the difficulty of measuring the necessary line strengths in X-ray spectra of AGN. However, we did use a calculation of this form with triplet line ratios in the case of MR 2251-178, discussed later in this thesis (Gibson et al. 2005).

2.4.8 Volume Filling Factor

The volume filling factor is an estimate of the fraction of space which is filled by the WA. A smooth, space-filling WA would have a filling factor of 1. A very clumpy WA would have a much smaller volume filling factor. The filling factor at a specific location is estimated by

$$f_v \equiv \frac{\langle n \rangle}{n}, \tag{2.11}$$

where $\langle n \rangle$ is the number density n averaged over space (e.g., Blustin et al. 2004).

2.4.9 Radius

Essential to most of the estimates of WA properties, the radius r of the WA from the central source is unfortunately difficult to determine. This is because radius is typically degenerate with the number density n, as in the ionization parameter formula $r = \sqrt{L_{ion}/n\xi}$. An absorber at $\xi = 100$ with $n = 10^6$ cm^{-3} would be $r = 10^{18}$ cm distant from an ionizing luminosity $L_{ion} = 10^{44}$ ergs s^{-1}. If the density is $n = 10^{10}$ cm^{-3}, the distance is $r = 10^{16}$ cm. This calculation is complicated further if we do not have simultaneous observations of the UV and X-ray continuum, both of which contribute to L_{ion}.

An upper limit on the WA location can be estimated in the following way (e.g., Blustin et al. 2004). Starting with the column density N in terms of the mean number density $\langle n \rangle$ and the volume filling factor f_v (§2.4.8), we have $N \approx \langle n \rangle \Delta r \approx n f_v \Delta r$. Then using the definition of the ionization parameter ξ,

$$N \approx \frac{L_{ion}}{\xi r^2} f_v \Delta r \Rightarrow \tag{2.12}$$

$$\frac{\Delta r}{r} \approx \frac{\xi r N}{L_{ion} f_v}. \tag{2.13}$$

Our rough approximation assumes that r is chosen near the midpoint of the WA at a location representative of the average WA properties. Then we have the constraint that $\Delta r / r \leq 1$ and hence

$$r \leq \frac{L_{ion} f_v}{\xi N}. \tag{2.14}$$

For $L_{ion} = 10^{44}$ ergs s^{-1}, $f_v = 1$, $\xi = 100$, and $N = 10^{22}$ cm^{-2}, we have $r \leq 10^{20}$. Upper limits derived in this way usually do not strongly constrain the absorber location.

2.4.10 Mass

If we assume an absorber mass density of $\rho \approx 1.2 m_p n$, where m_p is the proton mass, and a column density $N \approx n\Delta r$, we can estimate the mass, M_{WA}, of WA material subtending an angle $\Omega/4\pi$.

$$\begin{aligned} M_{WA} &\approx 4\pi r^2 \rho \Delta r \frac{\Omega}{4\pi} && (2.15) \\ &\approx 1.2 m_p n r^2 \Delta r \Omega && (2.16) \\ &\approx 1.2 m_p N r^2 \Omega. && (2.17) \end{aligned}$$

Assuming $\Omega \approx 1.6$, Blustin et al. (2004) estimated Seyfert WA masses of about 80 $M_{\odot}$. Compared to the rather large estimated outflow masses seen in WAs, this indicates that either the WA is transient or that material is frequently added to it.

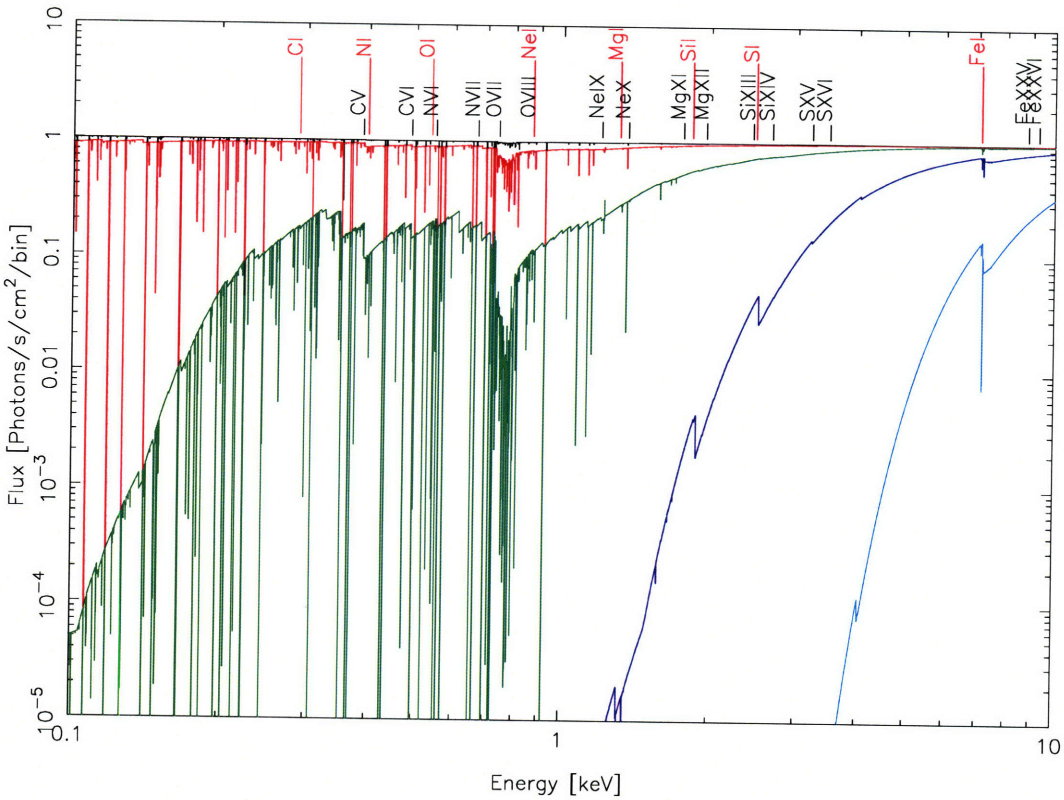

Figure 2-1: XSTAR WA transmission model with ξ fixed at 10 erg cm s^{-1}. Column densities are 10^{20} (black), 10^{21} (red), 10^{22} (green), 10^{23} (dark blue), 10^{24} (light blue) cm^{-2}. Theoretical locations of edges of H-like, He-like, and neutral ions are indicated, with the latter in red.

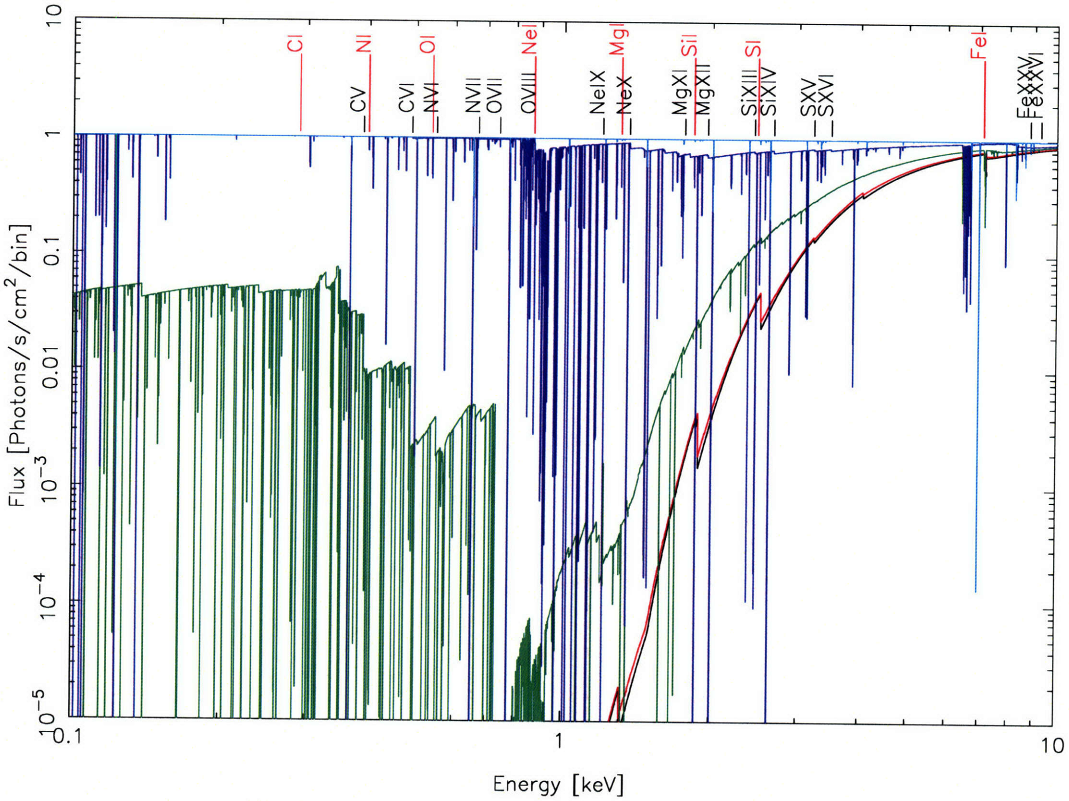

Figure 2-2: XSTAR WA transmission model with N_H fixed at 10^{23} cm^{-2}. Values of ξ shown are 10^0 (black), 10^1 (red), 10^2 (green), 10^3 (dark blue), 10^4 (light blue) erg cm s^{-1}. Theoretical locations of edges of H-like, He-like, and neutral ions are indicated, with the latter in red.

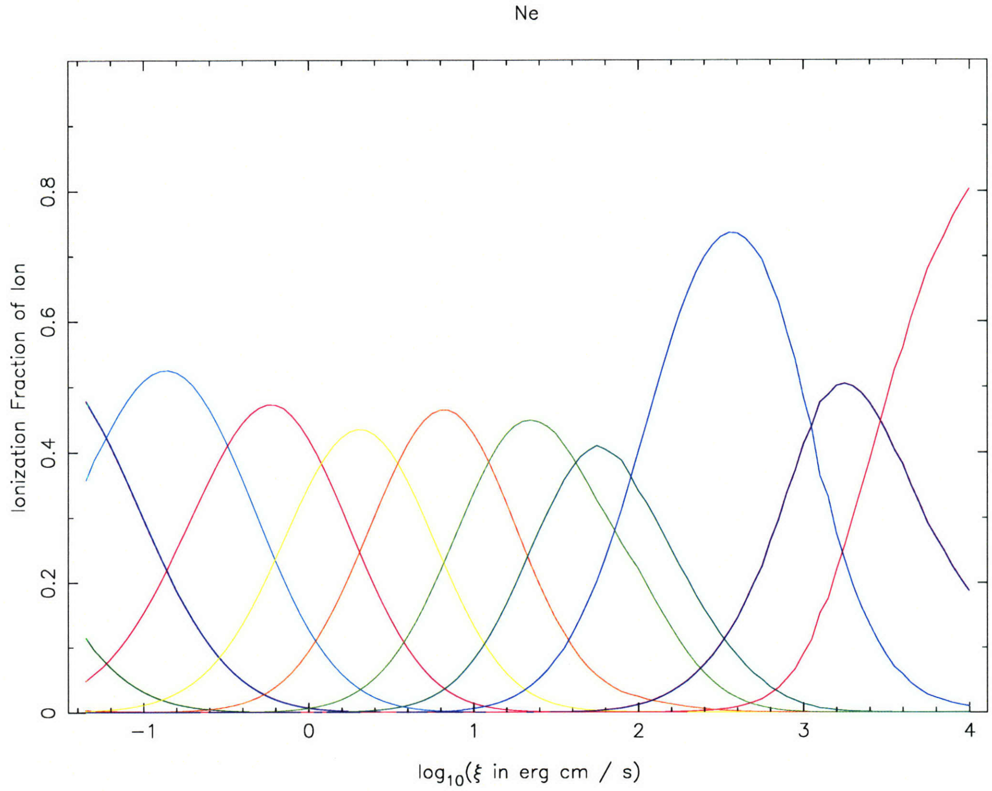

Figure 2-3: A sample plot of ionization fractions for neon produced with the photoionization modeling code described in this chapter. The He-like state (the third curve from the right) is very prominent and broad due to the strong UV component in the continuum.

Chapter 3

The History of Warm Absorbers

For over three decades now, researchers have been numerically modeling the ionization levels (and hence the absorption properties) of photoionized gas (e.g., Tarter et al. 1969; Kallman and McCray 1982). In 1984, it was proposed that variations in X-ray spectra of distant AGN were caused by an intrinsic, photoionized absorber. Since that time, high-resolution spectroscopy has revealed (often complex) systems of absorption lines and edges in many AGN. In this chapter, we discuss the history of spectroscopic observations of WAs in AGN. We include a discussion of important research questions which are closely related to the WA, such as the relation between the X-ray and UV absorbers and the possible presence of dust in the WA. We conclude with a brief summary of recent studies of two AGN which have strong, well-studied absorption systems: MCG -6-30-15 and NGC 3783. Throughout this chapter, we pay special attention to variability studies of AGN spectra.

3.1 MR 2251-178: The First Warm Absorber Discovered

MR 2251-178, at $z = 0.06398$ (Bergeron et al. 1983; Canizares et al. 1978), i.e., $cz \approx 19{,}200$ km s^{-1}, was discovered as an X-ray source by the *Ariel V* all-sky survey (Cooke, B. A., et al. 1978). It was the second quasar known to be an X-ray emitter, and the first to be identified from X-ray observations (Ricker et al. 1978).

Jules P. Halpern fit two *Einstein* monitor proportional count (MPC) spectra with an absorbed power law (Halpern 1984):

$$\frac{dN}{dE} = AE^{-(\alpha+1)}\exp(-\sigma(E)N_H) \text{ photons cm}^{-2}\text{ s}^{-1}\text{ keV}^{-1},$$

where N is the number of photons emitted, E is the photon energy, A is the "power law normalization" fit parameter, α is the "spectral index" fit parameter, N_H is the "equivalent neutral hydrogen column density" fit parameter, and $\sigma(E)$ is an integrated cross-section per hydrogen atom (Brown and Gould 1970). He found that the equivalent hydrogen column density, N_H, increased significantly from an upper limit of 5×10^{21} to $(2.3 \pm 1.2) \times 10^{22}$ cm^{-2} between the two observations, taken on 1979 June 1 and 1980 May 19, respectively. The spectral indices of the power law fits, 0.52 ± 0.17 and 0.72 ± 0.30, had not changed significantly, though the error bars on the measurements were admittedly large. Further analysis of the *Einstein* high resolution imager (HRI) count rates showed that the number of low energy (0.1-3 keV) counts was much higher in the 1980 observation than would be expected from extrapolation of the power law fit with *neutral* absorption. Even though the

HRI could not spectrally resolve the absorbed region, the number of counts in the entire 0.1-3 keV range was inconsistent with predictions of a neutral absorption model.

It was apparent that some form of absorption was responsible for the changes between the 1979 and 1980 spectra. In order to explain the complexity of the 1980 MPC and HRI spectra, Halpern considered two types of absorbers, which he called "cold" (neutral) and "warm" (ionized). The second option was favored because it naturally explained the relative transparency in the 1980 spectrum in (at least part of) the HRI bandpass. Low-energy opacity is due to L (and higher) shell electrons of abundant ions and to K shell electrons of ions with atomic numbers less than 8 (that of oxygen). In a gas which was ionized to the level where only H- and He-like oxygen survived, the gas would be largely transparent below 0.7 keV. Halpern used an early photoionization model (Halpern and Grindlay 1980; Halpern 1982) to fit the MR 2251-178 data and derived rudimentary constraints on the absorber temperature and radial distance from the continuum source. Although the electron temperature suggested by the fit, about 10^5 K, may seem relatively high, Halpern noted that it is actually "much cooler than a thermal plasma of similar ionization level," hence he described the absorber as "warm" rather than "hot."

3.2 Other Warm Absorbers

Warm absorbers (WAs) have since been invoked to explain the spectral charactistics of several well-studied galaxies.

Similarly to the spectrum of MR 2251-178, the soft X-ray spectrum of NGC 4151 showed evidence of absorption below 2 keV with a "soft excess" at lower energies. The absorption in NGC 4151 was initially interpreted in terms of a partial covering model in which a large column ($\sim 6 \times 10^{22}$ cm^{-2}) of cold gas covered about 90% of the continuum source, with the remaining 10% being relatively unobscured (Holt et al. 1980). This could arise, e.g., if the absorbing column were due to a small number (typically about two) of clouds moving randomly across the line of sight during an observation. Poisson fluctuations in the number of obscuring clouds would then account for the 10% leakage of soft flux.

However, (Yaqoob et al. 1989) analyzed 24 *EXOSAT* observations of NGC 4151 and found no evidence for a correlation between the cloud covering fraction and the absorber effective column density. They did, however, find a correlation between the effective absorbing column and the level of continuum flux in partial covering model fits. They pointed out that the soft excess could be explained by a warm absorber model in which ionization levels are high enough that edge cross sections do not significantly obscure soft X-rays, as Halpern had suggested earlier. Fixing the column density and spectral index to reasonable values, they found acceptable warm absorber fits to approximately 70% of the observations, and noted that allowing the column density and spectral index to vary would have improved their fit results.

In an early variability study, Nandra et al. (1990) broke a 3 day *Ginga* observation of the bright and highly variable active galactic nucleus (AGN) MCG–6-30-15 into seven consecutive segments of various sizes. They fit each spectrum separately with a WA model, finding that the level of ionization (as quantified by the "ionization parameter," discussed in Chapter 2) was strongly correlated with the flux level. However, the photon number index Γ and absorption column density N_H were assumed to be constant across all the fits. As later studies have shown that the continuum level and even shape can change even on intra-observation time scales, this assumption may have resulted in inaccurate fits. Nandra et al.

(1990) demonstrated that a WA model produced a significant improvement in the spectral fit over a simple powerlaw, and also that the spectrum of MCG–6-30-15 was variable, indicating that fits to the single integrated spectrum would result in an oversimplified description of the WA.

Attempts to characterize absorber variability with simplified models have been controversial. In the case of MR 2251-178, Pan et al. (1990) fit 15 *EXOSAT* observations with a WA model and concluded that the absorption column density decreased as flux increased. However, Pan et al. (1990) performed their fits with the power law spectral index set to a single value, assumed to represent an average for all the spectra. Walter and Courvoisier (1992) responded that it was unreasonable to assume a single value for all the power law indices; in fact, the data required otherwise. They found that a varying power law with a *constant* column density *cold* absorber were sufficient to satisfy the data. Adding to the list of interpretations, Mineo and Stewart (1993) fit a photoionized gas model against multiple spectra, finding that the gas column density remained roughly constant, while the ionization parameter varied.

NGC 5548 was another AGN which showed early evidence for a WA. Although Nandra et al. (1991) focused primarily on modeling the reflection component of *Ginga* and *EXOSAT* spectra in their paper, they found that their models of reflection from cold material required varying column densities in their fits. Because the largest columns were required in the lowest flux states, they surmised that they were not observing column density variation after all, but were instead observing ionization level variation in a warm absorber of some substantial (but essentially constant) column density. Their final model was a composite of both reflection and ionized absorption.

The nearby Seyfert 1 galaxy MCG–6-30-15 has been a source of much study, in part due to its brightness and variability. An ionized oxygen edge was detected from *Rosat* PSPC data by Nandra and Pounds (1992). The rest-frame energy of the edge was 0.825±0.017 keV, much higher than expected for neutral oxygen, but feasibly due to a blend of O VII and O VIII, which have edge energies of 0.739 and 0.871 keV, respectively. Assuming previous variation in the column density seen with *Ginga* was due to ionization changes over a time span < 9 months, an upper limit on the ionization time scale allowed the authors to derive a lower limit on the absorber density and an estimate of the absorber distance $r \approx N_H/n$ from the continuum source, where n is the approximate gas density. The authors found that $r < 2$ pc, indicating that the WA lay quite close to the continuum source.

Subsequent *ASCA* observations confirmed the presence of a strong edge at about 0.73 keV, consistent with an O VII edge (Fabian et al. 1994). The column density of the edge apparently varied between the two *ASCA* observations reported, taken approximately one month apart. Fits with photoionization models found $\log_{10}(N_H)$ to vary from 21.8 ± 0.1 to 22.13 ± 0.02. Though the cause of the variation remained unknown; Fabian et al. (1994) interpreted the observed correlation between column density and ionization parameter as an indication that material changes were occuring in the observer, rather than simple luminosity-driven changes in ionization level.

The change in column density in the MCG–6-30-15 WA merited another look. Reynolds et al. (1995) re-analyzed the *ASCA* observations used by Fabian et al. (1994) to search for WA variability with time in more detail. They confirmed the findings of Fabian et al. (1994), finding that the WA column density indeed doubled over three weeks. The ionization parameter ξ appeared to increase despite a significant decrease in ionizing luminosity. They split the observations further into shorter sections (of about 2 ks each) and fit the pieces with WA models. They were able to rule out the baseline hypothesis that N_H and the power law photon index Γ remained fixed while ξ varied proportionally to the ionizing flux. Defining the hardness ratio $R(x_1, y_1; x_2, y_2) \equiv C(x_1, y_1)/C(x_2, y_2)$, where $C(x, y)$ is the number (or rate) of counts between x and y keV, they found $R(2.5, 5; 0.4, 0.6)$ remained roughly constant while $R(2.5, 5; 0.7, 1.3)$ increased during one portion of the observation. This was attributed to changes in the WA, predominantly due to deepening of the O VIII edge. The O VII edge may also have increased in depth. The O VIII edge depth increase was associated with the previously-discovered doubling of N_H required by WA models. Reynolds et al. (1995) raised the possibility that inhomogeneities in the WA material and some degree of spatial extension of the continuum source could result in multiple lines of sight through the WA being observed in one integrated spectrum. In this case, recombination and photoionization time scale arguments based on a single-zone WA would be misleading. They also considered the possibility that the spectrum could be complicated by stratification (i.e., varying properties with radius) in the WA or that photoionization equilibrium models were an oversimplification of the absorber. They tentatively suggested that the edge variation was due to the passage of a warm cloud across the line of sight. Velocity arguments indicated that the cloud would be located in the broad line region (BLR).

A follow-up four-day observation of MCG–6-30-15 with *ASCA* by Otani et al. (1996) elaborated on the results and suggestions of Reynolds et al. (1995). They divided the observation into 17 pieces, each about 10 ks long. They found that the depth of the O VII edge remained roughly constant while the O VIII edge depth τ varied approximately as C^{-1}, where C is the instrumental count rate. This result, together with an apparent velocity difference between the two edges, supported the claim that WAs from two distinct absorbing regions were present in the line of sight. They claimed that the observed variation time scale of about $10,000$ s placed the O VIII absorber in the BLR with a small volume filling factor ($\Delta R/R < 0.003$), a density $n > 2 \times 10^7$ cm^{-3}, and a pressure $nT > 2 \times 10^{13}$ cm^{-3} K, similar to estimates of the BLR pressure. The O VII absorber, they claimed, was significantly farther out and more volume-filling, possibly associated with a torus wind. They noted that the failure of the O VII edge to vary with luminosity was mysterious in this model, though we note that the possibility of multiple (deflected) lines of sight through the WA raised by Reynolds et al. (1995) allows for seeing both absorbing systems without requiring that the inner system shield the outer system. Later studies showed that the feature attributed to the O VII edge had a more complicated structure than previously thought. Lee et al. (2001) found that the feature was actually composed of L shell edges of Fe combined with O VII absorption lines.

Ten years after its "discovery", observers were searching for the WA in samples of data. The *Ginga* LAC detector was sensitive to absorbing columns above a few $\times 10^{21}$ cm^{-2}. In a sample of 60 *Ginga* spectra of 27 Seyfert galaxies, Nandra and Pounds (1994) claimed that about half of the galaxies showed significant (confidence > 90%) improvement in their continuum fits when a WA model was added.

A survey of the *ASCA* spectra of 24 Seyfert 1 AGN supported the claim: half of the objects in the survey showed K-shell absorption edges from O VII and/or O VIII (Reynolds 1997). Including the two oxygen edges produced an improvement in the continuum fit at a 99% confidence level for 12 out of the 24 objects. The hardness ratio $R(2.5, 5; 0.7, 1.3)$ was found to vary (i.e., not constant at 90% confidence) for two sources: MCG–6-30-15 and NGC 3227. Reynolds (1997) also pointed out that rough calculations suggested that the WA mass outflow rate "greatly exceeds the accretion rate within Seyfert galaxies," and argued that rapid variability of the WA implied that some component of the WA was within $\sim 10^{17}$ cm of the central source. A similar study by George et al. (1998) of 23 *ASCA* observations of 18 objects found that more than half (13/18) of the objects contained a significant WA column. They further claimed that partial covering with a *warm* absorber improved several fits, and that including a model of emission from the ionized material also produced significant fit improvements.

Blustin et al. (2004) recently conducted a survey of WAs using published data in recent literature. Their paper contains a good summary of the approximations used to estimate absorber properties such as mass outflow rate and distance from the continuum source. We have discussed their results for WA properties in Chapter 2. They raise the interesting possibility that WAs come in two varieties – one at parsec-scale distances, and the other at distances compatible with a disk wind. Thus it may be that both the evaporating torus (Krolik and Kriss 2001) and disk wind (Elvis 2000) models are correct. Blustin et al. (2004) claimed that Seyferts tend to harbor the more distant (parsec-scale) WAs, while quasars show high-velocity winds launched from much smaller radii. Interestingly, they cited MR 2251-178 as a quasar which broke the pattern, as it did not contain a high-velocity outflow. Although recent flux levels of MR 2251-178 seemed to have fallen below the quasar threshhold, we did detect a high-velocity outflow in the 2002 *Chandra* HETG observation of MR 2251-178 (Gibson et al. 2005)!

3.3 The UV Absorber

Given that the Seyfert galaxy NGC 4151 was known to host an X-ray absorber with a large absorbing column, (Bromage et al. 1985) decided to search for UV absorption lines in that same galaxy using the *IUE* satellite. The search was successful: many line features were detected. The lines also exhibited variability. Equivalent widths of highly-ionized species (such as N V) were correlated with the non-thermal continuum flux (around 2500 Å), but were less correlated with the continuum at 1455 Å. The authors suggested that this was because the 2500 Å continuum region was associated with the source of ionizing ("seed") photons in the nucleus, while the 1455 Å continuum was diluted by other continuum components. On the other hand, several low-ionization species, while correlated in equivalent width among themselves, showed evidence of *anti*-correlation with the continuum. The velocity spread parameter b did not appear to change noticeably, leading the authors to conclude that absorption line variation was largely due to changes in column density of absorbing ions along the line of sight.

The *IUE* satellite observed hundreds of AGN and found UV absorption lines in several of them. Ulrich (1988) analyzed these spectra and found that these lines appeared in fewer than 10% of the Seyfert galaxies observed with *IUE*. When present, the lines were blueshifted with respect to emission lines at velocities up to -2500 km s^{-1}. The equivalent width of C IV absorption suggested column densities $N_H > 10^{19}$ cm^{-2}. Although the data at that time supported no significant correlation between UV and X-ray absorption, the author noted that such a correlation "would not be surprising," since gas at the predicted temperatures of $10^4 - 10^5$ K could produce lines in both the UV and X-rays.

A few years later, Mathur et al. (1994) used quasi-simultaneous *HST* and *ROSAT* observations of the UV and X-ray spectra of 3C 351 to claim that a link between the UV and X-ray absorbers had been detected. They employed photoionization models to simultaneously fit four UV lines (O VI, C IV, N V, and Lyα) and the X-ray continuum (constraining the ionization parameter and column density). The absorber fits for both regions were in agreement, leading the authors to conclude that "the X-ray and UV absorbers are one and the same." They noted that the quality of the fit depended strongly on the underlying continuum used. In this case, the continuum of 3C 351 had been constrained in the optical, infrared, and radio with previous observations, giving the authors confidence that their continuum model was correct. They further noted that UV absorption troughs extended through emission lines down into the continuum level, suggesting that both the continuum region and the line emission region (presumed to be the BELR) were at least partially covered by the absorber. They claimed that variations in equivalent widths of UV and X-ray lines need not be correlated as the lines were on the flat part of the curve of growth, so that changes in column density would have minimal impact on equivalent widths. They suggested that previous analyses of AGN with both UV and X-ray absorbers had mistakenly assumed that the absence of Mg II absorption was due to a small absorbing column rather than to high ionization levels, and also that previous instruments (e.g., *IUE*) had been unable to detect the O VI absorption that indicated a bridge between lower and higher ionization levels typically detected in the UV and X-rays, respectively. Equivalence of the UV and X-Ray absorbers was also claimed for other AGN: 3C 212 (Mathur 1994), NGC 5548 (Mathur et al. 1995), and PG 1114+445 (Mathur et al. 1998).

However, further observations in bright, well-studied AGN found difficulties in equating the UV and X-ray absorbers. The bright nearby AGN, NGC 4151, showed a considerable increase in both UV continuum levels and high-ionization absorption line strengths over about 4 years (Kriss et al. 1995). Narrow emission cores of He II also increased significantly. However, it was difficult to match the high-ionization lines to the high columns simultaneously measured for low-ionization lines and neutral hydrogen. Multiple zones were apparently required in the absorbing medium. The authors suggested that the absorbers could be clumps of high-density material suspended in a medium of more highly-ionized gas flowing away from the obscuring torus.

In other cases, one velocity component in the UV absorber could be related to the X-ray WA. A 1999 *FUSE* observation of Mrk 509 showed seven distinct kinematic components, one of which had the same ionization state and column density as the gas producing O VII and O VIII edges in X-ray spectra (Kriss et al. 2000). The ionization levels and column densities of the other components indicated little or no connection to the X-ray absorber. The authors suggested that the component with the highest outflow velocity could be far from the central source and associated with narrow emission line region (NELR) material.

Studies of the well-known variable AGN NGC 3516 came to similar conclusions. One study with *Astro-2* on the space shuttle *Endeavor* found that broad emission line ratios could not be acceptably modeled with a single-zone photoionization model (Kriss et al. 1996). Large differences between the velocity spread parameter b of high-ionization lines and neutral hydrogen and significantly different velocity shifts further argued against single-zone models. Finally, single-zone models were unable to account for all the absorption lines observed, while a multiple-zone model with column densities and ionization parameters spanning three orders of magnitude was able to consistently model both the UV and X-ray gas. An *HST* observation a few months later agreed with this result (Crenshaw et al. 1998). No significant variations were found in the equivalent widths or radial velocities of absorption lines, but the C IV line was resolved for the first time into four distinct kinematic components. Overall, the C IV optical depth was too large to correspond to the X-ray WA, but it was possible that one of the individual components could be associated with the WA.

The improved resolution and signal/noise of *HST* enabled studies of larger samples of AGN. It became obvious that the number of AGN with UV absorbers had been grossly underestimated with *IUE*. In fact, it now appeared that more than 50% of Seyfert 1 galaxies showed intrinsic UV absorption. Working with a sample of UV spectra from 17 Seyfert 1 AGN, Crenshaw et al. (1999) found that intrinsic UV absorption always includes high-ionization lines (from such ions as C IV, N V) and also Lyα. Of the 15 objects with near-UV spectra, only NGC 4151 showed evidence for low-ionization Mg II absorption. The absorbers were flowing outward at up to -2100 km s^{-1} and, at high resolution, split into multiple distinct kinematic components. As in previous studies, they found that the BLR was at least partially occulted by the UV absorber. On average, UV absorbers typically covered at least half the sky (unobscured by the Unified Model torus) as seen by the continuum source. They exhibited a wide range of physical properties, particularly ionization parameter, both from AGN to AGN and within the same AGN. Based on their relatively small sample, they concluded that there appears to be a connection between UV and X-ray absorbers, though they are not required to arise from the same material.

A recent *FUSE* survey has shown that, like X-ray absorbers, UV absorbers can be quite complex (Kriss 2001). All objects that showed UV or X-ray absorption in previous studies showed O VI absorption in the survey. Conversely, those objects showing O VI absorption in the survey were very likely to also show absorption at longer UV wavelengths or in X-rays. Half of the samples showed distinguishable blends in O VI absorption. A few showed single (unblended) absorption lines, while others showed smooth blends with undistinguishable velocity components. Line FWHM's were usually < 100 km s^{-1}, but generally spanned the range $50 - 750$ km s^{-1}. Outflow velocities ranged from -200 to -4000 km s^{-1}, with half slower than -1000 km s^{-1}. Kriss (2001) suggested that the UV absorbers may be clumps of gas embedded in a more tenuous medium, the latter being responsible for X-ray absorption.

3.4 Dust in WAs

IRAS 13349+2438 is an infrared-bright, radio-quiet QSO with a high polarization percentage. Its large reddening was previously (Wills et al. 1992) thought to be produced when the continuum light passed through a dusty inclined disk parallel to the host galaxy but probably between the BLR and NLR, while the polarized light was scattered into our line of sight from continuum light leaving through the polar regions of the galaxy. Using data from *ROSAT* PSPC observations of IRAS 13349+2438, Brandt et al. (1996) argued that the X-ray scatterers would probably be electrons, but the observed variability of the source would require (through a causality argument) that the scattering region be very near to the continuum source. Significant scattering would require the electrons to be very compact and Thomson-thick, "a very atypical mirror." Additionally, the low absorbing column measured assuming a cold absorber was quite small, inconsistent with the intrinsic column suggested by the reddening. The authors suggested instead that a "dusty warm absorber," in which dust was co-located with ionized absorbing gas, could explain the phenomena observed. Photoionized gas could be at a temperature low enough that large dust grains would be able to survive.

A discussion of the requirements for dust to survive in WA material was included in the survey report of Reynolds (1997). Two conditions are required for dust survival. Firstly, the absorber gas itself must be below the temperature at which sputtering will destroy dust, typically about 10^6 K. This is easily accomplished for photoionized gas. Secondly, the dust itself must be below the sublimation temperature (somewhat < 2000 K, depending on the grain type involved). The dust and gas temperatures may be different. In particular, the dust may be in equilibrium with the radiation field rather than the electron gas. If the dust radiates as a blackbody, it can survive at distances beyond about 10^{17} cm from the central source. The author found three classes of objects in the survey: unreddened objects with small O VII edges, reddened objects with larger O VII edges, and a small number of objects (NGC 3516 and NGC 3783) with little reddening but a large O VII edge. If associated with the WA, the dusty region would necessarily reside in the outer absorber (assuming a multizone absorber), since radiation would sublimate the dust at the high photoionization levels of the inner absorber. The author conjectured that the dusty outer absorber could be associated with the obscuring torus. In particular, since the dust was unlikely to condense out of cooling hot material (as the dust would be unable to cool to temperatures lower than the ionized gas temperature), it seems reasonable that the dusty absorber could be an outflow from the surface of a cold torus undergoing radiative heating.

The search for dusty WAs continued. Komossa and Fink (1997a) raised the question whether NGC 3227 contained a dusty WA, based on the reddening observed in the galaxy. However, their photoionization models (which included the effects of dust) were unable distinguish between a dusty and dust-free WA. Similar arguments were invoked by Komossa and Fink (1997b) in the case of NGC 3783 to explain broad line reddening and X-ray variability. Komossa and Bade (1998) demonstrated that a dusty WA model could successfully fit the X-ray spectrum of IRAS 17020+4544, a galaxy which had previously been suggested to contain a dusty WA (Leighly et al. 1997). Fits of dusty WA models to IRAS 13349+2438 produced perplexing results (Komossa and Breitschwerdt 1999; Siebert et al. 1999). Dust-free WA models significantly outperformed dusty WA models in fits to X-ray spectra (taken with *ROSAT* and *ASCA*), with the latter not even being statistically acceptable in the *ROSAT* case. Yet the primary issue remained: how to explain significant optical extinction without a corresponding warm absorption column? Siebert et al. (1999) offered several possibilities: variability in the spectra between observations could affect the optical and X-ray spectra differently, single-zone absorber models may be inadequate in this case, and instrumental effects may also be significant.

Transmission through dust can produce a polarization signature on spectra, although it is not conclusive evidence of the presence of dust; scattering by electrons or dust can also polarize the spectrum. After detecting a WA in the *ASCA* X-ray spectrum of IRAS 17020+4544, Leighly et al. (1997) hypothesized that the spectrum would also show strong polarization. Subsequent polarimetry supported that statement – the optical spectrum showed a continuum polarization rising from 3% to 5% from about 7000 Å down to 4000 Å. The polarization position angle was in agreement with the orientation of the host galaxy axis. Encouraged by this result, the authors analyzed a suite of galaxies known to have either cold or warm X-ray absorbers. They found that the galaxies with WAs were significantly more likely to have polarized spectra, supporting the proposed association of dust with the ionized absorbers (as against cold absorbers).

Because dust can impose a polarization signature on a spectrum either through scattering or transmission, it is natural to use polarization studies to search for dust in WAs. Grupe et al. (1997) found strong (> 1%) polarization in 3 of the 43 AGN in their soft X-ray selected sample and 3 of 17 in their optically selected sample. In general, the polarized AGN showed a higher level of reddening than unpolarized AGN. For the unreddened AGN, the authors argued that we have a direct, unobscured view of the inner accretion disk based on: the lack of cold X-ray absorption, rapid X-ray variability, the lack of reddening, and lack of polarization. The reddened AGN showed atypically strong narrow emission lines (in the optical spectrum), suggesting that the dust responsible for reddening was associated with the BLR (and thus did not affect the narrow emission line region). They found that optical reddening overpredicted the measured X-ray column density in their sample, again suggesting that gas associated with the dust is ionized. Finally, the authors presented some thoughts on how polarimetry can be used to map out the geometry of the components of unified AGN models and applied it to their data.

The highly variable Seyfert 1 galaxy MCG–6-30-15 has been at the center of the discussion of dusty WAs. The WA in MCG–6-30-15 had received much attention already by the late 1990's, and the reddening in the galaxy's spectra made it a natural laboratory for dusty WA studies. A multi-wavelength study conducted by Reynolds et al. (1997) collected optical, infrared, UV, and X-ray spectra in an attempt to understand the role dust plays in the AGN. The optical spectrum of MCG–6-30-15 is heavily reddened, while the UV spectrum is almost extinguished. Two methods of measuring reddening – optical continuum extinction (based on an assumed continuum spectral index) and decrements in the Hα / Hβ, Hδ / Hβ, and Hγ / Hβ ratios (assuming a standard value for these ratios) – agreed that $E(B-V)$ lay in the range $0.51 - 1.09$. The reddening from Balmer ratios was greater than that from the optical continuum. Assuming the Balmer lines originated farther out in the BLR, this implied that little dust existed between the BLR and the accretion disk assumed responsible for the optical continuum. An unusually large ratio of C IV to Hβ emission was cited as evidence that something was scattering BLR photons around the reddening material and into our line of sight. A scattering fraction of under about 5% would sufficiently enhance the UV flux over the heavily reddened optical flux to bring the intrinsic C IV / Hβ ratio down to a normal value. As in previous studies, it was found that the observed reddening overpredicted a cold X-ray absorbing column. Polarization fractions of 4-6% argued for scatterers in the nucleus. A dusty ionized absorber would explain the phenomena as long as the material were photoionized, since collisional ionization would require temperatures high enough to destroy the dust. Assuming dust is present in the WA, the authors used photoionization models that include a configurable mix of dust to fit the data. The fits were able to distinguish between varieties of dust, preferring those (graphites) that produced little or no neutral oxygen K edge. More recent studies of the (proposed) dusty WA of MCG–6-30-15 are discussed in section §3.5.1.

3.5 High-Resolution Spectroscopy of Some Famous AGN

WA studies suddenly became much more complex when high-resolution spectroscopy from *Chandra* and *XMM-Newton* became available. Edges could now be measured with much more accuracy and spectral lines were clearly detected. In many cases, the lines were even resolved, with FWHM's of a few 100 km s^{-1} or more. Outflow velocities could be measured up to a few 100 km s^{-1} accuracy as well. The ability to study lines from so many different ions (O VIII, O VII, Ne X, Ne IX, Mg XII, Mg XI, Si XIV, Si XIII, S XVI, S XV, Fe XVII, Fe XXVI, etc.) separately provided powerful new tests of absorber structure and properties. In this section, we discuss recent spectroscopy of two AGN, MCG -6-30-15 and NGC 3783, which have been observed for long exposure times with the *Chandra* HETG and therefore give us some of the best examples of AGN X-ray spectroscopy.

3.5.1 MCG–6-30-15

With high-resolution spectra from *XMM-Newton* and *Chandra* available, MCG–6-30-15 has been at the center of the dusty WA debate. The presence of the lines in the spectrum is indisputable, and several studies have been made of them. The edge structure has been strongly debated. Timing variability studies focusing on the continuum have also revealed structure in the continuum components.

Dusty WA or Relativistic Emission?

The standard WA model was challenged in an early high-resolution spectroscopy study with *XMM-Newton*. Comparing the spectrum of MCG–6-30-15 to that of Mrk 766, Branduardi-Raymont et al. (2001) claimed that WA model fits to the spectra were unacceptable for several reasons. The O VII and O VIII edges were apparently redshifted by $16,000$ km s^{-1}, indicating that ionized material was falling into the nucleus at a high velocity. Yet the instrument did not detect absorption lines at these velocity shifts, perhaps because velocity dispersions in this high-velocity material were large. The authors proposed a radically different model in which relativistically broadened emission lines of O VIII, N VII, and C VI were producing the "sawtooth" structure in the spectrum that had traditionally been attributed to absorption edges removing an underlying continuum. Model fits indicated that the disk parameters required for the relativistic lines were consistent with the disk parameters of the generally accepted relativistically broadened Fe Kα line. In addition to (and sometimes superimposed on) the broad emission lines, the authors found narrower absorption lines of Ne IX and Ne X, Fe XIX through Fe XXI, O VII and O VIII, N VII, and C VI flowing out at about -400 km s^{-1}. Abundance estimates based on the relativistic emission line model were somewhat different from solar values, especially for Mrk 766. Furthermore, the high electron density implied by the emission lines suggested a large optical depth for electron scattering above the accretion disk, suggesting that electron scattering effects should be apparent in the spectrum.

In contrast, a study of the initial *Chandra* HETGS spectrum supported the hypothesis of a dusty WA. In the view of Lee et al. (2001), the O VII edge was at rest in the system, but was somewhat obscured by lines and also absorption from L shell edges of neutral Fe. They divided the spectrum into high and low states, finding that oxygen lines were stronger in the high state. Many lines from O VII were detected at rest in the high state spectrum, supporting the suggestion that the edge would also be at rest. The O VIII edge was weak and obscured with lines from other species. The apparent redshift of the O VII edge could be explained with a combination of blended resonance lines and neutral Fe L edges. The Fe L absorption was in agreement with that expected from dust in the WA. The absorber must have multiple zones to account for the wide range of ionization levels observed.

In response, Sako et al. (2003) re-analyzed the *XMM-Newton* data and claimed that the dusty WA solution proposed by Lee et al. (2001) was an inadequate fit to their spectrum, while the relativistic line model was able to reproduce the data better. In particular, they found that applying a continuum model with the power law the black body temperature of Lee et al. (2001), an estimated black body normalization, and configurable ionic column densities and velocity dispersions produced a best-fit model that significantly overestimated the flux above 23 Å, where the *Chandra* MEG had a smaller effective area. We note, however, that this analysis overlooks the effects of spectral variability. As Kaspi et al. (2004) have found in the AGN MR 2251-178, it is possible for spectral components to vary significantly between observations. Column densities vary, and even the soft excess may vary. Sako et al. (2003) also claimed to detect two velocity components in some ions, at outflow velocities of -150 ± 130 and -1900 ± 140 km s^{-1}. The O VII column densities predicted by measuring the individual components in these lines were much too small to produce the O VII edge claimed by Lee et al. (2001). Absorption by iron oxide in dust predicts a specific Fe:O ratio which would require an O I edge that was not seen in the data. Sako et al. (2003) also noted that the lines they detected required a broad range of ionization levels, in agreement with claims by previous authors that absorbers covered multiple zones.

Follow-up studies used the spectrum of a second *XMM-Newton* observation with a longer exposure time and higher signal. Turner et al. (2003) calculated what an O VII absorption edge would look like if it were "eaten away" by the O VII absorption lines approaching the edge. They found that it looked very similar to the feature observed at 0.7 keV and thus explained the apparent redshift of the edge. Additionally, they found evidence for Fe I L edges in the 0.70-0.72 region with the fine structure between the L_2 and L_3 edges resolved. Fits with multiple-zone dusty WA models gave χ^2 values comparable to fits with relativistic emission lines, though neither set of fits was formally acceptable. Examining the difference spectrum between high and low states, the authors found that the difference spectrum divided by a power law was dominated by absorption. This suggests that a multiplicative absorption effect is present in the spectrum, while the relativistic emission lines, if present, would be additive. Dividing out the absorption function showed that there may be excess emission at soft energies, but that any O VIII emission was constrained to be at a level less than 20% of the continuum.

Further study of the *XMM-Newton* spectrum supported the dusty WA hypothesis. Turner et al. (2004) found 51 absorption lines (and one emission line) in the 2001 320 ks *XMM-Newton* data. A low O VII column density (as measured by O VII lines) had been cited by Sako et al. (2003) as evidence that the claim of O VII edge absorption by Lee et al. (2001) was incorrect. However, the new *XMM-Newton* data supported a larger O VII column density of $10^{18.36} - 10^{18.86}$ cm^{-2}. Furthermore, Turner et al. (2004) re-analyzed the earlier year 2000 *XMM-Newton* data and found a much higher column density than that measured by Sako et al. (2003). Measurements of the O I edge in the later data set supported an Fe:O ratio of 1:2, appropriate for iron oxide dust. Again, a re-analysis of the earlier data set found an O I edge optical depth 10 times larger than that previously reported by Sako et al. (2003). Together with Turner et al. (2003), this study appears to have undermined some of the primary claims against the dusty WA model.

WA Lines

The *XMM-Newton* spectrum of MCG–6-30-15 has revealed a large assortment of lines. In an earlier (year 2000) spectrum, Sako et al. (2003) found evidence for two different velocity components, at -150 ± 130 and -1900 ± 140 km s^{-1}. Turner et al. (2004) supported that conclusion in their analysis of the higher-exposure 2001 spectrum, placing the components at 80 ± 260 and -1970 ± 160 km s^{-1}. Using a line-finding algorithm detailed in their paper, Turner et al. (2004) found 51 absorption lines and one emission line (the O VII forbidden line) in the spectrum. For some lines (e.g., O VII) several resonance lines were found. Some elements had lines from almost every charge state present in the spectrum, indicating again that WAs can exhibit a very broad range of ionization states. Splitting the spectrum into high and low states showed that four lines had varied appreciably in equivalent width; this was more than expected by statistics and so considered to be a real effect. Assuming the line variability was due to ionization variation on a recombination time scale, the authors placed the low-ionization absorber at a radius $< 10^{19.5}$ cm and the high-ionization absorber at a radius $< 10^{17.0}$ cm. A second search for variability between the two observations (about one year apart) found little significant variability except that two lines (due to Ca XIV and Fe XXIII) had fallen below detectable levels in the second observation.

The Variable Continuum and Fe Kα Line

A long *RXTE* observation enabled researchers to study the continuum of MCG–6-30-15 with very precise time resolution, although the spectral resolution was only sufficient to distinguish the Fe Kα line. The Fe Kα line flux was consistent with being constant over time intervals on the order of days (though not on shorter time intervals of < 12 ks) and the 2 to 10 keV spectrum was found to harden with decreasing flux (i.e., the spectral index Γ increased with flux) (McHardy et al. 1998; Lee et al. 2000). Fe Kα flux appeared to increase after continuum flares. Depending on the precise energy bands measured, evidence has suggested that harder bands lag softer bands by anywhere from 50 to about 2000 s. This is in accordance with the idea that hard photons are upscattered from lower energy photons so that, in general, harder photons scatter more times, which requires a longer amount of time (Nowak and Chiang 2000; Reynolds 2000; Lee et al. 2000). Although somewhat difficult to measure, the power spectrum may indicate a spectral break at a few $\times 10^{-5}$ Hz, suggesting a black hole mass of a few $\times 10^{6}$ $M_{\odot}$ using rough scaling arguments (Hayashida et al. 1998; Nowak and Chiang 2000; Lee et al. 2000; McHardy et al. 2005). Additionally, Lee et al. (2000) pointed out that visual inspection of the *RXTE* light curve showed an apparent 33 hour period, though power spectrum analysis was unable to confirm this analytically.

A long 1999 *ASCA* observation containing approximately 400 ks of good exposure time was broken into spectral slices by Shih et al. (2002) in order to test for variability of the continuum and Fe Kα line. Instead of making "vertical" time slices, the authors split the spectrum "horizontally." I.e., they drew constant count rate slices through the observation light curve and extracted spectra from intervals corresponding to the same count rate. They extracted 12 spectra in this way. A correlation between count rate and photon index Γ had previously been suggested for Seyfert 1 galaxies by several authors (Perola et al. 1986; Nandra et al. 1991; Ptak et al. 1994; Mushotzky et al. 1993) and in the specific galaxies MCG–6-30-15 (Vaughan and Edelson 2001), NGC 5548 (Chiang et al. 2000), NGC 7496 (Nandra et al. 2000), and IC 4329A (Done et al. 2000). However, the long, high-signal *ASCA* observation enabled Shih et al. (2002) to analyze the relation in detail. They found that the relation between Γ and flux F was fit well by the relation $\Gamma = \Gamma_0 - KF^{-\delta}$, with Γ_0, K, and δ constants. They found $\Gamma_0 = 2.12^{+0.12}_{-0.03}$ and $\delta = 3.9^{+2.0}_{-1.7}$. Additionally, the photon index appeared to saturate at high flux levels to a maximum value of roughly 2.1 to 2.2. They interpreted this result in terms of two models. The first model was a combination of two power laws, one of which could represent a constant reflection component. The second model was the "thundercloud" model of Merloni and Fabian (2001), in which active coronal regions would trigger an avalanche of flares. Larger flare regions would produce brighter but softer spectra. The flux from the Fe Kα line did not appear to be correlated with the continuum count rate, even though the latter changed by a factor of 3 over the course of the observation. In fact, the line flux was consistent with remaining constant. This meant that the equivalent width of the broad line actually decreased with increasing continuum flux. In the context of a reflection model, this was somewhat surprising unless the continuum emission source were somehow changing spatially with time.

Researchers found the long 2001 *XMM-Newton* observation of MCG–6-30-15 very valuable for continuum and Fe Kα line variability studies. The rms spectrum showed that the iron line was less variable than the rest of the continuum (Fabian et al. 2002). Further analysis of the rms spectrum (Vaughan et al. 2003b) showed that σ_{RMS} increased with flux, indicating that the light curve was more variable at higher luminosity. The periodogram of the light curve was red noise (power $\sim f^{-\alpha}$, $\alpha > 1$) up to about 3×10^{-3} Hz, with white noise (power $\sim f^0$) above that frequency. The steep slope of the power spectrum indicates that there must be a break in the spectrum at low frequencies, though it was difficult to constrain the break frequency in the *XMM-Newton* data. Previous studies of *RXTE* data had found a break frequency at $5.1^{+5.1}_{-2.6} \times 10^{-6}$ Hz, about one tenth of the break frequency estimated from the *XMM-Newton* data. A study of the coherence functions of the light curves in different frequency bands found that the hard (2-10 keV) and soft (0.2-0.7 keV) spectra were nearly coherent at low frequency ranges (5×10^{-5} Hz), but became increasingly less coherent at higher frequencies (10^{-3} Hz). Additionally, the softer spectrum was found to lead the harder spectrum by about 200 s at lower frequencies, while at higher frequencies there was little or no lag between the two bands. The authors noted that the spectral variability of MCG–6-30-15 resembled, in some ways, that of the Galactic black hole candidate Cyg X-1. They discussed several phenomenological models to explain the variability of MCG–6-30-15, with particular emphasis on a model originally proposed by Lyubarskii (1997) in which variations in the accretion rate due to viscosity in the disk propagated inward to an X-ray producing region, which effectively stopped further propagation of the accretion variations.

Fabian and Vaughan (2003) followed up on the proposal by Shih et al. (2002) that the continuum could be expressed as a sum of two power laws. They identified the two power law components as firstly a reflection-dominated component (RDC) which was largely responsible for the Fe Kα line and remained roughly constant, and secondly a power law component (PLC) which varied over time but contributed little to the Fe Kα line. They identified the PLC with the difference spectrum in the 2001 *XMM-Newton* data and showed that it indeed contained little or no iron line. The PLC was also shown to have a roughly constant photon index; apparently it varied primarily in its normalization. Both components showed effects of the WA. To explain this, the authors considered several possibilities: that the accretion disk was corrugated so that reflection showed variable intensity over time, that the variations were due to relativistic beaming from groups of electrons sweeping their beams into our line of sight, and finally that gravitational light bending would bend PLC photons from one side of the disk around to be reflected on the other side so that the RDC would be due to an integrated set of PLC disk emitters.

Further analysis of the 2001 *XMM-Newton* data supported the authors' claims. Vaughan and Fabian (2004) began their analysis by noting that the reflection component was really present, as indicated by a high-energy reflection bump in *BeppoSAX* data as well as good fits to a relativistically blurred Fe Kα line model. Alternate models for the broad feature in the 3 to 7 keV region were considered and dismissed in favor of the relativistic iron line. Plots of the 3-10 keV flux against the 1-2 keV flux showed a linear correlation with a nonzero y-intercept. The authors interpreted this result to mean that a significant constant component, which they identified with the RDC of Fabian and Vaughan (2003), was present in the spectrum. They then split the spectrum into 10 horizontal slices according to light curve intensity. They found that the Fe Kα line was rather small in comparison to the continuum at high flux levels, but became very prominent at low flux levels. The difference spectrum, identified with the variable PLC of Fabian and Vaughan (2003), showed little evidence of an Fe Kα line feature. These results supported the RDC and PLC decomposition of the continuum in Fabian and Vaughan (2003). The rms spectrum again demonstrated that the Fe Kα line region showed less variation than the rest of the spectrum. Both the 2000 and 2001 *XMM-Newton* spectra show evidence of Fe XXV line absorption at about 6.7 keV. The absorption appears to have varied between observations.

Reynolds et al. (2004) searched for time variability in the broad Fe Kα line which apparently extends over a broad range of energies, perhaps 3 to 7 keV. Working with the 2000 *XMM-Newton* observation, they extracted the spectrum corresponding to the lowest count rates and subtracted it from the total spectrum. They found the narrow component of the Fe Kα line disappeared, indicating that it was roughly counstant. The equivalent width of the broad line also appeared to remain constant. I.e., the intensity of the line increased as the continuum increased. This result was at odds with previous observations, e.g., the claim of Lee et al. (2000) that the Fe Kα line flux appeared to remain constant with time (apart from flare events).

Recently, McHardy et al. (2005) have combined two long *RXTE* observations with *RXTE* monitoring data and the *XMM-Newton* observations to measure the power spectral density (PSD) of MCG–6-30-15 over a frequency range from 10^{-8} to about 2×10^{-3} Hz. The authors find that a bending power law is a better characterization of the PSD than a broken power law, but in any case, there is a characteristic break frequency at about $7.6^{+10}_{-3} \times 10^{-5}$ Hz. They suggest that the high, soft state of the Galactic black hole (GBH) Cyg X-1 is a better description of MCG–6-30-15, rather than the low, hard state previously claimed. Assuming linear scaling of break frequency with black hole (BH) mass, this suggests that the supermassive BH in MCG–6-30-15 has a mass of about $2.9^{+1.8}_{-1.6}\times10^{6}M_{\odot}$. This is a rather low estimate (though the error is large), but the authors support the low mass measurement through several other methods of measurement unrelated to the PSD.

3.5.2 NGC 3783

The Seyfert 1 galaxy NGC 3783 has recently been the focus of a deep, multiwavelength observing campaign in the UV and X-rays. The *Chandra* HETG observed NGC 3783 for about 900 ks in 2001, resulting in an X-ray spectrum of a (Seyfert 1) AGN with unprecedented resolution and signal-to-noise. The UV spectrum was observed with the *HST* Space Telescope Imaging Spectrograph (STIS) and also the Far Ultraviolet Spectroscopic Explorer (*FUSE*) telescope from 2000-2002. Both the UV and the X-ray absorption spectra are highly structured.

UV Spectrum

The combined UV spectrum showed absorption lines of O VI, N V, C IV, N III, C III, and Lyman lines up to Lyϵ in three different velocity components (outflowing at -1320, -724, and -548 km s^{-1})(Gabel et al. 2003a). The spectrum showed absorption from a metastable excited state of C III. Kriss et al. (1992) had previously used this line to determine electron densities in their study of the absorber of NGC 4151. Following their method, Gabel et al. (2003a) used the level balance equations for the population of this state of C III along with input from photoionization models to determine a lower limit on the electron density n_e of the absorber required to produce the C absorption lines seen in the spectrum. Their density limit was rather high: $n_e \approx 10^9$ cm^{-3}. Together with the ionization level of the absorber, this implied an upper limit on the absorber distance from the continuum source of 8×10^{17} cm. As an interesting example of the complexity (and consequences) of these sorts of calculations, this density limit was revised by several orders of magnitude in a later paper. Behar et al. (2003) had pointed out that the initial calculations used by Gabel et al. (2003a) had only accounted for one of the three levels in the triplet metastable state of C III. The other two levels have a much lower transition rate to ground and thus can be populated in gas of much lower densities. Gabel et al. (2005) applied a new test based on the distinction between the relative transition rates of these three metastable levels and found a much lower electron density of $n_e \approx 3 \times 10^4$ cm^{-3}. This also revised the absorber distance from the continuum source up to about 25 pc.

The UV spectrum showed evidence for a great deal of absorber structure. Following a method suggested by Ganguly et al. (1999), Gabel et al. (2003a) determined absorption covering fractions as a function of wavelength. The method can be summarized as follows. Suppose the underlying emission is a combination of line and continuum emission with fluxes F_l and F_c, respectively. The absorber may not cover the entire emission regions (in a two-dimensional projection); the covering factors are C_l and C_f for the two regions. The optical depth through the absorber, τ, is assumed to be the same for each emitter. Now consider only the continuum emission. A completely opaque absorber ($\tau \rightarrow \infty$) would allow only the uncovered fraction of light, $F_c(1 - C_c)$, to pass. We add an additional term, $F_c(C_c \exp(-\tau))$, to account for the flux transmitted through a non-opaque absorber. The line emission is treated similarly, so the final transmitted flux is given by:

$$F = F_c(C_c e^{-\tau} + 1 - C_c) + F_l(C_l e^{-\tau} + 1 - C_l). \tag{3.1}$$

Lyman lines up to Lyϵ are detected (with multiple components) in the UV spectrum of NGC 3783. The higher-order lines (Lyγ and Lyϵ) are strongly absorbed, indicating that the lower-order lines (Lyα and Lyβ) are saturated, so that $\exp(-\tau) \approx 0$ in the line centers and any photons in these regions are due to continuum not covered by the absorber. Using the two lines Lyα and Lyβ, Gabel et al. (2003a) solved for C_c and C_l for each of the velocity components. They found that the continuum source was well-covered by the absorber, in the 80-100% range for each velocity component. The absorber covering factor of BLR line emission varied widely from 3% to 84% for different kinematic components. They also found that the wings of the lines in the various velocity components had lower covering factors than the cores did. They attributed all of these findings to structure in the absorber. Even in a single velocity component, they found that different ions had significantly different covering factors and line widths.

In follow-up studies, Gabel et al. (2003b) showed that the complex structured absorber was also evolving on measureable time scales of weeks to years. One of the velocity components of the UV absorber decelerated in outflow velocity in two different observations, by 35 and 55 km s^{-1}. The authors suggested several possibilities for the deceleration, including the pull of gravity, interaction with the ambient medium, and mass loading. They also mentioned the possibility that the apparent deceleration was actually due to different patches of absorbing material moving across our line of sight. In this case, the absorber would not be decelerating necessarily, but observers would be seeing different regions of the absorber which have different intrinsic radial outflow velocities.

In addition to outflow velocities, line strengths varied. Gabel et al. (2005) reported that the lowest ionization species in each of the three (strongest) kinematic components varied over time, with absorption line equivalent widths inversely correlated to the continuum flux. They claimed this was evidence for photoionization-driven changes in the absorber.

X-Ray Spectrum

NGC 3783 was observed with the *Chandra* HETG for 55 ks in 2000, and again for 850 ks from February to June of 2001. The long exposure for this bright source resulted in an

X-ray spectrum which enabled an unprecedented level of study of WAs (Kaspi et al. 2002). Strong absorption lines from H- and He-like ions of N, O, Ne, Mg, Al, Si, and S are evident in the spectrum. There are also possible detections of H- and He-like Ar and Ca, as well as H-like C. Lines from lower-ionization ions such as Mg, Si, and S may also be present. A large number of lines from many ionization stages of Fe are found in the spectrum, including L and M shell absorption lines. The mean outflow velocity of these lines is -590 ± 150 km s^{-1}, and the mean line FWHM is 820 ± 280 km s^{-1}. The outflow velocity is consistent with the two lower-velocity components in the UV absorber.

The O VII and perhaps the Ne X absorption systems show evidence of containing two velocity components. For the former ion, the outflow velocities are -627^{+78}_{-48} and -1284^{+77}_{-38} km s^{-1}. These are again rather similar to the UV velocity components at about -1400, -720, and -560 km s^{-1}.

Kaspi et al. (2002) detected over 20 emission features in the spectrum, including the He-like ion line triplets from O, Ne, and Mg. They also detected radiative recombination continuum (RRC) emission from O VII and N VI, which both gave an estimated lower limit of 60,000 K for the absorber temperature.

There is a broad absorption feature in the spectrum from 15-17 Å, which Kaspi et al. (2002) attributed to a large number of inner-shell $2p - 3d$ line transitions of Fe M-shell ions. Recently, Holczer et al. (2005) have scrutinized the UTA region to identify a few individual lines. They found that these lines were at rest in the system frame and thus not associated with the outflowing WA. This led to an interesting case in which astrophysical observations of a distant source have prompted improvements in atomic physics. Gu et al. (2005) calculated the UTA line wavelengths with an improved theoretical methodology and found that previous predictions of line wavelengths had been systematically too small by 15-45 mÅ. Using the new line wavelengths, Gu et al. (2005) found that the UTA lines were outflowing at the same velocity as the rest of the WA, resolving the apparent discrepancy between UTA and WA velocities.

Netzer et al. (2003) searched for time- and luminosity-dependent variations in the WA. While they found that the continuum source varied strongly in intensity and shape, there was no evidence for absorber variation. The equivalent widths of the absorption lines were consistent with remaining constant between high and low states. This is in marked contrast with the variations detected in UV absorber line velocities and intensities (§3.5.2).

We note that their analysis left room for further, more complicated tests for variability. They broke the spectrum into "low" and "high" states based on the softness ratio of 15-25 Å flux to 2-10 Å flux. Entire observations were classified as belonging to either the low or high state. The low state is a combination of observation numbers 02090, 02091, 02092, and 02094 (of 170 ks exposure each), while the high state is composed from observations 00373 (55 ks) and 02093 (170 ks). Although Netzer et al. (2003) showed that the softness ratios of these spectra did not vary much over the course of a single observation, the continuum fluxes did vary significantly. The WA lines may respond in measurable ways to the overall continuum flux level on intra-observation time scales. The softness ratio test is an important constraint on absorber variation, but it is primarily sensitive to edge variation. Lines have much greater optical depths than edges, so we might expect to see variation in lines while the complex (overlapping) edge structure may not show evidence for variation.

Chapter 4

The High Resolution X-ray Spectrum of MR 2251-178 Obtained with the *Chandra* HETGS

This chapter was originally published in ApJ 627:83-96. The authors involved were: Gibson, R. R., Marshall, H. L., Canizares, C. R., and Lee, J. C.

Abstract

The QSO MR 2251-178 was observed with the *Chandra* High Energy Transmission Grating Spectrometer (HETGS) at a 2-10 keV luminosity of 2.41 × 10^{44} erg s^{-1} (using H_0 = 72 km s^{-1} Mpc^{-1}). We observe the source in a relatively low state. The light curve shows no evidence of variability. We present the zero-order image of MR 2251-178 and compare it to previous observations.

We find evidence of a highly-ionized, high-velocity outflow, which we detect in a resolved Fe XXVI Lyα absorption line. The outflow appears to have a large mass and kinetic energy flux compared to the estimated nuclear accretion rate and luminosity. We examine the possibility that other absorption features in the spectrum are associated with the high-velocity outflow.

We detect a narrow Fe Kα line and resolved forbidden line emission from Ne IX and O VII. Modeling the emitting material enables us to constrain its properties and conclude that it is not along our line of sight.

4.1 Introduction

MR 2251-178, at $z = 0.06398$ (Bergeron et al. 1983; Canizares et al. 1978), i.e., $cz \approx 19,200$ km s^{-1}, was discovered as an X-ray source by the *Ariel V* all-sky survey (Cooke, B. A., et al. 1978). It was the second quasar known to be an X-ray emitter, and the first to be identified from X-ray observations (Ricker et al. 1978).

This was the first quasar for which variable X-ray absorption was observed (Halpern 1984). The absorption was interpreted as changing ionization in a "warm absorber." Since that time, ionized (warm) absorbers have been observed in a majority of lower-resolution spectra of Active Galactic Nuclei (AGN's) (Reynolds 1997; George et al. 1998) and more recently with the high-resolution spectra of Seyfert 1 galaxies such as MCG -6-30-15 (Lee et al. 2001; Turner et al. 2003; Sako et al. 2003), NGC 3783 (Kaspi, S., et al. 2001; Kaspi et al. 2002; Gabel et al. 2003a,b; Netzer et al. 2003), NGC 4051 (Collinge et al. 2001), NGC 7469 (Blustin, A. J., et al. 2003), and others.

The region surrounding MR 2251-178 has also received attention. The quasar appears to be a member of a cluster of nearby galaxies (Phillips 1980) and is surrounded by a large cloud of ionized gas. [O III] emission from this nebula extends at least 230 kpc from the nucleus (Bergeron et al. 1983). The nebula appears to be more highly ionized than the nuclear region, with ionization decreasing from distances of 20 kpc inward to 3.4 kpc (Bergeron et al. 1983).

Much of the previous analysis of MR 2251-178 has been directed toward characterizing the absorber. Fitting 15 *EXOSAT* observations with a photoionization model, Pan et al. (1990) concluded that the absorption column density decreased as flux increased. However, Walter and Courvoisier (1992) were able to explain the observed variability with a power law fit of varying slope and cold absorption. Mineo and Stewart (1993) fit a photoionized gas model against multiple spectra, finding that the gas column density remained roughly constant, while the ionization parameter varied.

XMM-Newton observations combined with previous *ASCA* and *BeppoSAX* observations led Kaspi et al. (2004) to conclude that the variable X-ray continuum of MR 2251-178 could be modeled with a power law and some combination of (multiple) warm absorbers and a soft excess. The absorber properties (column density and ionization parameter) varied among observations, leading Kaspi et al. (2004) to suggest that different absorbing systems were moving into and out of the line of sight on a time scale of several months.

Absorption lines of Lyα, N V, and C IV, blueshifted -300 km s^{-1} from the rest frame on average, were detected in the ultraviolet (UV) by Monier et al. (2001). Absorption from C IV has been shown to vary over a period of four years, from which a maximum distance of 2.4 kpc between source and absorber was inferred (Ganguly et al. 2001). Recently, Kaspi et al. (2004) suggested that O VI, C III, and H I Lyman line absorption in a 2001 *FUSE* observation indicates the presence of at least four absorption systems with outflow velocities in the range of 0 to -600 km s^{-1}, and that the outflowing absorber may not fully cover the continuum source.

Evidence for a statistically significant Fe Kα emission line has been found in observations made by *ASCA* (Reynolds 1997), *BeppoSAX* (Orr et al. 2001), and *XMM-Newton* (Kaspi et al. 2004), with equivalent widths of 190, 62, and 53 eV, respectively. No evidence for a stronger line was found, although the possibility of a stronger line could not be completely ruled out in the earlier missions.

In this paper we present the *Chandra* High Energy Transmission Grating Spectrometer (HETGS) observation of MR 2251-178. We discuss the data reduction process (§4.2). We examine the zero-order grating image and compare it to images from previous observations (§4.3.1). We examine the light curve of MR 2251-178 for variability (§4.3.2). We fit the observed continuum with several models in order to characterize it and to test for a warm absorber (§4.3.3). We report the continuum flux in hard and soft energy bands and compare it to historical values (§4.3.4). We examine the spectrum for absorption and emission lines (§4.3.5), finding: a narrow Fe Kα line, significant absorption from high-velocity outflowing highly-ionized Fe (and possibly Si), and emission from low-velocity forbidden lines of Ne IX and O VII. We construct a photoionized plasma model (§4.4.1) and use it to derive a statistic expressing which lines we are able to detect with the HETGS at a given ionization level (§4.4.2). We discuss the highly-ionized, high-velocity outflow we detect in the spectrum (§4.4.3). An analysis of the properties of the system emitting the forbidden lines allows us to conclude (given certain assumptions) that it is not along our line of sight (§4.4.4). Finally, we conclude (§4.5) with a summary of our findings in relation to recent X-ray observations of MR 2251-178.

4.2 Observations and Data Reduction

We observed MR 2251-178 for 146 ks on 2002 September 11 and 12 (MJD 50814) with the *Chandra* HETGS (Weisskopf et al. 2000). Spectral data were reduced using version 2.3 of the standard CIAO distribution.[1] The standard CIAO Auxiliary Response Files (ARF's), used to determine the effective area of the instrument as a function of wavelength, were corrected for instrumental contamination (Plucinsky, P. P., et al. 2003; Marshall et al. 2003) using development version 1.1 of the `contamarf` software.[2]

In order to use the maximum available number of counts for line detection, we reduce the data using the method described in Ogle et al. (2000) to obtain a list of grating counts observed for both the HEG and MEG first- and second-order spectra. This differs from the standard CIAO reduction primarily in that it includes second-order counts and that counts are retained which would be rejected by the CIAO `acis_detect_afterglow` pipeline tool.[3] (See Juett et al. 2002 for a short discussion on retaining these counts.) We use these counts to identify and measure spectral lines and to construct the light curve. We do not use zero-order counts for the light curve, as the center of the zero-order image is affected by pile up (multiple counts in a single read out time frame).

4.3 Image and Spectral Analysis

In this section, we describe the results of our data analysis. We examine the zero-order image (§4.3.1) and light curve (§4.3.2), test various continuum models (§4.3.3), estimate the X-ray flux of the central source (§4.3.4), and present our analysis of lines we detect in the spectrum (§4.3.5).

4.3.1 Zero-Order Image

We obtain the zero-order image from the ACIS-S3 chip and smooth it adaptively using the CIAO tool `csmooth`[4] with an oversampling rate of 2:1 on each axis. The image is shown in Figure 4-1. At an angular diameter distance of 288 Mpc, $10''$ corresponds to about 12 kpc. Within about $2.5''$ from the central source, the image is dominated by the point spread function (PSF) of the instrument. Radial shadows of the mirror supports extend from the center of the image, but are not intrinsic to the source.

X-ray emission extends to the northeast, south, and particularly to the west by about $10''$. Previous VLA radio maps obtained by Macchetto et al. (1990) show 6 cm and 20 cm radio emission extending up to $20''$ in the east-west direction. The western 20 cm radio extension bends southward at a distance of $8''$ from the nucleus. On a larger scale, Shopbell et al. (1999) have found evidence for spiral structure with azimuthal symmetry in Hα images, with active Hα "arms" extending to the east-northeast and southwest.

---

[1] `http://asc.harvard.edu/ciao`

[2] `http://cxc.harvard.edu/cont-soft/software/contamarf.1.1.html`

[3] `http://as.harvard.edu/ciao/threads/acisdetectafterglow`

[4] `http://cxc.harvard.edu/ciao/ahelp/csmooth.html`

We search for any asymmetry near the central region that may indicate the presence of an X-ray jet. To do this, we obtain all zero-order image counts in an annulus between radii of 10 and 50 pixels (4.92″and 24.6″). The inner radius is chosen to stay outside the full width at half maximum (FWHM) of the zero-order PSF. Data are binned azimuthally into 12 bins of equal angular size in order to cancel out the 12-fold angular symmetry of the mirror support shadows. The resulting histogram is shown in Figure 4-2, plotted as counts against position angle counterclockwise from north at zero degrees. We do not find significant evidence for asymmetry, though the visible extensions to the west and northeast are reflected in the histogram. Vertical lines have been plotted on the histogram at -157″ and 23″ indicating the orientation of a faint, thin readout streak which has little impact on the azimuthal profile plotted here.

4.3.2 Light Curve

The light curve (Figure 4-3) is constructed using the 71,400 counts from the first-order HEG and MEG spectra which did not fall in the narrow region near the gaps between CCD detectors (the "chip gaps"). Because the ARF in a chip gap region varies strongly with position, these regions are excluded to prevent time variation of the detector dithering pattern from influencing the results. Although the ARF varies with position elsewhere, the variations are generally much smaller than across chip gaps. Counts are binned to 100 second bins. We find a mean of 48.0 counts per bin. A Kolmogorov-Smirnov test does not indicate significant variability in the count rate.

4.3.3 Continuum Models

Figure 4-4 shows the spectrum with background subtracted and adaptively binned to at least 100 counts per bin. We simultaneously fit both the High Energy Grating (HEG) and Medium Energy Grating (MEG) spectra to various models with the spectrum adaptively rebinned so that each bin contains at least 20 counts. HEG counts below 1.2575 Å and MEG counts below 1.585 Å are excluded from fits. MEG counts in 8 of the 31 bins at wavelengths above 20.24 Å are also excluded. (All wavelengths and energies in this section are observed-frame values, unless specified otherwise.) Omitted ranges represent bins where the ratio of scaled background counts to observed counts is greater than 10%. This results in the exclusion of one HEG bin and 9 MEG bins (after data had been rebinned to at least 20 counts per bin), leaving a total of 2574 bins to fit. Background counts were estimated by CIAO (taken from regions on the ACIS chips in the cross-dispersion direction directly outside spectral regions) and scaled by a factor of 1/9 to account for the larger chip area of the background regions compared to the spectral regions.

All models are multiplied by the XSPEC **phabs** model (with abundances from Anders & Grevesse 1989) to account for Galactic absorption with a hydrogen column density of $N_{\rm H} = 2.8 \times 10^{20}$ cm^{-2} (Lockman and Savage 1995). There is a known instrumental feature related to the mirror Ir M edge (briefly discussed in Juett et al. 2002) in both HEG and MEG spectra which we model as an edge at 2.05 keV with a *negative* optical depth fixed at -0.15.[5] Models are redshifted so fit parameters are given in the rest frame. All models are

---

[5] For more information, see the presentation about the telescope Ir M edge feature at the *Chandra* Calbiration Workshop, available at `http://cxc.harvard.edu/ccw/proceedings/03_proc/presentations/marshall2/index.html`.

standard XSPEC models unless described otherwise. Results are summarized in Table 4.1. Errors listed are 90% confidence limits.

We start with models that do not include ionized absorption. A simple power law gives a photon index of $\Gamma = 1.26^{+0.01}_{-0.01}$ and a reduced $\chi^2_\nu = 1.13$. This is the lowest photon index ever measured for MR 2251-178, although it is within the relatively large uncertainties of a few early measurements. Because other components required to characterize the continuum will affect the power law parameters, we draw no physical conclusion from this fact.

At low energies, several factors (e.g., soft excess or ionized absorption) may cause the spectrum to deviate from a simple power law, and thus the full-spectrum measurement of a power law index is not a direct indication of spectral hardness. Expecting that the spectrum at higher energies would be relatively free of these influences, we fit a power law to the portion of our spectrum which lies above 3 keV (in the observed frame), finding $\Gamma = 1.45^{+0.09}_{-0.09}$. (Omitting the rest-frame 5.0-7.5 keV band makes little difference in our measurement.) This is also flatter than most of the high-energy spectral fits of *ASCA*, *BeppoSAX*, and *XMM-Newton* observations reported by Kaspi et al. (2004).

To test for the presence a warm absorber, we construct a table model using version 2.1knn of the photoionization code XSTAR[6] (Kallman and Bautista 2001). The underlying spectrum for the model is taken to be the broken power law described below (§4.4.1). We assume a turbulent velocity of 100 km s^{-1}, a gas temperature of 1.4×10^5 K, and a gas density of $n = 10^8$ cm^{-3}. Abundances are fixed to solar values, except for nickel which we set to zero abundance in order to simplify the XSTAR calculation. We fit against the combined model `((powerlaw + bbody)` × `WA + WEM)`, where `WA` is the line-of-sight absorption for the plasma, `WEM` is the emission from the plasma predicted by XSTAR, and `bbody` is a black body intended to model any soft excess. The `WEM` emission model has a "norm" parameter, which roughly models the effect of a varying covering fraction. The "redshift" of the `WA` component is allowed to vary slightly from the systemic redshift to account for the possibility that the absorber may have a velocity shift relative to the system.

The addition of the ionized absorber produces a significant improvement (> 95% probability by the F test) to the pure power law model. The best fit parameters are given in Table 4.1. We find a column density of $\text{N}_H = 2.37^{+0.28}_{-0.15} \times 10^{21}$ cm^{-2} and an ionization parameter $\log(\xi) = 0.02^{+0.11}_{-0.10}$. Here we use the common definition $\xi = L_{ion}/nr^2$, where L_{ion} is the ionizing luminosity (continuum luminosity between 1 and 1000 Rydbergs), n is the gas density, and r is the radial distance from the continuum source. The column density is about 25% smaller than and inconsistent with the smallest column densities fit to the *ASCA*, *BeppoSAX*, and *XMM-Newton* observations by Kaspi et al. (2004).

Our best fit power law photon index $\Gamma = 1.46^{+0.01}_{-0.02}$ is consistent with 5 of the 14 high-energy power law fits reported by Kaspi et al. (2004) for previous missions. The other 9 fits they report are steeper. The warm emission (`WEM`) normalization and warm absorber velocity we fit are poorly constrained and are consistent with zero.

Models which do not include an ionized absorber are not identified by the F test as significant improvements over a pure power law. In particular, we fit the continuum with a `powerlaw + phabs` model to allow for excess cold absorption (above Galactic), as well as a `powerlaw + bbody` model to simulate a soft excess. Both models leave unacceptable residuals in the soft spectrum, as shown in Figure 4-5. We find that a black body is a better fit to the soft excess than a second power law. However, due to the relatively small number of spectral bins constraining the black body we do not attach strong physical significance

---

[6] `http://heasarc.gsfc.nasa.gov/docs/software/xstar/xstar.html`

to our black body fits.

Finally, we note that additional improvements in the fit statistic for all fits would come from modeling systematic uncertainties in the calibration which could amount to about 10-15% in the 1 to 2 keV range where the signal is strongest.[7]

4.3.4 Continuum Flux

Using the normalization and photon index from the simple power law fit, we integrate the unabsorbed power law to obtain a 2-10 keV flux of (2.56±0.02) $\times 10^{-11}$ erg cm^{-2} s^{-1} and a 0.5-2 keV flux of (7.23±0.05) $\times 10^{-12}$ erg cm^{-2} s^{-1}. Assuming a luminosity distance of 280 Mpc (derived from the redshift using the Wilkinson Microwave Anisotropy Probe (WMAP) cosmology of Spergel et al. 2003), we obtain a 2-10 keV luminosity of 2.41 $\times 10^{44}$ erg s^{-1}.

The 2-10 keV flux is lower than most previous measurements (see Table 4.2), but higher than the lowest value of 1.65 $\times 10^{-11}$ erg cm^{-2} s^{-1} in the *Ginga* observation reported by Mineo and Stewart (1993). We exclude the *EXOSAT* measurements of Pan et al. (1990) from this comparison because they were obtained under the assumption of a fixed common photon index. Historical measurements of the flux are shown for comparison in Figure 4-6.

4.3.5 Absorption and Emission Lines

Due to the low signal in the spectrum, we give special attention to the process of line detection. We rebin the data to several different multiples of the instrument resolution and find features in the spectra which stand out as line *candidates*. We use the following critera to test candidates for acceptance:

1. The counts present in a Gaussian fit of the line must deviate from the fit continuum by at least a Poisson confidence limit of 99.5%, not accounting for the number of trials used in detecting the feature.

2. Within statistical variation, a line present in one grating (HEG or MEG) should also be present in the other.

3. Within statistical variation, for a given grating (HEG or MEG), a line present in one grating order (+1 or -1) should also be present in the other.

4. The FWHM of the line should not be significantly smaller than the instrumental FWHM at the given wavelength.

The properties of all detected features which we identify as lines are summarized in Table 4.3. Errors given are 90% confidence ranges. Fits for emission and absorption lines are shown in Figure 4-7 and Figure 4-8, respectively.

Forbidden Emission Lines

We detect two emission lines at rest-frame wavelengths of 13.72 and 22.11 Å, corresponding to the forbidden emission lines of Ne IX and O VII. We test to see if the lines are resolved by subtracting the instrumental line width from the observed width in quadrature and find that both lines are significantly resolved with intrinsic widths of 650^{+340}_{-250} and 1700^{+670}_{-480} km s^{-1} and equivalent widths of 85^{+36}_{-33} and 620^{+210}_{-190} mÅ for [Ne IX] and [O VII], respectively.

---

[7] See the HETGS calibration web page at `http://space.mit.edu/ASC/calib/hetgcal.html`

Fe Kα Line

Previous X-ray missions have detected a narrow Fe Kα line at approximately 1.91 Å in the rest frame with equivalent widths of 190 eV (*ASCA*: Reynolds 1997), 62 eV (*BeppoSAX*: Orr et al. 2001), and 53 eV (*XMM-Newton*: Kaspi et al. 2004). We find a significant excess of HEG counts at 1.93 Å (rest frame). The Gaussian we fit is unresolved but consistent with the instrumental width at that wavelength (570 km s^{-1}). It has an equivalent width of 25^{+14}_{-13} eV ($7.4^{+4.2}_{-4.0}$ mÅ).

Fe XXVI in High-Velocity Outflow

There is a highly significant broad feature visible in the high-energy spectrum observed at about 1.81 Å, shown in Figure 4-9. Fitting the high-energy (> 3 keV) region of the HEG spectrum with a Galactic absorbed power law and an edge gives an optical depth of $0.174^{+0.16}_{-0.07}$ and a rest-frame edge energy of 7.18 keV (1.73Å). For an Fe K edge, this optical depth would imply a column density large enough to exhibit strong absorption features elsewhere in the spectrum.

Structure in the Fe K edge has recently been modeled by Kallman et al. (2004). If the feature we observe is an Fe K edge in the MR 2251-178 rest frame, it would be from relatively low ionization states of Fe, in which case we would expect to see a much stronger Fe L edge. The measured energy of the feature is too low to be due to Fe XXV or Fe XXVI, for which L edges would not be seen. Near-resonance absorption lines (see Table A1 of Kallman et al. 2004) require an unacceptably large column density ($N_H \gtrsim 10^{24}$) to produce the absorption measured. Although fitting with an edge does improve our χ^2 statistic, the fit systematically underestimates the bins blueward of the feature—the feature we observe is much narrower than a photoionization edge.

For these reasons, we do not believe that this feature is an edge. Previous detections of high-velocity outflows have similarly concluded that the features observed are lines, not edges. For example, Chartas et al. (2002) found that attempts to model a similar feature with an edge resulted in unacceptably large residuals on the blue side. The feature they observed was too narrow for an acceptable edge fit, just as in our case.

The most natural identification for the feature we observe is that it is absorption from the Lyman α line of Fe XXVI produced by an outflow moving at high velocity. In this scenario, we measure a velocity shift of $-12{,}700^{+2400}_{-2400}$ km s^{-1}, an intrinsic width of 3400^{+3100}_{-1900} km s^{-1}, and an equivalent width of -17^{+14}_{-10} mÅ. Because of the large velocity dispersion, this line may lie on the linear part of the curve of growth, in which case we may derive a corresponding column density of $N_H \approx 6.8\times10^{22}$ cm^{-2} ($N_{Fe} \approx 3.2\times10^{18}$ cm^{-2}), assuming a 50% ionization fraction. At ionization levels where Fe XXVI is abundant, other abundant elements are completely ionized, so this relatively large (equivalent hydrogen) column density does not require other features (lines or edges) to be present in the spectrum.

If we were to identify this feature with a Lyman α absorption line from a lower ionization stage of iron, even larger outflow velocities would be required, e.g., about -22,700 km s^{-1} for Fe XXV. Furthermore, we would have to explain why we do not see resonance lines from nearby ionization stages of iron. For even lower ionization stages, we would need to explain the lack of L edges in the spectrum.

Recently it has been noted (McKernan et al. 2004) that the spectra of several AGN show evidence for local (i.e., $z = 0$) absorption features. If the feature we observe at 1.81 Å is considered to be line absorption from local material (e.g., in our Galaxy), the most reasonable candidate would be resonance line absorption from Fe XXV, which would still require a blueshift of about -9,000 km s^{-1} from the Galaxy rest frame.

We note that Kaspi et al. (2004) observed an absorption feature at a system-frame energy of 6.97±0.11 keV (1.78± + 0.03 Å) which they also identified as an Fe XXVI Lyα line with an equivalent width of -28^{+20}_{-5} eV. The absorbing material would be moving at most a few thousand km s^{-1} in their measurement. This *XMM-Newton* observation was taken on 2002 May 18, 116 days before the *Chandra* observation reported in this paper. For comparison, the equivalent width of the line we measure at a system-frame wavelength of $1.71^{+0.01}_{-0.01}$ Å is -73^{+56}_{-40} eV. We detect no feature at a system-frame wavelength of 1.78 Å subject to the criteria for detection specified in §4.3.5.

Other Line Features: Two Alternative Scenarios

We detect another highly-significant (Poisson probability > 99.9%) absorption feature at about 15.10 Å (observed frame). The likely candidates are lines from Fe XVII, Fe XVIII, and Fe XIX as well as inner-shell absorption lines from Ne III, Ne IV, and Ne V (Behar and Netzer 2002).

There is an additional unresolved absorption feature observed at about 6.22 Å which we detect at of Poisson probability > 99.9%. This feature could correspond to absorption from the Si XIV Ly α line shifted by -16,940^{+200}_{-190} km s^{-1}.

It is difficult to identify these features with high confidence. We present arguments for two alternative scenarios for the gas. In the first scenario, the 15.10 Å line is from moderately ionized neon and the 6.22 Å line identification is problematic. In the second scenario, both lines are part of a highly-ionized, high velocity outflow.

Inner-Shell Lines of Mildly-Ionized Neon In this scenario, the line at 15.10 Å is attributed to mildly-ionized neon. The inner-shell absorption lines from low-ionization stages of Ne have oscillator strengths of approximately 0.10 to 0.15 in this region. In the most reasonable case, two Ne V lines theoretically predicted at 14.20 and 14.24 Å have combined to produce the feature. Assuming the absorption feature lies on the flat part of the curve of growth with a 50% ionization fraction, we derive a column density of about $N_H \approx 1.9 \times 10^{21}$ cm^{-2}. This is close to the column density we obtain with our best model fit, which requires a warm absorber with a hydrogen column density $N_H = 2.37^{+0.28}_{-0.15} \times 10^{21}$ cm^{-2} at an ionization stage $\log(\xi) = 0.02^{+0.11}_{-0.10}$. A moderate outflow velocity of -510^{+170}_{-150} km s^{-1} is required for a Ne V identification. Furthermore, the Ne V line modeled here is the feature predicted to be most detectable with the *Chandra* HETGS (in the sense of the "S" statistic described below in §4.4.2) at ionization levels where Ne V is abundant.

Our best fit ionization parameter, $\log(\xi) = 0.02^{+0.11}_{-0.10}$, is slightly above but consistent with the level where Ne V is predicted to be abundant ($-1.80 \leq \log(\xi) \leq 0.00$). However, for any $-1.15 < \log(\xi) < 0.60$, XSTAR models predict that the next higher stage, Ne VI, will be abundant. In fact, the abundance of Ne VI peaks at $\log(\xi) = -0.15$, a little less than the value of our best fit parameter. Our ionization model predicts the abundance of Ne VI to be about four times higher than the abundance of Ne V at $\log(\xi) = 0.00$. According to Behar and Netzer (2002), Ne VI has inner shell lines that should add, just as those of Ne V do in this scenario, to produce an equally strong feature observed at about 14.95 Å. This feature is not present in the spectrum. If we were to identify the 15.10 Å absorption feature we detect as Ne VI, a significant redshift would be required in the system frame.

In this scenario of the gas properties, we have no identification for the absorption feature observed at 6.22 Å.

In summary, the arguments in favor of the Ne V identification are:

1. The column density and ionization levels required are close to those of our best warm absorber model.
2. A moderate outflow velocity is sufficient for the identification.
3. The "S" statistic of §4.4.2 ranks Ne V favorably.

The arguments against the Ne V identification are:

1. We are unable to explain the absence of an Ne VI feature despite the fact that Ne VI should be more abundant than Ne V.
2. We have no straightforward explanation for the feature we detect at 6.22 Å.

Components of a Highly-Ionized, High-Velocity Outflow Alternately, we may attribute the feature at 15.10 Å to a resonance line of Fe XVII or Fe XVIII. Experimental line lists, e.g., the National Institute of Standards and Technology Atomic Database Version 2.0,[8] suggest that a strong Fe XVIII absorption line at 14.21 Å (lab frame) should be accompanied by a nearby Fe XVIII line at 14.26 Å (lab frame) which we do not detect. Thus, we are left with Fe XVII as a candidate.

Given that we already have seen evidence of a high-velocity outflow in Fe XXVI, it is reasonable in this scenario to identify the line observed at 15.10 Å as the 15.01 Å line produced by Fe XVII. The relative stability of neon-like iron and the large oscillator strength (> 2.3) for this line (Verner et al. 1996) allow for the possibility that we would detect this line but not lines from nearby ionization species. In this case, we measure a velocity shift of $-16{,}770^{+170}_{-150}$ km s^{-1}, an intrinsic width of 360^{+200}_{-130} km s^{-1}, and an equivalent width of -42^{+17}_{-13} mÅ.

Whereas the first scenario (involving low ionization stages of Ne) required relatively high column densities to fit the absorption line at 15.10 Å, a smaller column density of $N_H \approx 4.3 \times 10^{20}$ cm^{-2} is required for an Fe XVII identification. Although the lower ionization and higher column density of the first scenario are a better match for our best XSTAR fit, there is some degeneracy in the XSTAR models. In particular, a slightly worse fit ($\Delta\chi^2_\nu = 0.02$) exists at a column density and ionization stage matching the Fe XVII identification. An F test indicates that this absorption model, at a higher ionization level and lower column density, is an improvement over a pure power law at the 90% level, while the lower-ionization, higher-column-density model (our best fit) is significant at the 95% level.

In this scenario, the absorption feature observed at 6.22 Å is identified as Si XIV Lyα at a blueshift of $-16,940^{+200}_{-190}$ km s^{-1}. The measured velocities for Fe XVII and Si XIV are consistent with each other, supporting the mutual identification. The three ions identified in the outflow are abundant at the ionization stages listed in Table 4.4. There is a slight overlap in the regions where Fe XVII and Si XIV are abundant, although the peak abundances of the two ions are at very different stages. If the Fe XVII and Si XIV absorption is coming from different regions of outflow, the common outflow velocity may indicate that the outflow has reached its asymptotic velocity.

---

[8] `http://physics.nist.gov/cgi-bin/AtData/main_asd`

Our ionization models predict that O VIII should be abundant when Fe XVII is. Furthermore, the "*S*" statistic described in §4.4.2 predicts that O VIII should be more easily detected than Fe XVII in the allowed range of ionization. Thus in this scenario, it is problematic that we do not detect O VIII in our spectrum. An overabundance of iron to oxygen by a factor of at least four from solar values could resolve this discrepancy.

In summary, the arguments in favor of the Fe XVII identification are:

1. Fe XVII is abundant for many levels of ionization and the 15.01 Å line has a large oscillator strength, allowing for the feature to be present under a range of physical conditions, but not requiring additional lines from the same ion to appear.
2. Although high outflow velocities are required, we already have strong evidence for highly-ionized iron flowing out at high velocities.
3. The highly-ionized outflow scenario provides a natural identification for the feature at 6.22 Å as part of the outflow.

The arguments against the Fe XVII identification are:

1. Fe XVII is not abundant at the ionization levels of our best fit warm absorber, although there is degeneracy in the absorber models.
2. We detect no O VIII absorption, contrary to the prediction of our ionization models.

Comparison to RGS Spectrum

The combined *XMM-Newton* RGS1 and RGS2 spectra of 2002 May (Kaspi et al. 2004) show several strong emission lines, in particular O VIII Lyα and the resonance and forbidden lines of O VII. We see a strong O VII forbidden line in the *Chandra* HETGS spectrum, but no other emission (or absorption) from oxygen.

As mentioned above, Kaspi et al. (2004) found no evidence for a high-velocity outflow in the RGS spectra, although they did identify an Fe XXVI Lyα feature at lower velocities. They claim the 2002 RGS spectrum shows evidence for a feature at 14.2 Å (corresponding to our observed-frame 15.1 Å absorption line identification discussed in §4.3.5), but their feature appears weaker than what we detect. They associate the feature with Fe XVIII and propose that that absorption in the RGS2 spectrum in the 10-11 Å range may also be due to absorption from Fe XVII-Fe XIX, but the RGS1 spectrum is not available in this region to verify the reality of the feature. Because they do not quantify their line properties, it is difficult to compare their identifications to ours.

Kaspi et al. (2004) modeled the 2002 RGS spectrum with two absorption systems. One system was highly ionized and responsible for O VII and O VIII features, with a column density of $10^{21.5} - 10^{21.8}$ cm^{-2}. The other system was less ionized and responsible for O III and O IV lines, with a column density of about $10^{20.3}$ cm^{-2}. Our best fit model has the lower ionization level of the latter system but a much higher column density which approaches within a factor of a few of the former (high-ionization) system. Apparently, the ionization and/or geometric structure of the absorbing material have changed between observations.

4.4 Discussion

In the following sections we discuss the implications of our data analysis. We introduce the model we use to analyze the ionization state of absorbers and emitters we detect (§4.4.1), evaluate the two scenarios for line identifications (§4.3.5) in terms of the ability of the HETGS to detect spectral lines (§4.4.2), discuss the detection and implications of the highly-ionized, high-velocity outflow (§4.4.3), and consider the implications of the strong O VII and Ne IX emission we see without corresponding absorption lines (§4.4.4).

4.4.1 Ionization States

We may determine properties of the gas producing the spectral lines we observe by modeling the gas as a single-zone photoionized plasma. We use two different single-zone models. The first is a set of ion abundances calculated by XSTAR. The second model is a simplified version of the model presented by Krolik et al. (1981). The equilibrium state of the gas can be found as a function of the ionization parameter ξ, defined above in §4.3.3. For each value of ξ, the gas temperature and electron density are determined such that heating and cooling processes are in equilibrium. The heating processes considered are photoionization and Compton scattering. The cooling processes considered are radiative recombination, di-electronic recombination, Compton upscattering, bremsstrahlung, and collisional excitation producing line radiation. Abundances are taken from Anders and Grevesse (1989). We have compared the results of our model to the results produced by XSTAR using the same continuum and found reasonable agreement. Because XSTAR includes processes which we do not currently model (e.g., Auger processes), we quote numerical results using the XSTAR calculations, though the conclusions we draw are supported by both models.

In order to model the UV and X-ray continua accurately, we use a broken power law. The continuum mean intensity is:

$$4\pi J_\epsilon(\epsilon) \equiv \frac{\xi n}{4\pi} \left(\begin{array}{rc} N_u (13.6\text{ eV})^{-\alpha_{OX}}, & \epsilon \leq 13.6\text{ eV} \\ N_u \epsilon^{-\alpha_{OX}}, & 13.6\text{ eV} \leq \epsilon \leq 2\text{ keV} \\ N_x \epsilon^{1-\Gamma}, & 2\text{ keV} \leq \epsilon \leq 75\text{ keV} \\ 0, & 75\text{ keV} \leq \epsilon \end{array} \right) \text{ergs cm}^{-2}\text{ sec}^{-1}\text{ erg}^{-1} \tag{4.1}$$

The low-energy portion of the continuum J_ϵ, which we have set to be constant with energy, has little influence on our model. Using UV spectra published in Monier et al. (2001) and Ganguly et al. (2001) which were taken in 1996 and 2000, respectively, we calculate $\alpha_{OX} \approx 1.3$ for a power law between the previously-observed UV flux at 2500 Å and the 2 keV flux we observe with *Chandra*. N_u and N_x are chosen so that the UV and X-ray power laws are joined at 2 keV subject to the normalization condition

$$\int_{13.6\text{ eV}}^{13.6\text{ keV}} J_\epsilon(\epsilon) d\epsilon = \frac{L_{ion}}{(4\pi)^2 r^2}. \tag{4.2}$$

In practice, we use $N_x = 2.28 \times 10^{-4}$, $N_u = 0.619$, and $\Gamma = 1.26$ from our simple power law best fit. The high-energy cut-off at 75 keV is based on continuum fits from *BeppoSAX* observations taken in 1988 (Orr et al. 2001).

The ranges of temperature and ξ where O VIII, Ne X, Si XIV, Ne V, Fe XVII, and Fe XXVI make up at least 10% of their elemental abundances are given in Table 4.4. The numbers quoted are from the XSTAR calculation.

4.4.2 Analysis of Ionization Stages

The photoionized plasma models described above (§4.4.1) indicate abundance levels as a function of the ionization parameter ξ. However, because the continuum and instrument properties vary across the measured spectrum, absorption and emission features from a given abundant element may not be detected even when they are present. To quantitatively address the *Chandra* HETGS' ability to detect lines at a given wavelength, we consider a statistic based on the signal-to-noise ratio of an expected line observed with the HEG or MEG gratings. Define

$$S(\xi, i, j, \lambda) \equiv \lambda^2 \sqrt{\frac{C_\lambda(\lambda)}{FWHM(\lambda)}} A_i X_{ij}(\xi) f_\lambda, \tag{4.3}$$

where $C_\lambda(\lambda)$ is the number of continuum counts per Angstrom at the specified wavelength λ, $FWHM(\lambda)$ is the full width at half maximum of the grating instrument, A_i is the abundance of element i, $X_{ij}(\xi)$ is the fraction of element i ionized to stage j at ionization parameter ξ, and f_λ is the oscillator strength of the line we are considering. We test against all resonance lines tabulated in Verner et al. (1996) for elements of significant solar abundance.

The ionization fraction of Fe XVII peaks at $\log(\xi) \approx 1.95$. At that ionization stage, the lines with the highest statistic S are (in decreasing order of S) from the ions O VIII, Fe XVII, and Ne IX. The lines and statistic values are given in Table 4.5. At $\log(\xi) = 2.15$ the statistic for the Fe XVII line is highest in relation to (as a fraction of) that of O VIII, yet it is still a factor of about 3 lower than the statistic for the O VIII 18.97 Å line. Values are given in Table 4.6. In this, the best case, we find a ratio

$$\frac{S(10^{2.15}, Fe, XVII, 15.02)}{S(10^{2.15}, O, VIII, 18.97)} \approx 0.33. \tag{4.4}$$

Our ionization model predicts that O VIII is abundant across the ionization range where Fe XVII is found. Although the continuum is small in the region where we would expect to see the O VIII 18.97 Å line, line absorption with an equivalent width comparable to that of the Fe XVII line observed is not consistent with the number of counts we actually observe. If we attribute the absorption feature at 15.10 Å to Fe XVII, the fact that we do not observe a corresponding O VIII Lyα line may also indicate that the elemental abundance ratio of O to Fe is much less than solar.

The Si XIV feature, if real, may indicate a third ionization stage. Under assumed abundances, the S statistic for the Si XIV line would be inferior to lines of other ions, including O VIII. Because the Si XIV line was fairly weak, features that are less detectable may reasonably be missed. Still, the abundance of Si would need to be enhanced by a factor of at least 3 to become the most detectable line at $\log(\xi) \approx 2.9$.

In the alternate interpretation in which the absorption feature at 14.20 Å (rest frame) is a line (or lines) from Ne III, Ne IV, or Ne V, the respective lines from these ions are the most detectable lines (maximal S statistic) for the ionization stages ($\log(\xi) < 0$) where they would be found, although the S statistic for these lines is much lower than that previously calculated for Fe XVII, which is a factor of 5-10 higher overall. However, as discussed in §4.3.5, there are other problems with this scenario.

4.4.3 Highly-Ionized, High-Velocity Outflow

As discussed in §4.3.5, we detect a highly-significant spectral feature most naturally identified as Fe XXVI Lyα at a systemic blueshift of $-12,700^{+2400}_{-2400}$ km s^{-1}. This feature alone suggests we are observing a highly-ionized, high-velocity outflow with dynamical characteristics that will be discussed below. In one interpretation of the remainder of the spectrum, we identify two other absorption features with material at lower ionization levels flowing out at higher velocities (about 17,000 km s^{-1}).

Absorption lines indicative of very high velocity outflow have been detected in a handful of objects. These include three quasars that show broad absorption lines (BAL) in the UV (Chartas et al. 2002, 2003; Reeves et al. 2003), two narrow line Seyfert 1 galaxies (Pounds et al. 2003b,a), and the Seyfert 2 IRAS 18325-5926 (Lee et al., in preparation). Our detection adds to the mounting evidence that high velocity outflow could be common to many bright AGN and could constitute a major mass flux and (kinetic) energy flux in the nucleus (e.g Pounds et al. 2003a but see Kaspi 2004). It has been suggested that such outflows are associated with black holes accreting at or above the Eddington rate (Pounds et al. 2003a). However, since MR 2251-178 was well below its maximum observed luminosity during our observation (Figure 4-6), at least this outflow is not associated with super-Eddington accretion. It also shows the lowest observed velocities ($0.042c$ and possibly $0.056c$, compared to $0.08c$ to $0.4c$ observed in other AGN). So far, there is no systematic pattern to the velocities or the degree of ionization of the winds.

Dynamical Characteristics

In this section we will use the measured outflow characteristics to estimate characteristic radii of the absorbing material as well as mass and energy outflow rates. All calculations will be based on the Fe XXVI line alone, though we will include calculated values from Fe XVII and Si XIV when possible for completeness.

Following (Turner et al. 1993; Krolik and Kriss 2001), we estimate that the column density N is due to a line of sight through a thin spherical shell of thickness Δr so that $\Delta r \ll r$ and $N \approx n\Delta r$. Then,

$$\frac{\Delta r}{r} \approx \frac{\xi N r}{L_{ion}}, \tag{4.5}$$

implying that the absorber cannot be at a distance farther than

$$r_{max} = \frac{L_{ion}}{N\xi} \tag{4.6}$$

from the central source, where L_{ion} is the ionizing luminosity (between 1 and 1000 Ry), estimated throughout this section to be 10^{45} ergs s^{-1}. Using the column density estimated for the Fe XXVI line above, we obtain a maximal radius $r_{max} \approx 1 \times 10^{19}$ cm. This upper limit on the radius is a little larger than the maximum estimated value (when $f_{cov} = 1$) of the launching radius r_{launch} derived in equation (4.17).

We estimate the accretion rate required to give the observed luminosity as

$$\dot{M}_{acc} = \frac{L_{bol}}{\eta c^2} \tag{4.7}$$

$$= 1.1 \times 10^{25} \frac{L_{bol}}{10^{45} \text{ erg sec}^{-1}} \frac{0.1}{\eta} \text{ g sec}^{-1} \tag{4.8}$$

$$= 0.17 \frac{L_{bol}}{10^{45} \text{ erg sec}^{-1}} \frac{0.1}{\eta} \text{ M}_{\odot} \text{ yr}^{-1}, \tag{4.9}$$

where L_{bol} is the bolometric luminosity, η is the accretion efficiency (assumed to be within a factor of a few of 0.1), and c is the speed of light. We estimate $L_{bol} \sim L_{ion} \sim 10^{45}$ ergs s^{-1}.

Mass outflow rates may be estimated assuming the outflow is a section of a spherical shell subtending $\Omega/4\pi$ sr which expands at constant ionization parameter ξ (i.e., the density $n \propto r^{-2}$):

$$\dot{M} = 4\pi r^2 v n \frac{m_p}{0.7} f_{cov} \tag{4.10}$$

$$\approx \frac{4\pi L_{ion} v}{\xi} \frac{m_p}{0.7} f_{cov}, \tag{4.11}$$

where the ratio $(m_p/0.7)$ is the approximate mass per particle of a gas with solar abundances, v is the outflow velocity (here taken to be an absorption line blueshift), m_p is the proton mass, and $f_{cov} \equiv \Omega/4\pi$. Estimated mass outflow rates and kinetic energy outflows $(1/2\dot{M}v^2)$ are given in Table 4.7.

A related approximation in which we assume the column density $N \sim nr$ (Krolik and Kriss 2001) gives a similar outflow mass:

$$\dot{M} = 4\pi N r v f_{cov} \frac{m_p}{0.7} \tag{4.12}$$

$$= 2.68 \times 10^{27} f_{cov} \frac{r}{10^{18} \text{ cm}} \text{ g sec}^{-1} \tag{4.13}$$

$$= 41 f_{cov} \frac{r}{10^{18} \text{ cm}} \text{ M}_{\odot} \text{ yr}^{-1}, \tag{4.14}$$

where the values for Fe XXVI (including the column density derived above) were used. This is within a factor of a few of the outflow rate previously derived and shown in Table 4.7 if the flow is at a radius of a few $\times 10^{18}$ cm.

Unless the covering fraction, f_{cov}, of the outflow is very small or the bolometric luminosity, L_{bol}, is much higher than 10^{45} erg s^{-1}, the outflow mass and kinetic energy are somewhat larger (in the Fe XXVI case) or even orders of magnitudes larger (if Fe XVII and Si XIV are considered) than the total accretion rate and luminosity of MR 2251-178. If the covering fraction or the duration of the outflow activity were extremely small, our detection of the outflow would be extremely fortuitous. Either the outflow apparently plays a significant role in the mass and energy budgets of the active nucleus, possibly even exceeding the accretion rates, or else we need a very different interpretation of these features.

Launching Radius

In this section, we assume the second scenario of §4.3.5, i.e., that we have detected absorption lines of Fe XVII and Si XIV at high outflow velocities. While the putative Fe XVII and Si XIV lines correspond to different ionization stages, they are flowing out at nearly the same velocity, about -17,000 km s^{-1}. This may indicate that the outflowing wind has reached terminal velocity. In this case we may use equation (1) from Chartas et al. (2002)

to estimate the radius r_{launch} at which a radiation-driven wind is launched. We have:

$$\begin{aligned} r_{launch} &\sim \frac{2GM_{BH}}{v_{wind}^2}\left(\Gamma_f \frac{L_{UV}}{L_{Edd}} - 1\right) &(4.15)\\ &\sim 2.2 \times 10^{-9} \frac{L_{UV}\Omega}{v_{wind}^2} &(4.16)\\ &\sim 4.8 \times 10^{18} \frac{L_{UV}}{5 \times 10^{44}\ \mathrm{erg\ sec^{-1}}} f_{cov}\ \mathrm{cm}, &(4.17)\end{aligned}$$

where M_{BH} is the black hole mass, v_{wind} is the wind velocity, Γ_f is the force multiplier (an indication of the gas opacity, assumed to be 100) (Laor and Brandt 2002), Ω is the solid angle of material into which the source is radiating, $f_{cov} \equiv (\Omega/4\pi)$, and L_{UV} and L_{Edd} are the UV and Eddington luminosities, respectively. We consider $L_{UV} \sim 5 \times 10^{44}$ ergs s^{-1} to be a reasonable estimate of the UV luminosity based on the *FUSE* and Faint Object Spectrograph (FOS) spectra presented in Kaspi et al. (2004); Monier et al. (2001), respectively. For comparison, Kaspi et al. (2004) set a lower limit on the size of the broad line region (BLR) of $(1.2 \pm 0.2) \times 10^{17}$ cm and concluded (based on features of the *FUSE* spectrum) that the UV absorber they observed lies outside the BLR.

4.4.4 Covering Fraction

The resonance, intercombination, and forbidden lines of helium-like ions in AGN plasmas have recently been studied by Porquet and Dubau (2000). Radiative recombination favors the triplet ^{3}S and ^{3}P levels over the singlet ^{1}P level while collisional excitation favors the singlet ^{1}P level. The presence of strong forbidden emission lines ($1s^2\ ^1S_0\ -\ 1s2s\ ^3S_1$) is evidence that the plasma we observe is photoionized. All three lines may be seen in emission in the spectra of Seyfert 2 galaxies such as NGC 1068 (Kinkhabwala, A., et al. 2002; Ogle et al. 2003).

We detect strong, broad forbidden emission lines from helium-like oxygen and neon, but no corresponding resonance absorption (or emission) lines from these ions. Assuming the forbidden line emission is produced by warm absorber material, we model the warm absorber as a spherical shell which covers some fraction of the central source. Strong emission lines with no corresponding absorption could occur in the following scenarios:

1. The absorbing shell covers a large fraction of the source and is neither obscured nor expanding (or contracting) appreciably, so that photons scattered out of the resonance line along our line of sight are replaced by emitted (resonantly scattered) photons from other regions of the shell.
2. The radial velocity dispersion in the shell (along our line of sight) has become so large or so small that absorption lines are not detectable.
3. The shell covers less than about half of the source and we are looking through the shell so that the absence of absorption is due to physical properties of the absorber.
4. The emitting material is not along our line of sight.

Although we cannot completely rule out scenario 1, we note that it is problematic for several reasons. Warm absorbers (including the UV absorber previously detected in this system by Monier et al. (2001)) typically show outflow velocities of a few hundred km s^{-1}, but these velocities are sufficient to shift photons out of the line center, so that photons scattered out of the line of sight are unlikely to be replaced by photons scattered from the far side of the shell. Additionally, the central source, accretion disk, and perhaps other material would block photons scattering across the center of the shell, reducing the number of photons available to replace photons absorbed along our line of sight. In any case, the possibility that a warm absorber could have a covering fraction near unity would have significant implications for unified AGN models.

Regarding scenario 2, we note that the absorption lines detected in the UV by Monier et al. (2001) had FWHM's over 300 km s^{-1}, near to our instrumental FWHM of 390 km s^{-1}, which we use in the calculation below. The upper limit on column density which we derive below is proportional to the line width, so that a narrower line would actually improve our final result up to the point where it becomes undetectable. (Monte Carlo simulations indicate that a line with optical depth $\tau = 1$ across a FWHM as small as about 200 km s^{-1} would be detectable at 90% confidence more than 80% of the time.) Finally, we note that the forbidden emission line widths may suggest an upper limit on any absorption line FWHM if the absorbing material is also emitting forbidden-line photons (which are not significantly absorbed by intervening material). We will quantify our arguments about the absorption line FWHM in the discussion following.

The remainder of this section is an analysis of scenario 3. We show that it is inconsistent and hence untenable. We assume that the covering fraction of the warm absorber is small enough (e.g., $f_{cov} < 1/2$) that resonance line scattering does not significantly fill in absorption lines.

We may provide a limit on the covering fraction f_{cov} of the Ne IX absorber by considering the intensity of the forbidden line we observe and constraining the column density of the gas, given that we do not see resonance line absorption. We choose to work with the Ne IX line instead of the O VII line because the low number of continuum counts in the oxygen line region do not give strong constraints on the presence of any absorption line. We assume the ionized gas is uniformly distributed in a $4\pi f_{cov}$ steradian section of a spherical shell with a column density of N_{NeIX} along the line of sight.

We first define a parameter α_{Ne} such that

$$\alpha_{Ne} \equiv \frac{n_{NeX}}{n_{NeIX}}. \tag{4.18}$$

We may estimate α_{Ne} from photoionization models as a function of ξ. For helium-like ions, electrons recombine preferentially to the triplet levels which produce intercombination and forbidden lines, so the suppression of resonance lines is reasonable in a photoionized plasma. Because we see forbidden lines from helium-like ions (indicating that hydrogen-like ions are present and recombining with free electrons), we require our model to be at an ionization stage where hydrogenic ions of oxygen and neon are present. For hydrogenic atoms, we would expect to see resonance emission lines from recombination. Thus we interpret the absence of resonance emission lines from hydrogenic atoms as evidence that the rate of recombination into those ions is small. In particular, we assume that abundances of completely ionized oxygen and neon are small, so that little recombination into the hydrogen-like ions is occurring. For plasma states where the abundances of O VIII and Ne X are at least 10% of the total elemental abundance and the abundances of Ne XI and O IX are less than 10% of the total elemental abundance, we find $\alpha_{Ne} \approx 0.88$ and $(\xi/\alpha_{Ne}) \approx 210$. The temperature of our model is about 45,000 K in this plasma state.

From Mewe and Gronenschild (1981), we calculate an intercombination line branching ratio to the ground state of about 0.338 and a forbidden line branching ratio of very nearly 1. Using radiative recombination rates from Porquet and Dubau (2000) calculated at a temperature of 1.4×10^5 K (the lowest temperature available), we expect a total forbidden line rate of about $R_{Tot} \equiv 5.5 \times 10^{-12}$ cm^3 s^{-1}. The resonance line becomes optically thick ($\tau \geq 1$) and should be clearly detected across its entire FWHM for a column density $N \geq 2.9 \times 10^{16} \beta_{FWHM}$ cm^{-2}, where we define the parameter $\beta_{FWHM} \equiv$ FWHM/390 km s^{-1} in order to estimate the importance of line width considered in scenario 2. A large covering fraction or line width would raise the limit on column density, while a smaller line width would lower it. We are also ignoring the effect of resonance line photons emitted due to recombination. However, an estimation of this number of photons based on the strength of the forbidden line indicates that only a few of these photons would fall inside an instrumentally-wide line, which does not significantly affect our final result.

We expect a total forbidden line luminosity of

$$\begin{aligned} L_{Tot} &= E_f R_{Tot} \int n_e n_{NeX} dV & (4.19) \\ &\approx \alpha_{Ne} E_f n_e R_{Tot} (4\pi f_{cov} r^2) N_{NeIX} & (4.20) \\ &\leq 2.9 \times 10^7 \alpha_{Ne} \beta_{FWHM} \left(\frac{n_e}{10^{10}\ \mathrm{cm}^{-3}} \right) f_{cov} r^2 \ \mathrm{erg\ sec}^{-1}, & (4.21) \end{aligned}$$

where E_f is the energy of the forbidden line, n_e is the electron density, and r is the shell radius (assumed much larger than the thickness of the shell). This corresponds to a flux of

$$F_f \leq 3.1 \times 10^{-11} \alpha_{Ne} \beta_{FWHM} \left(\frac{n_e}{10^{10}\ \mathrm{cm}^{-3}} \right) f_{cov} r_{pc}^2 \ \mathrm{erg\ cm}^{-2}\ \mathrm{sec}^{-1}, \qquad (4.22)$$

where r_{pc} is the shell radius in parsecs.

Given that we actually measure a flux of about 1.8×10^{-14} erg cm^{-2} s^{-1} in the forbidden emission line, we can constrain:

$$\alpha_{Ne} \beta_{FWHM} \left(\frac{n_e}{10^{10}\ \mathrm{cm}^{-3}} \right) f_{cov} r_{pc}^2 \geq 5.9 \times 10^{-4}. \qquad (4.23)$$

By the definition of ξ,

$$n r^2 \equiv \frac{L_{ion}}{L_x} \frac{L_x}{\xi}, \qquad (4.24)$$

where L_x is the 2-10 keV luminosity we observe. At these ionization levels, $(n_e/n) \approx 1.2$. Combining this with equation (4.23), we find that our model requires

$$f_{cov} \geq 0.20 \frac{L_x}{L_{ion}} \frac{\xi}{\alpha_{Ne} \beta_{FWHM}}. \qquad (4.25)$$

Using the constraint on (ξ/α_{Ne}) mentioned above, we find that

$$f_{cov} \geq 42 \beta_{FWHM}^{-1} \frac{L_x}{L_{ion}}. \qquad (4.26)$$

Recall that we had assumed in this scenario that f_{cov} was less than roughly 1/2. If we assume the line to be narrower than the instrumental width, β_{FWHM} will decrease and our constraint will only get stronger, up to the point where the line becomes undetectable. For a line even as wide as the Ne IX forbidden line we measure ($FWHM \sim 1500$ km s^{-1}), our constraint on f_{cov} is only relaxed by a factor of a few. Thus it is unlikely that velocity dispersion effects (scenario 2) could explain the absence of an absorption line.

We see no evidence in previous UV observations (Monier et al. 2001; Ganguly et al. 2001; Kaspi et al. 2004) that (L_x/L_{ion}) could be small enough to bring the constraint on f_{cov} (equation (4.26)) down to acceptable values. Even if we add a large excess to our UV continuum model, this will lower the value of (L_x/L_{ion}), but it will increase the value of (ξ/α_{Ne}), as fewer X-ray photons will be available at a given value of ξ to ionize the helium-like elements. Furthermore, because of the large L shell cross section in the UV of Ne VIII, Ne IX should be strongly abundant at the ionization ranges we are considering, yet we do not see it in absorption. Thus the homogeneous partial shell model (option 3 enumerated above) is incorrect.

We are left with option 4. We conclude that we are not looking through the gas which is emitting the forbidden lines we observe. We may be looking through a hole in the emitting material, or the material may simply be out of our line of sight. The forbidden lines are much wider than the characteristic thermal width for gas at the ionization stages under consideration, suggesting that the emitting material is moving at a wide range of velocities. The ionization level of the gas is similar to that observed in warm absorbers in other AGN. We speculate that the emitting gas is a warm absorber which is not along our line of sight, though it may have been at one time.

Analyzing the continua of previous observations of MR 2251-178, Kaspi et al. (2004) found in one case changes in the absorber ionization and column density without corresponding changes in luminosity, and in another case changes in luminosity without changes in column density and ionization. They suggested that these changes, which are observed on time scales of several months to years, are explained by physical motion of the warm absorber gas. Physical motion of (cold) absorbing gas was originally considered by Halpern (1984), who argued that the variability of the absorption in MR 2251-178 was better explained by changing ionization structure in a warm absorber. Now the question has evolved to whether we are seeing the effects of physical motion in a warm absorber.

Measurable physical motion of the warm absorber has implications for unification models. Warm absorbers apparently have considerable geometric structure, and variations in absorption properties are not simply due to viewing angle and ionization stage. We have shown analytically that plasma at warm-absorber levels of ionization is not uniformly (spherically) distributed about the central source. The highly ionized, high-velocity outflow we also observe in this data set indicates that ionized absorbers can also have significant structure along the line of sight, e.g., absorption can come from multiple systems with significantly different dynamic qualities.

We conclude this section by noting that this observation of MR 2251-178 raises several important questions about the properties of warm absorbers and their role in AGN unification models. What is the distribution of ionized material perpendicular to and along the line of sight, now that we know it is significantly structured and changing on observable time scales? Is there a connection between the warm absorber and the highly ionized, high-velocity outflow? Does the outflow supply material to the warm absorber, or are the two separate systems? What are the underlying features in the continuum below 2 keV? If they are absorption edges, what distribution of ions and ionization stages is required to fit them, and where are the corresponding absorption and emission lines? High resolution spectroscopy will hopefully enable us to answer many of these questions as the study of AGN progresses.

4.5 Conclusions

The *Chandra* HETGS has enabled us to obtain a high-resolution X-ray spectrum from MR 2251-178. We have observed it in a relatively low state. We do not detect any variability in the continuum. Morphologically, we do not find any large asymmetries that would signal the presence of an X-ray jet, though we do see emission extended to the west, south, and northeast.

The remainder of our conclusions are concerned with characterizing the ionized absorption evident in the X-ray spectrum. We see evidence for at least two absorbing systems: a low-ionization absorber which is evident in the continuum and a high-velocity outflow evident in Fe XXVI line absorption and possibly other lines. We also see forbidden line emission from helium-like oxygen and neon which appears not to be concentrated along our line of sight.

Our best continuum fit requires both ionized absorption and some form of soft excess. In addition to a narrow Fe Kα line, we see lines from at least two dynamic systems of highly-ionized gas: the forbidden emission lines of helium-like neon and oxygen nearly at rest in the system, and a broad absorption line from Fe XXVI at a high outflow velocity. We see two additional absorption lines and describe two different scenarios in which they could arise. In the first case, the strong 15.10 Å feature could be due to Ne V inner-shell absorption at a typical outflow velocity while the weaker feature is unidentified. In the second scenario, both features are components of a highly-ionized, high-velocity outflow, presumably related to the Fe XXVI feature.

On the basis of the Fe XXVI identification alone, we find that the outflow appears to be carrying away a significant amount of mass and energy from the nucleus compared to its accretion rate. In the second scenario, in which we identify multiple ionization stages in the outflowing wind, we find evidence of dynamical and likely spatial structure which may indicate an asymptotic velocity and a launching radius for the wind.

We use the measured properties of the forbidden line emission from Ne IX and O VII together with the absence of resonance line absorption to constrain the covering fraction of the emitting gas. By modeling the photoionized emitter under the influence of a realistic continuum, we determine (given certain assumptions detailed above) that the emitting gas cannot be distributed in a uniform spherical shell about the central source. We conclude that the emitter is not along our line of sight, suggesting that the emitting material may be a warm absorber which is not in view. We appear to have a relatively unobstructed view into the nucleus of MR 2251-178 in this observation.

It has been suggested by Kaspi et al. (2004) that physical motion of the warm absorber gas would explain the variation in warm absorber properties, such as absorbing column and ionization level, which they observed on time scales of several months. In fact, our observation, taken 116 days after the 2002 *XMM-Newton* observation they primarily report, appears to have an unusually low absorption column density and ionization level compared those they fit to 14 observations taken over about ten years. They fit the 2002 *XMM-Newton* RGS spectrum with a second absorber which more closely matches the ionization level of our best fit absorber, but is at a much lower column density than ours. Additionally, we see strong absorption features (line absorption from Fe XXVI and likely Fe XVII or Ne V) which, though not quantitatively evaluated, do not appear strongly in their spectrum. It is tempting to speculate that the high-ionization absorber they observed has moved out of view, but is still detected by us in forbidden emission lines, while the low-ionization absorber they fit at low column has moved into the line of sight, along with clouds responsible for the other phenomena we observe. In any case, it seems quite clear that the non-spherical geometric structure of warm absorber material in MR 2251-178 has important consequences for the X-ray spectra we observe.

4.6 Acknowledgements

This work was supported in part by by NASA through contracts NAS8-01129 and SAO SVI-61010. JCL thanks and acknowledges support from the *Chandra* fellowship grant PF2-30023 – this is issued by the *Chandra* X-ray Observatory Center, which is operated by SAO for and on behalf of NASA under contract NAS8-39073.

Model[a]	Photon Index	Power Law Norm[b]	Other	Reduced χ^2_ν
power law	$1.26^{+0.01}_{-0.01}$	$3.10^{+0.02}_{-0.02} \times 10^{-3}$	(none)	1.13
(power law+black body)× ×WA+WEM	$1.46^{+0.01}_{-0.02}$	$4.20^{+0.03}_{-0.03} \times 10^{-3}$	N_H: $2.37^{+0.28}_{-0.15} \times 10^{21}$ cm^{-2} log(ξ): $0.02^{+0.11}_{-0.10}$ WABS Vel.: -330_{-220} km s^{-1} WEM Norm: $0.0^{+7.7} \times 10^{-7}$ black body norm:[c] $1.94^{+0.18}_{-0.17} \times 10^{-4}$ black body kT: $93.2^{+2.1}_{-2.2}$ eV	1.06

[a] All fits include fixed Galactic absorption using the XSPEC **phabs** model and an instrumental Ir M edge (described in the text).

[b] In units of photons keV^{-1} cm^{-2} s^{-1} at 1 keV.

[c] In units of L^{39} / D^2_{10}, where L_{39} is source luminosity in units of 10^{39} erg s^{-1} and D_{10} is distance to the source in units of 10 pc.

Table 4.1: Model fit results. Errors shown are 90% confidence limits for individual parameters. If an error is not given, the fit was poorly constrained.

Year(s)	Mission	Γ	Flux[a]
1975	*Ariel V* 2A (Cooke, B. A., et al. 1978)	(none)	8.7±2.0
1981	*Ariel V* 3A (McHardy et al. 1981)	(none)	3.6±0.5
1977	*SAS-3* (Ricker et al. 1978)	1.5±0.5	2.5±0.4
1979-80	*Einstein* (Halpern 1984)	$1.52^{+0.17}_{-0.17}$	2.93
		$1.72^{+0.35}_{-0.30}$	3.04
1983-84	*EXOSAT* (Pan et al. 1990)[b]	$1.31^{+0.37}_{-0.20}$ to $2.13^{+0.58}_{-0.49}$	1.86 to 3.27[c]
1989	*Ginga* (Mineo and Stewart 1993)	1.51±0.09	1.65±0.02
1993	*ASCA* (Reynolds 1997)[d]	1.65±0.02	4.50
1998	*BeppoSAX* (Orr et al. 2001)	1.61±0.01[e]	$4.03^{+0.20}_{-0.12}$
			$4.19^{+0.42}_{-0.42}$
2000	*XMM-Newton*[f] (Kaspi et al. 2004)	1.66±0.06	3.30±0.13
2002	*XMM-Newton*[f] (Kaspi et al. 2004)	1.54±0.02	2.10±0.05
2002	*Chandra*	1.26±0.01	2.56±0.02

[a] Flux is in 10^{-11} erg cm^{-2} s^{-1} and is for the unabsorbed 2-10 keV continuum unless noted otherwise. Errors are shown where provided by the original author.

[b] Out of 15 measurements we show the minimum and maximum values reported for the photon index and flux. All reported flux values are shown in Figure 4-6.

[c] Flux measurement assumes a fixed Γ of 1.7. The values cited for Γ were then fit separately.

[d] The combined set of ASCA observations starting Nov. 6, 1993 which was reported by Reynolds (1997) is used here.

[e] Two observations were combined for measurement of Γ.

[f] The power law for the *XMM-Newton* observations was fit to the 3-11 keV band with the 4.5-7.5 rest-frame band excluded. The 2-10 keV flux was calculated from this power law.

Table 4.2: List of observations.

Ion	Lab Wavelength (Å)	Observed Wavelength (Å)	System Wavelength (Å)	Velocity Shift[a] (km s^{-1})	$\sigma_{measured}$ (km s^{-1})	$\sigma_{intrinsic}$ (km s^{-1})	EW (mÅ)
Fe Kα[b]	1.94	$2.056^{+0.002}$	$1.934^{+0.002}$	-900^{+310}	390^{+260}_{-390}	(unresolved)	$7.4^{+4.2}_{-4.0}$
Ne IX forbidden	13.6984	$14.59^{+0.02}_{-0.02}$	$13.72^{+0.01}_{-0.02}$	380^{+320}_{-340}	650^{+340}_{-250}	630^{+350}_{-260}	85^{+36}_{-33}
O VII forbidden	22.1012	$23.53^{+0.05}_{-0.05}$	$22.11^{+0.05}_{-0.05}$	-140^{+650}_{-650}	1700^{+670}_{-480}	1700^{+670}_{-480}	620^{+210}_{-190}
Fe XXVI Lyman α	1.7798	$1.81^{+0.01}_{-0.01}$	$1.71^{+0.01}_{-0.01}$	$-12{,}700^{+2400}_{-2400}$	3400^{+3100}_{-1900}	3300^{+3200}_{-1800}	-17^{+14}_{-10}
Ne V[c] $(1s-2p)+(1s-3p)$	14.221[d]	$15.10^{+0.01}_{-0.01}$	$14.20^{+0.01}_{-0.01}$	-510^{+170}_{-150}	380^{+190}_{-120}	350^{+210}_{-130}	-42^{+17}_{-13}
Fe XVII[c] $2p^6-2p^5 3d$	15.014	$15.10^{+0.01}_{-0.01}$	$14.20^{+0.01}_{-0.01}$	$-16{,}770^{+170}_{-150}$	390^{+190}_{-120}	360^{+200}_{-130}	-42^{+17}_{-13}
Si XIV[e] Lyman α	6.1822	$6.216^{+0.004}_{-0.004}$	$5.842^{+0.004}_{-0.004}$	$-16{,}940^{+200}_{-190}$	180^{+230}_{-180}	(unresolved)	$-4.8^{+4.1}_{-2.8}$

[a] Blueshift (outflow) is negative.

[b] The velocity shift of the Fe Kα line was computed assuming the Fe I rest wavelength of 1.94 Å.

[c] Two possible identifications of the feature at 15.10 Å are listed here. See §4.3.5 for details.

[d] Two inner-shell lines were averaged together.

[e] See §4.3.5 for a discussion of this line identification.

Table 4.3: System-frame ($z = 0.06398$) properties of detected lines. Error shown is the 90% confidence limit for fits. All values are in rest frame.

Ion	$\log(\xi)^a$	Temperature (10^5 K)
O VIII	0.90-2.50	0.30-5.38
Ne X	1.55-2.90	0.56-12.6
Si XIV	2.20-3.35	1.96-42.7
Ne V	-1.80-0.00	0.14-0.22
Fe XVII	1.40-2.40	0.45-3.74
Fe XXVI	≥ 3.05	≥ 18.0

[a] Values given (in cgs units) indicate the range where a particular ion accounts for at least 10% of the total element abundance.

Table 4.4: Gas properties predicted by XSTAR model.

Ion	Rest λ (Å)	$S(\xi, i, j, \lambda)^a$
O VIII	18.97	9.40
Fe XVII	15.02	2.81
Ne IX	13.45	2.19

[a] The "S" statistic, an indication of the statistical significance of an (hypothetical) line, is described in §4.4.2 and equation (4.3).

Table 4.5: Most-detectable lines when Fe XVII is abundant ($\log(\xi) = 1.95$).

Ion	Rest λ (Å)	$S(\xi, i, j, \lambda)^a$
O VIII	18.97	6.97
Fe XVII	15.02	2.29
Ne IX	13.45	1.51

[a] See description in text and equation (4.3).

Table 4.6: Most-Detectable Lines When Fe XVII Is Abundant ($\log(\xi) = 2.15$).

Ion	$\dot{M}$ (g s^{-1})	$\dot{M}$ (M$_\odot$ yr^{-1})	$\frac{1}{2}\dot{M}v^2$ (erg s^{-1})
Fe XXVI	$1.4 \times 10^{28} f_{cov}$	$220 f_{cov}$	$1.1 \times 10^{46} f_{cov}$
Fe XVII	$5.6 \times 10^{29} f_{cov}$	$8900 f_{cov}$	$7.9 \times 10^{47} f_{cov}$
Si XIV	$1.1 \times 10^{29} f_{cov}$	$1700 f_{cov}$	$1.6 \times 10^{47} f_{cov}$

Table 4.7: Outflow Mass and Energy Estimates. Values may be compared to an estimated accretion rate $\dot{M}_{acc} = 1.1 \times 10^{25}(L_{bol}/10^{45}$ erg sec$^{-1})(0.1/\eta)$ g sec^{-1} and X-ray luminosity of 2.41×10^{44} erg s^{-1} (see text).

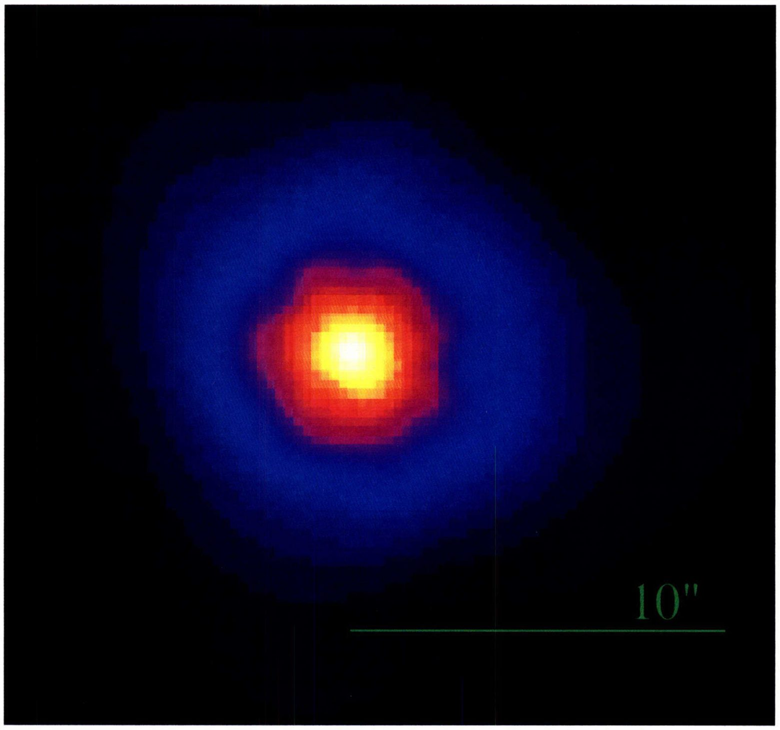

Figure 4-1: Smoothed zero-order image from ACIS-S3 chip. Two pixels are approximately $1''$. $10''$ are approximately 12 kpc. North is up and west is to the right. There are possible extensions to the northeast, south, and particularly west on a scale of $10''$.

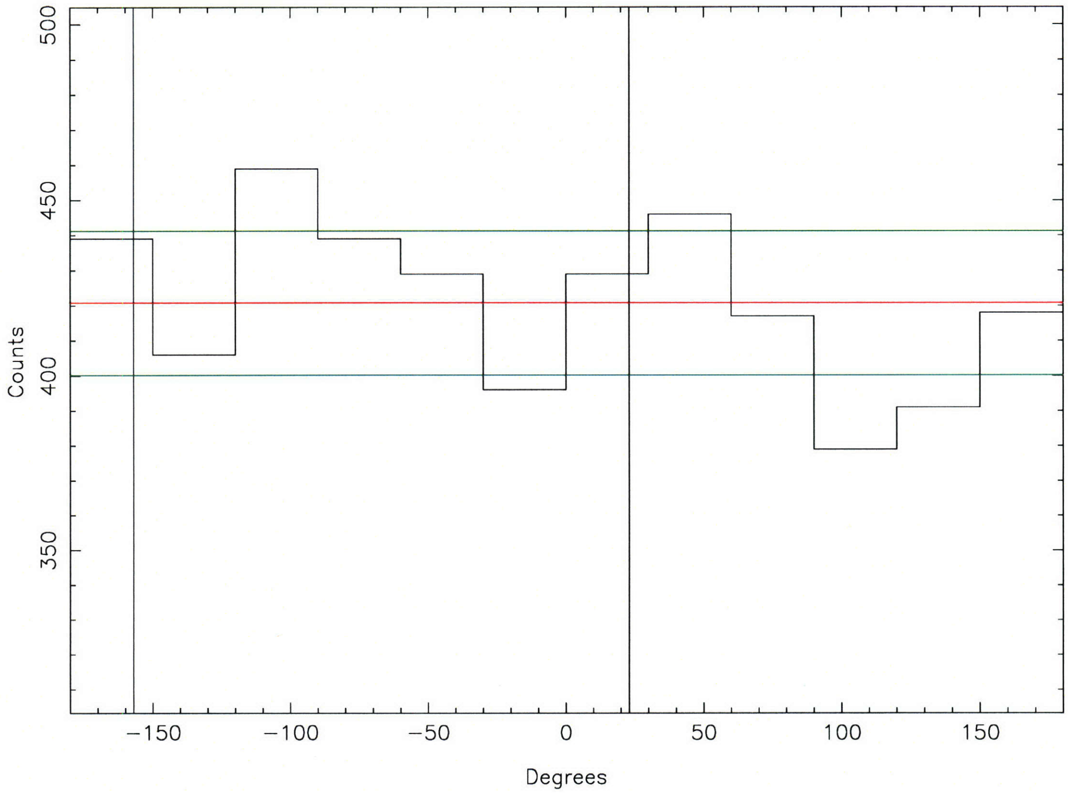

Figure 4-2: Azimuthally binned histogram of counts between 10 and 50 pixels from central source. Horizontal lines show the mean (red) and 1σ deviations. Position angle is degrees counterclockwise from north at zero. Two vertical lines at -157″ and 23.0″ indicate the orientation of a faint, thin readout streak.

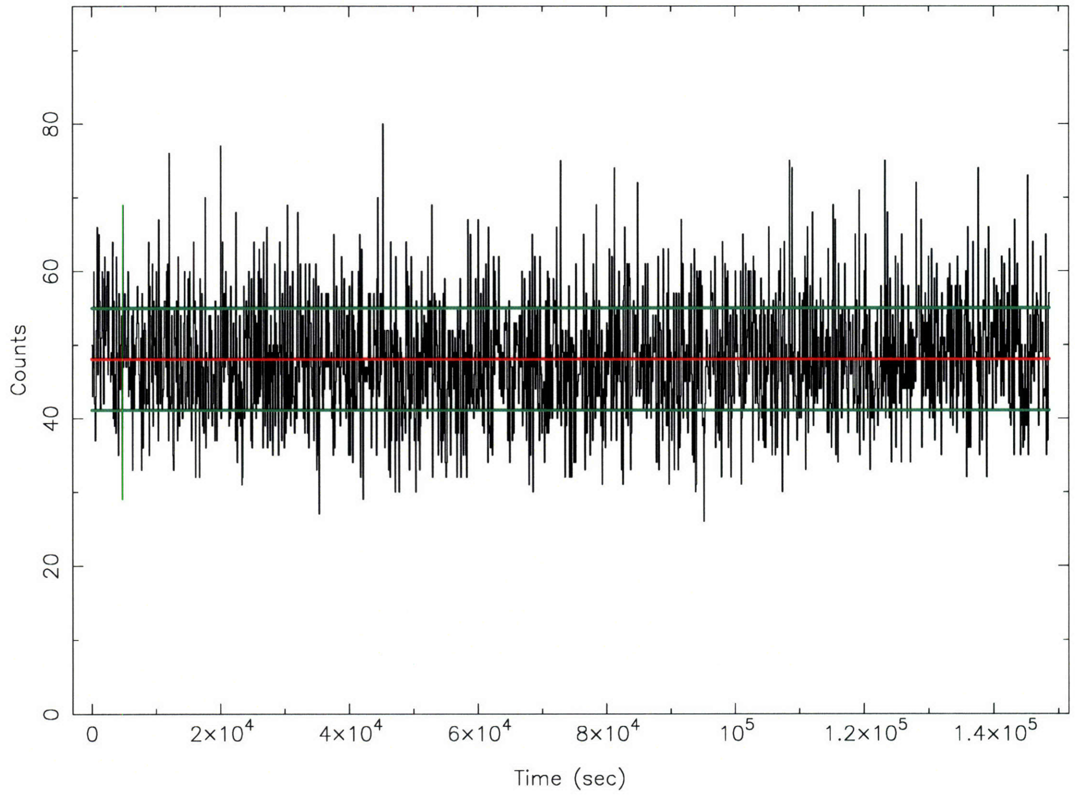

Figure 4-3: Light curve from first-order HEG and MEG counts in 100-second bins. Horizontal lines show the mean (red) and 1σ deviations (green).

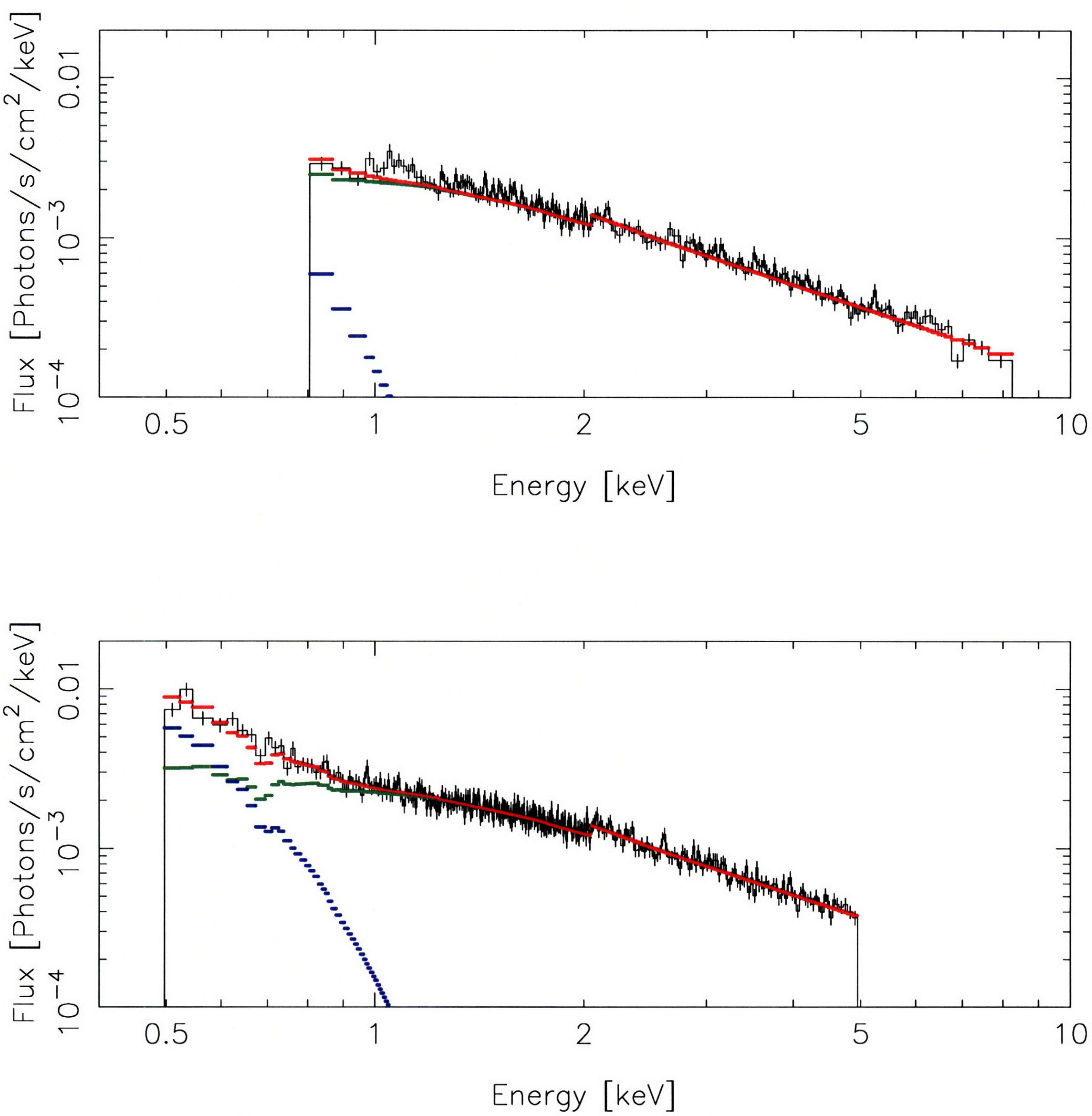

Figure 4-4: *Chandra* first-order observed-frame spectrum binned adaptively to at least 100 counts per bin, in the observed frame. HEG is top, MEG is bottom. The best-fit power law plus black body model with an XSTAR absorption model is overlaid in red. Model components are also shown individually, with the absorbed power law in green and the absorbed black body in blue. An instrumental "reverse edge" feature at 2.0 keV is evident (modeled), as is the systematic deviation between HEG and MEG spectra in the 1-2 keV range (not modeled).

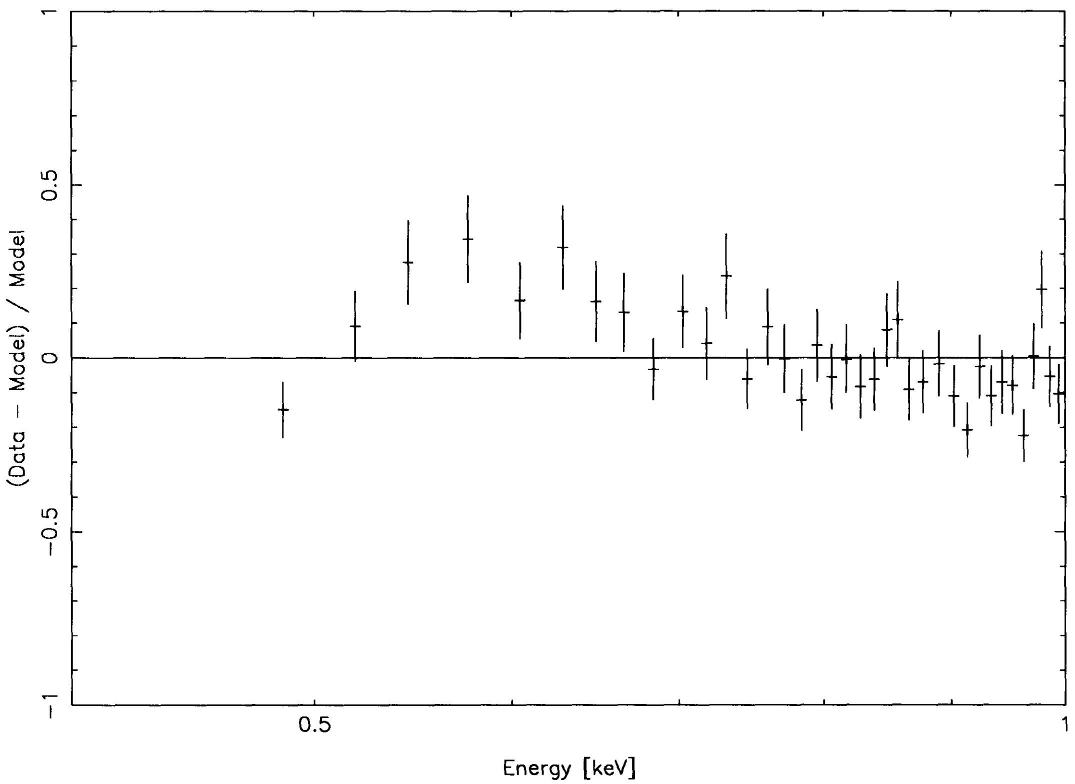

Figure 4-5: Differential between the MEG observed spectrum and a model with a Galactic absorbed power law and black body in the soft X-ray region (0.4-1.0 keV). The model is too low in the 0.5-0.8 keV region, and is possibly too high in the 0.8-1.0 keV region. An ionized absorption model (e.g., the XSTAR model described in the text) improves the fit of this residual. The spectrum is binned adaptively to at least 100 counts per bin.

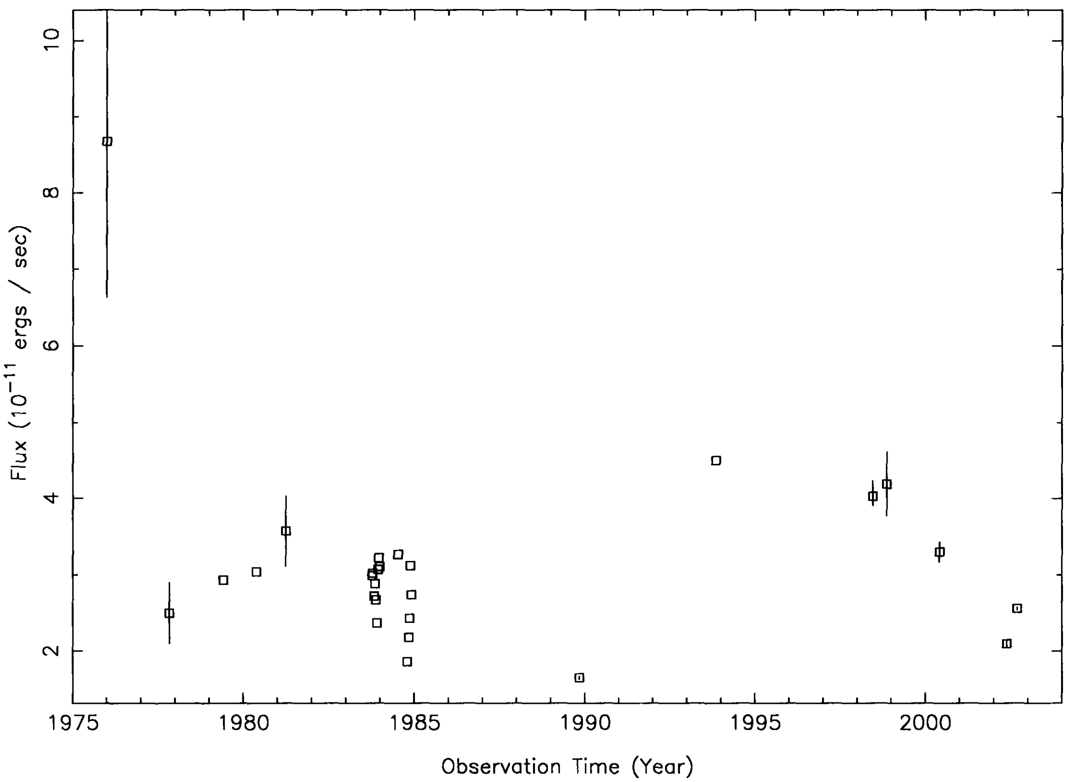

Figure 4-6: 2-10 keV fluxes measured from power law with galactic absorption. The sources (mission and authors) of this data are given in Table 4.2. Error bars are shown where given by the original author. The 2-10 keV flux we measure in this *Chandra* observation (the rightmost, i.e., most recent, point) is lower than that observed on most previous observations.

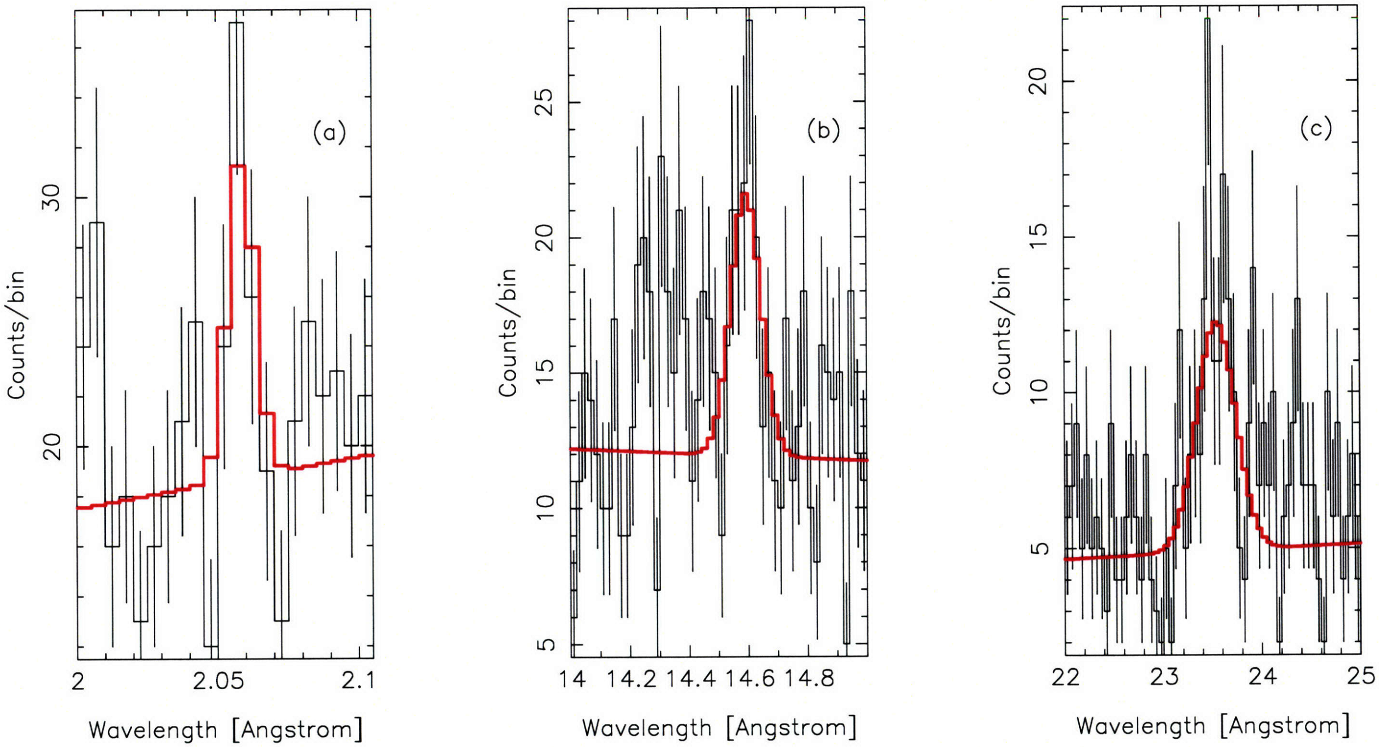

Figure 4-7: Emission lines (shown in observed frame) detected in spectrum, shown with Gaussian and local linear continuum fit. The lines are: a) Fe Kα, b) Ne IX forbidden, and c) O VII forbidden.

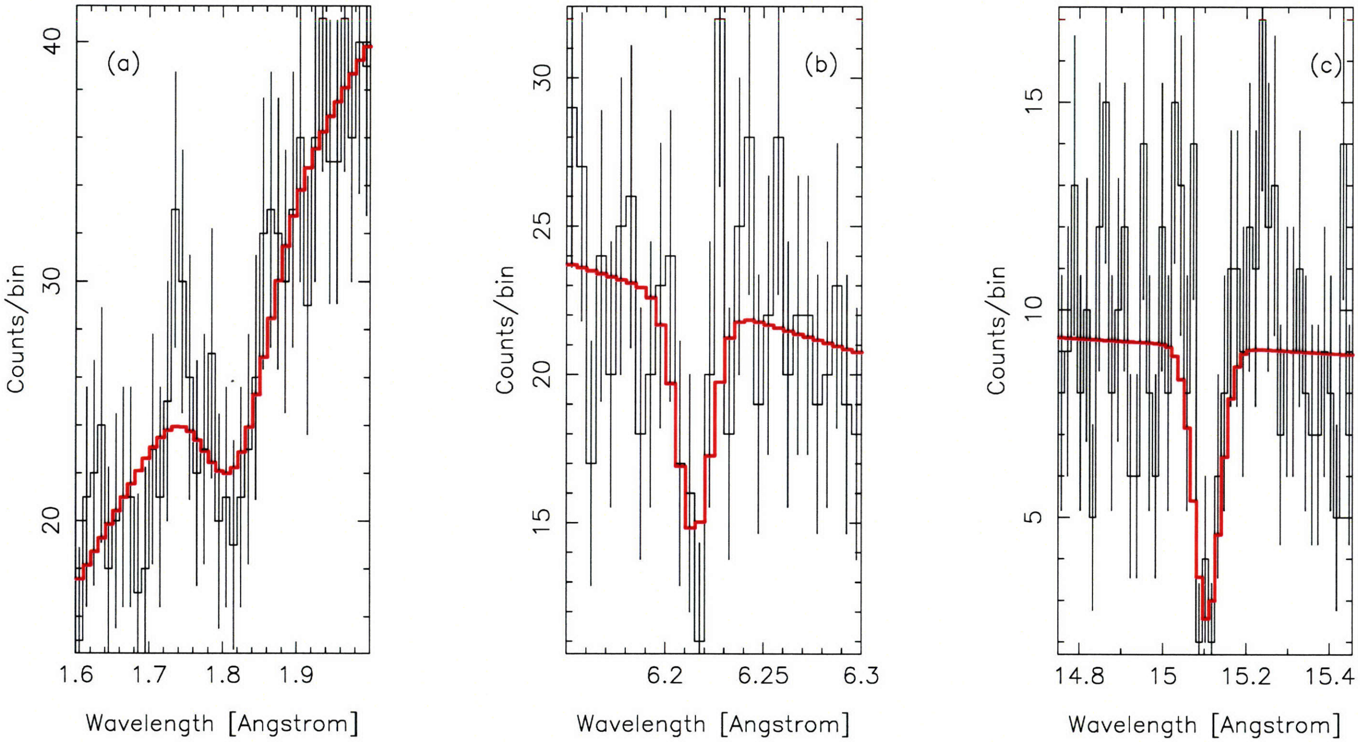

Figure 4-8: Absorption lines (shown in observed frame) detected in spectrum, shown with Gaussian and local linear continuum fit. The lines are: a) Fe XXVI resonance α, b) Si XIV resonance α, c) Fe XVII $2p^6 - 2p^5 3d$.

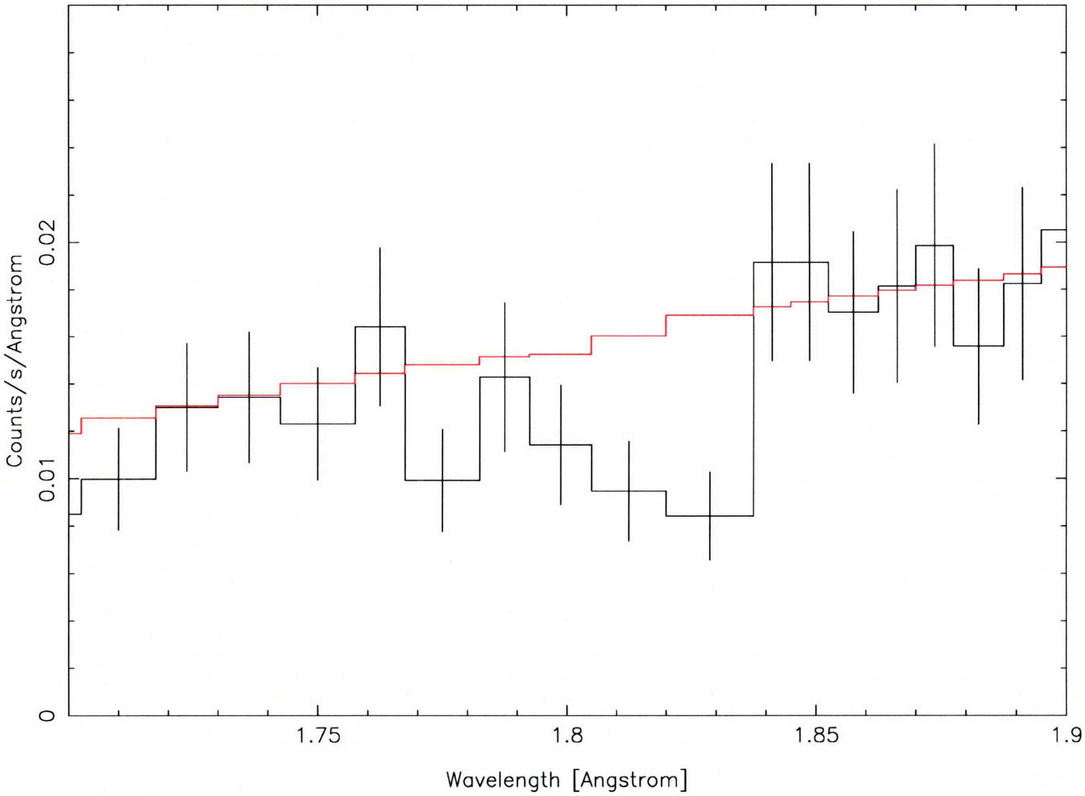

Figure 4-9: Highly-significant feature attributed to absorption from the resonance α line of Fe XXVI, flowing out (blueshifted) at about 12,700 km s^{-1}. Data are binned to at least 20 counts per bin and shown in the observed frame. The model shown is our best-fit continuum model described in the text.

Chapter 5

Line Variability in the High Resolution X-ray Spectrum of MCG -6-30-15

This chapter was originally published in ApJ 627:83-96. The authors involved were: Gibson, R. R., Marshall, H. L., Canizares, C. R., and Lee, J. C.

Abstract

The recent 540 ks *Chandra* HETGS spectrum of the well-studied, variable Active Galactic Nucleus (AGN) MCG -6-30-15 shows strong $1s - 2p$ absorption lines from many ions. The spectrum was obtained over a period of about ten days, and the large number of counts in the spectrum makes it ideal for testing variability on short time scales. We apply quantitative tests for line variability to the $1s - 2p$ absorption lines of H- and He-like Ne, Mg, Si, and S. We find significant correlations and anti-correlations between lines as a function of time, much as we would expect if ionization levels in the absorber were varying. We also find evidence for variation in at least one $1s - 2p$ resonance absorption line as a function of luminosity.

We consider several possibilities to explain the line variation. First we consider factors that could change ionization levels in the absorber: radial motion, density variation, luminosity variation, and continuum shape variation. None of these individually can explain the line variation, though we cannot completely constrain continuum shape variation without simultaneous knowledge of the ultraviolet (UV) continuum. Other factors, considered individually, are also unable to explain all the variation: multiple changing continuum components, variable obscuration, and changes in velocity dispersion. Changes in line emission are an unlikely cause of significant absorption line variation, but we are unable to fully constrain them. Variability could be due to a changing line of sight through a structured absorber. Modeling such scenarios should produce useful constraints on continuum emission mechanisms and absorber structure.

5.1 Introduction

Warm absorbers (WAs) were first proposed to explain variability in the soft X-ray spectra of AGN. Changes in the soft X-ray continuum of the *Einstein* spectrum of MR 2251-178 were attributed by Halpern (1984) to varying ionization levels in a photoionized ("warm") absorber. With high-resolution spectroscopy we now resolve absorption lines and measure time-integrated properties of the WA. But early research with lower-resolution spectroscopy used variability studies to support and characterize the WA model. For example, Yaqoob et al. (1989) found a correlation between the absorbing column and the level of continuum flux in the spectrum of NGC 4151, while Nandra et al. (1990) divided a 3 day *Ginga* observation of MCG -6-30-15 into seven time segments to demonstrate that the level of ionization was strongly correlated with the flux level.

We now have sufficient data to test for variation in individual X-ray spectral lines, with the goal of further constraining WA structure. Some such tests have already been carried out. For example, Netzer et al. (2003) found that the soft X-ray continuum of NGC 3783 changed over time scales of 20-120 days. Although researchers have found several absorbers with multiple kinematic components in the combined spectra (Kaspi et al. 2002) of NGC 3783, Netzer et al. (2003) did not find significant differences between equivalent widths (EWs) of lines from these absorbers in high and low spectral states. Turner et al. (2004) found that four lines (out of about 50) showed evidence for likely variation between the high and low states of a 320 ks *XMM-Newton* observation of MCG -6-30-15.

In the UV, line variability has been detected in several cases. For example, Ganguly et al. (2001) found that the C IV doublet in the QSO MR 2251-178 disappeared after a previous detection four years prior. This was taken as further support for the case that WAs are intrinsic to AGN. More recently, Scott et al. (2004b) found variation in some of the kinematic components of the Lyβ and O VI absorption lines of the Seyfert 1.5 galaxy Mrk 279.

The AGN MCG -6-30-15, at redshift $z = 0.00775$, has been one of the primary sources for WA variability studies. It has been studied extensively with X-ray spectroscopy, and each generation of study has yielded new information. Fabian et al. (1994) discovered a change in the column density of the O VII edge in two *ASCA* spectra taken about one month apart. They suggested the change in column density was due to material changes in the WA, not just to changing ionization levels. In a follow-up study of the same data, Reynolds et al. (1995) found that the ionization level appeared to be increasing even while the ionizing luminosity was decreasing. They pointed out that multiple lines of sight through the WA might be contributing to a single observed spectrum, so that spectral variability could be tied to changes along these individual lines of sight. Reynolds et al. (1995) also raised the possibility of stratification in the WA, i.e., change of WA physical properties with radius, which would mean that single-zone models of the WA were an oversimplification. They tentatively suggested that the variability was due to the passage of an ionized broad line region (BLR) cloud across the line of sight.

A follow-up long observation of MCG -6-30-15 with *ASCA* provided more data for time-variation studies. Otani et al. (1996) found that the depth of the O VII edge remained roughly constant while the O VIII edge varied approximately as the inverse of the continuum count rate. Because the two edges occur at different ionization stages, and because of an apparent difference in velocity offset between the two edges, Otani et al. (1996) suggested that two distinct WAs were present. The high-ionization absorber, located within the BLR, was responsible for the O VIII edge. The low-ionization absorber was located much farther from the continuum source, though the fact that it was not observed to vary with luminosity was surprising. In recent years, high-resolution spectroscopy has shown that the soft X-ray continuum and absorption are complex. Features from multiple ionization stages and outflow velocities can be found in the spectrum (e.g., Branduardi-Raymont et al. 2001; Lee et al. 2001; Sako et al. 2003; Turner et al. 2003).

Apart from absorption signatures, the continuum of MCG -6-30-15 shows complex variability in other respects. *RXTE* observations have shown that the 2-10 keV spectrum hardens as the flux decreases, i.e., the power law photon index Γ increases with flux (McHardy et al. 1998; Lee et al. 2000; Vaughan and Edelson 2001). Depending on the precise energy bands measured, hard bands appear to lag soft bands by anywhere from 50 to about 2000 s, consistent with the model that high-energy photons are Compton upscattered (and hence delayed) low-energy photons (Nowak and Chiang 2000; Reynolds 2000; Lee et al. 2000). Additionally, there is a suggestion of a 33 hour period in the *RXTE* light curve (Lee et al. 2000).

The long 1999 *ASCA* observation provided the ability to take a different kind of look at the spectrum of MCG -6-30-15. Instead of making "vertical" slices to produce spectra from selected time intervals, Shih et al. (2002) split the spectrum "horizontally" into luminosity-selected spectra. I.e., they formed spectra by grouping together data from small time intervals which had similar instrumental count rates. They were able to specify a functional form which adequately fit the observed relationship between the photon index Γ and flux. This led to a discussion of models describing the processes responsible for generating the continuum flux. Fabian and Vaughan (2003) and Vaughan and Fabian (2004) modeled recent *XMM-Newton* spectra as a combination of two components, a phenomenological model previously suggested by Shih et al. (2002). The data indicated that one of the components, which they called the "reflection-dominated component" (RDC), remained constant and was largely responsible for the broad Fe Kα line seen in the spectrum. They called the second component the "power law component" (PLC), and identified it as a power law with varying normalization but nearly constant photon index. The PLC contributes little to the Fe Kα line.

Recent studies of the AGN MR 2251-178 have revisited the questions raised by variability. Although MR 2251-178 is the original WA for which ionization variation was detected, it appears that we now have evidence for other types of variability in that AGN. Fitting photoionization absorption models against the historical set of continuum observations, Kaspi et al. (2004) found that column densities appeared to vary on time scales of perhaps several months, even when ionization changes were taken into account. They suggested that clouds moving across the line of sight could be responsible. Indeed, a recent *Chandra* observation shows evidence for ionized WA material in the AGN which is not in our line of sight, assuming a simple spherical absorber geometry (Gibson et al. 2005). Thus the WA in MR 2251-178 appears to have significant non-radial structure.

This paper is part of a study to understand WAs in AGN by examining variability in recent high-resolution X-ray spectra. As mentioned above, several explanations for observed absorber variability have been offered in previous studies. These explanations include: variation of ionization level, cloud motion across the line of sight, and multi-zone structure in the WA. In this paper, we concentrate on some specific types of variability we detect in the high-resolution *Chandra* HETG spectrum of MCG -6-30-15. The principal conclusions we present in this paper are that:

1. The X-ray line profiles are sufficiently complicated and variable that care must be taken when deriving physical properties from a line in a time-integrated spectrum.
2. Although there is evidence that ionization effects are important, the variation we detect cannot be explained as due to changing ionization levels caused by luminosity variation alone. We discuss other possible causes of variation in line strength.

The study of line variability in high-resolution X-ray spectra is complex and rather new. This paper is not intended to be an exhaustive study of the line variability in MCG -6-30-15. Rather, we establish here that lines are varying and that the variation mechanisms are complex. In future studies, we will further quantify the variation in high-resolution spectra of MCG -6-30-15 and other AGN.

5.2 Observations and Data Reduction

The *Chandra* HETGS conducted four observations of MCG -6-30-15 from 19 May 2004 to 27 May 2004 for a total usable exposure time of about 520 ks. We processed the data using version 3.1 of the CIAO tools.[1] Much of our data analysis is conducted using a development version of the ACIS Grating Light Curve (AGLC) package to construct counts spectra sampled on time intervals which are subsets of the total observation time. Information about the AGLC package is available at `http://space.mit.edu/CXC/analysis/aglc/`. We analyze the data using a development version of the Interactive Spectral Interpretation System (ISIS) tool (Houck and Denicola 2000).[2]

Whenever possible, we work directly with counts spectra to compute line properties. The continuum flux can, in most spectral regions, be represented locally by a linear function. Multiplying the continuum flux by the instrument response and exposure time gives a continuum for the counts spectrum. We use Auxiliary Response Files (ARFs) computed with CIAO 3.1 to determine the instrument response. These represent the instrument effective areas and quantum efficiencies to the extent they were understood at the time the CIAO 3.1 tools were produced. They do not include the most recent calibration updates but are believed to be accurate within 10%, and are adequate for our purposes in this paper.

5.3 Spectral Analysis

We refer to the spectrum of MCG -6-30-15 with all four observations combined as the "time-integrated" spectrum. The Fe Kα line region of this spectrum has already been published by Young et al. (2005), who found evidence for a relativistically broadened Fe Kα line and an outflow of highly ionized Fe at about -2000 km s^{-1}. In this paper, we focus primarily on $1s-2p$ resonance absorption lines of He- and H-like ions of Ne, Mg, Si, and S. Assuming these ions are present in the absorber, their $1s-2p$ lines would be among the strongest found in the spectrum at wavelengths where the MEG grating has the largest effective area. Most (but not all) of these lines are strongly evident in the time-integrated spectrum. These lines can saturate at large ion column densities, so that the amount of absorption does not vary strongly with column density. For this reason, we also briefly examine the $1s-3p$ lines of the candidate ions. Because the $1s-3p$ lines have smaller absorption oscillator strengths than the $1s-2p$ lines, they require higher column densities to saturate, and may therefore show evidence of variability even when the $1s-2p$ lines do not.

In this section, we analyze absorption line features in the HETG spectrum as a function of time and luminosity. Because accurate continuum fitting is an important requirement for our study, we first discuss at length the method we use to determine continua in line regions (§5.3.1). Then we present the method we use to test lines for variability (§5.3.2). We test for line variability as a function of time (§5.3.3) and luminosity (§5.3.4). We follow

---

[1] http://asc.harvard.edu/ciao/

[2] ISIS is available at http://space.mit.edu/ASC/ISIS/

up our luminosity variability tests with further testing of the Mg XII resonance line (§5.3.5) and conclude with a discussion of $1s - 3p$ lines (§5.3.6).

5.3.1 Fitting the Continuum

In order to measure absorption line strengths, we must accurately estimate the continuum which is being absorbed. Several factors complicate continuum fits. Firstly, the HETG response varies with wavelength. In some cases, the ARF can vary dramatically over a few bins. Secondly, there may be intrinsic narrow spectral features that affect the continuum fit, such as nearby absorption or emission lines. Thirdly, we must use an appropriate fit algorithm. In some cases, we will be fitting segments of spectra which have fewer than 15 counts per bin. In this case, the χ^2 statistic is not applicable (e.g., Gehrels 1986).

In order to accurately estimate the continuum, we adopt the following scheme. We assume the continuum flux can be approximated as a straight line over the fit region. We choose the fit region to be relatively small (≤ 0.6 Å) so that a line should be a good approximation to the local continuum. For any continuum flux, we can determine a corresponding count rate by multiplying the flux by the instrument ARF and the exposure time. We maximize the statistical likelihood to find the continuum flux model which best reproduces the observed counts. In practice, this means we minimize the C statistic given in Equation (5) of Cash (1979). Unlike the χ^2 statistic, the C statistic is appropriate for Poisson-distributed data, even when the number of counts per bin is small.

In several of the fit regions there are obvious absorption features which can adversely influence the continuum fit. Because these features influence a small number of bins compared to the entire fit region, they do not dramatically affect the fits, but removing them from the fit does improve the fit quality. We have visually selected several strong, narrow features which we exclude from the fit region. We also exclude the absorption line region, taken to be 0.03 Å on each side of the line center, from the fit. Finally, we truncate the fit region to exclude bins with residuals where atomic line lists indicate strong lines could be present. The continuum fit regions and the excluded regions are listed for each line in Table 5.1. The continuum fit is acceptable in the sense that the probability of higher χ^2 over the fit bins is $< 80\%$ in all cases except for Si XIII and S XV. The latter line was not strongly detected, while the former line is adjacent to a strong feature in the ARF and the fit region is also likely influenced by a complicated mix of emission and absorption features from nearby lines which we have not excluded. The continuum surrounding the Mg XII $1s - 2p$ line, which figures prominently in our analysis, was particularly well fit, with $\chi^2 = 22.4$ for 22 degrees of freedom.

These results indicate that our continuum fitting methodology is appropriate. We are further encouraged by the fact that the results of our variability tests changed little when we tried other, less accurate fitting methods. For example, using a χ^2 statistic and allowing nearby absorption lines to influence the continuum fit results in underestimating the actual continuum, but does not strongly affect the results of our variability tests. We use the fit method described in this section throughout the paper.

In Figure 5-1, we show Gaussian fits to line regions for the $1s-2p$ lines of H- and He-like Ne, Mg, Si, and S. Strong $1s-2p$ absorption lines are present for Ne, Mg, and Si. The S XV region does not show a strong absorption feature. A weaker line is detected for S XVI. In this paper, we are not using the properties of the time-integrated lines, but for completeness we have listed in Table 5.2 the fit properties including the velocity shift, intrinsic width, and EW of each line. We also list any regions which were excluded from the continuum fit.

The time-integrated line properties reported here are for informational purposes only and are not essential to our analysis. A full analysis of the time-integrated spectrum will be published in a future paper (Lee et al. 2006, in preparation).

5.3.2 Line Variability

An equivalent width (EW) is a measure of the strength of a line with respect to the surrounding continuum. We calculate EWs from counts spectra by summing over equally-spaced bins:

$$EW \approx \sum_{i=1}^{N} \frac{S(i) - C(i)}{C(i)} \Delta\lambda, \tag{5.1}$$

where there are N bins in the line, the number of observed counts per bin is given by $S(i)$, the number of continuum counts is given by $C(i)$, and $\Delta\lambda$ is the bin width. We use the first order spectrum of the MEG rather than the HEG because the larger effective area of the former results in many more counts in the regions of interest. A larger number of counts enables us to break the spectrum into smaller time slices. We bin the MEG spectrum to 0.01 Å per bin and typically choose N so that we are summing over a region several times larger than the instrumental FWHM of approximately 0.02 Å. Determining which wavelength to use as the centroid is somewhat difficult, as we wish to test line regions that have no strong profile in the total time-integrated spectrum and we also wish to test the possibility that lines move over time. In general, we place the centroid at the expected rest wavelength in the system frame except in cases where the integrated spectrum shows a line blueshifted enough that shifting the centroid will visibly result in a better correspondence with the line center.

This method of measuring EWs is not exact. For example, it gives incorrect results when the line is wider than N bins. However, it is a useful diagnostic tool to discover underlying trends in the data. We will use the results of these measurements as an initial guide for our data analysis. In order to be precise, we will refer to our measurements as "truncated equivalent widths" (TEWs), to distinguish the fact that we are only summing over a fixed number of line bins. For narrower lines, TEWs are effectively similar to EWs. All of the resonance lines we fit (shown in Figure 5-1) in the time-integrated spectrum have FWHMs narrower than 0.07 Å; the broadest line Si XIV) has FWHM $\approx$ 0.04 Å.

We measure TEWs as a function of both time and luminosity. To measure time variation, we split the observations into 39 ks time slices and construct counts spectra for the region of interest for each time slice. We discard incomplete time segments. To measure variation with luminosity, we use a more complicated procedure. We break the entire set of observations into a large number of spectra, each corresponding to a time slice of about 3 ks. We order the slices according to the 2-10 keV flux measured by counting up flux in HEG bins. (Note that pile up is not an important issue in the dispersed spectrum.) We then combine the ordered spectra in groups of some specified number. As an example, we show as horizontal dashed lines in Figure 5-2 the luminosity slices we would use for the case where each group contains 11 of the 3 ks slices and there are 16 groups in total.

The effective area of the MEG is, for the most part, constant in time at a given wavelength. Notable exceptions are regions near bad pixels and chip gaps on the ACIS detector. Due to the dithering motion of the satellite during an observation, wavelengths close to one of these regions will see a varying detector response as less responsive regions move into and out of the dispersion position corresponding to a given wavelength. The 3 ks time slice duration was chosen to be a multiple of the dithering period (approximately 1 ks) so that variations in the response will be smoothed out. We have also examined the ARFs and determined that the wavelengths we are interested in are typically outside the regions where bad pixels and chip gaps could strongly affect our TEW measurements.

We calculate the error on TEW measurements using the following formula:

$$\Delta TEW = \Delta\lambda\sqrt{\sum_{i=1}^{N}(\Delta x_i)^2}, \tag{5.2}$$

where

$$\Delta x_i \equiv \sqrt{\frac{S(i)}{C(i)^2} + \left(\frac{\Delta C(i)}{C(i)}\right)^2\left(\frac{S(i)}{C(i)}\right)^2}. \tag{5.3}$$

The first term under the radical is the error associated with measuring the counts observed in the line region. When summed over $N = 7$ bins, there are a sufficient number of counts that the error distribution is nearly Gaussian, hence we have assumed $\Delta S(i) = \sqrt{S(i)}$. The second term is the error associated with the continuum fit, which we estimate based on simulations. In most cases, the first term dominates. There is no covariance error term because the continuum fits exclude the line region.

We assume a gas number density of 10^8 cm^{-3}, although the results depend little on density in this regime. We forced the Ni abundance to zero to simplify the calculations but otherwise used solar abundances for abundant ions up to and including Fe (Grevesse et al. 1996). Table 5.3 shows the ranges of the ionization parameter ξ for which He- and H-like ions of relevant elements are present for our continuum model. ξ is defined as L_{ion}/nr^2, where L_{ion} is the source luminosity between 13.6 eV and 13.6 keV, n is the absorber number density, and r is the distance between the source and absorber.

In order to interpret our results in terms of photoionization models, we have calculated ionization fractions of abundant elements for a generic UV and X-ray continuum using the photoionization modeling code XSTAR.[3] The exact continuum shape is difficult to determine without simultaneous UV spectroscopy, is difficult to estimate without understanding the complex absorption processes below 2 keV, and in any case varies on short ($<$ 10 ks) time scales (e.g., Shih et al. 2002), at least in X-rays. Therefore, we assume a generic continuum shape and focus on relative behavior of ionization fractions between ions, which is less dependent on continuum shape than individual values of ionization fractions are (§5.4.2).

We model the continuum as a broken power law. The flux density of each power law component is $F_\epsilon \propto \epsilon^{-\alpha}$, where ϵ is the photon energy and F_ϵ is in units of ergs cm^{-2} s^{-1} erg^{-1}. The break energy is at 2 keV. For the ultraviolet region, we use $F_\epsilon \propto \epsilon^{-1.8}$, while for the X-ray region we use $F_\epsilon \propto \epsilon^{-1.0}$. The continuum is cut off at 100 keV. The continuum we use is an approximation of the instantaneous state of the variable continuum. The value of the ionization parameter ξ should be considered to be only an estimate of the true ionization level. The model is most useful for comparing relative values of ionization levels between two ions. Small changes in the continuum shape do not affect relative ionization fractions as strongly as they affect the overall ionization level. For further exploration of this subject, see §5.4.2.

---

[3] http://heasarc.gsfc.nasa.gov/docs/software/xstar/xstar.html

The best candidates to test are the $1s-2p$ resonance lines of H- and He-like Ne, Mg, Si, and S. While we detect absorption lines from many other ions in the time-integrated spectrum, these lines have strong absorption oscillator strengths and appear in a wavelength region where the MEG effective area is large, so there are many counts to work with. Because the Si XIV $1s-2p$ line falls in a region where the MEG ARF varies strongly with wavelength, we choose not to test this line for variability. We ignore the S XV line region because we do not detect a line in the time-integrated spectrum and there is also a weak ARF feature in this region, though we note that no significant variability results were detected when this line region was tested. The Si XIII line also has structure in the ARF on the red side of the line. This structure is not as strong as the Si XIV case and is constant over time, so it should not affect variability tests that rely on relative changes (such as the correlation tests in §5.3.3). With these caveats, we keep it in our list of lines. Overall, we have six lines to test.

5.3.3 Time Variability

We test the $1s-2p$ resonance lines described in §5.3.2 for variation with time in 39 ks bins,[4] summing the TEWs over $N = 7$ wavelength bins (0.07 Å). To explicitly test for variability, we take the set of TEWs that we measure for each line and calculate the χ^2 statistic for the best fit to a constant value. The strongest candidate for variability is Mg XI, which varies at 94.7% confidence. The only other candidate varying at $\geq 90\%$ confidence is Si XIII (91.3% confidence). The other line candidates (and confidence of variation) are: Mg XII (86.8%), S XVI (86.2%), Ne IX (54.4%), and Ne X (44.3%). Given that we have tested six lines for variability, these results (with four of six cases having confidences $\geq 85\%$ and two of six $\geq 90\%$) suggest that TEWs may indeed be varying. We also note that lines may vary with time in ways that our test would not detect. For example, lines may vary with smaller amplitudes or on different time scales than we are testing.

Figure 5-3 shows the TEWs for each of the lines as a function of time. There appear to be correlations (or anti-correlations) between pairs of lines, most notably in the first six time slices. To test this observation formally, we use Spearman's rank-order correlation test. We apply the test to all 13 time slices for each possible pair of ions. The test indicates that the TEWs of lines from Ne IX and Si XIII are correlated at 97.1% confidence. Lines of Ne X and Si XIII are anti-correlated at 95.4% confidence, while lines of Mg XI and Mg XII are anti-correlated at 99.9% confidence. Figure 5-4 shows these relations in detail. For each correlation or anti-correlation mentioned, we plot the fractional TEW about the mean, i.e. $(TEW - \langle TEW \rangle)/\langle TEW \rangle$ in order to emphasize the variation. The lines of the He-like ions Ne IX and Si XIII are correlated, while the lines of He-like and H-like ion pairs Ne IX/Si XIII and Mg XI/Mg XII anti-correlate. The anti-correlation between He-like and H-like Mg is particularly strong. We have tested 15 pairs of lines for correlation and found three above 95% confidence, including one at 99.9% confidence. There is therefore significant evidence for an anti-correlation in variation between at least Mg XI and Mg XII.

The Mg XI and Si XIII $1s-2p$ lines have a large number of continuum counts in the MEG, allowing for studies at higher time resolution than 39 ks. We find no significant correlations between Mg XI and Si XIII using time bins of 39, 20, 10, or 5 ks.

For the strongest anti-correlation (between Mg XI and Mg XII), we have enough counts in the spectrum to test for (anti-)correlation using shorter time slices. In fact, we find

---

[4] The time bins were chosen to fit neatly into the available exposure times of the four 2004 observations.

anti-correlations at 93.7% confidence for time slices of 20 ks, but only 77.1% and 63.5% for 10 and 5 ks, respectively. There may be several reasons for the decline in confidence of variability with shorter time scales. For example, because each ion has a different ionization equilibration time scale (e.g., Krolik and Kriss 2001), different response times to changes in the ionizing continuum may wash out correlations if the time slices we use are not much longer than the ionization time scales. It would be very interesting and informative to model in detail the time variation of ionization levels driven by the varying ionizing continuum. Such a study is beyond the scope of this paper, but will be considered in future work. The strength of the (anti-)correlation between lines may also decrease at shorter time scales simply because smaller numbers of counts are used for the calculations, leading to increased scatter in the data.

The results of our tests for (anti-)correlations between lines are qualitatively consistent with variations caused by changes in ionization. Table 5.3 shows, for the ions of interest, that there is typically a wide range of ξ between ionization fraction peaks. In the range between peaks, the ionization fraction of the He-like ion is decreasing while that of the H-like ion is increasing with ξ. Changes in ξ in this region (perhaps caused by varying luminosity) will cause anti-correlations between such ions.

Nonetheless, explaining the variability as due to ionization changes caused by luminosity variation is problematic. He-like ions in our sample have ionization thresholds above 2 keV, so we would expect the 2-10 keV continuum to control the ionization levels of He- and H-like ions. However, we do not find any significant correlation between TEWs and the 2-10 keV flux; no ion shows a correlation (or anti-correlation) confidence $\geq 90\%$. We will investigate further the behavior of $1s-2p$ lines as a function of luminosity in §5.3.4.

If the correlation between the time variation of the Ne IX and Si XIII lines is real, it is not possible to find a single ionization level ξ_0 for the entire absorber such that perturbations about ξ_0 would cause all the correlations and anti-correlations in the data. This is not surprising; we have already noted that multiple ionization stages are required to explain all the lines present in time-integrated spectra. However, the detection of coherent variation among these ionization stages does place some constraints on their geometric structure. A model of the absorber would need to explain the lack of strong correlation between the continuum and individual ionization components while simultaneously predicting the correlations between pairs of components. Further modeling of the absorber is beyond the scope of this paper, but the discussion in this section shows the need for models of structured absorbers.

Finally, we note that a study of the HETG spectrum of NGC 4051 by Collinge et al. (2001) found that absorber properties were different for He- and H-like ions. In this case, He-like ions were found in one velocity component, while H-like ions were found in another. The authors noted that this contradicted photoionization models, since the He-like ion Si XIII is formed at ionization levels similar to the H-like ions of Ne and Mg, and would therefore be expected to evolve as the H-like ions do. Collinge et al. (2001) suggested that this may indicate the absorber is not in photoionization equilibrium, but instead that the ion behavior is dependent on ionization potential, in which case Si XIII would be expected to behave as the other He-like ions. In our case, we see correlated behavior between He-like ions and anti-correlations between He-like and H-like ions regardless of the predictions of ionization models.

5.3.4 Luminosity Variability

Following the procedure described in §5.3.2, we test $1s - 2p$ lines to see whether they vary as a function of luminosity. We test by summing TEWs across $N = 7$ wavelength bins of 0.01 Å each. We split the observations into 3 ks segments, order those segments by 2-10 keV flux, and combine them in groups of size M to form spectra for which we measure TEWs.

The entire set of four observations can be broken into 176 different 3 ks segments. Re-ordering by luminosity and combining them in groups of size M gives $\lfloor 176/M \rfloor$ TEW measurements. For our initial measurements with $N = 7$, we choose M for each line so that there are at least 50 counts expected in the continuum for all N bins combined at the lowest flux level. We perform these tests for each of the $1s - 2p$ lines in our sample. In Figure 5-5 we show the pattern of TEWs as a function of 2-10 keV luminosity for each of the six lines.

In three of six cases we find that the measured TEWs are inconsistent with being constant at 85% confidence or more, including 2 of 6 at $\geq 95\%$ confidence. The three ions with the greatest confidence of variability are Mg XII, Si XIII, and S XVI at confidences of 98.9%, 96.6%, and 88.0%, respectively. As for the case of variation with time, these results suggest that line variation is occuring.

Our strongest candidate for variability, the $1s - 2p$ line of Mg XII, shows an even higher confidence of variability if we narrow the line region we use to calculate TEWs. Taking $N = 5$ and $N = 3$ (and keeping M unchanged) gives confidences of 99.7% and 99.9%, respectively. We conclude that the $1s - 2p$ line of Mg XII is a strong candidate for variability.

5.3.5 Further Testing of the Mg XII Line

In this section, we study the 35 luminosity ordered spectra of the Mg XII line region in more detail, looking for further evidence of variability. For each spectral bin in each luminosity slice, we wish to calculate the statistical likelihood of obtaining the number of counts that we observe, with the constraint that the line optical depth in each bin remain constant across the entire observing time.

For simplicity, assume we are working in a single spectral wavelength bin. (We apply the same procedure to each spectral bin.) For each luminosity slice, we fit a linear continuum to the spectrum near the line region, excluding the 8.40-8.55 Å region where the line resides. Suppose the continuum counts in each of the i luminosity slices is fit to be X_i counts and that we actually observe c_i counts in the spectra. We wish to find a single multiplier, f, for all the luminosity slices, so that the joint probability of finding c_i counts in spectrum i is maximized, given an expected rate of counts $f \times X_i$.

The likelihood is maximized when

$$f = \sum_i c_i / \sum_i X_i. \tag{5.4}$$

This gives us one value of f for each spectral bin. Given that we have 15 spectral bins and 35 luminosity slices, we can calculate a total of $15 * 35 = 525$ Poisson probabilities for our best-case model of the line depth as specified by the value f for that line. Each of these probabilities represents the Poisson probability $P(x \geq c_i, f * X_i)$ that we would observe more counts than we actually do. In the case of the Mg XII line, we observe an excess of low-count spectral bins. Out of 525 cases, we find 8 probabilities $\geq 99.5\%$ that we would obtain more counts. Using the binomial distribution, we calculate the probability of this many cases occuring randomly to be 0.6%. The fact that we have a large number of probabilities $\geq$ 99.5% in the maximum-likelihood scenario may indicate that deviations from the most probable configuration are characterized by excess absorption (i.e., the observed number of counts is unexpectedly low, indicating a high probability of obtaining more counts in a purely random Poisson process), though other explanations are possible. This supports our result in §5.3.4 that the Mg XII line is varying. Applying this same test to the other $1s-2p$ lines produces inconclusive results.

All of the 8 probabilities over 99.5% came from the 8.40−8.50 Å region. (All wavelengths in this discussion are given in the observed frame.) We also included the 8.50 − 8.55 region in our test. Since the line is centered at approximately 8.48 Å, this means that the bins with unexpectedly low numbers of counts were near to or blueshifted from the line center. The region on the red side of the line showed less evidence for variation.

Finally, we note that our criterion for variability is rather crude, as we only look at excess probabilities in the tails of the distribution. More powerful tests (applied to larger data sets) may be able to distinguish variation beyond what we find here.

5.3.6 Line Saturation and $1s-3p$ Lines

For small column densities N_i of a given ion, absorption lines have EWs which are proportional to N_i. The absorption EW saturates as N_i increases, so that large changes in column density may produce only small changes in EWs. In our study, we have concentrated on the relatively strong $1s-2p$ absorption lines of various ions. The weaker $1s-3p$ lines, having much smaller oscillator strengths, are less susceptible to saturation. In principle, they could give stronger indications of variability than we find for the $1s-2p$ lines.

Unfortunately, the $1s-3p$ lines in the data are rather weak. In all cases (excepting S XVI), the EWs we measure for these lines are less than half those of the $1s-2p$ lines. In some cases (e.g., Mg XII), we do not detect any significant $1s-3p$ line at velocities consistent with those measured for the $1s-2p$ lines. Even in cases where we do detect lines, the error in those measurements is large compared to the measured EW, so that tests for variability of these lines are inconclusive.

A detailed study of the $1s-2p$ and $1s-3p$ lines in the time-integrated spectrum will be presented in an upcoming paper (Lee, et al. 2006, in preparation). For the purposes of this study we conclude that, although the $1s-2p$ lines may be affected by saturation to some extent, they are probably not strongly saturated, or else we would expect to see stronger $1s-3p$ lines. In particular, the ion Mg XII, which receives the most attention in this paper, has no detectable $1s-3p$ line.

Of course, even if the $1s-2p$ lines are saturated, they can still vary. Variation in the EW of saturated lines suggests large changes in ionic column densities. For example, the EW measured in the time-integrated spectrum for Mg XII is -7.9 ± 1.7 mÅ. When we order spectral slices by luminosity, we find that the strongest line has an EW of -27.2 ± 5.2 mÅ. Depending on the parameters used in a curve of growth analysis, this could indicate changes in the column density by orders of magnitude. Detailed curve of growth studies are beyond the scope of this paper, but will be presented in the upcoming paper (Lee, et al. 2006, in preparation). We also note that the non-linearity of the curve of growth means that errors in EW measurement can lead to large uncertainty in column density estimation.

5.4 Discussion

It is common to use a curve of growth analysis to associate the EWs of measured lines with an ionic column density N_i and a velocity spread parameter b. Varying EWs would then be due to changing column densities or changes in the spread of velocities in the absorbing material. Column densities might vary because the overall number density of particles in the absorber itself is changing, as happens when a cloud moves across our line of sight. Column densities may also vary when ionization fractions change due to changes in ionization level of the absorber.

Other causes of variation are possible which are not covered by the underlying assumptions of the curve of growth. In particular, line emission may fill in the absorption line, moving it off the curve. This line emission may vary, resulting in a varying line profile. Another possibility is that we are looking along different lines of sight at different times. Continuum photons may be scattered or gravitationally bent into our line of sight from multiple sources in the nucleus, or photons from the same source may take different paths to reach our detector. Multiple bright emitters may be geometrically dispersed so that, at different times, the paths from them to our detector pass through regions with different physical properties.

Because the anti-correlations over time described in §5.3.3 suggest varying ionization, we consider first the implications and constraints of varying ionization levels. We derive ionization time scales for the ions under study (§5.4.1), then we consider possible causes of ionization variation (§5.4.2) such as variation in: absorber distance (§5.4.2), absorber density (§5.4.2), luminosity (§5.4.2), and continuum shape (§5.4.2). In following sections, we discuss other, more complex scenarios: variable unabsorbed continuum components (§5.4.3), cloud motion (§5.4.3), variable emission (§5.4.3), and changes in absorber velocity dispersion (§5.4.3).

5.4.1 Ionization Time Scales

In this section, we estimate a lower limit on the absorber density assuming that ionization levels are changing to cause the observed variability. This calculation applies only to scenarios where line variation is due to changes in ionization level in an absorber with constant equivalent hydrogen column density N_H along our line of sight. Because the luminosity-selected spectra were assembled from 3 ks time slices of spectrum that were (typically) well-separated in time (see Figure 5-2), the variability we detect in these spectra suggests that the lines may be varying on time scales smaller than tens of ks. If the variation time scale was much longer than 3 ks, we would not expect that the ionization level would track the continuum when the spectrum was split into 3 ks segments, making it less likely that any variability would be detected as a function of luminosity. For the following analysis, we assume an upper limit to the ionization time scale of 39 ks, corresponding to the time scale for which we detected (anti-)correlations between lines (§5.3.3).

We have calculated ionization time scales for ions of interest assuming ionization levels are driven by photoionization (PI) rates, collisional ionization (CI) rates, and radiative recombination rates (RR) into and out of each ion. We estimate the ionization time scale as

$$\tau_i(\xi, n) \equiv \frac{n_i}{|dn_i/dt|} \tag{5.5}$$

$$= \frac{n_i}{|PI_{in} - PI_{out} + CI_{in} - CI_{out} + RR_{in} - RR_{out}|}, \quad (5.6)$$

where ξ is the ionization parameter, n is the total gas number density, n_i is the number density of the ion in question, and t is time. To calculate τ_i, we use photoionization cross sections from Verner et al. (1995); Verner and Yakovlev (1995), collisional ionization rates from Voronov (1997), and radiative recombination rates from Aldrovandi and Pequignot (1973); Shull and van Steenberg (1982); Arnaud and Rothenflug (1985); Verner and Ferland (1996). Calculating the ionization rates requires a prior assumption of ionization fractions, electron density n_e, and electron temperature T_e, which we calculate as a function of ξ with XSTAR photoionization models. Because we are calculating PI, CI, and RR rates using different data than XSTAR, our calculations will naturally be calculated slightly off the equilibrium point determined by XSTAR (where the time scale is technically infinite). We also test a range of nearby ξ and T to ensure our estimates are consistent at various off-equilibrium points.

We use a fiducial broken power law with spectral index $\alpha_{OX} = 1.8$ in the UV and soft X-rays (13.6 eV to 2 keV), $\alpha_X = 1.0$ above 2 keV, and a cutoff energy of 100 keV. We use XSTAR version 2.1 kn3.[5] We have tested our results against other continuum shapes, and found that differences in time scale are within a factor of 2.

For H- and He-like Ne, Mg, and Si, we find that for values of $\log(\xi)$ near 2 and a number density n, the time scales τ can be estimated roughly by $\tau \times n \sim 10^{11}$ s cm^{-3}. Ionization changes on a time scale ≤ 39 ks (see §5.3.3) would require a minimum gas number density

$$n_{min} \sim 10^6 \text{ cm}^{-3}. \quad (5.7)$$

This is not a strong constraint on the density, which could easily be much higher. As noted above, the variations may be occuring on shorter time scales corresponding to higher densities.

An absorber with a column density $N_H = 10^{21}$ cm^{-2} would have a scale size $r \sim N_H/n < 10^{15}$ cm along the line of sight. This is not a strong constraint on the absorber size, and in any case involves the approximation that the absorber density is constant along the line of sight. Because absorbers can apparently show significant geometric structure (e.g., Gibson et al. 2005), we do not draw conclusions about the absorber geometry from this limit.

5.4.2 Changes in Column Density Due to Ionization

The $1s - 2p$ resonance absorption line of Mg XII appears to be stronger at some times and weaker at others, as is shown in Figure 5-4. The anti-correlation with Mg XI line strength suggests that the time variation is real and perhaps related to changes in ionization level of the absorber (§5.3.3). The pattern of variation is complex; it is neither monotonic with time (Figure 5-4) nor with luminosity (Figure 5-5). In the following sections, we consider the possibility that the variation is due to ionization changes in the absorber.

The equilibrium ionization state of an optically thin photoionized gas can be determined as a function of the continuum shape and an ionization parameter $\xi \equiv L_{ion}/nr^2$ described in §5.3.2. Ionization changes can in principle occur on time scales much shorter than the length of an observation. Changes in ionization level affect the ionic column densities along our line of sight, which in turn determine the strength of absorption lines in our spectrum from

---

[5] XSTAR is available at `http://heasarc.gsfc.nasa.gov/docs/software/xstar/xstar.html`.

a given ion. In the following sections, we consider possible causes of ionization variation: radial variation (§5.4.2), density variation (§5.4.2), continuum luminosity variation (§5.4.2), and continuum shape variation (§5.4.2).

Ionization Variation Due to Radial Distance

Radial variation affects the ionization level of the plasma through geometric dilution of the ionizing continuum. The assumption typically made in photoionization models – that the ionizing continuum falls off as $1/r^2$ – is an approximation; it assumes that the continuum expands radially without significant scattering and that the absorber is thin so that the continuum is not appreciably attenuated by the absorber itself.

Assuming L_{ion} and n remain constant, $\Delta\xi/\xi = -2\Delta r/r$. Radial (outflow) velocities of 1000 km s^{-1} correspond to $\Delta r = 10^{13}$ cm in 10^5 seconds of observing time. The absorber would therefore have to be within a few$\times 10^{13}$ cm of the central source in order to show appreciable changes in ionization level on intra-observation time scales. This is within 100 gravitational radii ($r_g \equiv GM_{BH}/c^2$) for the black hole of estimated mass $M_{BH} = 3\times 10^6 M_{\odot}$ in MCG -6-30-15 (McHardy et al. 2005). This is not plausible: an ionization level of $\xi = 1000$ (required for highly ionized Si lines) for an ionizing luminosity of $L_{ion} = 10^{44}$ ergs s^{-1} would require an absorber number density $n = L_{ion}/\xi r^2 > 10^{14}$ cm^{-3}. Furthermore, absorption lines are typically seen in outflow, which in this scenario would mean that ionization levels would only *decrease* as the radius increases, contrary to the anti-correlated TEW variation seen in Mg XI and Mg XII (§5.3.3).

Ionization Variation Due to Density

At $\xi = 100$, our photoionization model indicates the electron temperature is about 10^5 K. (The actual values of ξ and T could be different, but our conclusions would not be much altered.) The adiabatic sound speed c_s in an ideal gas at that temperature is about 30 km s^{-1}. Structural changes in the WA can occur at the speed of sound on a time scale ≤ 40 ks for an absorber size $r_{max} \leq (40 \text{ ks})c_s \approx 10^{11}$ cm. We assume an upper limit to the gas density of $n_{max} \approx 10^{11}$ cm^{-3}, above which we would expect the O VII forbidden line to be strongly suppressed by collisional depletion (Porquet and Dubau 2000), contrary to our data (Lee et al. 2006, in preparation). An absorber with a typical equivalent hydrogen column density $N_H = 10^{22} \sim n\Delta r$ would need to be nearly maximal in both size and density.

Such an absorbing cloud would lead an extremely precarious existence. It would have a maximum mass (assuming a constant density profile) of $M_{max} = (4/3)\pi r_{max}^3 n_{max} m_p = 7 \times 10^{20}$ g. Such a cloud of mass M would have a gravitational binding energy of $|E_G| = (3/5)GM_{max}^2/r_{max} \leq 2 \times 10^{23}$ erg. Since $M_{max} \propto r_{max}^3$, a smaller absorber (at maximal density) would be less tightly bound.

The gravitational binding energy is small compared to the thermal energy, the kinetic energy of the outflowing absorber, and also the energy supplied by the continuum to ionize the absorber's hydrogen atoms. On the basis of these estimates we conclude that any cloud small enough to be varying at the speed of sound on intra-observation time scales cannot be gravitationally bound. This scenario thus requires some method of confining the absorber. Complications for such a confinement model include:

1. The absorber density must be able to both decrease and increase so that the ionization level can both rise and fall.

2. An absorber of such small size could easily move across the line of sight during a single observation if it has a transverse velocity of a few $\times 10$ km s^{-1}.

This argument shows that complex models are required if we attribute line variation to density fluctuations at the speed of sound. This does not rule out the possibility that some WA components may be gravitationally confined and not varying. Nor does it constrain confinement models for WA clouds, which have been proposed previously (Krolik et al. 1981; Krolik and Kriss 1995). Rather, we conclude that density variation cannot easily explain the line variation in our data.

Ionization Variation Due to Luminosity

Our observations cover a 2-10 keV luminosity range of $\Delta \log(L) \approx 0.56$. We wish to know whether the line variation with luminosity we detect (§5.3.4) can be attributed to luminosity variation alone. To test this hypothesis, we construct a naïve model in which the TEWs are considered to be EWs of lines on the linear part of the curve of growth, so that the TEWs are proportional to ionic column densities and hence to ionization fractions, which are themselves a function of the 2-10 keV source luminosity. We use the ionization fractions calculated from the XSTAR model described in §5.3.2. Two multiplicative constants, A and B, are required in our fit. Firstly, assuming the ionizing luminosity is proportional to the 2-10 keV X-ray luminosity, A signifies the ratio between the ionization parameter ξ and the mean 2-10 keV flux $\langle f_{2-10} \rangle$, i.e., $A \equiv \xi / \langle f_{2-10} \rangle$. Secondly, we multiply the negative of the ionization fraction F_A by B to obtain the TEW, i.e., $B \equiv -TEW/F_A$. In practice, strong lines such as these $1s - 2p$ resonance lines would lie on or near the flat part of the curve of growth so that the EW would saturate at large column densities, where the ionization fraction of the associated ion is highest. This means that in reality, TEWs are less responsive to luminosity changes than in our model. Thus our model *over*estimates variation.

We fit each line separately to allow for the possibility of multiple ionization zones in the absorber. The fits are shown as dotted lines in Figure 5-5. The fits to three $1s - 2p$ lines are rejected by the χ^2 distribution: Mg XII at confidence 98.9%, Si XIII at confidence 95.6%, and S XVI at confidence 93.9%. These lines were previously considered to be candidates for variability in that they were inconsistent with a constant fit at least at the 85% confidence level (§5.3.4).

Apparently, line strengths are varying with luminosity in ways that simple ionization models can not explain. In the case of S XVI, our model is unable to explain the positive TEWs (corresponding to line emission) seen at lower luminosities, hence it chooses B so that TEWs are about zero. The case of emission line variation influencing TEWs will be considered in §5.4.3.

Our fit values for A give the values of ionization parameter ξ reported in Table 5.4 for each of the lines. Comparison with Table 5.3 shows that the fit values are slightly below the level for which the ionization fraction peaks for all ions except Mg XI, which is slightly above the peak. Our model has chosen a range where ionization fractions for most ions are increasing slightly — but not strongly — with ξ. This results in a general trend of absorption lines strengthening slowly with luminosity. It is somewhat surprising that a multi-zone absorber would be configured so that the $1s - 2p$ lines we measure are preferentially produced at an ionization level somewhat smaller than where individual ions peak in ionization fraction.

We naturally expect absorption lines to vary with luminosity due to changes in ionization state of the absorber. We have demonstrated that luminosity variation *alone* is an insufficient explanation for the line variation overall, but it may certainly be a contributing factor to the variation. Without developing a more complex model of absorber response to luminosity changes that includes a full curve of growth treatment, continuum shape variation, and a non-zero absorber response time to continuum variation, it is difficult to determine the extent to which TEWs are influenced by luminosity variation.

Ionization Variation Due to Continuum Shape

While the overall normalization of the photoionizing continuum is expressed implicitly in the ionization parameter ξ, the shape of the continuum may vary and alter the ionization state of the absorber. In general, the UV continuum strength strongly influences the ionization state of ions in our study up to the He-like state, while X-ray photons are required to create H-like and fully stripped ions. Because we do not have simultaneous, complete coverage of the UV continuum of MCG -6-30-15, we can only estimate the UV continuum shape. We assume the UV continuum is specified by a power law flux $f_\epsilon \propto \epsilon^{-\alpha_{OX}}$ ergs cm^{-2} s^{-1} erg^{-1} with $\alpha_{OX} \approx 1.8$ taken from a Hubble Space Telescope (HST) survey of QSOs at redshift $z > 0.33$ (Telfer et al. 2002). However, there is evidence that the extreme UV (EUV) spectrum may be much harder for AGN in general (Scott et al. 2004a), so we also consider the effects of a flatter UV spectrum.

Figure 5-6 shows ionization fractions of He- and H-like ions of Ne, Mg, and Si as a function of ξ calculated with XSTAR for three different continua. In each case, the continuum is composed of two power laws constrained to meet at 2 keV. Below 2 keV, we use a power law index $\alpha_{OX} = 1.8$ for the top two plots and $\alpha_{OX} = 1.3$ for the bottom plot. Above 2 keV, we use a second power law with $\alpha_X = 1.0$ for the top plot and $\alpha_X = 0.4$ for the bottom two plots. The X-ray spectral indices are chosen because they represent the outer boundaries of the variable power law we measure with the HETGS. The continuum is cut off above 100 keV. For convenience, we refer to the three continua as C_0, C_1, and C_2 specified by $(\alpha_{OX}, \alpha_X) =$ (1.8, 1.0), (1.8, 0.4), and (1.3, 0.4), respectively. Because we can measure the 2-10 keV luminosity L_{2-10}, we plot ionization fractions against L_{2-10}/nr^2 rather than against $\xi \equiv L_{ion}/nr^2$, using the ionization parameter described in §5.3.2. We convert from L_{ion} to L_{2-10} by calculating the ratio of the two luminosities from our continuum models.

For the top two plots (for C_0 and C_1) in which only the X-ray spectral index is varied, some differences in ion fractions are apparent between the different continuum shapes. The differences are small, with regions of significant ionization fraction varying by no more than about $\Delta \log(\xi) \leq 0.3$. The peak of Si XIII ionization fraction varies little with respect to the Ne X peak in all of the models.

Because the anti-correlation between Mg XI and Mg XII was the strongest we measured, we choose to work with those ions. At $\log(L_{2-10}/nr^2) = 1.35$, approximately where the ionization fraction curves for the two ions cross, we find that the ionization fraction of Mg XI increases by about 20% between continua C_0 and C_1, while the ionization fraction of Mg XII decreases by about 20%. On the linear part of the curve of growth where the EW is proportional to ionic column density, this would result in 20% changes of EWs for these ions, which is smaller than the error bars in Figure 5-4. In fact, strong X-ray absorption lines tend to lie on the flat part of the curve of growth where much larger changes in ionic column density are required to show appreciable changes in EW, so that EWs would be even less responsive to X-ray continuum variation. The variation from continuum C_0 to C_2

is similar.

However, Shih et al. (2002) found in a study of a long *ASCA* observation of MCG -6-30-15 that the continuum shape varies with luminosity: L_{2-10} increases as the X-ray spectrum softens. We have considered only variations due to changing continuum shape at a constant L_{2-10}. Combining the two effects would tend to increase the magnitude of EW variations. Modeling these effects is beyond the scope of this paper, though in future research, we intend to study the time-varying response of ionized absorbers to continuum variation. In order to accurately compare the results of these time-varying models to astrophysical data, it will be most helpful to have simultaneous UV and X-ray continuum measurements.

5.4.3 Other Causes of Variation

In §5.4.2, we considered causes of line variation that directly influenced the ionization level of the absorber. In the following, we consider mechanisms that can affect the EW of a line in other ways. We consider the possibility that the continuum is made of multiple varying components (§5.4.3), cloud motion across the line of sight (§5.4.3), variable emission lines (§5.4.3), and changing line velocity dispersions (§5.4.3). Because these mechanisms do not directly influence ionization levels, they will have difficulty explaining the anti-correlations over time between He- and H-like ion line strengths (§5.3.3).

Unabsorbed Continuum Components

Previous studies of MCG -6-30-15 have suggested that the continuum of MCG -6-30-15 may actually be a combination of multiple components, e.g., a power law and a reflection-dominated component added together (e.g., Shih et al. 2002; Vaughan and Fabian 2004). If one of those components is unabsorbed, while the other is affected by line absorption, it could result in anti-correlations between line strengths at different wavelengths, as seen in Figure 5-4. For example, if the continuum is composed of a constant, absorbed component and a variable, unabsorbed power law, the variable component may change shape with time such that it is decreasing at the wavelength of the Mg XI $1s-2p$ line while increasing at the wavelength of the Mg XII $1s-2p$ line. This would result in an apparent anti-correlation in EWs of the two lines.

While this is technically possible, it does not seem to be a likely scenario. The fact that we observe correlations and anti-correlations across the $1s-2p$ lines of five different ions places strong constraints on the type of continuum variation that is allowed. We see a correlation between the lines of Ne IX and Si XIII at system-frame wavelengths of about 13.45 and 6.65 Å respectively while we see an anti-correlation between the Mg XI and Mg XII at 9.17 and 8.42 Å. This would require the unabsorbed continuum to rise and fall in a complicated pattern. Assuming the continuum shape is in some way correlated with luminosity, this scenario is unable to explain TEW variation that is not monotonic with luminosity.

Changes in Column Density Due to Cloud Motion

Halpern (1984) considered the possibility that changes in the soft X-ray absorption in the spectrum of MR 2251-178 could be due to clouds moving across our line of sight, but eventually rejected that hypothesis in favor of a model in which ionization levels were changing. Since that time, other studies have raised the possibility of varying obscuration. For example, Reynolds et al. (1995) raised the possibility that cloud motion could be the cause of ionized edge variation in MCG -6-30-15. Recently, Kaspi et al. (2004) fit archived spectra of MR 2251-178 with a photoionization model and found evidence that column densities were varying. They suggested that clouds moving across the line of sight on a characteristic time scale of a few months may be responsible. Gibson et al. (2005) detected structure in the WA perpendicular to the line of sight in a *Chandra* HETGS observation of MR 2251-178 which was taken through a "hole" in the WA. This further indicates that motion of the WA tangential to the line of sight could produce a varying pattern of absorption with time.

We do see evidence for multiple absorbing systems in the overall spectrum: time-integrated spectral lines appear at different velocity offsets (Table 5.2), and the Mg XII line may have a non-Gaussian morphology (Figure 5-1). Multiple absorber components might be a result of several absorbing clouds being situated along our line of sight. But it is difficult to construct a model in which significant variation can be obtained while using a sufficiently large number of clouds to provide for consistent absorption over the course of our observation (and previous observations). Most importantly, the anti-correlations between lines at different ionization levels cannot be easily explained due to cloud motion alone. We see, for example, in Figure 5-4 that Mg XI lines become weaker as Mg XII lines strengthen, and *vice versa.* In a moving-cloud scenario, there is no reason why this should be the case. If a cloud that had a large amount of Mg XII moved into view, this would not decrease the amount of Mg XI in the observed column, and (depending on the ionization level) could even increase it significantly.

Emission Line Variation

Some emission line photons are undoubtedly present in the absorption line regions of the spectrum. For example, at low luminosities, the S XVI line region may have an excess of counts over the continuum (Figure 5-5). It is difficult to determine how many emission line photons are present in a line region. These emission lines could conceivably be varying, changing the line profiles over time. The emitter need not be physically associated with the WA; emission line photons in the X-ray spectrum could originate from various locations in the nuclear region.

Changes in the geometry of the absorbing and emitting regions could produce time-varying emission lines. For example, an obscuring cloud could move across a line emission region and scatter the emitter's line photons out of view. These sorts of scenarios suffer from the same complications as the moving-absorber scenario in §5.4.3: it is difficult to explain why He-like ion absorption lines should weaken as H-like ion absorption lines strengthen, and *vice versa.*

A more likely possibility is that ionization changes are occurring in the emitter, which enhance photons in lines of one ion at the expense of others. Ionization changes in the emitting material are subject to similar constraints as those considered for the absorber in §5.4.2. In this case, it may be possible to use other lines in the $1s - 2p$ "triplet" as a proxy for the resonance line emission. Resonance line photons are created primarily when electrons are excited or recombine and cascade down to the $1s-2p\ ^1P_1$ level, then decay to ground. Forbidden line photons decay to ground from the $1s - 2p\ ^3S_1$ level. The latter are preferentially populated by recombination events, so (in a photoionized gas where collisions are not de-populating levels significantly) we would normally expect to see more emission from the forbidden line. Furthermore, absorption cross-sections for the forbidden lines are small compared to the resonance cross-sections, so that the lines should be relatively undiminished by intervening absorbers. The Mg XI forbidden line is an ideal test case, as the strongest anticorrelation in TEWs was found between Mg XI and Mg XII. Just as with the resonance absorption lines, we do not see significant time variability in the forbidden line on 39 ks time scales, in the sense described in §5.3.2. We also do not see any correlation between the forbidden emission line and resonance absorption lines of Mg XI or Mg XII in time bins of 39 ks.

In general, it is difficult for emission line variation to be the fundamental cause of absorption line variation. Emission line photons are emitted from material presumed to exist in many different parts of the AGN at various ionization stages. It is unlikely that the emitters would vary coherently in ionization state, so that the emission line photons we receive represent an average ionization state for the different regions. Furthermore, any emitting photons that are Doppler shifted by more than a few × 100 km s^{-1} from the absorber velocity will be shifted out of the absorption line region.

These factors make it difficult to construct a scenario in which emission line photons dominate the line variation we detect. Future X-ray spectroscopy missions with even higher resolution than the HETG may resolve individual emission components, but for our study it is most likely that line variation is caused by some property of the absorber.

Changes in Equivalent Width Due to Velocity Dispersion

The velocity dispersion parameter b has the effect of moving the curve of growth upward (to larger values of EW $/\lambda$) as it increases (e.g., Spitzer 1978). As with the cloud motion scenarios, it is difficult to imagine a configuration in which velocity dispersions are anti-correlated between He- and H-like ions as lines from both types of ions strengthen and weaken several times over the course of our observations. Because velocity dispersions (when resolved) are due to gas motion rather than a Maxwellian temperature distribution, any mechanism for variation would require changes in the bulk motion or turbulent velocities of the absorber. Such changes on large scales seem unlikely.

5.5 Conclusions

In this paper, we have tested for variability in the $1s - 2p$ resonance lines of Ne IX, Ne X, Mg XI, Mg XII, Si XIII, and S XVI in the recent *Chandra* HETGS spectrum of MCG -6-30-15. We find that lines are indeed varying, both as a function of luminosity (in the sense that TEWs are formally inconsistent with a constant value) and as a function of time (at least in the sense that TEWs of lines are correlated or anti-correlated between ion species).

This study has demonstrated two important points for the ongoing interpretation of AGN X-ray spectra. Firstly, lines can vary over the course of an observation. Caution is therefore warranted in the analysis of spectra integrated over long observation times. Secondly, while our results indicate that variation in ionization levels may contribute to observed variability, ionization variation cannot be explained as simply due to luminosity variation of the central source.

With this in mind, we have examined several possible explanations for line variability in the HETGS spectra of MCG -6-30-15. We have ruled out any simple scenarios of variation due to:

1. Changes in absorber distance from the ionizing source

2. Changes in absorber density at the speed of sound

3. Changes in a single-zone absorber ionization level due to source luminosity variation
4. Changes in the ionizing *X-ray* continuum
5. A multiple-component continuum with different levels of absorption in the components
6. Cloud motion across the line of sight
7. Changes in the absorber velocity dispersion

We have additionally commented on and constrained scenarios of variation due to:

1. Changes in the UV ionizing continuum
2. Emission line variation

There is one more possibility we would like to suggest for further study. Recent studies of MR 2251-178 have shown that the WA may have structure perpendicular to the line of sight (Kaspi et al. 2004; Gibson et al. 2005). Current models of continuum emission, such as hot spots in the disk or the light-bending model of Miniutti and Fabian (2004), predict that the continuum emitter could also be moving around. It may be that our line of sight through the absorber is changing over the course of an observation, either due to the continuum emitter moving behind the absorber, or to the absorber itself moving perpendicular to the line of sight. Different regions of the absorber may have different physical characteristics, and if we are looking through an equilibrated absorber at each time slice, this could naturally produce correlations and anti-correlations among line strengths such as those seen in §5.3.3. Modeling such an absorber is difficult work and will be the subject of future study. Such models have the potential to draw connections between continuum emission processes (probably in the inner accretion disk) and the absorber structure (which may be parsecs away).

Spectral variability studies require X-ray spectroscopy with high resolution and a large collecting area. Future spectroscopy missions will certainly contribute to our understanding of the variability of WA in AGN, and therefore to our understanding of the structure and physical processes in the overall nuclear region.

There is a strong need for more detailed models of structured ionized absorbers. In particular, we need to understand better the effects of time variation of the ionizing source on a structured absorber. We also need to explore the possible forms of absorber physical structure, including spatial extent, motion, and density. We intend to pursue such models in future studies.

5.6 Acknowledgements

This work was supported in part by by NASA through contracts NAS8-01129 and SAO SVI-61010. We appreciate helpful comments from the anonymous referee which have strengthened this study.

Ion	Lab Wavelength (Å)	Continuum Fit Region Å)	Exclusion Region(s) (Å)
Ne IX	13.447	13.2 – 13.7	13.510 – 13.640
Ne X	12.134	11.9 – 12.5	12.140 – 12.400
Mg XI	9.169	9.05 – 9.50	9.210 – 9.270 9.310 – 9.410 9.440 – 9.470
Mg XII	8.421	8.30 – 8.65	8.455 – 8.52 8.40 – 8.46
Si XIII	6.648	6.50 – 6.90	6.670 – 6.850
Si XIV	6.182	6.00 – 6.40	6.160 – 6.220
S XV	5.102	4.80 – 5.20	5.005 – 5.070
S XVI	4.729	4.50 – 5.02	4.740 – 4.800 4.830 – 4.880

Table 5.1: Continuum Regions for Line Fits.

Ion	Lab Wavelength (Å)	Shift ($\mathrm{km\ s^{-1}}$)	Intrinsic σ[a] ($\mathrm{km\ s^{-1}}$)	EW (mÅ)
Ne IX	13.447	-110±30	262±45	-30.8±3.1
Ne X	12.134	-222±28	245±45	-24.9±2.3
Mg XI	9.169	-148±47	230±68	-11.4±1.3
Mg XII	8.421	-272±50	170±100	-7.8±1.0
Si XIII	6.648	-185±45	81±450	-7.87±0.81
Si XIV	6.182	-1570±150	840±170	-10.3±1.5
S XV	5.039[b]	...	...	...
S XVI	4.729	-1780±360	...[c]	-2.6±1.3

[a] The instrumental broadening is subtracted in quadrature from the measured line width.

[b] This line is not strongly detected in our analysis.

[c] The S XVI line is not resolved.

Table 5.2: $1s - 2p$ Resonance Line Time-Integrated Properties for Selected Ions. The errors listed indicate the 68% confidence region for the fits.

Ion	log(ξ) at Peak Ionization Fraction	log(ξ) Range[a]
O VII	1.30	0.10 to 2.45
O VIII	2.25	1.20 to 3.15
Ne IX	2.05	0.90 to 3.05
Ne X	2.85	2.05 to 3.75
Mg XI	2.55	1.60 to 3.45
Mg XII	3.25	2.50 to >4.00
Si XIII	2.95	2.10 to 3.80
Si XIV	3.55	2.85 to >4.00
S XV	3.25	2.55 to >4.00
S XVI	3.90	3.10 to >4.00

[a] Values given (in cgs units) indicate the range where a particular ion accounts for at least 10% of the total element abundance.

Table 5.3: Gas Properties Predicted by XSTAR Model for $\alpha_{OX} = -1.8$, $\Gamma_X = 2.0$.

Ion	log(ξ)
Ne IX	1.35
Ne X	2.55
Mg XI	2.75
Mg XII	3.14
Si XIII	2.54
S XVI	3.86

Table 5.4: Ionization Parameters ξ for Fits to TEWs. ξ is in ergs s^{-1} cm^{-1}.

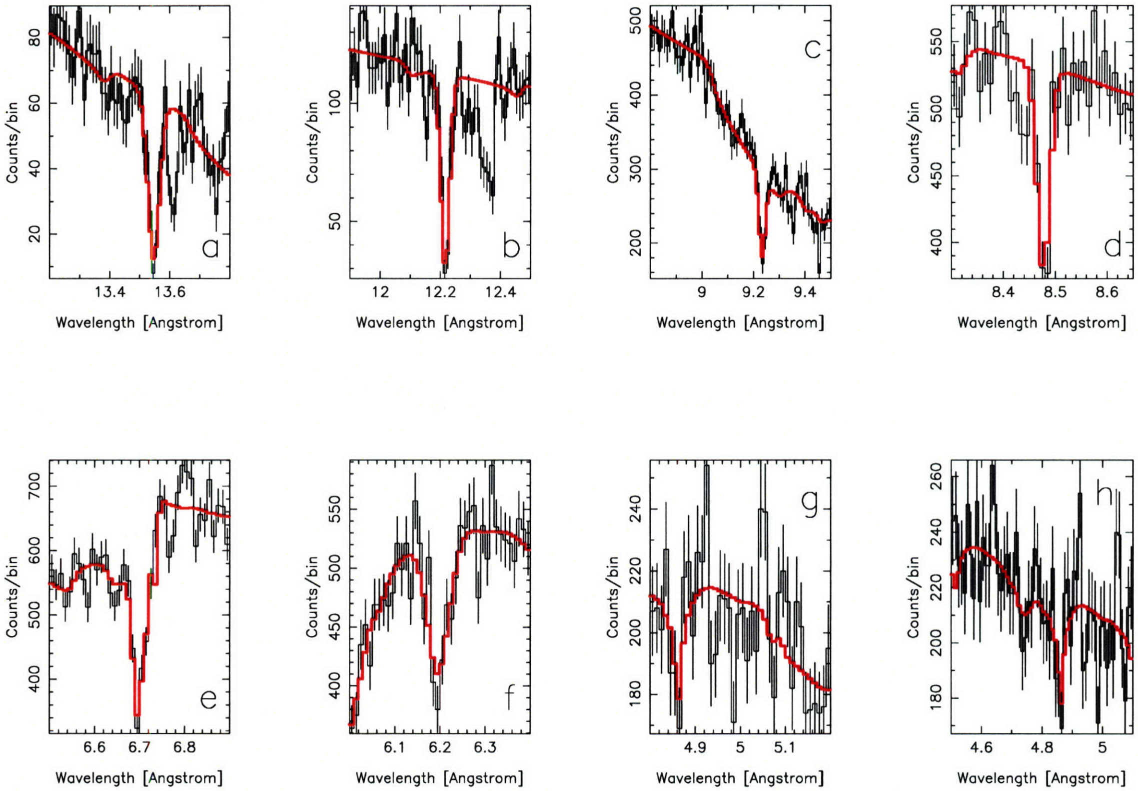

Figure 5-1: Fits to MEG counts spectra for $1s - 2p$ lines of selected ions. The panels show the fits for: a) Ne IX, b) Ne X, c) Mg XI, d) Mg XII, e) Si XIII, f) Si XIV, g) S XV (not detected), h) S XVI. The linear continuum fit to the flux has been multiplied by the MEG ARF and exposure time to produce a number of model counts per bin. The ARF varies with wavelength, so that the continuum shape appears to be non-linear. The line-like feature at about 4.85 Å in plots g and h is instrumental.

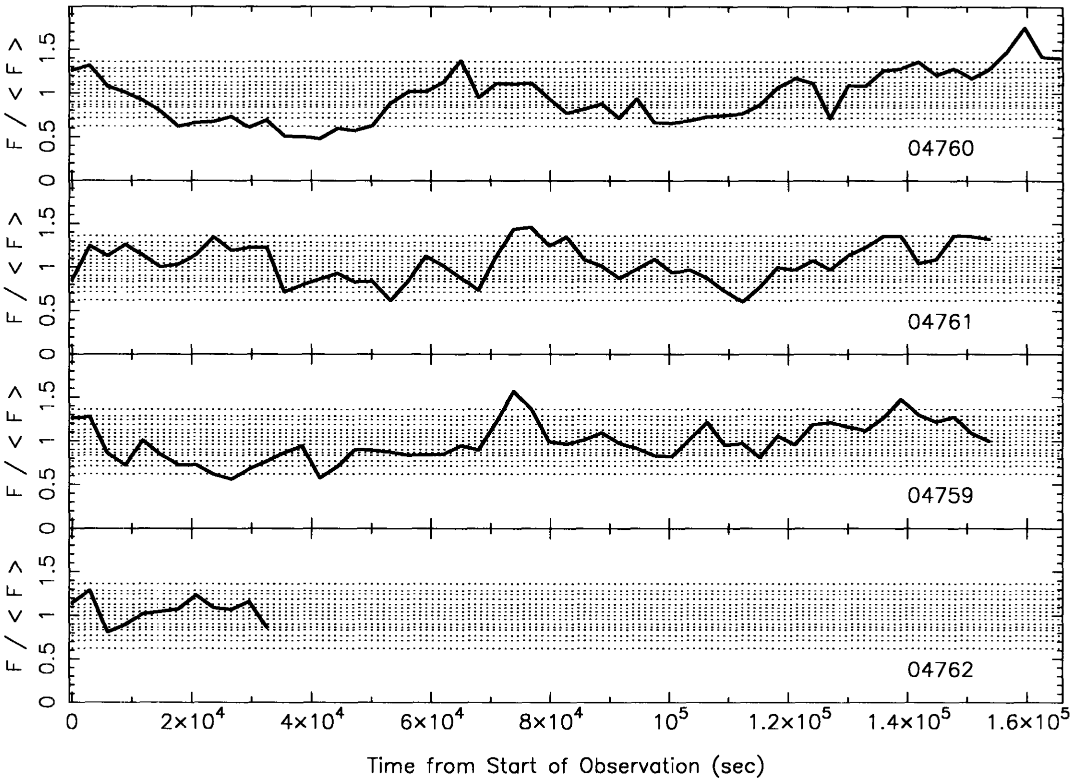

Figure 5-2: Flux slices used to make luminosity-selected spectra. The solid lines represent the 2-10 keV flux measured in the HEG for each of the four observations. The x-axis is the time since the start of the observation for each of the four observations. The y-axis is the measured flux divided by the average flux of 3.6×10^{-11} ergs cm^{-2} s^{-1}. The horizontal dashed lines indicate the boundaries between which counts were taken for the luminosity-selected spectra. The *Chandra* observation id number is marked for each of the four observations. The observations are shown in chronological order.

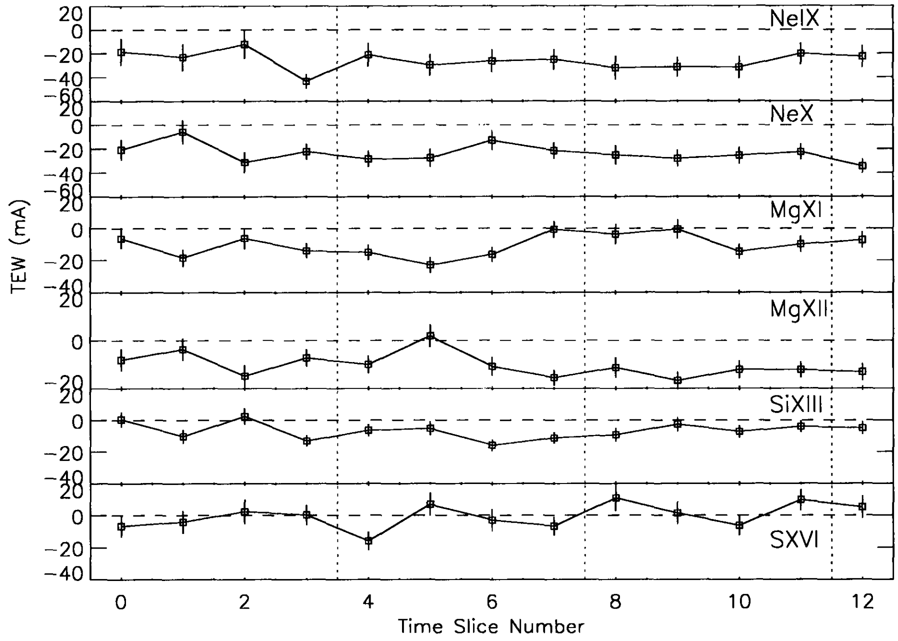

Figure 5-3: TEWs as a function of time. Each time bin is 39 ks long. Vertical dotted lines mark gaps between the observations that are a few days long or less. The observations are ordered chronologically, so that (from left to right) we are showing *Chandra* observation id's 04760, 04761, 04759, and 04762. The horizontal dashed line indicates $y = 0$. From top to bottom, the lines shown are the $1s - 2p$ lines of Ne IX, Ne X, Mg XI, Mg XII, Si XIII, and S XVI.

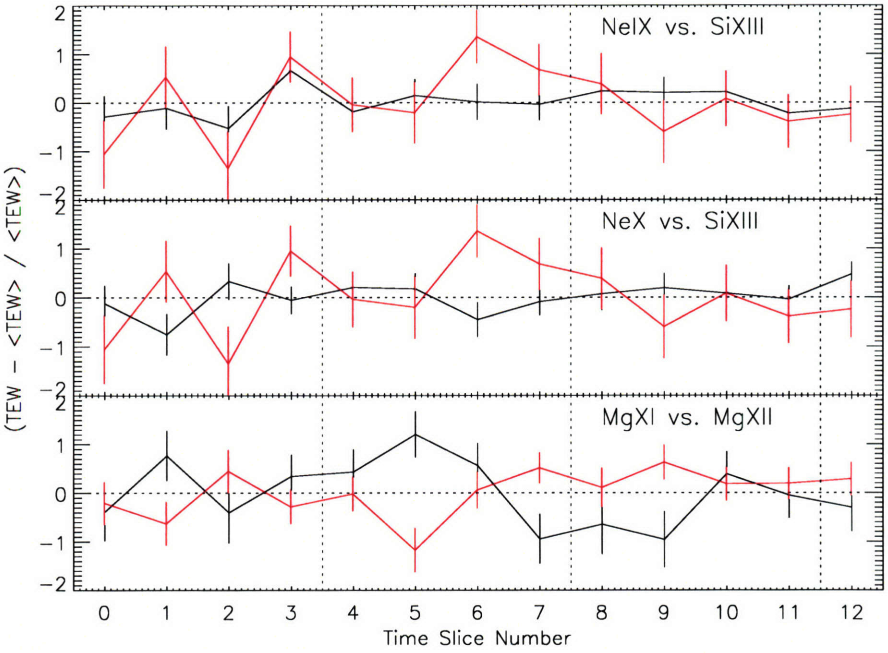

Figure 5-4: Comparing line TEWs to test for correlation. Time bins are 39 ks with vertical dotted lines indicating longer gaps between chronologically-ordered observations, as in Figure 5-3 and horizontal dashed lines indicating $y = 0$. The y-axis is (TEW - $\langle$ TEW $\rangle$) / $\langle$ TEW $\rangle$, where $\langle$ TEW $\rangle$ is the mean TEW for each line. From top to bottom, the lines shown are in black (red) the $1s - 2p$ lines of: Ne IX (Si XIII), Ne X (Si XIII), and Mg XI (Mg XII).

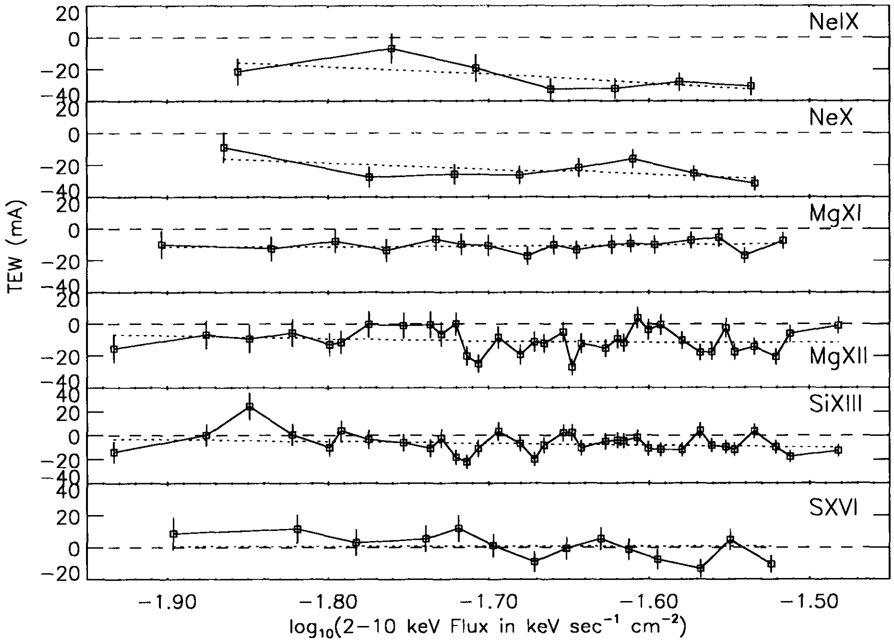

Figure 5-5: TEWs as a function of luminosity for $1s - 2p$ absorption lines tested for variation. The x-axis is the logarithm of the 2-10 keV flux measured in the HEG. The horizontal dashed line indicates where TEW = 0. Absorption lines have TEW < 0; emission lines have TEW > 0. The dotted line is a fit to the curves with a simplified photoionization model described in §5.3.4.

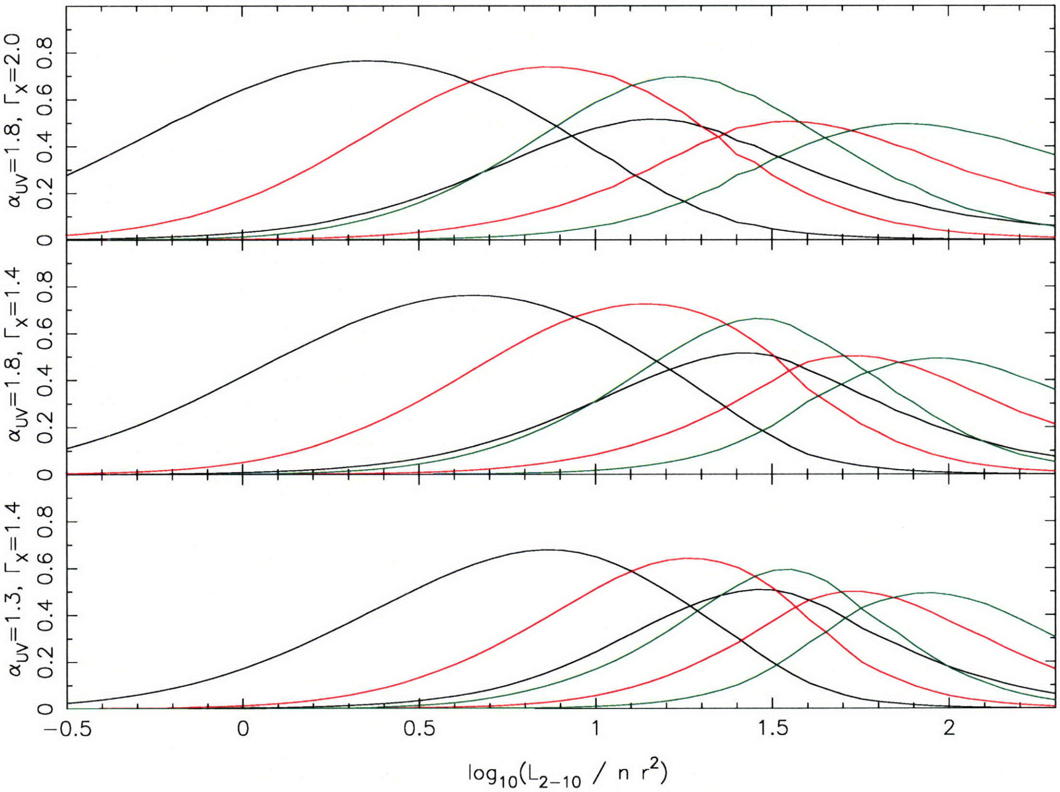

Figure 5-6: Ionization fractions calculated with XSTAR. The x axis is the logarithm of L_{2-10}/nr^2, where L_{2-10} is the 2-10 keV luminosity, n is the absorber number density, and r is the absorber distance from the continuum source. This is the equivalent of $\xi \times L_{2-10}/L_{ion}$, where L_{ion} is the luminosity from 13.6 eV to 13.6 keV. The ionizing flux is assumed to be two power laws with a cutoff at 100 keV. The UV power law (up to 2 keV) has a spectral index denoted α_{OX}, while the X-ray power law (above 2 keV) has a spectral index α_X. From top to bottom, the continuum models have $(\alpha_{OX}, \alpha_X) = (1.8, 1.0)$, $(1.8, 0.4)$, and $(1.3, 0.4)$. The ions plotted are: Ne IX and Ne X (black), Mg XI and Mg XII (red), Si XIII and Si XIV (green).

Chapter 6

A Search for Warm Absorber Variability in *Chandra* HETG Spectra

Warm (photoionized) absorbers (WAs) are found along the line of sight in about half of Seyfert 1 Active Galactic Nuclei (AGN) (Reynolds 1997; George et al. 1998). WAs are evident in the *Chandra* High Energy Transmission Grating (HETG) spectra of several AGN with tens of absorption lines at multiple velocity shifts and ionization stages in some cases (e.g., Lee et al. 2001; Kaspi et al. 2002).

There is much yet to learn about the physical states, structure, and environment of WAs. For example, the distance from the continuum source to the absorber can vary by several orders of magnitude between two contemporary WA models (e.g., Elvis 2000; Krolik and Kriss 2001). Observations have so far been unable to distinguish conclusively between these two locations proposed for the WA, and it may be that both are possible (e.g., Blustin et al. 2004). If we could understand better the physics of WAs and the forces that influence them, we would learn important information about the inner workings of AGN, which could in turn help us understand the mechanisms that AGN use to influence their large-scale surroundings.

Photoionized gas modeling codes such as XSTAR[1] or CLOUDY[2] can produce complex, detailed models of idealized WAs. These codes are widely used in studies of AGN absorbers. Unfortunately, it is not clear how accurately they reflect the real conditions in AGN, which may be very complex. AGN absorbers may not be equilibrated, may be highly spatially structured, may have multiple velocity components, and may vary over time due to a number of different factors. To complicate matters further, the ionizing continua of AGN are clearly varying in X-rays (e.g., Shih et al. 2002), and we must consider that the ultraviolet (UV) continuum is also varying. Ionization fractions of elements can vary significantly as the ionizing continuum varies, but we do not generally have simultaneous knowledge of the absorber spectrum and the full ionizing continuum.

Even when photoionization models fit the observed spectrum well, there is ambiguity in the physical interpretation of the results. The ionization level of an equilibrated absorber depends on both the absorber density and distance from the central source, so that the absorber density and location cannot be determined from ionization levels alone. Other

---

[1] `http://heasarc.gsfc.nasa.gov/xstar/xstar.html`

[2] `http://www.nublado.org/`

measures of absorber properties, such as ionization time scales, can provide a second constraint to resolve this degeneracy.

Measuring line variability is difficult. Modern, high-resolution X-ray spectroscopy allows precise measurements of individual spectral lines, but studies are limited by telescope collecting areas and observing time constraints. A large number of counts is necessary to clearly define lines on short time periods. We have presented some tests of line variability in Chapter 5 for the spectrum of MCG -6-30-15. The methods used in Chapter 5 required many counts in the line region and therefore could not be used to characterize variability for AGN in general.

In this chapter, we consider two other approaches to test for and characterize spectral variability in AGN which have been observed with the *Chandra* HETG. These studies are attempts (for the first time, to our knowledge) to search for short time scale absorber variability in a large set of AGN using high-resolution X-ray spectroscopy. Our studies will be constrained by the number of counts available in our sample spectra.

In the first study, we calculate the normalized excess variance (NEV) of AGN spectra as a function of photon energy. This tells us how spectra are varying beyond the Poisson variations expected as part of the observing process. Because of the short exposure times and limited number of counts available in most spectra, we will not be able to take advantage of the full HETG resolution in this study. Our modeling is further complicated by the fact that absorbers vary in a highly non-linear way with column density and ionization level, so that long computations are required to accurately model even simple absorber variation. Accordingly, this study is only a starting point for future work. Our aim is to determine whether varying absorbers can potentially explain the short-term variation seen in AGN spectra, and to place some general constraints on such models.

In our second study, we use Poisson statistics to determine whether spectral bins are varying with respect to the continuum significantly more than expected due to the stochastic measurement process. This allows us to determine a confidence level that the underlying physical processes governing the number of counts in a bin are varying. In this study, we will work at higher spectral resolution, but over somewhat longer time scales.

Much of our data analysis is conducted using a development version of the ACIS Grating Light Curve (AGLC) package to construct counts spectra sampled on time intervals which are subsets of the total observation time. Information about the AGLC package is available at `http://space.mit.edu/CXC/analysis/aglc/`. We analyze the data using a development version of the Interactive Spectral Interpretation System (ISIS) tool.[3]

6.1 Observations and Data Reduction

We searched the *Chandra* archive for HETG observations of AGN which resulted in MEG spectra with at least a few tens of thousands of counts. In some cases, a single observation produced enough counts to merit inclusion in our sample. In other cases, we combine data from multiple observations. We combine observations whenever possible, with the exception of the MCG -6-30-15 observations. This is a bright, well-studied Seyfert 1 AGN which has been the subject of many variability studies. Because we have spectra of MCG -6-30-15 from two different epochs (about 120 ks in 2000, and 520 ks in 2004) with a large number of counts, we choose to analyze them separately to see if MCG -6-30-15 has evolved on multi-year time scales.

---

[3] `http://space.mit.edu/ASC/ISIS/`

All spectra were reduced using CIAO 3.2 or 3.3 as described in the threads on the *Chandra* web site. In cases where multiple observations were added, the ARFs were weighted according to exposure. Table 6.1 is a list of the targets in our study, along with the redshift, AGN type, cumulative exposure, and total number of first order MEG counts for each target.

Because *Chandra* HETG observations are commonly taken only of AGN expected to produce a large number of counts, our survey sample consists primarily of bright, nearby AGN. In fact, 13 of the targets are Seyfert 1 AGN. The strong obscuration of Seyfert 2 objects makes it difficult to obtain a large number of counts from any but the brightest Seyfert 2 AGN. There are two Seyfert 2 objects in the sample. The most distant object in the sample is the bright quasar 3C 273, at $z = 0.158$. Two objects are classified as quasars, although one of them – MR 2251-178 – has dimmed considerably since its initial quasar classification. Finally, there are 2 BL Lac objects on our list.

6.2 Analysis of Normalized Excess Variance Spectra

There are a large number of ways in which an absorber may vary to influence an AGN spectrum. For this study, we assume the absorber parameters which vary (column density and ionization level) are normally distributed. Gibson et al. (2006) have shown that the absorber can vary in a complicated way as a function of luminosity. Complex geometries of time-varying absorbers and continuum emitters may work together to cause the observed variation. As a result, our assumption of normal distribution may be far from accurate; we consider it simply to be a useful approximation for the purposes of this study.

Our attempts at modeling variability are further complicated by the fact that spectral variability is not due to absorber variation alone. There are clearly components in the spectrum responsible for variation above 2 keV, and these components likely affect the variability below 2 keV where the absorber is most influential. Without knowing how other continuum components vary, it is difficult to determine what the contribution of the absorber is, if any.

Markowitz et al. (2003) used *RXTE* monitoring data to calculate the NEV spectra of seven Seyfert 1 galaxies. They found that variability was frequently stronger in soft X-ray regions, as would be expected if the spectrum softened with increasing flux. The NEV showed a dip in the Fe Kα line region, supporting the claim that the Fe Kα line was less variable than the continuum. They did not consider variability below 3 keV where the WA would be most influential.

The fractional variance (i.e., the square root of the NEV) has previously been analyzed for *XMM-Newton* observations of MCG -6-30-15 by Vaughan and Fabian (2004). They assumed that the continuum was constructed from a sum of a constant component and a component which varied in normalization, but not shape. They derived the shape of the constant component from flux-flux plots using a method described by Taylor et al. (2003). Using this two-component form for the fractional variance, Vaughan and Fabian (2004) derived the result that the energy dependence of the NEV spectrum is determined only by the constant component. They found that the constant component derived from their flux-flux analysis fit their overall *XMM-Newton* spectrum well, though it dit not fit as well to a subset of their spectrum taken from 45 consecutive ks when the source was in a low state. We note that both the method used to derive the constant spectral component and the formula they used to calculate the NEV spectra depend on the same underlying assumptions about the continuum components, and this may have influenced their fit results. In this study, we prefer to derive a theoretical NEV spectrum from models of absorber variability, rather than constructing it from an analysis of the observed spectrum.

Goosmann et al. (2006) have modeled the fractional variance spectrum which would be produced by a collection of random magnetic flares reflecting off the accretion disk surface. Their model reproduced the decreased variability in the Fe Kα line region. The exact shape of the fractional variance spectrum in that region can be used in their model to constrain physical parameters such as the supermassive black hole spin and the disk inclination.

Astrophysical observations of the galaxies in our sample span durations of several tens to hundreds of ks. Vaughan et al. (2003a) showed that NEV spectra drawn from observations taken over such time scales can be observation-dependent. The underlying physical processes may have variations that occur over longer time scales than those sampled, so that the calculated NEV will vary depending on when the source was observed. Even if the underlying processes do not change, the measured variance will vary over time if the variance is calculated from an observation segment which is shorter than the longest time scale in the physical processes. In some cases, repeated measurements of the variance may not even converge to a single value. Although we cannot account for processes occuring on time scales longer than our observations, the error bars we use appear to represent very well the scatter in the calculated NEV spectra (plotted as a function of energy), so we do not expect that our error estimates are unrealistic. Also, Goosmann et al. (2006) find that the shape of the NEV spectrum is less susceptible to variation than the overall normalization.

Recently, Gierliński and Done (2006) have posted a manuscript on astro-ph in which they describe NEV models applied to the *XMM-Newton* spectra of MCG -6-30-15, 1H 0707-495, and NGC 4051. They do not formally fit their models to the data, but find that their model gives " a very good description of the shape of the 0.3-10 keV" NEV. Besides the fact that they do not formally fit their models, the most important difference between their study and ours is that they smear the absorber by a Gaussian with $\sigma = 0.3c$ when modeling the NEV. This is an extreme requirement to place on the absorber, which effectively smears out absorber lines. In our fits, we do not smear over lines, and the variation in strong lines inhibits the fits in much of our parameter space. Gierliński and Done (2006) also construct their models using Monte Carlo simulations of a large number of spectra. While the number of spectra (3000) they randomly generate is probably large enough to produce accurate models consistently, we note that our experience shows that a somewhat smaller number of random spectra (about 600) is not sufficient. Because WA variation is very non-linear, a small number of randomly generated spectra at the extreme regions of the parameter space may strongly affect the model spectrum. We prefer to generate our spectra deterministically, using the methods described in §6.2.2.

In this study of excess variance we are looking for very general results. Only the data sets with the longest exposures (NGC 3783 and MCG -6-30-15) have enough counts to allow using the full spectral resolution of the HETG. For our survey of spectral variability, we prefer to treat each AGN the same, so we use a common time slice duration Δt and wavelength bin width $\Delta\lambda$ for each AGN. A large bin width of $\Delta\lambda = 0.5$ Å still allows for a good number of bins (≈ 30) below 2 keV where the absorber is expected to be influential, while probing a short time scale of $\Delta t = 5$ ks. We are interested to see:

1. Whether short-term variation is common in AGN.

2. Whether different AGN types have characteristic or common forms of variation.

3. Whether there is evidence for short-term variation due to continuum components

other than the absorber.

4. Whether absorber variation can explain some or all of the short-term variation.
5. What physical parameters would describe a candidate absorber variation model.

Because $\Delta\lambda = 0.5$ Å is much wider than the instrumental resolution and, more importantly, than WA absorption lines, we refer to this test as "broad-band." We will also present "narrow-band" spectra for MCG -6-30-15 and NGC 3783 with $\Delta\lambda$ comparable to the instrumental FWHM.

In this section, we describe the procedures by which we calculate fractional variability spectra for each of the objects in our sample (§6.2.1). Then we present our results for a variable absorber model (§6.2.2) and for an alternate model where the NEV is due to a varying power law (§6.2.3).

6.2.1 Calculating Fractional Variability Spectra

The NEV of a spectrum at a given wavelength is the (normalized) RMS variation in excess of that expected from purely statistical variation. For a series of N time slices indexed by $i \in \{0, 1, ..., N-1\}$ with counts x_i in a given spectral region, we calculate the sample mean $\overline{x}$ and unbiased sample variance s^2 as:

$$\overline{x} \equiv \sum_{i=0}^{N-1} x_i \tag{6.1}$$

$$s^2 \equiv \frac{1}{N-1} \sum_{i=0}^{N-1} (x_i - \overline{x})^2. \tag{6.2}$$

We know that the observation process will introduce a variance equal to the Poisson variance, $\overline{x}$, which we subtract away to obtain the variance of underlying physical processes. Finally, we divide the result by $\overline{x}^2$ to obtain a dimensionless measure of the (square of the) fractional variability, which is the NEV:

$$f_{var}^2 \equiv \frac{s^2 - \overline{x}}{\overline{x}^2}. \tag{6.3}$$

We caution that the magnitude of f_{var} should be interpreted with caution. The choice to normalize by $\overline{x}^{-2}$ is essentially arbitrary. To avoid ambiguity, we interpret f_{var}^2 in terms of physical models. Unless otherwise specified, in this chapter we calculate the NEV using the same parameters for every AGN, with time slices of $\Delta t = 5$ ks and wavelength bins of $\Delta\lambda = 0.5$ Å.

Suppose we model the number of photons produced as a combination of two processes. The first process produces a constant number A of photons per time slice, while the second produces a time variable number $B(t)$. Then the total number of counts received at a given time is $C(t) = A + B(t)$, and the NEV is

$$F_{var}^2 = \frac{\sum(B(t) - \overline{B(t)})^2}{(A + \overline{B(t)})^2}. \tag{6.4}$$

We use a capital "F" to distinguish the model from data. In this calculation, we have left out the second numerator term which accounts for Poisson processes introduced during the measurement process, as we are simply producing a theoretical model to characterize intrinsic variability.

Now consider a model in which photons are produced with a rate defined by $C(t) = NB(t)$, where N is some normalizing constant and $B(t)$ is a time-variable multiplier. This form is appropriate for modeling systems in which a constant continuum is modified by time-varying absorption. In this case, the intrinsic fractional variability is particularly straightforward, as the norm N cancels out:

$$F_{var}^2 = \frac{\sum(B(t) - \overline{B(t)})^2}{(\overline{B(t)})^2}. \tag{6.5}$$

In some cases, we have multiple *Chandra* observations of a single source. These observations may be taken over relatively short periods of a few days, as for the 2004 MCG -6-30-15 observation, or they may be spread over periods of months to years. For observations taken months or years apart, the continua show obvious evolution. We are interested in looking for shorter-term variations, so it makes no sense to combine time slices from all observations in our calculations. Instead, we calculate the fractional variability separately for each observation and add the results as follows.

Suppose there are M observations with the i^{th} observation having squared fractional variability $f_{var,i}^2$, sample variance s_i^2, and mean counts $\overline{x}_i$. We define the combined NEV as:

$$f_{var,comb}^2 \equiv \frac{\sum_{i=0}^{M} \overline{x}_i^2 f_{var,i}^2}{\sum_{i=0}^{M} \overline{x}_i^2} \tag{6.6}$$

$$= \frac{\sum_{i=0}^{M} (s_i^2 - \overline{x}_i)}{\sum_{i=0}^{M} \overline{x}_i^2}. \tag{6.7}$$

If all the fractional variabilities are the same, so that $\forall i,\ f_{var,i}^2 = f_0^2$, then $f_{var,comb}^2 = f_0^2$. If all the observations have the same number of mean counts, then $f_{var,comb}^2 = \overline{f_{var,i}^2}$. For each observation, we estimate errors on the NEV following the formulae in Appendix 2 of Edelson et al. (2002). We add the errors as required by Equation (6.6) to obtain the error on $f_{var,comb}^2$.

In Figure 6-1, we show the calculated values of $f_{var,comb}^2$ for the Seyfert 1 AGN in our sample. In each case, we show the system-frame energies on the x-axis. We have omitted points from regions where the background counts were > 10% of the total counts. Figure 6-2 emphasizes the behavior with spectral energy for the Seyfert 1 objects by dividing out the mean $\overline{f_{var,comb}^2}$ for each object and plotting the result on a linear scale. Figure 6-3 shows squared fractional variabilities of AGN which are not Seyfert 1 types.

The variability spectra for which we have the best data (i.e., have the smallest error bars and fewest dropped bins due to high background) typically extend out to high energies. Absorber variation (unless it is extreme) would influence the spectrum only below about 2 keV. Several sources appear to decrease in $f_{var,comb}^2$ with increasing energy, including the spectra for NGC 3783 and MCG -6-30-15. Other sources seem flat with energy. A few, such as Mrk 421, even increase with energy.

It is interesting to compare the two spectra with the highest signal to noise, those of MCG -6-30-15 (2004 epoch) and NGC 3783. The NEV of MCG -6-30-15 decreases at lower energies (< 1 keV), while that of NGC 3783 increases. Both appear to have a local minimum at about 0.9 keV (13.8 Å). If this feature is real, it could be due to (forbidden) line emission from ions such as Ne IX, which would remain relatively constant if it were emitted over a large spatial extent. MCG -6-30-15 also has a single low-variability point at about 16.8 Å (0.74 keV) where the O VII edge lies. Perhaps some radiative recombination continuum (RRC) emission from a large spatial region is providing a relatively constant component at this energy. The O VIII RRC lies at about 0.87 keV, and may be contributing to the lower variability at about 0.9 keV.

The long exposures of the 2004 MCG -6-30-15 and NGC 3783 observations allow us to look at variation with greater spectral resolution. We have calculated the (squared) fractional variability for these two AGN with time slices of length $\Delta t = 10$ ks and spectral bins of $\Delta\lambda = 0.02$ Å, comparable to the MEG FWHM. The NEV spectra for MCG -6-30-15 are shown in Figures 6-4 through 6-7, and the spectra for NGC 3783 are shown in Figures 6-8 through 6-12. In each case, we have plotted the spectrum flux in the lower panel for comparison. In both cases, the NEV spectra are rather noisy, and do not show strong, narrow features at wavelengths of strong spectral lines. This indicates that either the WA is not varying, or that Equation 6.5 does not accurately describe the varying processes in the spectrum. The features seen in the low-resolution NEV spectrum at 0.74 and 0.9 keV are not strongly evident in the high-resolution spectrum, though there are weak features at these energies.

6.2.2 Modeling a Variable Absorber

As we showed in §6.2.1, the definition of NEV which we are using makes it straightforward to model the variability expected due to a changing ionized absorber. We describe here a model we have constructed which calculates the fractional variability due to an absorber which varies with a Gaussian-distributed hydrogen column density and ionization level.

We used the precalculated grid17 table model available at the XSTAR web site[4]. This grid was calculated for a power law continuum (with spectral index $\alpha = 1.0$) and a turbulent velocity 100 km s^{-1}. We then use the grid to produce a series of models, each of which determines a set of F_{var}^2 values according to Equation (6.5).

For each model, we construct an array S_{N_H} of 25 column densities which are normally distributed with mean $\overline{N_H}$ and variance $\sigma_{N_H}^2$. We then construct a second Gaussian-distributed array $S_{\log_{10}(\xi)}$ of ionization parameters with mean $\overline{\log_{10}(\xi)}$ and variance $\sigma_{\log_{10}(\xi)}^2$. The input values for our model are all possible pairs $(N_H, \log_{10}(\xi))$ with $N_H \in S_{N_H}$ and $\log_{10}(\xi) \in S_{\log_{10}(\xi)}$. We use these inputs to the XSTAR table model to generate 625 absorption spectra and then apply Equation (6.5) to obtain an expected fractional variability spectrum.

Several examples of model results are shown in Figures 6-13 and 6-14. The axes of these plots are logarithmically scaled, so the model spectra should be compared to the NEV spectra in Figures 6-1 and 6-3. The model NEV values generally drop off significantly above 2 keV, except at high ionization levels. This indicates that our model will have difficulty matching observed NEV spectra above 2 keV, but may still contribute strongly to the NEV spectrum at lower energies. We also note that the region from 0.7 to 1 keV shows strong variability in our models, due to the influence of WA lines and edges in that region. We do not generally see this feature in the real NEV spectra. Our models were calculated with wavelength bins of size $\Delta\lambda = 0.5$ Å. We have also calculated model spectra for narrower wavelength bins (not shown). In these spectra, individual WA lines vary quite

---

[4] `http://heasarc.gsfc.nasa.gov/xstar/xstar.html`

strongly and stand out noticably from the NEV spectrum. We do not see such features in the higher-resolution NEV spectra we calculated for NGC 3783 and MCG -6-30-15 (Figures 6-4 through 6-5 and 6-8 through 6-12).

We test our model result against the observed NEV spectrum for MCG -6-30-15 using the χ^2 statistic and find best-fit values of $\overline{N_H} = 10^{22.6}$, $\sigma_{N_H} = 10^{20.6}$, $\overline{\log_{10}(\xi)} = 2.0$, and $\sigma_{\log_{10}(\xi)} = 0$. We tested a range of values for $\overline{N_H}$ from 10^{20} to $10^{22.9}$, σ_{N_H} from 10^{19} to 10^{22}, $\log_{10}(\xi)$ from 0.2 to 3.8, and $\sigma_{\log_{10}(\xi)}$ from 0 to 1. We fit only the spectral range from 0.5 to 2.0 keV. Our best fit has $\chi^2 = 257$ for 27 spectral bins and four parameters and is thus strongly rejected by the χ^2 statistic. Figure 6-15 shows a plot of the model fit to the observed fractional variability. The fit is visibly inadequate.

Because of the combined effect of photoionization edges, models such as this one work better when variability increases at lower energies. We visually selected a second AGN from the spectra shown in Figures 6-1 and 6-3 for a second fit attempt. The AGN we selected, NGC 4151, is a Seyfert 1 (as classified by SIMBAD) at $z = 0.0033$. Its fractional variability is comparatively low at higher energies, but rises steeply with decreasing energy below 1 keV. The best fit parameters are: $\overline{N_H} = 10^{22.8}$, $\sigma_{N_H} = 10^{20.6}$, $\overline{\log_{10}(\xi)} = 2.2$, and $\sigma_{\log_{10}(\xi)} = 0$, similar to those for MCG -6-30-15. The result is much better, with a $\chi^2 = 34.8$ for 22 degrees of freedom, but the model is still rejected at the 96% confidence level. Figure 6-16 shows the best fit.

There is some subjectivity in the fitting process, since we have arbitrarily chosen the range of spectral energies over which the fit is performed. We already know that variation at high spectral energies cannot be easily accounted for by absorber variations, and it may be that our fit range is too broad. In support of this, we try fitting a smaller energy range, 0.5-1.5 keV. This time, we obtain a formally acceptable fit, with $\chi^2 = 17.3$ for 18 degrees of freedom. The fit parameters are: $\overline{N_H} = 10^{22.8}$, $\sigma_{N_H} = 10^{19.8}$, $\overline{\log_{10}(\xi)} = 1.0$, and $\sigma_{\log_{10}(\xi)} = 0$. Figure 6-17 shows the model fit.

In the model described here, $\log_{10}(\xi)$ is normally distributed. We have also tried a model in which ξ itself was normally distributed. The results were similar, as the best fit for MCG -6-30-15 and NGC 4151 depended little on ξ variation.

6.2.3 Modeling a Variable Power Law

We can also use Equation 6.5 to model the effect of a single varying power law which produces a continuum $C(t) = N\exp(-\Gamma(t))$, where $\Gamma(t)$ varies with time. We used the same method as in §6.2.2 to fit an NEV model due to Gaussian variations in the power law photon index Γ. We tested pairs of means $\overline{\Gamma}$ and variance σ_Γ^2 with a range of values $\overline{\Gamma}$ from 1.0 to 3.0 and σ_Γ from 0.05 to 2.0. The fit is formally unacceptable and worse than the pure absorption variation model in §6.2.2. The single power law with constant norm and varying photon index varies in a quite different way from MCG -6-30-15. (This is not relevant to the results of Vaughan and Fabian (2004), who fit a different continuum model composed of one constant component and a power law which varied only in normalization.)

A time-variable power law norm and a constant photon index will produce an NEV constant with energy. It is possible that the high-energy variability seen in several AGN in our sample could be explained by such a model. Modeling a spectrum which varies in both continuum and WA properties is very complex and beyond the scope of this introductory study. A large parameter space would have to be searched, and the WA ionization level should be tied in some realistic way to the variable continuum.

6.3 Testing for Varying Absorption Lines

In §6.2, we searched a sample of AGN for short-term variations at low spectral resolution. In this section, we take advantage of the spectral resolution of the *Chandra* MEG to search for variability in narrow wavelength bins. For each AGN in our sample, we use Poisson statistics to determine whether wavelength bins are varying more than expected due to any amount of absorption in each bin. The process is described in §6.3.1. In §6.3.2 and §6.3.3, we describe the results of our test.

6.3.1 Testing For Line Variability in the Whole Spectrum

In this section, we describe the algorithm we use to determine where line variation may be occurring in a spectrum. The same algorithm is applied to each AGN in our sample, so for the sake of discussion we consider only a single AGN. The `garf_gaps` function provided with the AGLC software identifies spectral regions which are affected by chip gaps or bad pixels. We flag these regions and do not consider them in our test.

We use AGLC to break the MEG spectrum into 3 ks time slices with a wavelength resolution of $\Delta\lambda = 0.01$ Å. We order the 3 ks slices according to some rank, either observation time or 2-10 keV luminosity. We also associate with each slice the CIAO ARF calculated for that observation, allowing us to convert from counts spectra to flux spectra. (On 3 ks time scales, the ARF is relatively constant.)

For every spectral bin at wavelength λ_0, we wish to fit a linear continuum to the surrounding spectrum while ignoring the region about λ_0, so that any line at that wavelength will not strongly affect the continuum fit. We fix two parameters, $\Delta\lambda_{cont}$, and $\Delta\lambda_{line}$. Then, for every spectral bin at wavelength λ_0, we perform the following procedure:

1. Specify a set of spectral bins B composed of all bins with central wavelengths $\lambda \in \{x \mid ((x \geq \lambda_0 - \Delta\lambda_{cont}) \wedge (x \leq \lambda_0 - \Delta\lambda_{line})) \vee ((x \geq \lambda_0 + \Delta\lambda_{line}) \wedge (x \leq \lambda_0 + \Delta\lambda_{cont}))\}$.

2. Determine a grouping factor G such that when the rank-ordered 3 ks slices are combined into groups of size G (i.e., each group is a combination of G 3 ks slices), the mean number of counts per bin in the spectral bins B is at least C_{min} for all groups. The group size G will generally vary for each spectral bin for which the test is run. Call the resulting number of (full) groups N_g.

3. If it is not possible to find a G that fits the requirements of Step 2, then there are not enough groups to perform variability tests. Flag the spectral bin at λ_0 as unused, move to the next bin, and restart the procedure.

4. Otherwise, for each group, fit a linear continuum to the spectrum in bins B. Use the ARF to fit the flux, as opposed to fitting counts, which will be structured at some wavelengths due to a varying ARF across bins. Using the continuum fit, determine the number of expected continuum counts C_i in the bin at wavelength λ_0 for group i.

5. For group i, given C_i and the number of observed counts, x_i, a maximum likelihood analysis tells us that the expected number of counts N_i in that bin is $N_i = f \times C_i$, where $f = \sum_i x_i / \sum_i C_i$.

6. For each group, calculate the Poisson probability P_i of observing at least x_i counts given an expected rate N_i of counts: $P_i \equiv P(x \geq x_i, N_i)$.

For our study, we used $\Delta\lambda_{cont} \equiv 0.2$ Å, $\Delta\lambda_{line} \equiv 0.05$ Å, $C_{min} \equiv 10$, $N_{g,min} = 5$.

The Poisson probabilities P_i for all G groups should be uniformly distributed. We can build a test for variability based on this fact. After performing the above operations, we have an array of probabilities for every wavelength bin in the spectrum which was not flagged as unusable. If the intrinsic properties of the spectrum are not changing, these probabilities should be uniformly distributed. Assuming our continuum fits are reasonably accurate, continuum variation should not affect the list of probabilities, since our statistical test "divides out" the influence of the continuum in step 5.

The minimum number of Poisson probabilities in a given bin is $N_{g,min}$, and many bins will have more probabilities. In order to make our test more sensitive, we group the bin probabilities together so that all probabilities in M adjacent spectral bins are now grouped into a single "macro-bin." We have tried several different values for M, but generally prefer to use $M = 2$. If the original spectral resolution was $\Delta\lambda = 0.01$ Å, then each array will contain at least $2 \times N_{g,min}$ probabilities corresponding to a macro-bin width of $2 \times \Delta\lambda = 0.02$ Å, similar to the MEG FWHM. We only consider macro-bins constructed from contiguous sets of bins which have not been flagged as unusable.

In order to determine if the intrinsic spectral properties (e.g., absorption or emission) are varying in a source, we look for macro-bins in which the Poisson probabilities are not uniformly distributed. Non-uniformity does not tell us the mechanism of variation; it simply contradicts the assumption that some constant intrinsic process absorbs (or emits!) at some constant multiple rate of the (varying) continuum. (This includes a multiple rate of 1, corresponding to no absorption or emission beyond the continuum.)

To prove non-uniformity, and hence intrinsic variability, we must devise a test which assigns some confidence to the assertion that the Poisson probabilities in a macro-bin are not uniformly distributed. We adopt three different tests of non-uniformity in a given macro-bin. In each case, we take as inputs the array $P_{mac,i}$ of Poisson probabilities in macro-bin i. We also specify a confidence threshhold $T_{conf} \equiv 99.5\%$.

Test 1: In this test, we calculate the probability that we would see fewer values of $P_{mac,i} > T_{conf}$ in a macro-bin (assuming a uniform distribution) than we actually do see. This is calculated using the binomial distribution, and indicates whether there is an excess of Poisson probabilities at the high end of the hypothetically uniform distribution. In our test, high Poisson probabilities correspond to anomalously low count rates, which could be caused by strong absorption.

Test 2: In this test, we calculate the probability that we would see fewer values of $P_{mac,i} < (1 - T_{conf})$ in a macro-bin (assuming a uniform distribution) than we actually do see. This is calculated using the binomial distribution, and indicates whether there is an excess of Poisson probabilities at the low end of the hypothetically uniform distribution. In our test, low Poisson probabilities correspond to anomalously high count rates, which could be caused by strong emission.

Test 3: In this test, we apply a Kolmogorov-Smirnov (KS) test to the array of probabilities to get a confidence level rejecting the hypothesis of uniformity. The KS test is not sensitive to deviation in the distribution tails, which Tests 1 and 2 are designed to catch. Non-uniformity could be caused by variation in intrinsic absorption or emission levels. The KS test returns only a lower limit on the confidence of variation.

We use these tests in several ways to test for variation in individual AGN and in the combined sample. Applying Tests 1, 2, and 3 to the AGN in our sample, we find that Test 1 generally returns the strongest case for variation. This is satisfying, because Test 1 is specifically designed to detect anomalously high absorption in spectral slices. Unless otherwise specified, we work with $M = 2$, indicating that we are combining Poisson probabilties into 0.02 Å bins.

6.3.2 Line Variability Test Results for Individual AGN

We apply Tests 1, 2, and 3 to each AGN in our sample. For each test, we look for an excess of confidence values above 99.5%, indicating that a large number of spectral macro-bins have deviated from purely random fluctuations. In general, we do not find such excesses in the individual AGN in our survey. Perhaps the most significant case for variability is the test for variation with luminosity in NGC 3783, which has 3 of 234 confidences over 99.5% for Test 1 for macro-bins of size $M = 2$. According to the binomial distribution, this can happen by pure chance 11% of the time. Given the large number of AGN tested, we do not consider this result significant. However, we have tested all possible wavelength bins in the spectrum regardless of whether we would expect to see line absorption at those wavelengths. Thus it is most accurate to say we have not detected strong evidence for narrow-band spectral variability across spectra as a whole.

Using the same results for Tests 1, 2, and 3, we restrict our test to consider only macro-bins which are near theoretical wavelengths for strong atomic lines. We consider all wavelengths within -1000 to 0 km s^{-1} of the $1s - 2p$ lines of He- and H-like Ne, Mg, Si, and S, as well as strong inner shell lines of Ne VII, Ne VIII, Mg IX, Mg X, Si XI, Si XII, S XIII, and S XIV. We do not find any stronger evidence for variability when restricting our tests to these regions.

6.3.3 Line Variability Test Results for the Aggregate Sample

In this section, we combine all the AGN in our sample to search for variability in the sample as a whole. We use the results of Tests 1, 2, and 3 for macro-bins of size $M = 2$. From each AGN, the tests give a single probability for each wavelength macro-bin which was considered acceptable for our tests. (As discussed in §6.3.1, we only accepted bins with a sufficiently high number of counts and which did not fall near a region with a highly structured ARF.) We de-redshift these wavelengths and then add the probabilities to an empty sample grid. Considering wavelengths in the system frame allows us to compare spectra of different AGN, although individual lines may still fall at slightly different wavelengths in the spectrum due to the intrinsic velocities of the absorbers.

There are two different ways to test for variability in the aggregate sample. Firstly, we may stack the confidence probabilities given by Tests 1, 2, and 3, so that only one probability per macro-bin per AGN is associated with the aggregate result. This puts all AGN on an equal footing, as even the spectra with the longest exposures will contribute only one probability per bin. It is not obvious what the distribution of these numbers should be, so we run Monte Carlo simulations to calculate confidence limits for the stacked results. In the second case, we combine the Poisson probabilities for each wavelength bin and each spectral slice for all the AGN. In this case, spectra with long exposures will be weighted more strongly than those with short exposures. The Poisson values should be uniformly distributed regardless of which AGN they were drawn from, so we can apply standard tests for uniformity to the aggregate sample. We describe these tests and their results in detail in the rest of this section.

Case 1: All AGN on Equal Footing

In this test, we combine the results of Tests 1, 2, and 3 for each macro-bin in each AGN into 3 spectra (one for each test). We add the probabilities, so at each wavelength we have a number representing the sum of the probabilities produced by Tests 1, 2, and 3 for the appropriate macro-bin(s) in each AGN.

The set of macro-bins used was sparse in the spectrum of each AGN, i.e., there were gaps in the set of macro-bins due to rejected regions with low numbers of counts or complicated ARFs. Because the HETG zero order of each spectrum was typically aimed at (nearly) the same spot on the *Chandra* CCDs for each observation, chip gaps will tend to fall in the same spectral regions for each observation. This means that some wavelengths will have a large number of macro-bin measurements, while others will have few or none. To quantify this, we construct a control spectrum with the same wavelength grid as our macro-bins. We add 1 to the appropriate bin in the control spectrum for every probability determined by Tests 1, 2, and 3. Thus the control spectrum represents the number of probabilities that have been collected for a given wavelength. (Because we are binning the control spectrum more coarsely than the macro-bins, each AGN can contribute multiple times to a bin in the control spectrum.)

It is not obvious what the distribution of summed results of Tests 1, 2, and 3 should look like. In order to calculate 90% confidence regions for the sum of these probabilities, we randomly generate 1000 sets of uniformly-distributed probabilities corresponding to the Poisson probabilities described in Step 6 of the survey algorithm. We apply Tests 1, 2, and 3 to these simulated values just as for the measured values. We then find the ranges occupied by the upper and lower 5% of the test results and consider these to lie outside the 90% confidence regions. In summary, we produce 1000 sets of simulated data for each AGN, assuming there was no variation (i.e., the Poisson probabilities corresponding to variation in individual spectral slices were uniformly distributed).

Figure 6-18 shows our results for the case where spectral slices are ordered by 2-10 keV flux. In the top three panels of each figure, we show the accumulated probabilities from Tests 1, 2, and 3 divided by the control spectrum. In the bottom panel, we show the control spectrum. Figure 6-19 shows the results for time-ordered spectra.

For the flux-ordered case, Test 1 shows an excess of bins above the 90% confidence range. There are no bins outside the range on the low side, but 55 out of 290 (19%) on the high side. This is almost four times the 5% we would expect to find in the upper tail by random chance. Some of these are certainly spurious, while others may indicate real variability. We list each of the variation candidate bins in Table 6.2 along with possible line identifications. We list lines having an absorption oscillator strength ≥ 0.1 and within 0.04 Å of the center of candidate bins, as 0.04 Å is the bin resolution we used for this test. This does not account for the possibility that lines could be velocity shifted by more than 0.04 Å, which at 10 Å, this corresponds to about 1200 km s^{-1}. The table contains 6 lines which are $1s - 2p$ resonance lines of the He-like or H-like ions CaXX, ArXVII, SiXIV, SiXIII, AlXIII, and AlXII.

When we order the spectral segments by time, we achieve similar results: 48 out of 300 (about 16%) significances lie above the 90% confidence range for Test 1. In this case, we find 5 resonance $1s - 2p$ lines of He-like or H-like ions as candidate line identifications, but the ions involved are different from the luminosity-ordered spectra. The ions with significant $1s-2p$ line variation are: FeXXVI, ArXVIII, SiXIII, MgXI, and NeX.

If we assume there are 8 abundant ions (Ne, Mg, Al, Si, S, Ar, Ca, and Fe) with He- and H-like $1s-2p$ resonance lines in the spectral range of our test, there are 16 possible resonance lines in the spectrum. Since we declared matches when the lab wavelength was within 0.04 Å of the significant region, the resonance lines cover $16\times 0.08 = 1.28$ Å out of the approximately $300 \times 0.04 = 12$ Å covered by test bins. Therefore, if the significant bins are randomly distributed, each one has about a 10% chance of falling near a $1s-2p$ resonance line, giving roughly $55 \times 0.10 = 5.5$ matches just by random chance. This is similar to the number of matches we actually find, so we do not attribute any strong significance to the line identifications. In light of this calculation, the lines listed in Table 6.2 should not be considered true line identifications.

Evidence for variation was found by examining the upper tail of probabilities in Test 1. It is not surprising that Test 3 did not detect significant variation, as it relies on the KS test which is not sensitive to the tails of probability distributions. An excess of probabilities in the high tail of Test 1 means that there were a large number of cases where the number of counts in a time slice in a given bin were much smaller than expected. This could be due to absorption varying over time.

We do not see a similar excess of significant bins in the upper tail of Test 2. This indicates that unexpectedly high numbers of counts, perhaps due to variable emission, are not as common. In fact, we find a similar number (15-19%) of bins that lie in the lower tail of the 90% confidence region for Test 2 as for the Test 1 upper tail. This corresponds to a deficit of wavelength bins that have unexpectedly high numbers of counts compared to a constant emission rate model.

Case 2: All Spectral Slices Weighted Equally

In the second test for variability in the aggregate sample, we keep track of every Poisson probability generated for each wavelength bin in every spectral slice of each AGN in our sample. We then apply Tests 1, 2, and 3 to the collection of probabilities associated with each (rest-frame) wavelength bin. For the first aggregate test, we had at most one probability per bin per AGN; in this test we can have a much larger number of probabilities to analyze. Because the KS statistic depends on the number of input data points, it is much more discriminating in this case.

Figure 6-20 shows the results of this test for luminosity-ordered spectral slices, and Figure 6-21 shows the results for time-ordered slices. We plot the logarithm of the probability returned by Tests 1, 2, and 3. In each case, a low probability indicates a strong deviation from a uniform distribution of input values and, ultimately, from Poisson-distributed data. The results from Test 2 are weaker than from Tests 1 and 3, again indicating that unexpectedly high count rates are not commonly seen in the data. The wide-band structure in test 3 is comparable to the (inverted) control spectrum in Figure 6-18, which is not surprising since the KS test statistic depends on the number of input data points.

Applying Test 1 to luminosity-ordered spectral slices, we find 4 out of 290 spectral bins have probabilities $\leq 1\%$. For the time-ordered case, we find 4 of 300 bins. This result is not significant, as we would expect about that number of probabilities $\leq 1\%$ just from random chance. However, Test 3 shows stronger results. For the luminosity ordered case, the KS test finds 12 of 290 bins with probabilities $\leq 1\%$, and for the time-ordered case, the number is 20 out of 300. Both these results are highly significant. The probabilities in these bins are apparently strongly non-uniformly distributed.

For all tests described in this section, the region around the SiXIII $1s-2p$ line (at 6.65Å) is flagged as a strong candidate for variability. There is a strong "inverse edge" feature in the ARF at about 6.05 Å, but this feature should not affect our study, as we have excluded bins from that region and the SiXIII line is typically redshifted to higher wavelengths. There is a feature in the ARF at about 6.75 Å which can affect measurements of the line, as seen in the case of MCG -6-30-15 (Gibson et al. 2006). We have accounted for the ARF in our continuum fits, and we have chosen time slices that are a multiple of the instrument dither time, so it would be somewhat surprising if structure in the ARF were affecting this measurement. The line was also a strong candidate for variation in the aggregate sample test described in §6.3.3. The SiXIII $1s-2p$ line is apparently a good candidate for future variability studies, with the caveat that care must be taken to ensure that instrumental features are not influencing the measurements.

The KS test also shows strong variation at about 7.65 Å, which could possibly be attributed to blueshifted AlXII. Other strong candidates for variability include lines at about 3.45 and 4.07 Å. These could be attributable to various inner-shell lines of Ar ions (Behar and Netzer 2002).

Finally, we consider the possibility that lines are varying at significant blueshifts from their rest-frame wavelengths. The test described in this section shows some evidence for line variation, and we have a large number of Poisson probabilities generated for our sample, which allows us to search in narrow wavelength regions. Our test grid has wavelength bins of size 0.04 Å, corresponding to about 3000 km s^{-1} at 4 Å. We restrict our analysis to the wavelengths of the strong lines considered in §6.3.2. We test for variability in the aggregate set of bins associated with these lines after blueshifting them by some multiple of -3000 km s^{-1}. We estimate the significance of variability using Tests 1 and 3 applied to the Poisson probabilities in these regions.

Figures 6-22 and 6-23 show our results. Test 3, based on the KS test, shows stronger evidence for variability once again, and variability may be stronger in the luminosity-ordered case for blueshifts between 0 and -15,000 km s^{-1}. We do not see the same trend for time-ordered spectral slices, and it is difficult anyway to estimate the significance of the apparent trend in Figure 6-22 of higher variation at lower velocities. There could be systematic reasons for the apparent trend, such as incorrect continuum fits due to strong lines (nearly at rest) being included in the continuum fit region, although in that case, we would expect the same trend to appear in both luminosity- and time-ordered cases. Given these difficulties, we do not attribute strong significance to the apparent trend for the luminosity-ordered case, but consider it worthy of further study in the future.

6.4 Conclusions

We have calculated NEV spectra for AGN in the *Chandra* archive which have been observed with the HETG. For two AGN, NGC 3783 and MCG -6-30-15, there are enough counts in the observations to produce NEV spectra with spectral resolution comparable to that of the MEG. We did not find evidence for stronger or weaker variation in line absorption regions. We then calculated NEV spectra with poor wavelength resolution ($\Delta\lambda = 0.5$ Å), but on short time scales ($\Delta t = 5$ ks). The spectra showed a variety of different shapes. We attempted to fit two of the NEV spectra, those for MCG -6-30-15 and NGC 4151, with a model that would attribute the spectral variations in the soft X-rays solely to absorber variation. This model was not formally successful in fitting the NEV spectrum.

Simple models of fractional variability involving normally-distributed variations in the WA or power law photon index alone are inadequate to describe the short-term (5 ks) variations which are occuring in the 0.5 to 10 keV NEV spectra of MCG -6-30-15 and NGC 4151. Rather than attempting to fit the variability spectrum of each AGN in the study, we have instead used these results to draw some general conclusions.

1. Short-term continuum variation is present in almost every AGN in the HETG archive.
2. There is no obvious trend of continuum variation characteristics with AGN type, though we do not have a large enough sample to draw strong conclusions about any type except Seyfert 1 AGN.
3. The variations extend out to energies well beyond 2 keV. In most cases, the fractional variability (as defined in §6.2.1) decreases with increasing energy, but some AGN (e.g., Mrk 421) behave otherwise.
4. Some, but not all, AGN have highest NEV below 2 keV.
5. Fitting two AGN, MCG -6-30-15 and NGC 4151, with variable absorber models indicates that the absorber may contribute to the observed variability.
6. If the fit region is restricted to soft X-rays, a varying WA can account for the observed NEV in at least the case of NGC 4151.
7. Given that some other physical process is responsible for at least the high-energy variability, the choice of which energy range to fit has significant consequences for the fit results.

We obtained similar results for our fits to the 0.5 to 2 keV NEV spectra of MCG -6-30-15 and NGC 4151. In each case, the model preferred little or no ionization variation. A rather high absorbing column was required ($N_H \approx 10^{22.6}$ cm^{-2}) with about 1% variation about that column. Such a strong absorbing column would be expected to produce strong absorption lines. This column density is similar to that found for the highly ionized absorber component in the 2000 MCG -6-30-15 spectrum model of Lee et al. (2001). Detailed modeling of the 2004 observation of MCG -6-30-15 has not yet been completed (Lee et al. 2006, in preparation), but we note that Netzer et al. (2003) have claimed that the absorbers in NGC 3783 have a combined column of about 4×10^{22} cm^{-2}. This is not far from the results of our model fits for MCG -6-30-15 and NGC 4151.

Since continuum variation can be probed without high spectral resolution, the *Chandra* HETG is not needed for studies of this type. In some cases spectral data from other instruments (e.g., the *Chandra* ACIS-S) will be affected by spectral pile up, in which photons enter the detector faster than the detector can be read out. This will distort the measured spectrum and also the variability spectrum. It may be possible to use data archives from previous missions (such as *ASCA*) to produce variability spectra. It would be interesting to see if the NEV spectra change significantly over years or decades.

This study has shown the need for a better understanding of continuum models. Before proceeding further with this study, it would be most helpful to understand how the continuum varies across the spectrum. While the soft X-ray region shows variability presumably due to both the continuum and the absorber, the hard X-rays should be relatively unaffected by the absorber. A better understanding of the continuum emitter variation, constrained by the high-energy spectrum, would allow us to isolate the variability attributed to the absorber alone.

In the second part of this study, we quantified the count variations in each spectral bin of each AGN spectrum available to us, excepting spectra that were too dim for good statistics and spectral regions known to be dominated by chip gaps or bad pixels. We found evidence that bins were varying with respect to the surrounding continuum by occasionally containing an unexpectedly low number of counts compared to the expected rate for a model with constant absorption and emission. This could be due to variable absorption mechanisms. We did not see an excess of unexpectedly high numbers of counts in wavelength bins, which would indicate variable emission processes. In several cases, the wavelength bins which showed significant variation matched up to resonance $1s-2p$ lines of abundant ions. However, because the number of matched ions was not much greater than we would expect by random chance, we do not attribute great significance to the line identifications.

The results of this test show that searches for line variability in AGN are a worthwhile pursuit, and can be expected to show positive results. The recent study by Gibson et al. (2006) of MCG -6-30-15 is an example of a search in a single AGN which has detected line variability on intra-observation time scales and yielded interesting physical constraints. We are unable to draw strong conclusions about the variability mechanisms in AGN from this current study, as our method has combined observations taken over time scales ranging from days to years.

We draw the following conclusions from the second part of this study.

1. Survey tests for narrow-band (line) variability are feasible and show evidence for narrow-band variability.

2. The variability we detected may be due to varying absorption processes. Further study is needed to confirm this.

3. In tests of the aggregate sample of AGN, we found some evidence that variation is occuring on narrow wavelength scales. The $1s-2p$ line of SiXIII was a strong variability candidate in all our tests, and future studies should examine this line closely. Structure in the MEG ARF near this line should be considered carefully.

4. We did not detect a significant excess of unexpectedly large counts in wavelength bins, which would be attributed to varying emission processes.

5. Survey tests for narrow-band (line) variability should continue as the archive of high-resolution spectroscopy grows.

6. Some statistical tests are stronger than others for detecting variability. It would be valuable to develop and/or apply stronger statistical tests.

As in the case of the NEV models, we add the caveat that our tests depend on an accurate measure of the continuum flux. If the continuum flux varies in a complicated way in the fit region (< 0.5 Å), it could upset our estimates of the expected count rate in a line region. Of course, this would also be evidence for narrow-band variation in the spectrum, but it need not be attributed to absorber variation. Future tests for line variability will hopefully address this possibility.

In this chapter, we have presented introductory studies searching for short-term variability in narrow spectral features of AGN. This field of study is rather new, as high-resolution

X-ray spectroscopy with sufficient signal-to-noise has only become available in recent years. We find significant evidence that variability is occuring, although the exact nature of the variability is difficult to determine with existing data. A deeper understanding of the underlying physical processes would require more long spectroscopic observations and a better understanding of the physical processes responsible for variations in the continuum emission. We look forward to conducting further variability studies in the future, and emphasize the need for high-resolution X-ray spectroscopy satellites capable of collecting large numbers of counts from distant AGN.

6.5 Acknowledgements

This work was supported in part by by NASA through contracts NAS8-01129 and SAO SVI-61010.

Name	Redshift z	AGN Type[a]	Exposure[b] (ks)	MEG 1st Order Counts[b]
3C 120	0.033	Seyfert 1	57	46,000
3C 273	0.158	Quasar	200	360,000
Ark 564	0.0249	Seyfert 1	49	64,000
Centaurus A	0.00182	Seyfert 2	98	64,000
Fairall 9	0.047	Seyfert 1	80	38,000
H1426+428	0.129	BL Lac	140	140,000
IC 4329A	0.016	Seyfert 1	59	130,000
M81*	0.00014	LINER	280	59,000
MCG -6-30-15 (2000b Only)	0.0078	Seyfert 1	65	61,000
MCG -6-30-15 (2004 Only)	0.0078	Seyfert 1	520	370,000
MR 2251-178	0.064	Quasar?	150	46,000
Mrk 290	0.030	Seyfert 1	250	78,000
Mrk 421	0.030	BL Lac	45	150,000
Mrk 509	0.034	Seyfert 1	58	57,000
Mrk 766	0.0083	Seyfert 1	89	51,000
NGC 3783	0.0098	Seyfert 1	890	600,000
NGC 4151	0.0033	Seyfert 1	290	180,000
NGC 4593	0.009	Seyfert 1	79	77,000
NGC 5506	0.006	Seyfert 2	89	28,000
NGC 5548	0.017	Seyfert 1	230	110,000
NGC 7469	0.016	Seyfert 1	140	78,000
PKS 2155-304	0.117	BL Lac	200	420,000

[a] AGN types are taken from the SIMBAD database or, in the case of MR 2251-178, from the literature.

[b] Except for MCG -6-30-15, in cases where multiple observations are available, the exposure and counts reflect the combined data.

Table 6.1: Galaxies included in variability survey.

System Frame Wavelength (Å)	Identified	Lab Frame Wavelength (Å)	Oscillator Strength
1.90, 1.94, 2.02	Fe Kα[a]		
2.42			
2.54			
2.66			
3.02, 3.06	CaXX[b]	3.02	0.416
3.22	CaXVI, CaXVII, CaXVIII	3.20, 3.22, 3.25	0.519, 0.685, 0.638
3.30	CaXIII, CaXIV, CaXV	3.23, 3.30, 3.27	0.154, 0.262, 0.431
3.34	ArXVII, CaXII, CaXIII, CaXIV	3.67, 3.34, 3.32, 3.30	0.156, 0.102, 0.154, 0.156
3.54			
3.90			
3.94	ArXVII[b]	3.95	0.717
4.10	ArXII, ArXIII	4.12,4.09	0.256, 0.411
4.78			
5.14, 5.18	SXII, SXIII	5.18, 5.13	0.234, 0.672
5.58			
5.74			
5.82			
5.90	SiXI	5.90	0.136
5.94			
6.02			
6.22	SiXIV[b]	6.18	0.416
6.54			
6.62, 6.66	AlXII, SiXIII[b]	6.64, 6.65	0.159, 0.701
6.70	SiXII	6.72	0.615
6.78	SiXI	6.78	0.656
6.86	SiX	6.85	0.430
6.90	SiIX, AlX, SiX	6.93, 6.91, 6.86	0.346, 0.134, 0.209
7.18	AlXIII[b]	7.17	0.416
7.34			
7.54 – 7.70			
7.74	AlXII[b]	7.76	0.693
8.10	AlVIII	8.11	0.328
8.18	MgIX, AlVII	8.20, 8.19	0.132, 0.137
8.70			
9.06	FeXXII	9.04	0.125
9.38	MgIX	9.38	0.631
9.46	MgVIII	9.50	0.207
9.54	MgVIII, FeXXI	9.51, 9.51	0.188, 0.189
9.94			
10.30			
10.38			
11.06			
12.22			
12.34	FeXXI	12.36	0.964
15.54	FeXIV	15.56	0.422

[a] The Fe Kα line wavelength varies with ionization stage of the emitting ion.

[b] This line is a $1s - 2p$ resonance line of either the He-like or H-like ion.

Table 6.2: Wavelengths with excess variability.

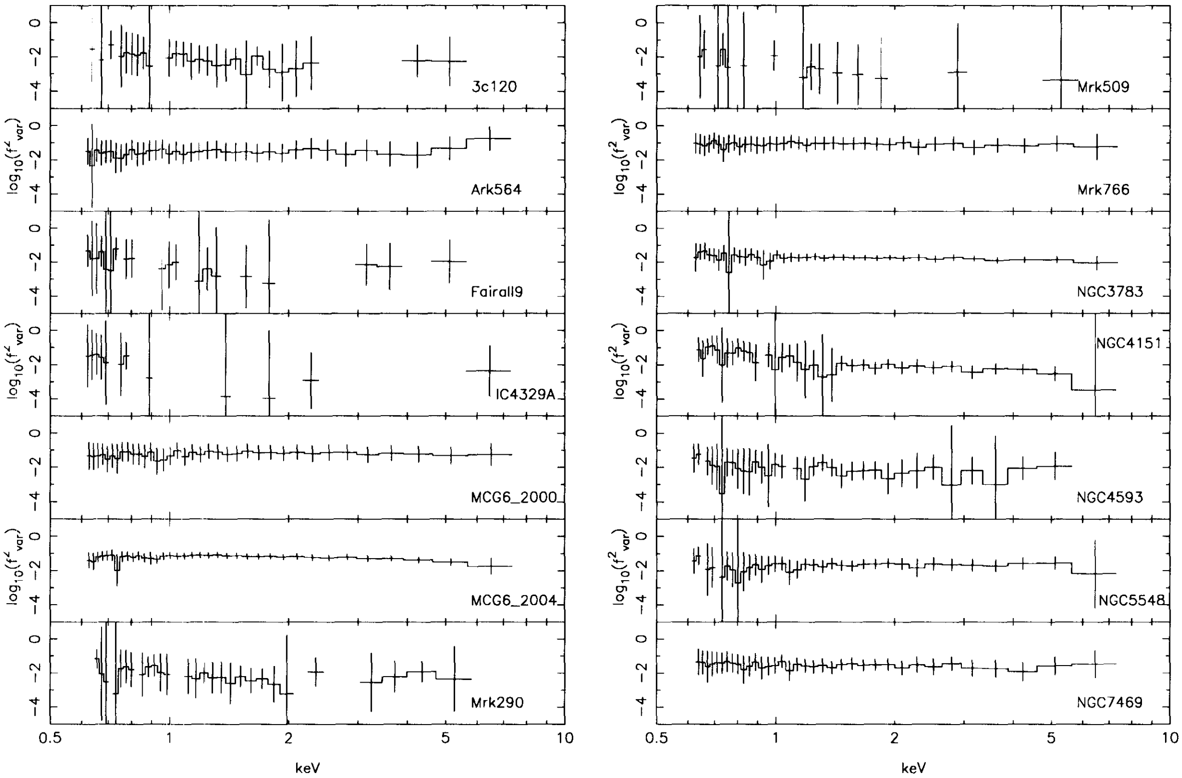

Figure 6-1: Logarithms of NEV for 13 Seyfert 1 AGN. We calculate the NEV for each AGN using time slices of $\Delta t = 5$ ks and wavelength bins of $\Delta\lambda = 0.5$ Å. MCG -6-30-15 is shown twice using data from two different observation epochs. The 2000 observation only uses the second half of the observation, as the first half shows a high background in soft X-rays. The y axis is the same for each observation to emphasize the relative magnitudes of the NEV. In some cases, this means that plot points are "off the charts," as for Mrk 509. We have omitted points at frequencies where the background is stronger than 10% of the source counts, leading to sparse spectra in some cases, as for Fairall 9. The x axis energies are shown in the system frame of each observed AGN.

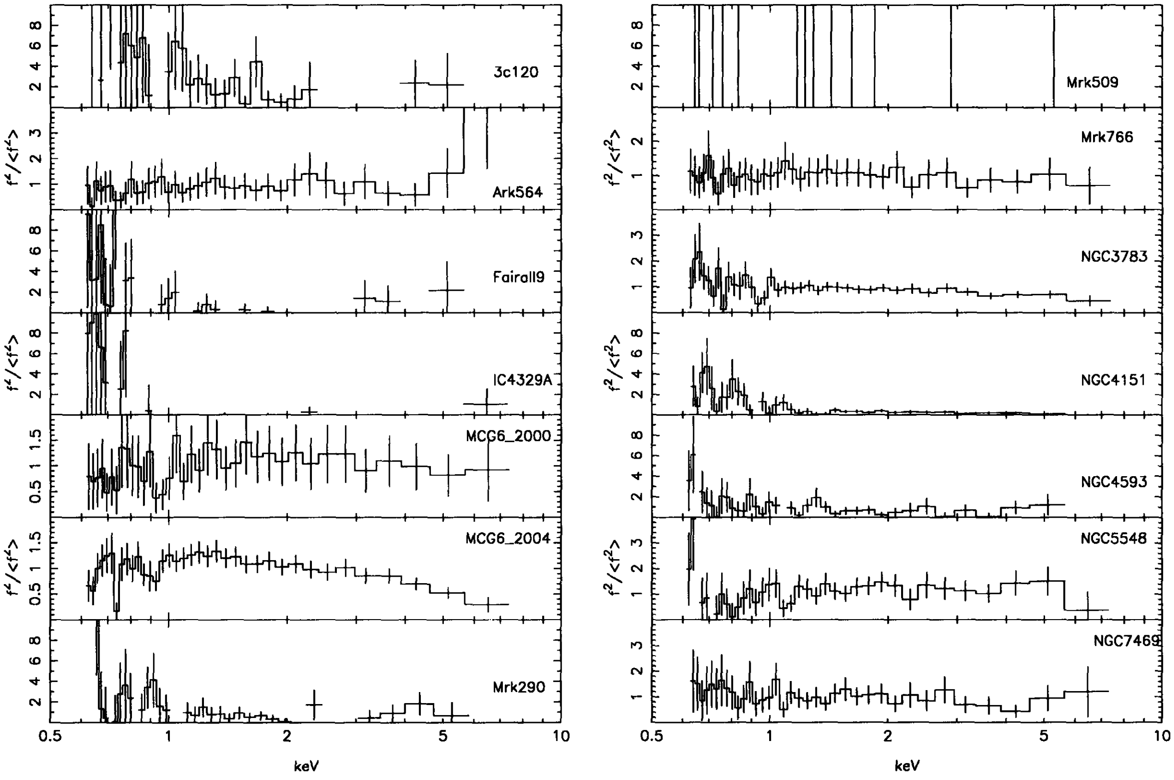

Figure 6-2: Same as Figure 6-1, but the NEVs have been divided by the mean NEV for each source, and the results are plotted on a linear plot.

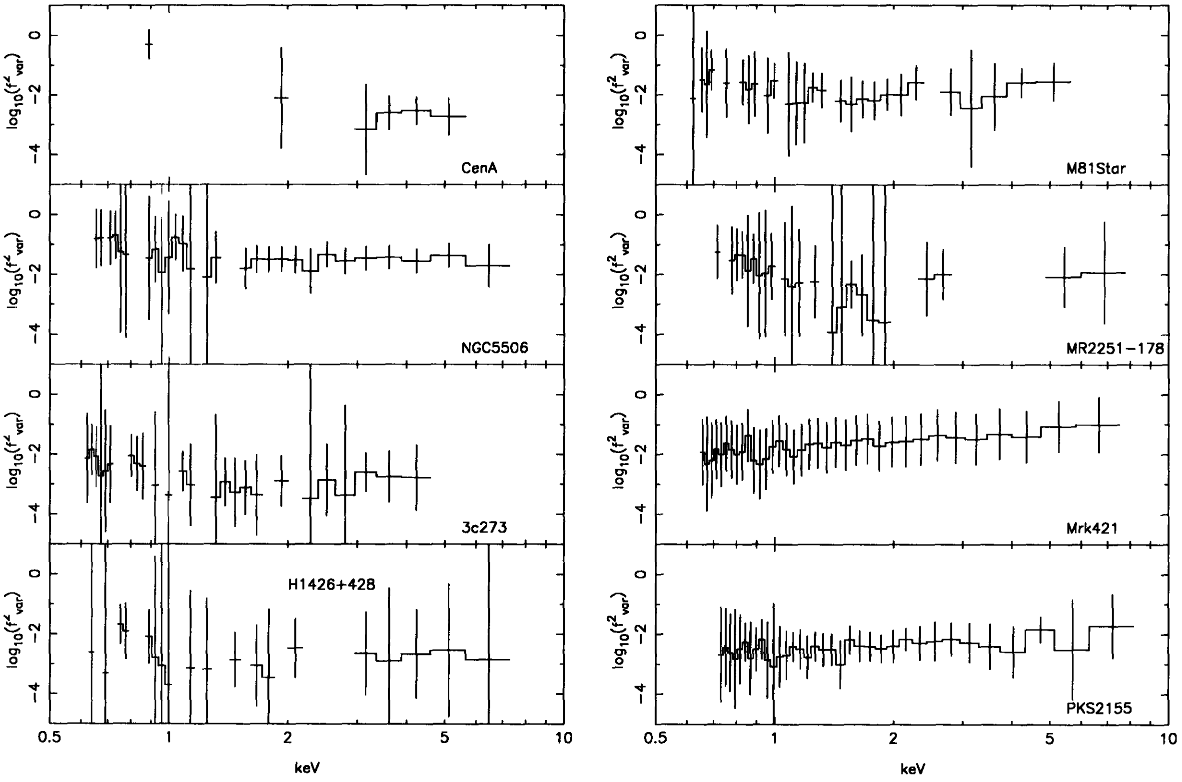

Figure 6-3: Same as Figure 6-1 but showing NEVs for 8 AGN which are not Seyfert 1 objects.

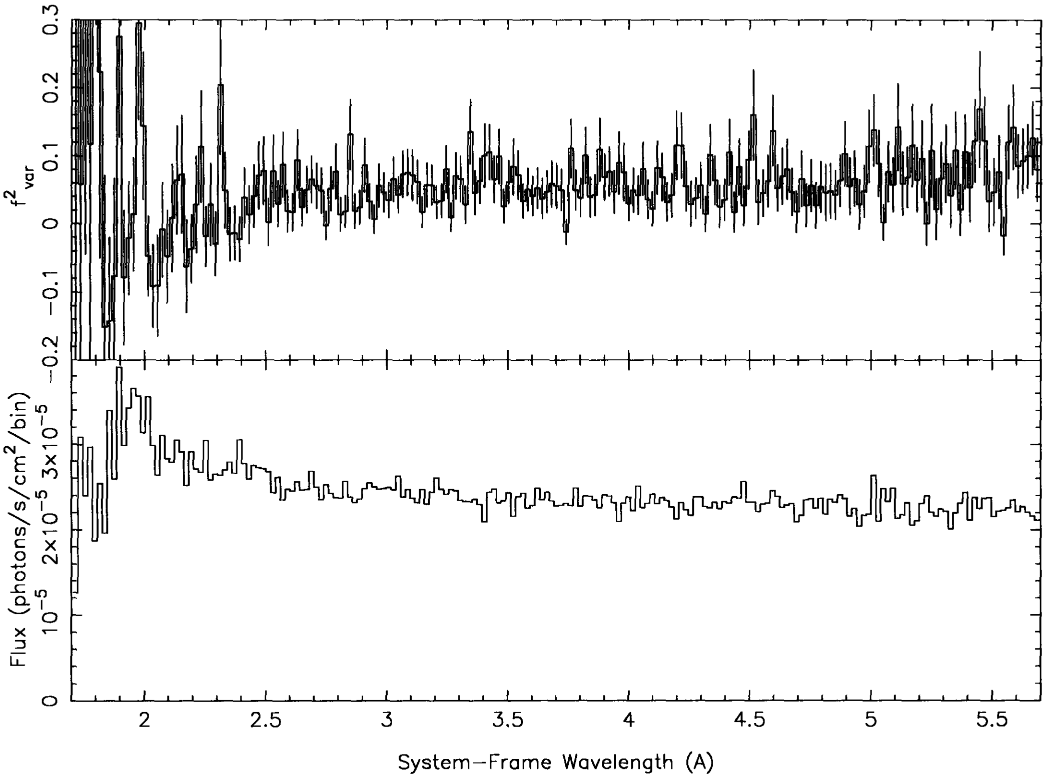

Figure 6-4: The top panel shows the NEV f^2_{var} calculated for MCG -6-30-15 as in Equation (6.3). Here we have used $\Delta t = 10$ ks and $\Delta\lambda = 0.02$ Å. Only the first three 2004 observations are included in the calculation, as the fourth is too short. The bottom panel shows the MEG flux in the same wavelength range.

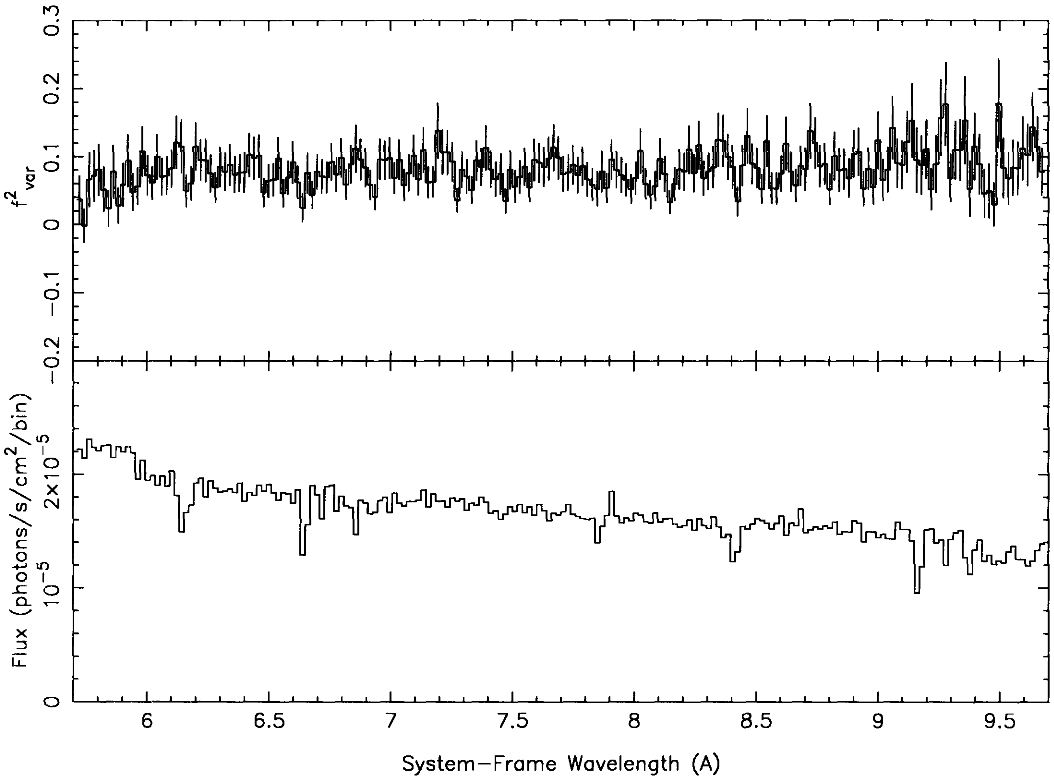

Figure 6-5: Same as Figure 6-4, but for a different wavelength range.

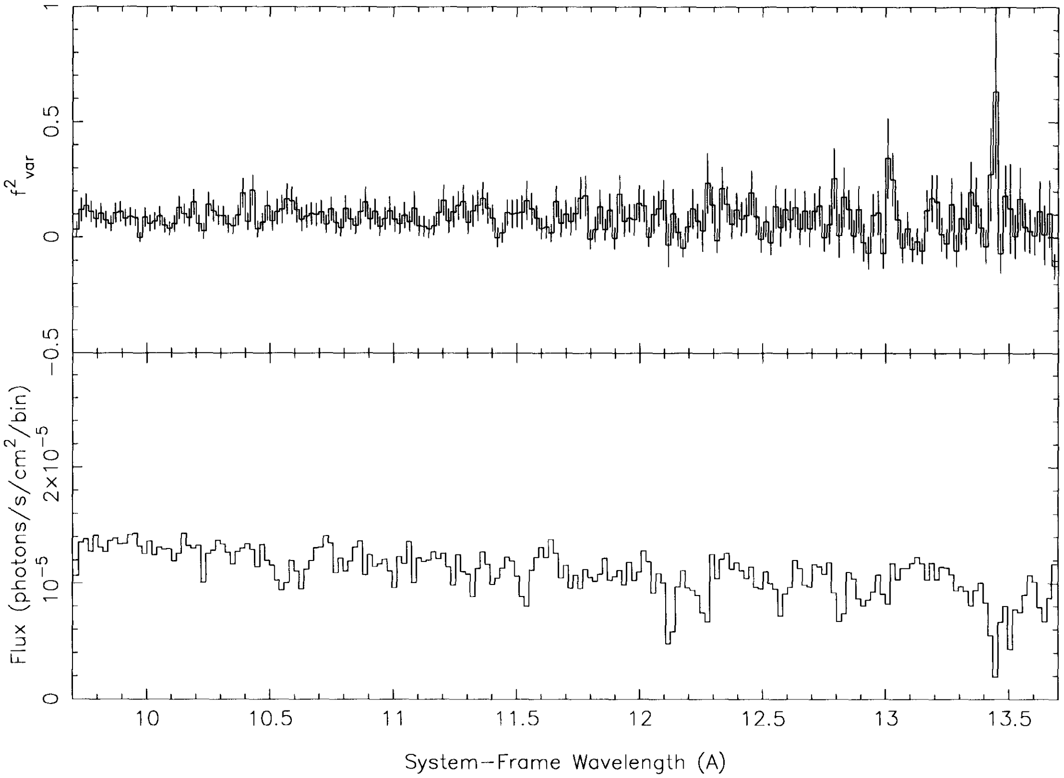

Figure 6-6: Same as Figure 6-4, but for a different wavelength range.

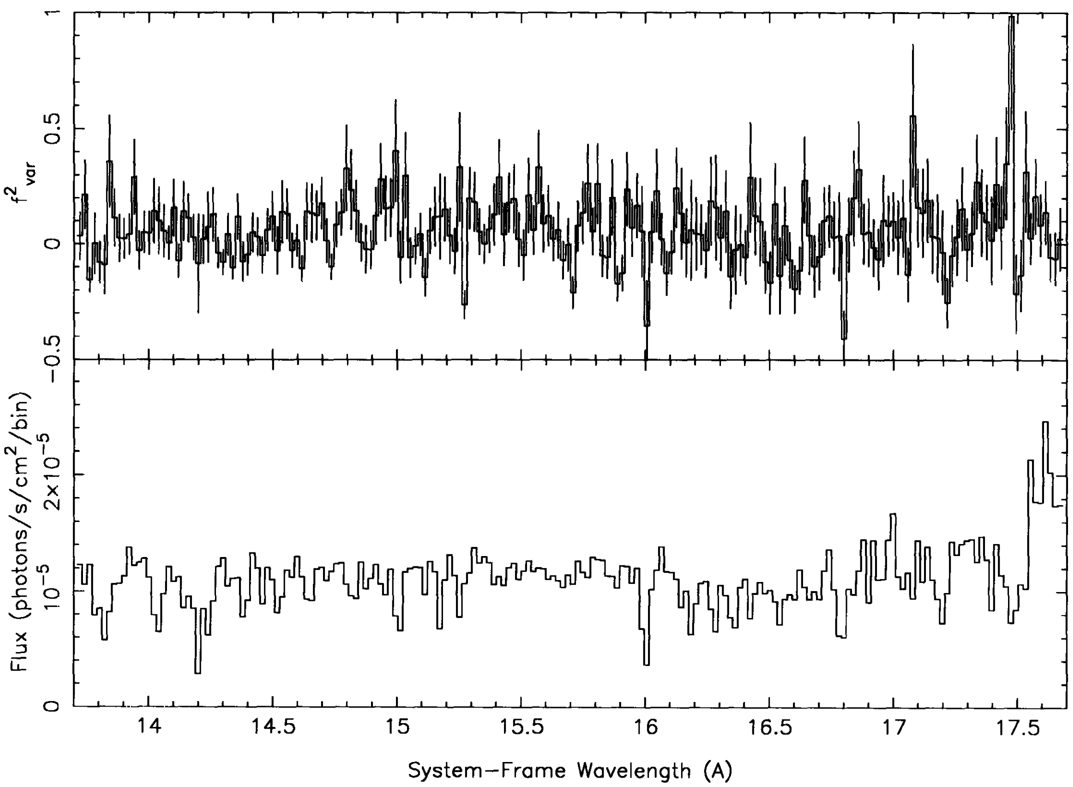

Figure 6-7: Same as Figure 6-4, but for a different wavelength range.

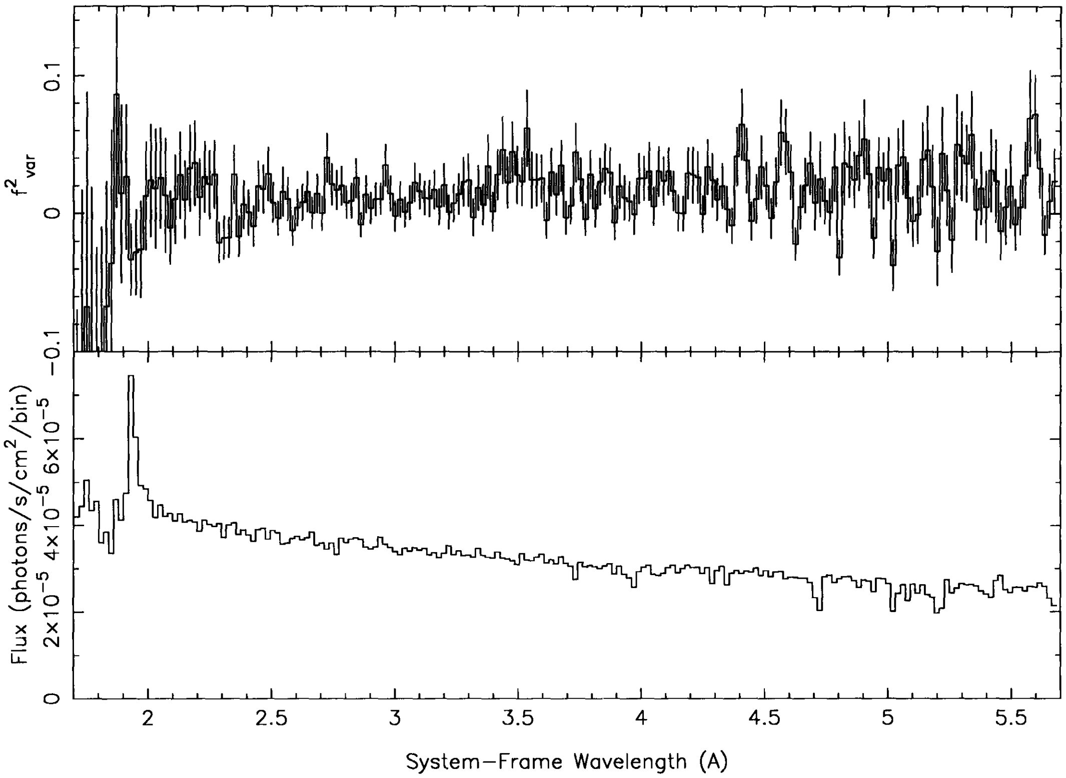

Figure 6-8: The top panel shows the NEV f^2_{var} calculated for NGC 3783 as in Equation (6.3). Here we have used $\Delta t = 10$ ks and $\Delta\lambda = 0.02$ Å. Only the 2001 observations are included in the calculation, as the 2000 observation is too short. The bottom panel shows the MEG flux in the same wavelength range.

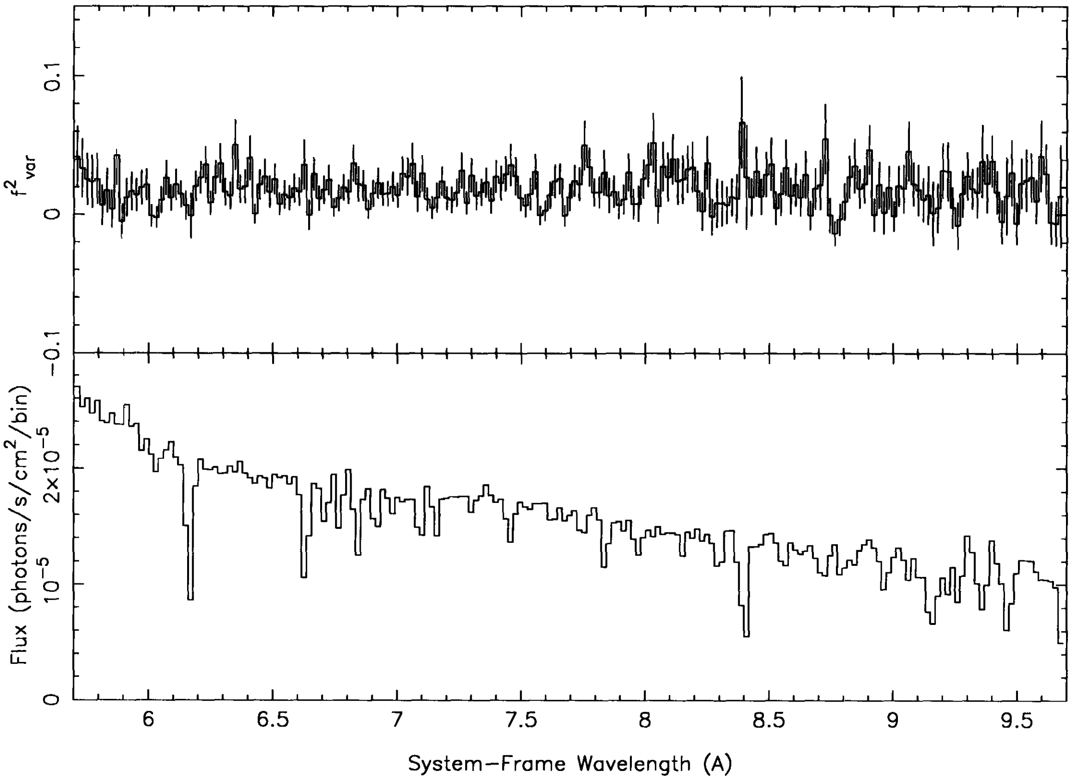

Figure 6-9: Same as Figure 6-8, but for a different wavelength range.

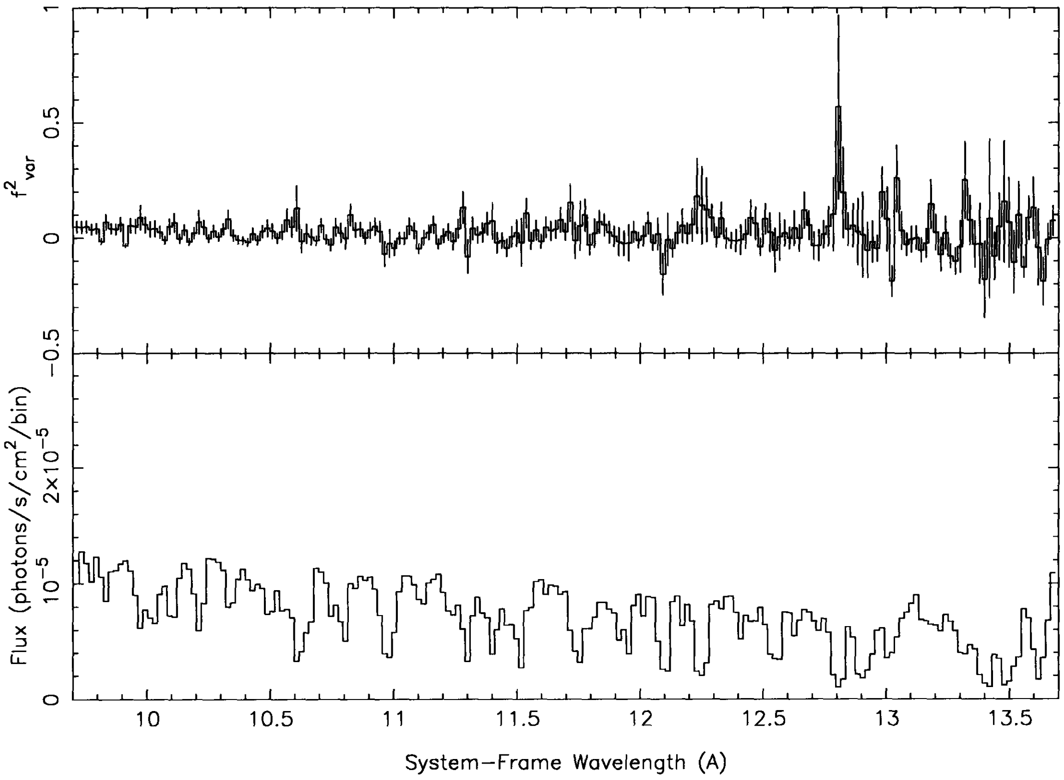

Figure 6-10: Same as Figure 6-8, but for a different wavelength range.

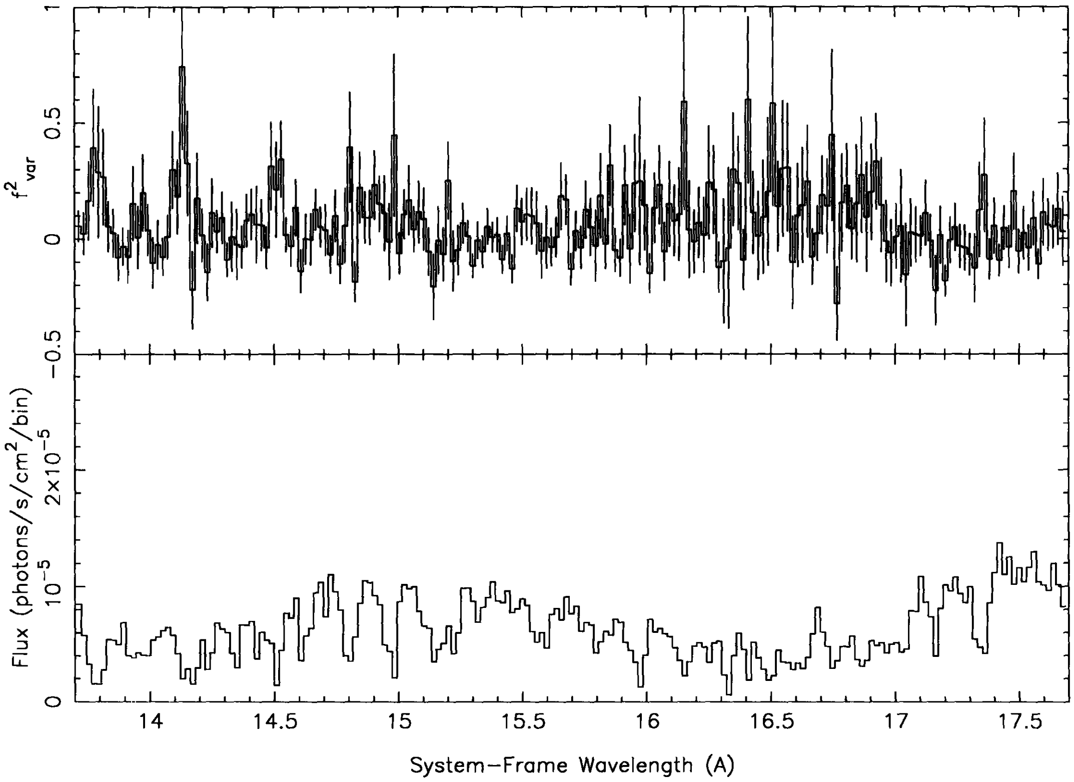

Figure 6-11: Same as Figure 6-8, but for a different wavelength range.

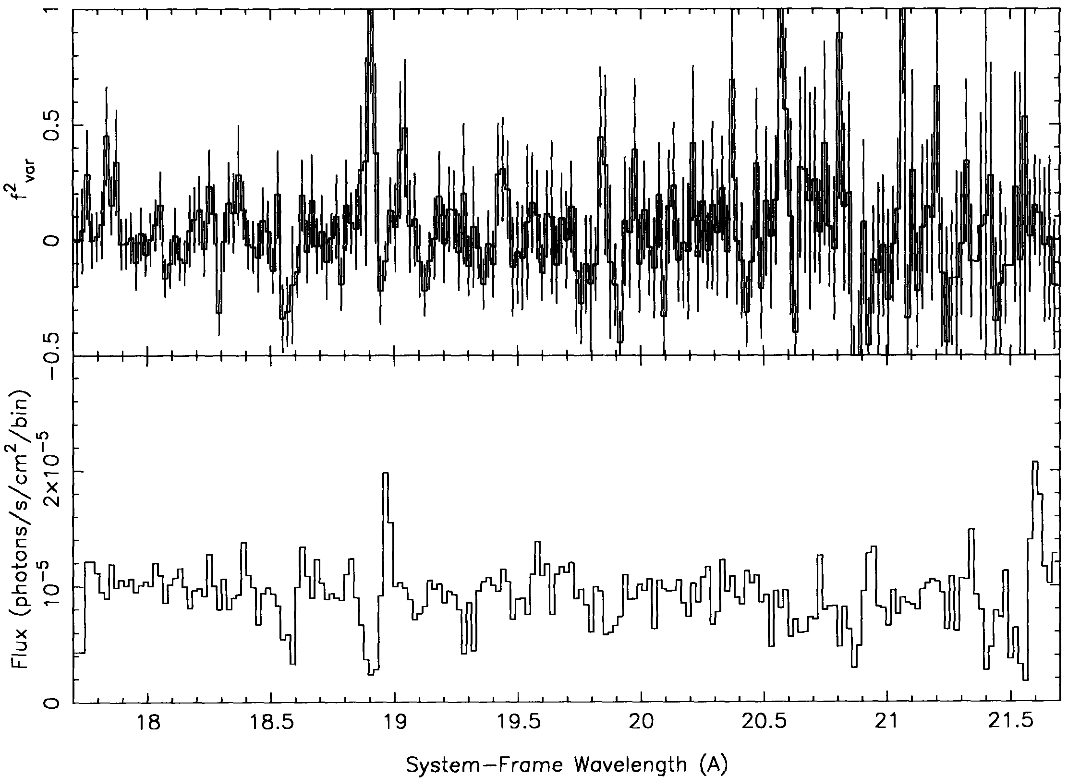

Figure 6-12: Same as Figure 6-8, but for a different wavelength range.

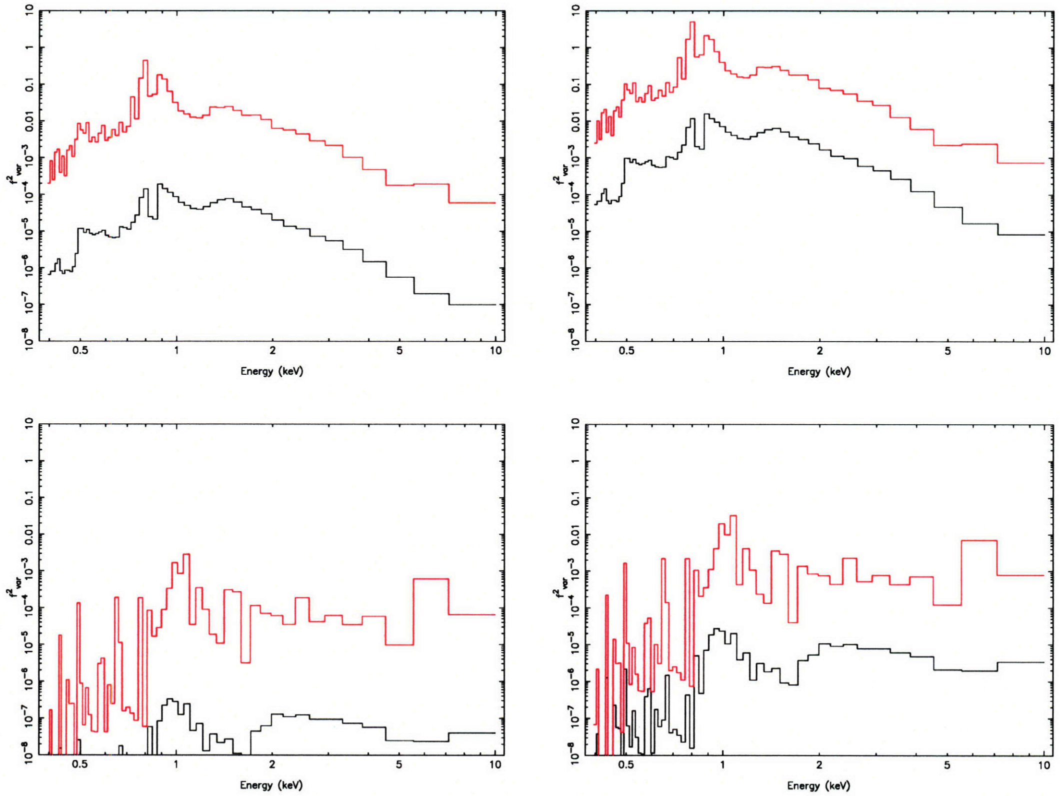

Figure 6-13: Sample NEV spectra for the model described in §6.2.2. In this figure, we compare the effects of varying the column density at a fixed ionization level. For each panel, we give the model parameters as ($\log_{10}(\overline{N_H})$, $\log_{10}(\sigma_{N_H})$, $\overline{\log_{10}(\xi)}$, $\sigma_{\log_{10}(\xi)}$). The model parameters are: top left black (23, 20, 2, 0); top left red (22, 20, 2, 0), top right black (23, 21, 2, 0), top right red (22, 21, 2, 0), bottom left black (23, 20, 3, 0), bottom left red (22, 20, 3, 0), bottom right black (23, 21, 3, 0), bottom right red (22, 21, 3, 0).

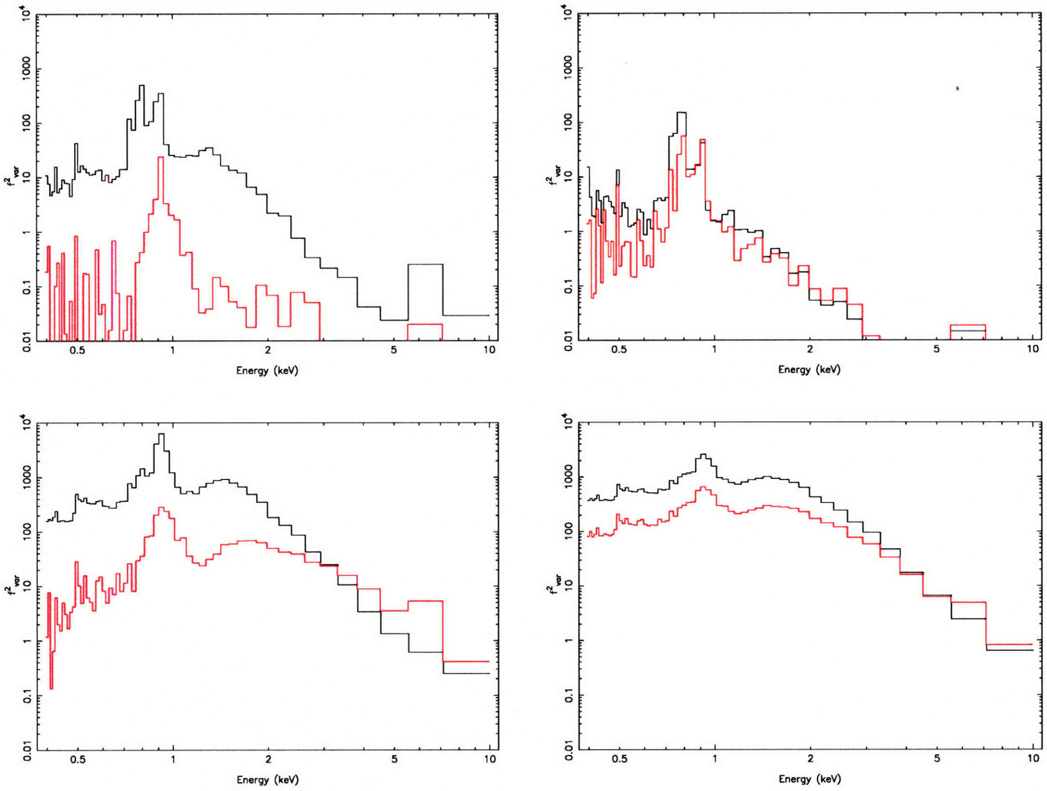

Figure 6-14: Sample NEV spectra for the model described in §6.2.2. In this figure, we compare the effects of varying the ionization level at a fixed column density. For each panel, we give the model parameters as $(\log_{10}(\overline{N_H}), \log_{10}(\sigma_{N_H}), \overline{\log_{10}(\xi)}, \sigma_{\log_{10}(\xi)})$. The model parameters are: top left black (22, 0, 2, 0.5); top left red (21, 0, 3, 0.5), top right black (21, 0, 2, 1), top right red (21, 0, 3, 1), bottom left black (23, 0, 2, 0.5), bottom left red (23, 0, 3, 0.5), bottom right black (23, 0, 2, 1), bottom right red (23, 0, 3, 1).

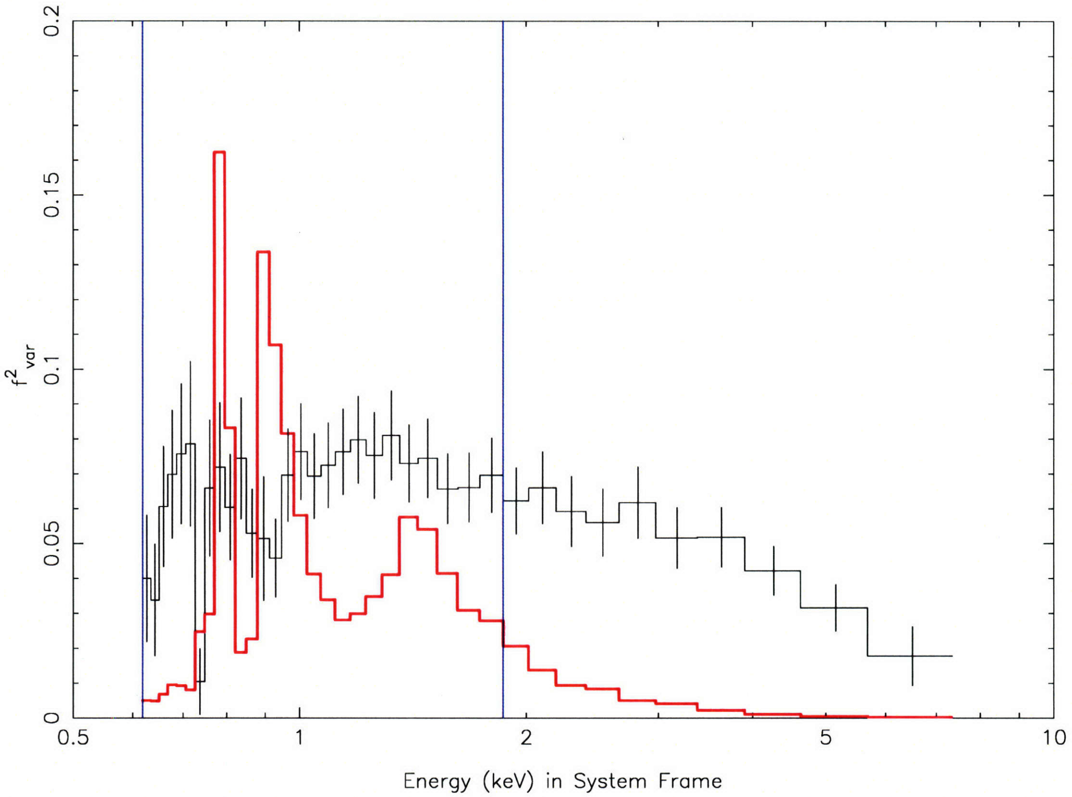

Figure 6-15: The NEV of MCG -6-30-15 is shown black. The green histogram shows the best model fit for an ionized absorber with Gaussian variations in column density and ionization. This fit is visually inadequate and is formally rejected by the χ^2 statistic. The model and best parameters are described in §6.2.2.

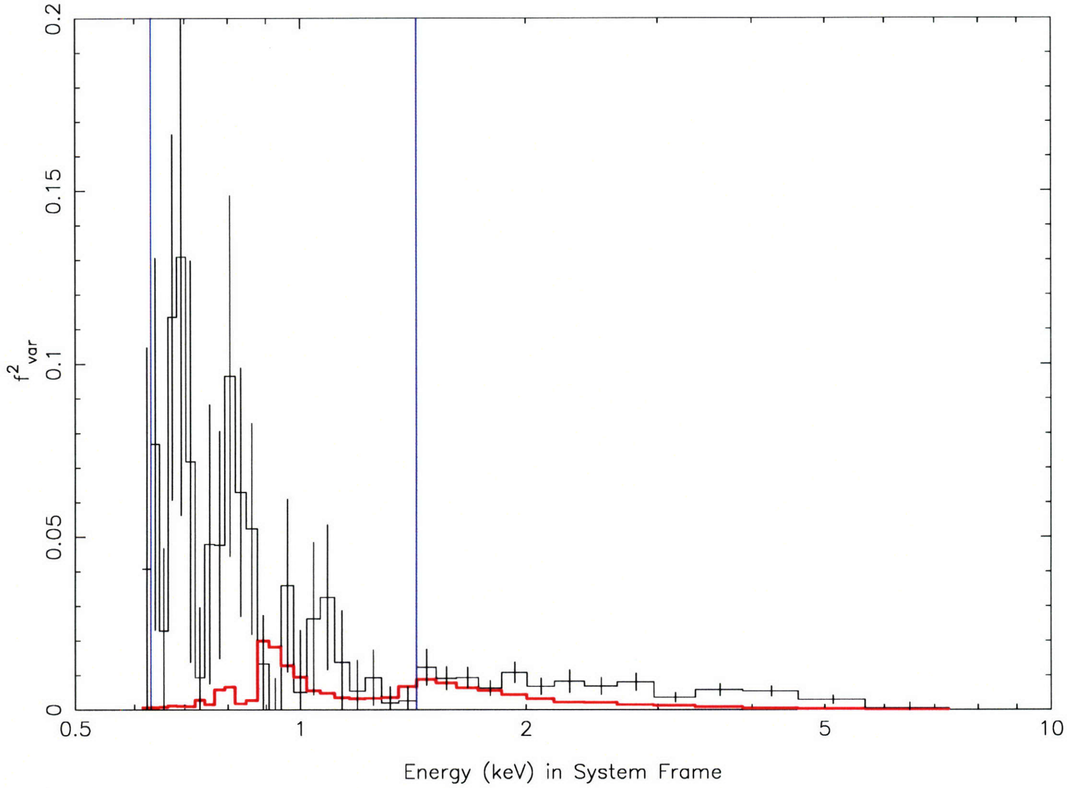

Figure 6-16: The NEV of NGC 4151 is shown black. The red histogram shows the best model fit for an ionized absorber with Gaussian variations in column density and ionization. The model and best parameters are described in §6.2.2.

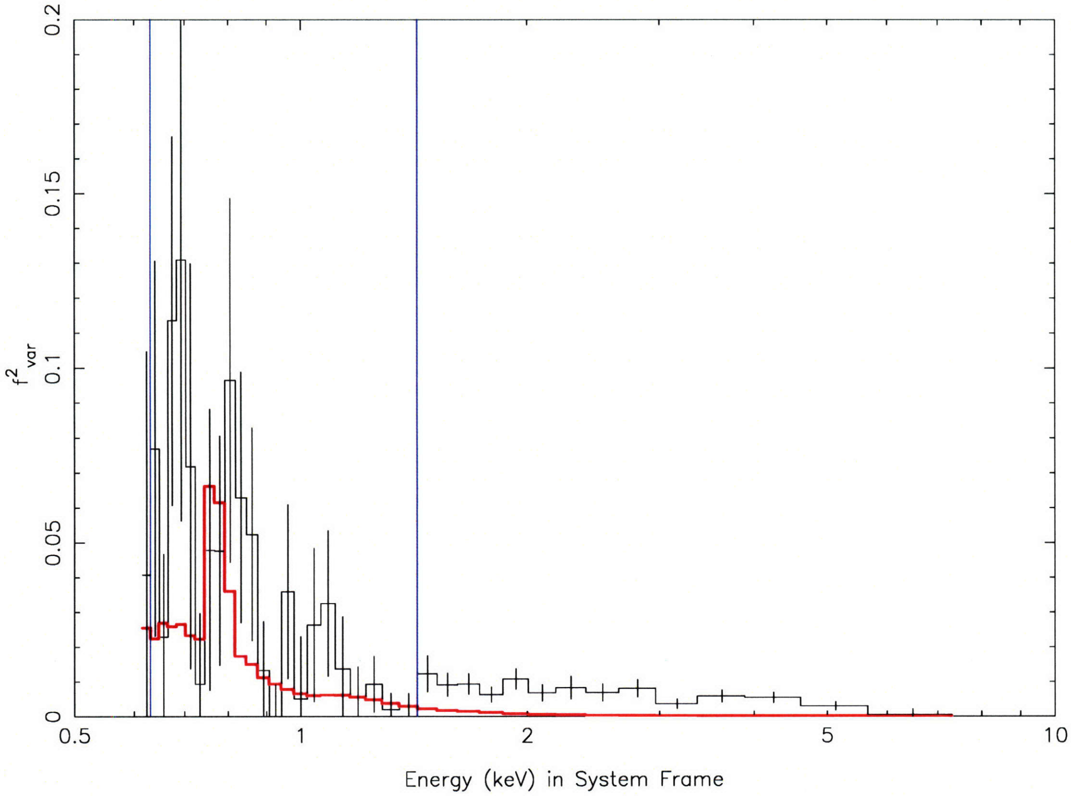

Figure 6-17: Similar to Figure 6-16, but showing the best model fit only on the energy range 0.5-1.5 keV. The fit shown is formally acceptable.

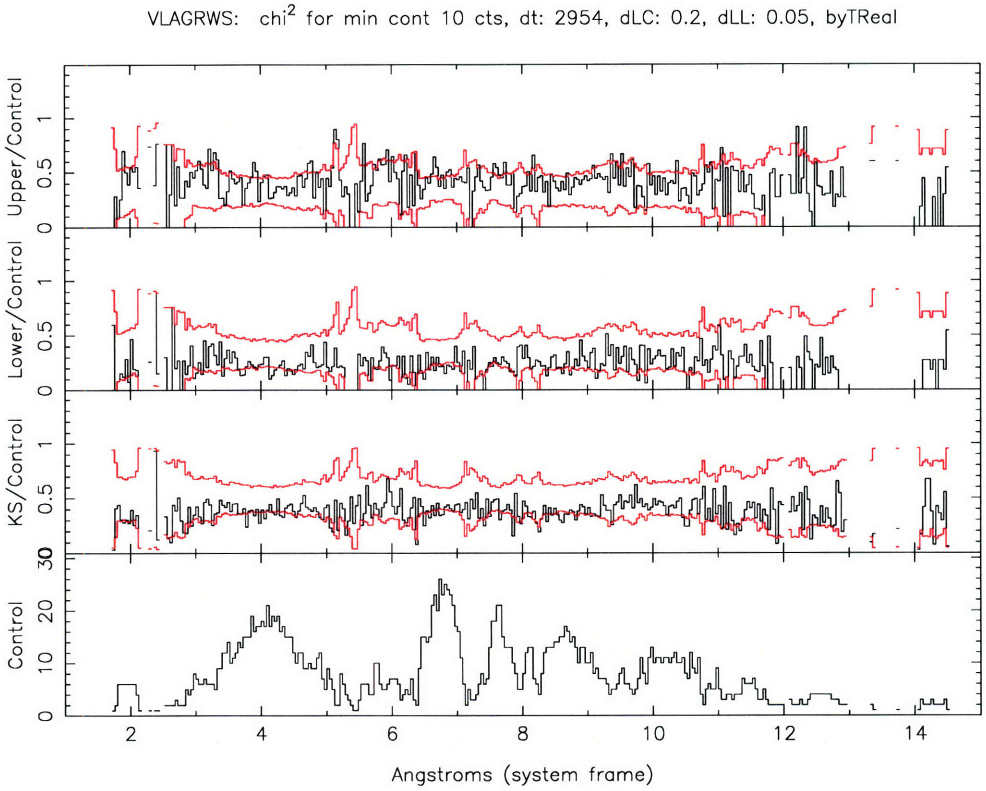

Figure 6-18: Summed probabilities of variation according to Tests 1, 2, and 3 (described in §6.3.1), which look for excess variability in the upper tail, lower tail, and KS statistic applied to the (assumed uniform) distribution of Poisson probabilities which measure variability about the expected count rate. The top 3 panels show the results for Tests 1, 2, and 3, divided by a control spectrum. The bottom panel shows the control spectrum. In this case, all probabilities from the 3 tests were considered. The histogram in red shows the 90% confidence limits for our test that variation is occuring. The spectral segments were ordered by 2-10 keV luminosity.

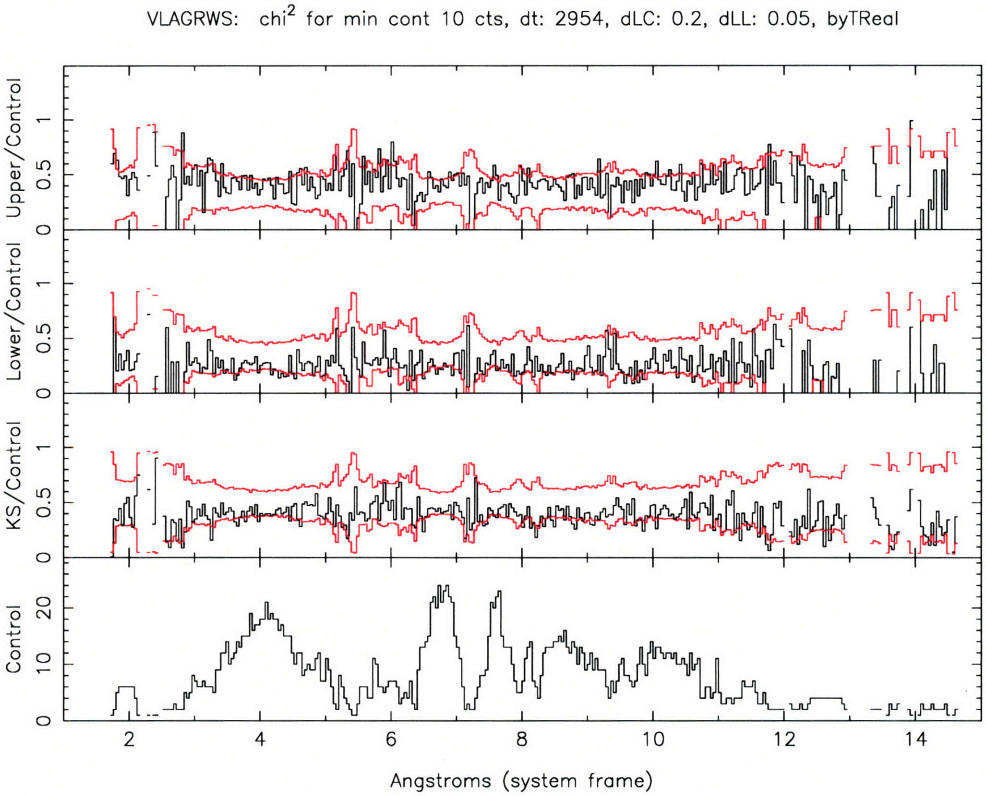

Figure 6-19: Integrated probabilities of variation according to Tests 1, 2, and 3 (described in §6.3.1), which look for excess variability in the upper tail, lower tail, and KS statistic applied to the (assumed uniform) distribution of Poisson probabilities which measure variability about the expected count rate. The top 3 panels show the results for Tests 1, 2, and 3, divided by a control spectrum. The bottom panel shows the control spectrum. In this case, all probabilities from the 3 tests were considered. The histogram in red shows the 90% confidence limits for our test that variation is occuring. The spectral segments were ordered by time.

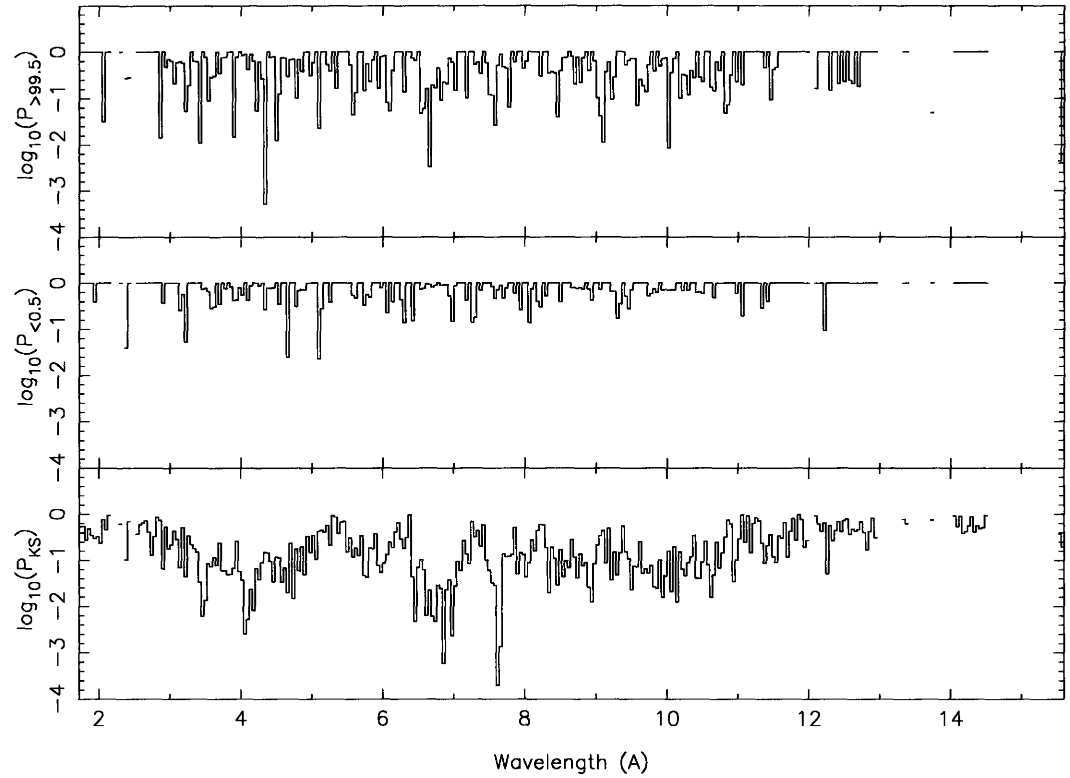

Figure 6-20: Results of Tests 1, 2, and 3 applied to the set of all Poisson probabilities at a given (rest frame) wavelength for all AGN combined. In this case, the Poisson probabilities were determined from luminosity-ordered spectral slices. Low values on the y axis roughly correspond to low probabilities of greater deviation from uniformity. For a detailed discussion, see §6.3.3.

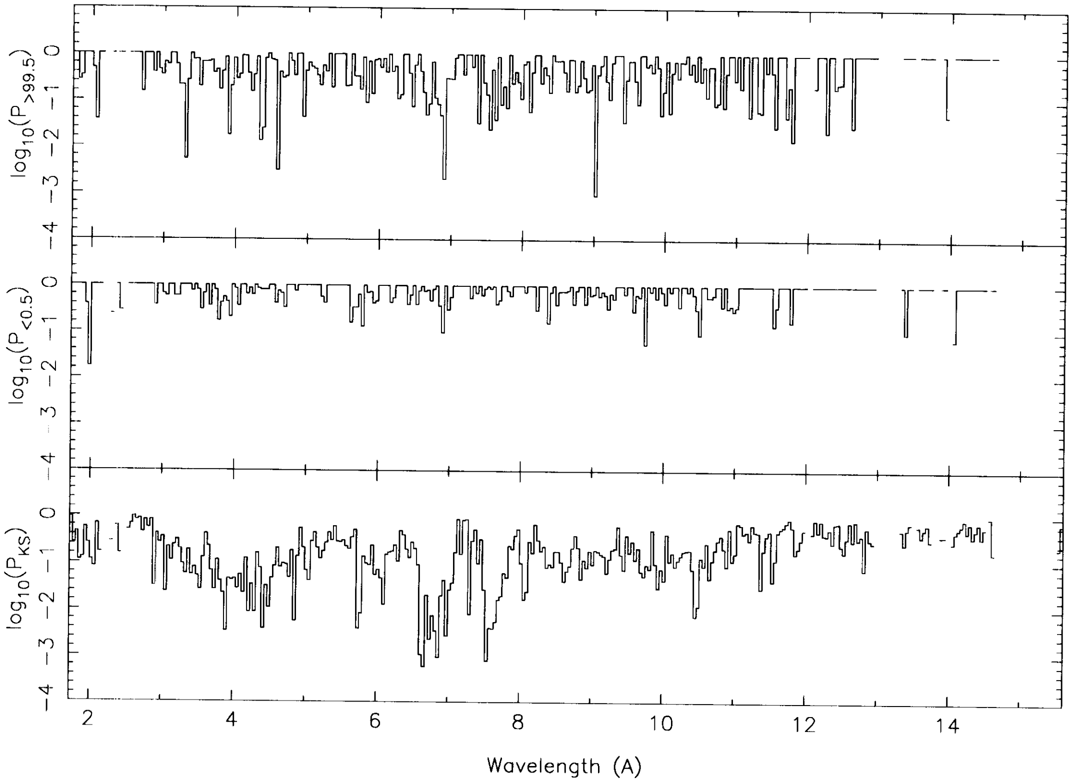

Figure 6-21: Same as Figure 6-20, but for time-ordered spectral slices.

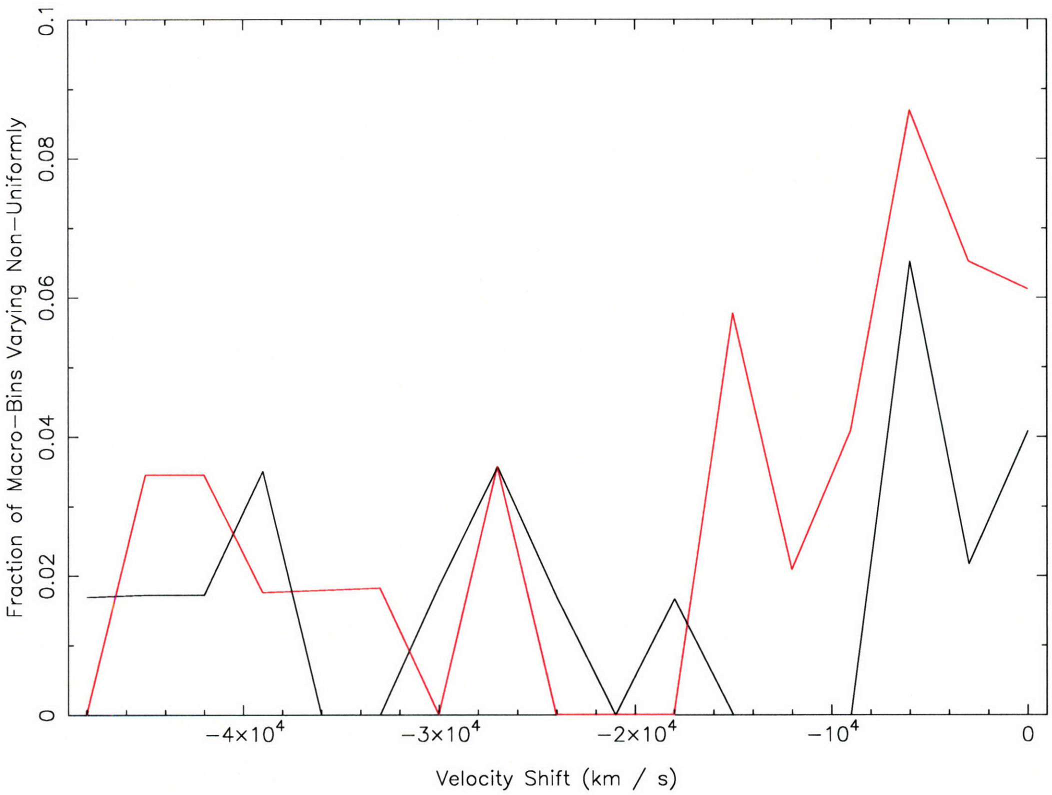

Figure 6-22: Results of Tests 1 and 3 applied to the cumulative Poisson probabilities in macro-bins corresponding to blueshifted strong absorption line candidates. The Poisson probabilities were calculated from luminosity-ordered spectral slices. The test results are plotted as a function of the blueshift. The results of Test 1 are plotted in black, and Test 3 results are in red.

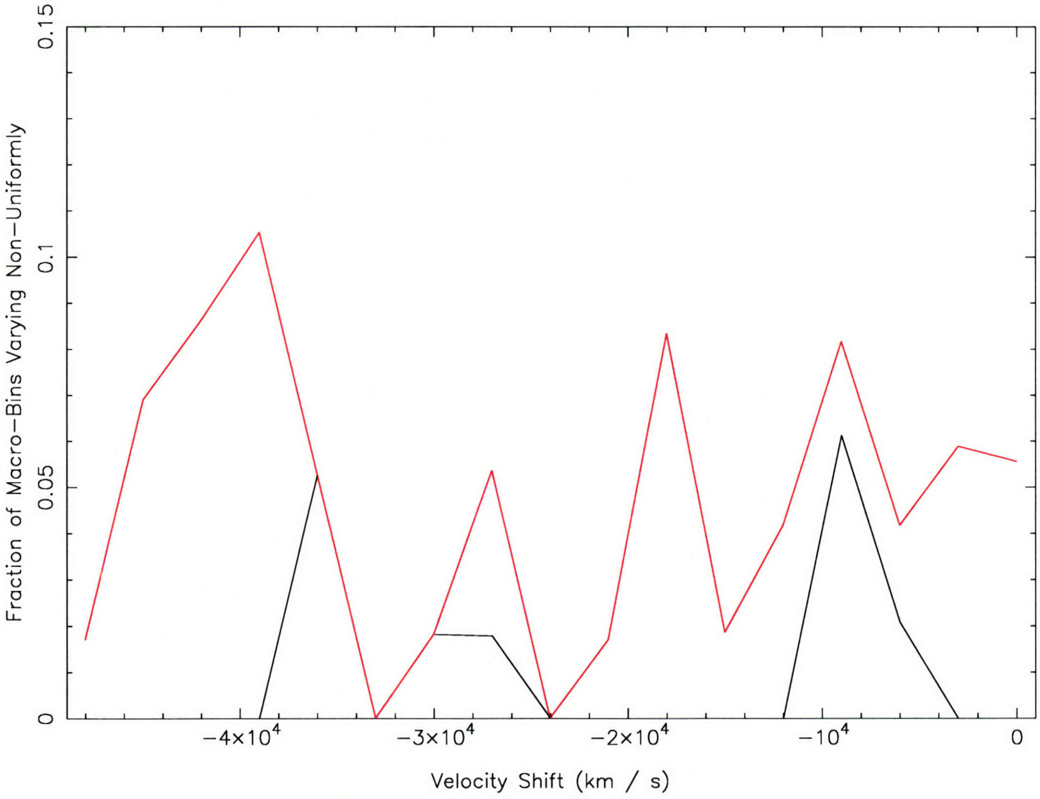

Figure 6-23: Same as Figure 6-22, but the Poisson probabilities were calculated for time-ordered spectral slices.

Chapter 7

Conclusions

In this chapter, we summarize the conclusions drawn from previous chapters of this thesis and comment on their implications for future observations and modeling of Active Galactic Nuclei (AGN) X-ray warm absorbers (WAs).

7.1 Study of MR 2251-178

MR 2251-178 is a well-studied AGN which is variable in many respects. The continuum shape has been observed to change over time, the power law spectrum has hardened and softened, and flux levels have risen and fallen. The absorbing column is assumed to vary based on continuum fits, although these fits were performed assuming a fixed power law spectral index. The power law index in fact varies, which may result in erroneous estimates of the absorber column and density.

Recent high-resolution observations with *XMM-Newton* and *Chandra* have shown that lines are also varying in the spectrum. Kaspi et al. (2004) detected tens of lines in the 2002 *XMM-Newton* spectrum which we did not detect in the HETG observation taken 4 months later (Gibson et al. 2005). A preliminary look at the unpublished LETG observation taken 3 months after the HETG observation shows that the lines have evolved again, with weaker forbidden emission and no absorption in the FeXVII line we associated with a highly-ionized, high-velocity outflow (HIHVO).

The continuum of MR 2251-178 varied among the *XMM-Newton*, HETG, and LETG observations. During the HETG observation, the continuum was unusually hard and absorbed by a relatively low column. We fit the continuum with a power law, ionized absorption, and a soft excess, but still found unacceptable residuals around 1 keV that we could not explain (Gibson et al. 2005).

The WA material in MR 2251-178, presumably responsible for absorbing the X-ray spectrum and producing the (forbidden) emission lines, has a complex geometric structure. We showed that it cannot be shaped like a section of a spherical shell, and that it was (in September, 2002) relatively thin along our line of sight. Previous studies have suggested that absorber clouds may be moving across our line of sight on time scales of a few months (Kaspi et al. 2004).

The HIHVO apparently carries a large amount of mass and energy out of the nucleus (compared to the nuclear accretion rate), unless it is very small in angular extent or very short-lived. Assuming we correctly identify the absorption features for FeXVII and SiXIV as part of the HIHVO, the outflow contains a range of ionization zones and velocity components. The FeXVII and SiXIV components both flow outward at about $-17,000$ km s^{-1}, while the FeXXVI component flows outward at about $-13,000$ km s^{-1}.

The HIHVO was not detected in the *XMM-Newton* observation, though Kaspi et al. (2004) did note an absorption feature they ascribed to FeXXVI nearly *at rest*. Our preliminary look at the LETG data found no HIHVO absorption in the FeXVII feature near 15 Å. The LETG is not sensitive enough at high energies to search for the FeXXVI feature. Forbidden emission lines in the soft X-rays were also weaker than in the HETG spectrum. The soft X-ray continuum was brighter in the LETG observation, raising the possibility that the absorption and emission features have been covered by a soft continuum component that was not as strong in the HETG observation. It is also possible that the HIHVO disappeared a few months after the HETG observation. It may have moved off the line of sight or it may have been ionized to undetectable levels.

7.2 Study of MCG -6-30-15

MCG -6-30-15 is a well-studied nearby AGN with a continuum known to vary on short (1 ks) time scales. The absorber is known to be complex, with multiple ionization levels and velocity components (e.g., Lee et al. 2001; Sako et al. 2003; Turner et al. 2003). A study of a 320 ks *XMM-Newton* observation found evidence that 4 lines (out of about 50 detected) varied between high and low spectral states (Turner et al. 2004).

Our variability analysis of $1s - 2p$ lines of He- and H-like ions in the 520 ks HETG observation of MCG -6-30-15 found that lines are indeed varying (Gibson et al. 2006). As a function of time, we found significant anti-correlations between equivalent widths (EWs) of He- and H-like ions, and a correlation between the He-like ions NeIX and SiXIII. The anticorrelations rule out scenarios which rely on simply adding material along the line of sight, such as intervening clouds. Photoionization models would actually predict that, if ionization changes alone were responsible for the variation, the He-like ion SiXIII would be correlated, rather than anti-correlated, with MgXI. This may indicate that the absorber is not in photoionization equilibrium, which would mean that the ubiquitous use of photoionization models to analyze WAs is inappropriate. Another possible explanation is that the different absorption lines arise in different sections of the absorber along the line of sight, each at a different ionization level. This would require some mechanism to alter the absorber properties in a correlated way. For example, patches of absorber with different densities would have different ionization levels and could vary by the influence of the photoionizing continuum.

We also found that at least one line is varying in strength (EW) as a function of luminosity. A fit with a naïve photoionization model found that ionization variation due to luminosity alone was not sufficient to explain the line variation. Combined with the anticorrelations observed between lines over time, this means that the WA variation is a complex phenomenon. We ruled out several possible explanations that could individually cause variability, including: changes in absorber position, density, ionization due to continuum shape and level; multiple continuum components with different levels of absorption; cloud motion across the line of sight; and changes in the absorber velocity dispersion. We also considered unlikely variation due to changes in the ultraviolet (UV) continuum and the influence of varying underlying emission lines. The variability could be a complex combination of these effects, or we suggest it could be due to structure in the absorber. We may be looking through different patches of the absorber (arranged perpendicularly to the line of sight) at different times, particularly if the continuum source is moving around behind the absorber. The continuum source is not expected to move more than a few tens of gravitational radii in at least some models (e.g., Miniutti and Fabian 2004), so this would suggest that the WA has structure on similar scales.

7.3 Survey of HETG Spectra of AGN

In Chapter 6, we searched for and attempted to characterize variability in a sample of archived HETG AGN spectra which have a sufficently high signal-to-noise. We constructed normalized excess variance (NEV) spectra for each of the AGN in our sample and attempted to fit two of the spectra with a simple model of a varying absorber. In the second part of this study, we searched the HETG spectra of each AGN in an attempt to detect variations across the entire spectrum which were in excess of that expected during the measurement process.

We calculated NEV spectra to characterize short term ($\Delta t = 5$ ks) variations in broad $\Delta\lambda = 0.5$ Å wavelength ranges. We found that all the AGN had excess variance in their spectra. The NEV spectra came in different shapes, with some showing stronger variation at longer wavelengths, while others showed a rising trend of variation in the hard (> 2 keV) X-rays. For the two AGN with the longest exposure, NGC 3783 and MCG -6-30-15, we constructed NEV spectra at higher resolution and did not find evidence for NEV structure in line absorption or emission regions.

The NEV spectra generally show continuum variation out to hard X-ray energies well above the region (< 2 keV) which we would expect to be influenced by the WA. This indicates that other processes besides absorber variation are driving the short term, broadband variability. We fit a model of absorber variation to the NEV spectra of MCG -6-30-15 and NGC 4151 at lower energies (< 2 keV), but were not able to find an acceptable fit. Restricting the fit region to 0.5 to 1.5 keV did give an acceptable fit to the NGC 4151 NEV spectrum. Given that we observe strong variations above 2 keV, and given that other studies have had some success fitting a two-component continuum model (e.g., Vaughan and Fabian 2004), it seems most likely that continuum emission variation is significant (and perhaps even dominant) across the X-ray spectrum.

This does not rule out the possibility that absorber variability is responsible for significant continuum variation on short time scales. It may be possible to detect absorber variation by looking in narrow wavelength ranges, comparable to the FWHM of the instrument. We devised a test to search through AGN spectra for non-Poissonian variation. We did not find evidence of variation in individual AGN, but we did find significant variation when the probabilities for all AGN were combined at each wavelength. The variation consisted of an excess of wavelength bins in time slices with an unexpectedly low number of counts over a narrow wavelength range, possibly due to varying absorption. We found no excess of bins with unexpectedly high numbers of counts. In all our tests, the SiXIII $1s-2p$ line was strongly indicated as a variation candidate, and we recommend that future studies pay particular attention to this line.

7.4 Conclusions and Future Study

This thesis has shown that WA variation can be detected on measurable time scales as short as a few tens of ks. Before we discuss the physical implications of our results, we will briefly consider the implications of our study for current and future X-ray spectroscopy.

Only with high-resolution X-ray missions (*Chandra* and *XMM-Newton*) in the last several years has it become possible to directly measure absorption lines from a WA. Previously, researchers made physical claims about WAs based on broader spectral features, such as edges (e.g., Otani et al. 1996) or the soft X-ray continuum (e.g., Kaspi et al. 2004; Halpern 1984). Recent studies have shown that edge structures can actually be more complex (e.g., Lee et al. 2001; Turner et al. 2003; Kallman et al. 2004) than previous models considered. Fits of continuum models of WAs can experience a large amount of degeneracy. They can be complicated by ambiguity over the number of absorbing systems presenct and uncertainty about the shape of the underlying continuum, among other factors.

While many claims based on broad-band spectral features may be correct, the most accurate measurements of absorber properties will be obtained from spectral lines, which have a much larger optical depth than edges and can usually be unambiguously identified. Earlier tests for line variability had shown mixed results. Some evidence indicated that lines in MCG -6-30-15 could vary on observable time scales (Turner et al. 2004), while a study of NGC 3783 found no evidence for variation in individual lines (Netzer et al. 2003).

In this thesis, we have developed and implemented several tests for line variability, again with mixed results. We detected line variability in MCG -6-30-15. Our continuum fits to MR 2251-178 also indicated an unusually low absorbing column, and we detected a HIHVO which may be transient. Interestingly, MR 2251-178 and MCG -6-30-15 are sources for which previous absorber variability has been detected (Halpern 1984; Turner et al. 2004). They are also known to have highly variable continua.

Our survey for line variability presented in Chapter 6 gives evidence that narrow-band variability is occuring in the spectra of AGN generally. The variability primarily consists of unexpectedly low counts at times in a narrow wavelength range. This could be due to enhanced absorption. We did not see variation in the other direction, with an unexpectedly high number of counts possibly attributable to varying emission processes.

Our test did not detect variation in individual AGN. Future work will concentrate on improving the testing methodology. For example, if we know there are absorption lines in the time-integrated spectrum, we can limit our search to those regions in hopes of finding more significant results. A test like this was successful in the case of MCG -6-30-15 (Gibson et al. 2006). We also need to develop and/or apply stronger statistical tests (e.g., for non-uniformity), which will enhance our ability to detect variation. (See also the methods which were not powerful enough to detect variability presented in the Appendix to Chapter 5.)

Further high-resolution spectroscopy is required to test for absorber variability. Our archive sample is limited by the amount of exposure time granted to observers. For bright AGN, this can be quite short, so that we cannot get a get good look at absorber lines. We recommend that more emphasis be placed on obtaining longer exposures of spectra of bright AGN with known WAs. Repeat observations of these AGN would allow tests of variability on multi-year time scales.

In has become clear in the course of our study that a better understanding of continuum emission processes is essential to further analyses of absorber variability. We have several comments on this subject.

1. Previous studies of absorber variability have depended on assumptions about the underlying X-ray continuum (such as a constant power law photon index) which have been shown in recent studies to be incomplete or inaccurate.

2. The NEV spectra presented in Chapter 6 demonstrate that short-term, broad-band

variations are ubiquitous in AGN, and are likely due at least in part to continuum variation.

3. WA variation has frequently been attributed to ionization changes caused by variation of the ionizing continuum. We have shown that line variation in MCG -6-30-15 cannot be simply attributed to changes in the ionizing luminosity (Gibson et al. 2006). We know how a hypothetical ionizing continuum should affect the absorber. If we better understood the continuum (in both X-rays and the UV), it would enable us to place stronger constraints on the processes influencing the WA.

4. The soft X-ray continuum may be composed in part of broad emission lines (e.g., Crummy et al. 2006). If these emission lines are varying appreciably, they could influence tests for absorption line variability.

There are several implications of the studies presented in this thesis for models of WA and AGN in general.

7.4.1 Complex Geometry of the Absorber/Emitter

Our study of MR 2251-178 showed that the material responsible for emitting and absorbing X-ray lines is not structured as a section of a spherical shell. This calculation was based on the fact that we saw a large amount of line emission compared to absorption from the same ion. This could be due to emission from material distributed (non-spherically) around the nucleus, or it may be that there are thin patches in the absorbing material along our line of sight.

The disk wind model of Elvis (2000) allows for X-ray line emission from regions further down the flow than the cylindrical launching region where the WA is located. This could enhance line emission compared to absorption along the line of sight. However, these flow regions have large velocity dispersions, as they are responsible for the broad emission lines in AGN. The forbidden lines in MR 2251-178 are rather narrow (e.g., 700 km s^{-1} for NeIX, 1700 km s^{-1} for OVII) compared to the high-ionization UV line widths of 5000 km s^{-1} or more (Leighly and Moore 2004) the wind is supposed to produce. More modeling is needed to explain what regions of the disk wind would be expected to emit in X-rays, and what physical processes could influence these regions. If the broad emission line regions of the flow emit in X-rays, they would also absorb X-ray lines, and we would therefore expect to see along some lines of sight broad absorption lines outflowing at high speeds. In fact, in MR 2251-178, we did see a high-velocity outflow with at least one line having a FWHM of about 7800 km s^{-1}. However, this line was extremely highly ionized, which makes it difficult to understand how it could co-exist with ions at lower ionization levels in that region of the wind. We also detected other components of the high-velocity outflow which had much smaller line widths.

In the second case, it may be that a hole has opened up in the region of the flow we are looking through. Elvis (2003) suggests that a thin wind may be launched from the accretion disk as a line-driven wind. If we are seeing a hole in the wind, then the launching mechanism must be erratic, or the structure of the wind is changing rapidly. If the wind is launched at 10,000 km s^{-1} from 1000 gravitational radii for a supermassive black hole (SMBH) with mass 10^7 $M_\odot$, it would take about 2-3 weeks for a parcel of material to travel through the region associated with the WA. This is not very different from the few month time scale for absorber variation proposed by Kaspi et al. (2004). More modeling of disk winds is certainly needed in order to understand what types of winds may be launched. If variable obscuration can be associated with clumpiness in the launched wind, WA variability could be an important probe of the accretion disk processes launching the wind.

Unlike the disk wind model, the evaporating torus WA model does not try to explain a large number of diverse effects as due to geometry. As a result, geometric constraints on the WA do not have as much impact on the torus model. The absorbing and emitting material may be distributed around the nucleus. There may be an excess of forbidden line emission produced by the accretion disk, which has no immediate relation to the WA outflow in this model. Covering 50% of the solid angle (Reynolds 1997; George et al. 1998) at parsec-scale distances requires a large (parsec-scale) absorber. The absorber may be patchy, but these patches would be small compared to the estimated absorber size in order to cross the line of sight in a few months.

7.4.2 Density Constraints

We detected variation in absorption lines in the spectrum of MCG -6-30-15 that anti-correlated between He- and H-like ions and correlated between two He-like ions. If these variations are due to ionization level changes in the WA, then ionization time scales suggest that the WA must have a particle number density $n \geq 10^6$ cm^{-3}.

A density this high could be problematic for the torus evaporation model. A typical column density of about 10^{22} cm^{-2} requires a WA thickness $\Delta r \sim N_H/n < 10^{16}$, which means that the WA would be much thinner than the parsec-scale extent of the inner edge of the torus. It is difficult to imagine how the WA could cover a large fraction of the sky in the form of such a thin sheet.

Based on their sample of Seyfert 2 nuclei, Risaliti et al. (2002) infer that $n = 10^6$ cm^{-3} is an upper limit for the torus density. Therefore, the WA would actually be denser than the torus it evaporates from, which is unrealistic. Any absorption variation attributed to spherical clouds moving at Keplerian speeds would require densities a few orders of magnitude higher than $n = 10^6$ cm^{-3}, as pointed out by Risaliti et al. (2002). Of course, we do not expect the variation in MCG -6-30-15 to be caused primarily by intervening clouds, as these would not produce anti-correlations in absorption line strengths.

In the disk wind case, a WA at 1000 gravitational radii from a 10^7 M$_\odot$ SMBH (about 1.5×10^{15} cm) would have to be about $r = N_H/n < 10^{16}$ cm thick in order to have a column density of 10^{22} cm^{-2}. The density lower limit is not a strong constraint on the disk wind model.

It is not certain that the anti-correlations are caused by ionization changes, thus this density constraint may be moot. For a discussion of whether ionization variation can be at least partly responsible for the anti-correlations, see Gibson et al. (2006). If the anti-correlations are not caused by ionization changes, this strengthens the claim in Gibson et al. (2006) that the variation may be caused by looking along different lines of sight through a structured absorber.

7.4.3 Dynamic Components: the HIHVO

Our study of MR 2251-178 revealed the presence of an HIHVO which may be transient, as it was not observed in the *XMM-Newton* spectrum taken 3 months earlier, and it carries mass and energy out of the nucleus at a rate which is much higher than the accretion rate. Either the HIHVO must either be very short-lived or Ω (the solid angle subtended by the wind) must be very small, or else the flow would carry a large amount of mass/energy compared to the AGN accretion budget.

The high velocity (4-6% of the speed of light) of the HIHVO seems to distinguish it from ordinary WAs, which typically have outflow velocities < 2000 km s^{-1}. HIHVOs in other AGN have been found at velocities ten times higher. Chartas et al. (2002) estimated that an HIHVO in APM 08279+5255 was located about 2×10^{17} cm from the central source. This is smaller than the parsec-scale torus, but in agreement with the disk wind model for a large SMBH. We were not able to strongly constrain the location of the HIHVO in MR 2251-178.[1]

Interestingly, Blustin et al. (2004) concluded that photoionized absorbers come in two varieties. The typical WAs are associated with evaporating torii, while the more rare HIHVOs are associated with a disk wind. Although several of the sources with HIHVOs in their sample were high-luminosity quasars, they cited MR 2251-178 as a counterexample to the hypothesis that HIHVOs are associated with high luminosities. MR 2251-178 is a bright quasar (although it has dimmed in recent years) for which no HIHVO had been detected. Our subsequent detection of an HIHVO (Gibson et al. 2005) in this source removes MR 2251-178 from the list of two counterexamples provided by Blustin et al. (2004).

It is tempting to associate the HIHVO with a disk wind, given its high outflow velocity, mass and energy flow rate, and likely transience. This would indicate that the disk wind is very dynamic, and can change appearance over a few months. However, the large outflow velocities of HIHVOs do not fit well into the paradigm of Elvis (2000). In the case of MR 2251-178, the disk wind model may imply that the HIHVO was launched either unusually rapidly from the disk, or in a direction along our line of sight (not perpendicular to the disk).

7.4.4 Variation Due to Structure?

We concluded that luminosity variation was insufficient to fully explain the line variation we saw in MCG -6-30-15, and that intervening clouds were not able to explain the line anti-correlations over time. After considering several other possible causes, we suggested that either the variation was due to a complicated mix of causes, or it could be explained more simply by structure in the WA perpendicular to our line of sight. The WA could be moving across our line of sight, or we could be looking along different lines of sight through the WA because the continuum source is moving around.

This claim, if verified, could allow some very interesting studies of AGN structure. In effect, long observations of varying WAs could be giving us a two-dimensional view of the absorbing regions. Spatial regions with greater absorption could correspond to clouds confined in an outflowing wind. This would allow measuring the distribution and properties of these clouds, if we either assume the absorber is moving across the line of sight or if we are given a model of the spatial distribution of continuum emission. If the variation is due to a moving continuum source, it would put interesting constraints on current continuum emission models such as the gravitational light-bending model, which allows the source to move by about 20 gravitational radii (Miniutti and Fabian 2004).

Because we don't know the size of the continuum emitting region, we don't know what the scale sizes of absorber structure are in this scenario. A SMBH of mass 10^7 $M_\odot$ with

---

[1] Arguments using the light-crossing time to deduce scale size are not appropriate for absorbers, which represent a small projected area along the line of sight. For example, transverse motion at low speeds can lead to strong and rapid changes in the absorption, if the absorber is structured.

a continuum source moving over 20 gravitational radii would illuminate absorber structure over about 10^{12} cm. (Actually, the size would be somewhat smaller, as the continuum emission region will be projected at some angle to our line of sight.) If the variation is due to transverse motion of the absorber at 1000 km s^{-1}, we would expect to see about 10^{12} cm pass by every 10 ks.

These scale sizes are very small compared to a parsec-scale torus. Structures of this size have very small gravitational binding energy compared to their kinetic and thermal energy, and would need to be confined or constantly regenerated, as has previously been suggested for WA clouds (e.g., Krolik and Kriss 2001).

7.4.5 Absorber Variation Is Dominated by Continuum

In Chapter 6 of this thesis, we found that, while WA variation may contribute to the short-term (5 ks time scale) variablity of AGN spectra, the spectral variability is dominated by other processes. The significant amount of variability above 2 keV suggests that the continuum is varying on short time scales, probably across the entire X-ray spectrum. Continuum variability studies have been pursued for some AGN, particularly MCG -6-30-15 (Vaughan and Fabian 2004). It will be difficult to interpret broad-band WA models (i.e., models which do not rely primarily on line fits) fit to AGN continua with confidence until we understand the underlying continuum.

7.4.6 The Future

Testing for variability requires significantly more data than is necessary for a single high quality, time-integrated spectrum. This means that variability studies will generally be required to choose between time resolution and spectral resolution. This choice will determine the type of study which can be conducted.

Lower spectral resolution still allows for an adequate study of the time-varying continuum. As discussed in Chapter 6, data from *RXTE*, *XMM-Newton*, and *Chandra* have already been used to produce RMS spectra. Future studies will hopefully use the measured variation to constrain continuum emission models. Understanding continuum emission better will allow us to make stronger statements about WA variation.

Future missions can benefit WA studies by providing high resolution spectroscopy with a large effective area. The *Constellation-X* development team is targeting a 2 eV FWHM at 6 keV for the microcalorimeter instrument. This would be an excellent improvement over even the *Chandra* HETG. Such resolution would have important consequences for absorber studies.

Firstly, higher resolution will allow us to search for structure in the broad features attributed to HIHVOs. The non-Gaussian shape of the absorption features in HIHVOs may reveal discrete components in the HIHVO, which we could compare to other lines in the spectrum seen at different outflow velocities, or it may reveal a smooth smear that could be used to characterize the wind properties by constraining outflow models.

Analyzing absorption lines from the "ordinary" WA could also produce extra-ordinary results. UV absorbers are frequently seen to have multiple kinematic components, and these components have even been seen to vary independently (e.g., Scott et al. 2004b). Measuring these components would certainly address current questions about the relationship between UV and X-ray absorbers. It would also reveal whether the X-ray absorption region is highly structured along the line of sight. Line studies of time-integrated spectra typically assume that absorption lines are from single-component absorbers. Finding that the X-ray absorber has multiple components could impact conclusions from many contemporary studies of line strengths.

Such high resolution may also enable us to distinguish emission lines from absorption lines. The (assumed) blending of emission and absorption lines in current-day spectra complicates analyses, and being able to measure them separately will allow us to estimate the solid angle covered by the absorber, which would in turn give better constraints to other derived quantities. Varying covering factors could be attributed to structure in the absorber perpendicular to the line of sight, and could be used to characterize the physical structure of the absorber (and perhaps any confining medium in which it resides).

Finally, we imagine an idealized scenario in which long exposures of AGN are taken with very high resolution spectrometers. Velocity structure in absorption lines will help us to distinguish the various components in the absorber. Variation studies of those velocity components will place density constraints on each component in cases where components vary due to luminosity-induced ionization changes. Together with column density measurements and ionization modelling of sets of lines, we may be able to determine a robust density map of the absorber along the line of sight. Combined with reverberation mapping transfer functions which estimate emission region structure based on emission line time delays, future analyses of X-ray spectroscopy will have much to say about the enigmatic structure of AGN.

Bibliography

F. C. Adams, D. S. Graff, M. Mbonye, and D. O. Richstone. Formation of Supermassive Black Holes in Galactic Bulges: A Rotating Collapse Model Consistent with the $M_{BH} - \sigma$ Relation. *ApJ*, 591:125–137, July 2003.

Adelman-McCarthy, J. K. et al. The Fourth Data Release of the Sloan Digital Sky Survey. *ApJS*, 162:38–48, January 2006.

S. M. V. Aldrovandi and D. Pequignot. Radiative and Dielectronic Recombination Coefficients for Complex Ions. *A&A*, 25:137–+, May 1973.

E. Anders and N. Grevesse. Abundances of the elements - Meteoritic and solar. *Geochim. Cosmochim. Acta*, 53:197–214, January 1989.

R. Antonucci. Unified models for active galactic nuclei and quasars. *ARA&A*, 31:473–521, 1993.

R. R. J. Antonucci and J. S. Miller. Spectropolarimetry and the nature of NGC 1068. *ApJ*, 297:621–632, October 1985.

N. Arav, Z.-Y. Li, and M. C. Begelman. Radiative acceleration in outflows from broad absorption line quasi-stellar objects. 2: Wind models. *ApJ*, 432:62–74, September 1994.

M. Arnaud and R. Rothenflug. An updated evaluation of recombination and ionization rates. *A&AS*, 60:425–457, June 1985.

J. N. Bahcall, S. Kirhakos, D. H. Saxe, and D. P. Schneider. Hubble Space Telescope Images of a Sample of 20 Nearby Luminous Quasars. *ApJ*, 479:642–+, April 1997.

M. C. Begelman and B. B. Nath. Self-regulated black hole accretion, the M-σ relation and the growth of bulges in galaxies. *MNRAS*, 361:1387–1392, August 2005.

E. Behar and H. Netzer. Inner-Shell 1s-2p Soft X-Ray Absorption Lines. *ApJ*, 570:165–170, May 2002.

E. Behar, A. P. Rasmussen, A. J. Blustin, M. Sako, S. M. Kahn, J. S. Kaastra, G. Branduardi-Raymont, and K. C. Steenbrugge. A Long Look at NGC 3783 with the XMM-Newton Reflection Grating Spectrometer. *ApJ*, 598:232–241, November 2003.

J. Bergeron, M. Dennefeld, A. Boksenberg, and M. Tarenghi. MR 2251-178 - A nearby QSO embedded in a giant H II envelope. *MNRAS*, 202:125–143, January 1983.

A. J. Blustin, M. J. Page, S. V. Fuerst, G. Branduardi-Raymont, and C. E. Ashton. The nature and origin of Seyfert warm absorbers. astro-ph 0411297, 2004.

Blustin, A. J., et al. Multiwavelength studies of the Seyfert 1 galaxy NGC 7469 II. X-ray and UV observations with XMM-Newton. *A&A*, 403:481–492, May 2003.

W. N. Brandt, A. C. Fabian, and K. A. Pounds. ROSAT PSPC observations of the infrared quasar IRAS 13349+2438: evidence for a warm absorber with internal dust. *MNRAS*, 278:326–336, January 1996.

G. Branduardi-Raymont, M. Sako, S. M. Kahn, A. C. Brinkman, J. S. Kaastra, and M. J. Page. Soft X-ray emission lines from a relativistic accretion disk in ¡ASTROBJ¿MCG -6-30-15¡/ASTROBJ¿ and ¡ASTROBJ¿Mrk 766¡/ASTROBJ¿. *A&A*, 365:L140–L145, January 2001.

G. E. Bromage, A. Boksenberg, J. Clavel, A. Elvius, M. V. Penston, G. C. Perola, M. Pettini, M. A. J. Snijders, E. G. Tanzi, and M. H. Ulrich. Detailed Observations of NGC4151 with IUE - Part Four - Absorption Line Spectrum and Variability. *MNRAS*, 215:1–+, July 1985.

G. V. Brown, P. Beiersdorfer, D. A. Liedahl, K. Widmann, S. M. Kahn, and E. J. Clothiaux. Laboratory Measurements and Identification of the Fe XVIII-XXIV L-Shell X-Ray Line Emission. *ApJS*, 140:589–607, June 2002.

R. L. Brown and R. J. Gould. Interstellar Absorption of Cosmic X Rays. *Phys. Rev. D*, 1: 2252–2256, April 1970.

C. R. Canizares, J. E. McClintock, and G. R. Ricker. Spectrophotometry of the X-ray QSO MR 2251-178. *ApJ*, 226:L1–L4, November 1978.

B. J. Carter, D. G. Fabricant, M. J. Geller, M. J. Kurtz, and B. McLean. Star Formation in a Complete Spectroscopic Survey of Galaxies. *ApJ*, 559:606–619, October 2001.

W. Cash. Parameter estimation in astronomy through application of the likelihood ratio. *ApJ*, 228:939–947, March 1979.

G. Chartas, W. N. Brandt, and S. C. Gallagher. XMM-Newton Reveals the Quasar Outflow in PG 1115+080. *ApJ*, 595:85–93, September 2003.

G. Chartas, W. N. Brandt, S. C. Gallagher, and G. P. Garmire. CHANDRA Detects Relativistic Broad Absorption Lines from APM 08279+5255. *ApJ*, 579:169–175, November 2002.

D. Chelouche and H. Netzer. Dynamical and Spectral Modeling of the Ionized Gas and Nuclear Environment in NGC 3783. *ApJ*, 625:95–107, May 2005.

J. Chiang, C. S. Reynolds, O. M. Blaes, M. A. Nowak, N. Murray, G. Madejski, H. L. Marshall, and P. Magdziarz. Simultaneous EUVE/ASCA/RXTE Observations of NGC 5548. *ApJ*, 528:292–305, January 2000.

M. J. Collinge, W. N. Brandt, S. Kaspi, D. M. Crenshaw, M. Elvis, S. B. Kraemer, C. S. Reynolds, R. M. Sambruna, and B. J. Wills. High-Resolution X-Ray and Ultraviolet Spectroscopy of the Complex Intrinsic Absorption in NGC 4051 with Chandra and the Hubble Space Telescope. *ApJ*, 557:2–17, August 2001.

Cooke, B. A., et al. The Ariel V /SSI/ catalogue of high galactic latitude /absolute value of B greater than 10 deg/ X-ray sources. *MNRAS*, 182:489–515, February 1978.

D. M. Crenshaw, S. B. Kraemer, A. Boggess, S. P. Maran, R. F. Mushotzky, and C. Wu. Intrinsic Absorption Lines in Seyfert 1 Galaxies. I. Ultraviolet Spectra from the Hubble Space Telescope. *ApJ*, 516:750–768, May 1999.

D. M. Crenshaw, S. P. Maran, and R. F. Mushotzky. Resolving the Intrinsic C IV Absorption in the Seyfert 1 Galaxy NGC 3516. *ApJ*, 496:797–+, March 1998.

J. Crummy, A. C. Fabian, L. Gallo, and R. R. Ross. An explanation for the soft X-ray excess in active galactic nuclei. *MNRAS*, 365:1067–1081, February 2006.

T. Di Matteo, V. Springel, and L. Hernquist. Energy input from quasars regulates the growth and activity of black holes and their host galaxies. *Nature*, 433:604–607, February 2005.

C. Done, G. M. Madejski, and P. T. Życki. The Relativistic Iron Line Profile in the Seyfert 1 Galaxy IC 4329A. *ApJ*, 536:213–224, June 2000.

R. Edelson, T. J. Turner, K. Pounds, S. Vaughan, A. Markowitz, H. Marshall, P. Dobbie, and R. Warwick. X-Ray Spectral Variability and Rapid Variability of the Soft X-Ray Spectrum Seyfert 1 Galaxies Arakelian 564 and Ton S180. *ApJ*, 568:610–626, April 2002.

M. Elvis. A Structure for Quasars. *ApJ*, 545:63–76, December 2000.

M. Elvis. Quasar Atmospheres: Toward a "Low" Theory for Quasars. astro-ph 0311436, 2003.

A. C. Fabian. Cooling Flows in Clusters of Galaxies. *ARA&A*, 32:277–318, 1994.

A. C. Fabian, H. Kunieda, S. Inoue, M. Matsuoka, T. Mihara, S. Miyamoto, C. Otani, G. Ricker, Y. Tanaka, M. Yamauchi, and T. Yaqoob. ASCA observations of the warm absorber in MCG-6-30-15: The discovery of a change in column density. *PASJ*, 46: L59–L63, June 1994.

A. C. Fabian, J. S. Sanders, S. Ettori, G. B. Taylor, S. W. Allen, C. S. Crawford, K. Iwasawa, R. M. Johnstone, and P. M. Ogle. Chandra imaging of the complex X-ray core of the Perseus cluster. *MNRAS*, 318:L65–L68, November 2000.

A. C. Fabian and S. Vaughan. The iron line in MCG-6-30-15 from XMM-Newton: evidence for gravitational light bending? *MNRAS*, 340:L28–L32, April 2003.

A. C. Fabian, S. Vaughan, K. Nandra, K. Iwasawa, D. R. Ballantyne, J. C. Lee, A. De Rosa, A. Turner, and A. J. Young. A long hard look at MCG-6-30-15 with XMM-Newton. *MNRAS*, 335:L1–L5, September 2002.

G. J. Ferland, K. T. Korista, D. A. Verner, J. W. Ferguson, J. B. Kingdon, and E. M. Verner. CLOUDY 90: Numerical Simulation of Plasmas and Their Spectra. *PASP*, 110: 761–778, July 1998.

L. Ferrarese and D. Merritt. A Fundamental Relation between Supermassive Black Holes and Their Host Galaxies. *ApJ*, 539:L9–L12, August 2000.

J. R. Gabel, D. M. Crenshaw, S. B. Kraemer, W. N. Brandt, I. M. George, F. W. Hamann, M. E. Kaiser, S. Kaspi, G. A. Kriss, S. Mathur, R. F. Mushotzky, K. Nandra, H. Netzer, B. M. Peterson, J. C. Shields, T. J. Turner, and W. Zheng. The Ionized Gas and Nuclear Environment in NGC 3783. II. Averaged Hubble Space Telescope/STIS and Far Ultraviolet Spectroscopic Explorer Spectra. *ApJ*, 583:178–191, January 2003a.

J. R. Gabel, D. M. Crenshaw, S. B. Kraemer, W. N. Brandt, I. M. George, F. W. Hamann, M. E. Kaiser, S. Kaspi, G. A. Kriss, S. Mathur, R. F. Mushotzky, K. Nandra, H. Netzer, B. M. Peterson, J. C. Shields, T. J. Turner, and W. Zheng. The Ionized Gas and Nuclear Environment in NGC 3783. III. Detection of a Decreasing Radial Velocity in an Intrinsic Ultraviolet Absorber. *ApJ*, 595:120–126, September 2003b.

J. R. Gabel, S. B. Kraemer, D. M. Crenshaw, I. M. George, W. N. Brandt, F. W. Hamann, M. E. Kaiser, S. Kaspi, G. A. Kriss, S. Mathur, K. Nandra, H. Netzer, B. M. Peterson, J. C. Shields, T. J. Turner, and W. Zheng. The Ionized Gas and Nuclear Environment in NGC 3783. V. Variability and Modeling of the Intrinsic Ultraviolet Absorption. *ApJ*, 631:741–761, October 2005.

R. Ganguly, J. C. Charlton, and M. Eracleous. Variable Ultraviolet Absorption in the Spectrum of MR 2251-178. *ApJ*, 556:L7–L10, July 2001.

R. Ganguly, M. Eracleous, J. C. Charlton, and C. W. Churchill. Intrinsic Narrow Absorption Lines in Keck HIRES Spectra of a Sample of Six Quasars. *AJ*, 117:2594–2607, June 1999.

S. García-Burillo, F. Combes, E. Schinnerer, F. Boone, and L. K. Hunt. Molecular gas in NUclei of GAlaxies (NUGA). IV. Gravitational torques and AGN feeding. *A&A*, 441: 1011–1030, October 2005.

K. Gebhardt, R. Bender, G. Bower, A. Dressler, S. M. Faber, A. V. Filippenko, R. Green, C. Grillmair, L. C. Ho, J. Kormendy, T. R. Lauer, J. Magorrian, J. Pinkney, D. Richstone, and S. Tremaine. A Relationship between Nuclear Black Hole Mass and Galaxy Velocity Dispersion. *ApJ*, 539:L13–L16, August 2000.

N. Gehrels. Confidence limits for small numbers of events in astrophysical data. *ApJ*, 303: 336–346, April 1986.

R. Genzel, R. Schödel, T. Ott, A. Eckart, T. Alexander, F. Lacombe, D. Rouan, and B. Aschenbach. Near-infrared flares from accreting gas around the supermassive black hole at the Galactic Centre. *Nature*, 425:934–937, October 2003.

I. M. George, T. J. Turner, H. Netzer, K. Nandra, R. F. Mushotzky, and T. Yaqoob. ASCA Observations of Seyfert 1 Galaxies. III. The Evidence for Absorption and Emission Due to Photoionized Gas. *ApJS*, 114:73–+, January 1998.

A. M. Ghez, S. Salim, S. D. Hornstein, A. Tanner, J. R. Lu, M. Morris, E. E. Becklin, and G. Duchêne. Stellar Orbits around the Galactic Center Black Hole. *ApJ*, 620:744–757, February 2005.

L. Giacconi, H. Gursky, F. Paolini, and B. Rossi. Evidence for X-rays from Sources Outside the Solar System. *Phys. Rev. Lett.*, 9:439–443, 1962.

R. Giacconi, P. Rosati, P. Tozzi, M. Nonino, G. Hasinger, C. Norman, J. Bergeron, S. Borgani, R. Gilli, R. Gilmozzi, and W. Zheng. First Results from the X-Ray and Optical Survey of the Chandra Deep Field South. *ApJ*, 551:624–634, April 2001.

R. R. Gibson, C. R. Canizares, H. L. Marshall, A.J. Young, and J. C. Lee. Line Variability in the High-Resolution X-Ray Spectrum of MCG –6-30-15. *in submission*, 2006.

R. R. Gibson, H. L. Marshall, C. R. Canizares, and J. C. Lee. The High-Resolution X-Ray Spectrum of MR 2251-178 Obtained with the Chandra HETGS. *ApJ*, 627:83–96, July 2005.

M. Gierliński and C. Done. Energy-dependent variability and the origin of the soft X-ray excess in AGN. astro-ph 0605129, 2006.

R. W. Goosmann, B. Czerny, M. Mouchet, G. Ponti, M. Dovčiak, V. Karas, A. Różańska, and A.-M. Dumont. The structure and X-ray radiation spectra of illuminated accretion disks in AGN. III. Modeling fractinal variability. astro-ph 0604156, 2006.

L. J. Greenhill, D. R. Jiang, J. M. Moran, M. J. Reid, K. Y. Lo, and M. J. Claussen. Detection of a Subparsec Diameter Disk in the Nucleus of NGC 4258. *ApJ*, 440:619–+, February 1995.

N. Grevesse, A. Noels, and A. J. Sauval. Standard Abundances. In S. S. Holt and G. Sonneborn, editors, *ASP Conf. Ser. 99: Cosmic Abundances*, pages 117–+, 1996.

D. Grupe, B. J. Wills, D. Wills, and K. Beuermann. Scattering and absorption in soft X-ray selected AGN: an optical polarization survey. astro-ph 9712149, 1997.

M. F. Gu, T. Holczer, E. Behar, and S. M. Kahn. Inner Shell Absorption Lines of FeVI – FeXVI: A Many-Body Perturbation Theory Approach. *N/A*, astro-ph/0512410, December 2005.

J. P. Halpern. X-ray spectra of active galactic nuclei. *Ph.D. Thesis*, 1982.

J. P. Halpern. Variable X-ray absorption in the QSO MR 2251 - 178. *ApJ*, 281:90–94, June 1984.

J. P. Halpern and J. E. Grindlay. X-ray photoionized nebulae. *ApJ*, 242:1041–1055, December 1980.

G. Hasinger, R. Burg, R. Giacconi, M. Schmidt, J. Trumper, and G. Zamorani. The ROSAT Deep Survey. I. X-ray sources in the Lockman Field. *A&A*, 329:482–494, January 1998.

K. Hayashida, S. Miyamoto, S. Kitamoto, H. Negoro, and H. Inoue. Central Black Hole Masses in Active Galactic Nuclei Inferred from X-Ray Variability. *ApJ*, 500:642–+, June 1998.

T. Holczer, E. Behar, and S. Kaspi. Is the Fe M-Shell Absorber Part of the Outflow in Active Galactic Nuclei? *ApJ*, 632:788–792, October 2005.

S. S. Holt, R. F. Mushotzky, E. A. Boldt, P. J. Serlemitsos, R. H. Becker, A. E. Szymkowiak, and N. E. White. X-ray spectral constraints on the broad-line cloud geometry of NGC 4151. *ApJ*, 241:L13–L17, October 1980.

J. C. Houck and L. A. Denicola. ISIS: An Interactive Spectral Interpretation System for High Resolution X-Ray Spectroscopy. In N. Manset, C. Veillet, and D. Crabtree, editors, *ASP Conf. Ser. 216: Astronomical Data Analysis Software and Systems IX*, pages 591–+, 2000.

T. Kallman and M. Bautista. Photoionization and High-Density Gas. *ApJS*, 133:221–253, March 2001.

T. R. Kallman and R. McCray. X-ray nebular models. *ApJS*, 50:263–317, December 1982.

T. R. Kallman, P. Palmeri, M. A. Bautista, C. Mendoza, and J. H. Krolik. Photoionization Modeling and the K Lines of Iron. *ApJS*, 155:675–701, December 2004.

S. Kaspi. High resolution X-ray spectra of quasars. astro-ph 0405563, 2004.

S. Kaspi, W. N. Brandt, I. M. George, H. Netzer, D. M. Crenshaw, J. R. Gabel, F. W. Hamann, M. E. Kaiser, A. Koratkar, S. B. Kraemer, G. A. Kriss, S. Mathur, R. F. Mushotzky, K. Nandra, B. M. Peterson, J. C. Shields, T. J. Turner, and W. Zheng. The Ionized Gas and Nuclear Environment in NGC 3783. I. Time-averaged 900 Kilosecond Chandra Grating Spectroscopy. *ApJ*, 574:643–662, August 2002.

S. Kaspi, H. Netzer, D. Chelouche, I. M. George, K. Nandra, and T. J. Turner. The Properties and Evolution of the Highly Ionized Gas in MR 2251-178. *ApJ*, 611:68–80, August 2004.

Kaspi, S., et al. High-Resolution X-Ray Spectroscopy and Modeling of the Absorbing and Emitting Outflow in NGC 3783. *ApJ*, 554:216–232, June 2001.

T. Kato. Radiation from a hot, thin plasma from 1 to 250 A. *ApJS*, 30:397–449, April 1976.

Kinkhabwala, A., et al. XMM-Newton Reflection Grating Spectrometer Observations of Discrete Soft X-Ray Emission Features from NGC 1068. *ApJ*, 575:732–746, August 2002.

S. Komossa and N. Bade. Properties of dusty warm absorbers and the case of IRAS17020+4544. *A&A*, 331:L49–L52, March 1998.

S. Komossa and D. Breitschwerdt. Dusty warm absorbers: the case of IRAS 13349+2438. astro-ph 9906377, 1999.

S. Komossa and H. Fink. Evidence for a dusty warm absorber in NGC 3227? *A&A*, 327: 483–492, November 1997a.

S. Komossa and H. Fink. Soft X-ray properties of the Seyfert 1.8 galaxy NGC 3786. *A&A*, 327:555–561, November 1997b.

J. Kormendy and D. Richstone. Inward Bound—The Search For Supermassive Black Holes In Galactic Nuclei. *ARA&A*, 33:581–+, 1995.

G. A. Kriss. FUSE observations of warm absorbers in AGN. astro-ph 0106285, 2001.

G. A. Kriss, A. F. Davidsen, W. P. Blair, C. W. Bowers, W. V. Dixon, S. T. Durrance, P. D. Feldman, H. C. Ferguson, R. C. Henry, R. A. Kimble, J. W. Kruk, K. S. Long, H. W. Moos, and O. Vancura. Hopkins ultraviolet telescope observations of the far-ultraviolet spectrum of NGC 4151. *ApJ*, 392:485–491, June 1992.

G. A. Kriss, A. F. Davidsen, W. Zheng, J. W. Kruk, and B. R. Espey. The Far-Ultraviolet Spectrum of NGC 4151 as Observed with the Hopkins Ultraviolet Telescope on Astro-2. *ApJ*, 454:L7+, November 1995.

G. A. Kriss, B. R. Espey, J. H. Krolik, Z. Tsvetanov, W. Zheng, and A. F. Davidsen. Far-Ultraviolet Observations of NGC 3516 Using the Hopkins Ultraviolet Telescope. *ApJ*, 467:622–+, August 1996.

G. A. Kriss, R. F. Green, M. Brotherton, W. Oegerle, K. R. Sembach, A. F. Davidsen, S. D. Friedman, M. E. Kaiser, W. Zheng, B. Woodgate, J. Hutchings, J. M. Shull, and D. G. York. Far Ultraviolet Spectroscopic Explorer Observations of Intrinsic Absorption in the Seyfert 1 Galaxy Markarian 509. *ApJ*, 538:L17–L21, July 2000.

J. H. Krolik. *Active Galactic Nuclei: From the Central Black Hole to the Galactic Environment.* Princeton University Press, 1999.

J. H. Krolik. Warm Absorbers in AGN: A Multi-Temperature Wind. In *X-ray Spectroscopy of AGN with Chandra and XMM-Newton*, pages pp. 131–+, 2002.

J. H. Krolik and M. C. Begelman. Molecular tori in Seyfert galaxies - Feeding the monster and hiding it. *ApJ*, 329:702–711, June 1988.

J. H. Krolik and G. A. Kriss. Observable Properties of X-Ray–heated Winds in Active Galactic Nuclei: Warm Reflectors and Warm Absorbers. *ApJ*, 447:512–+, July 1995.

J. H. Krolik and G. A. Kriss. Warm Absorbers in Active Galactic Nuclei: A Multitemperature Wind. *ApJ*, 561:684–690, November 2001.

J. H. Krolik, C. F. McKee, and C. B. Tarter. Two-phase models of quasar emission line regions. *ApJ*, 249:422–442, October 1981.

Y. Krongold, F. Nicastro, N. S. Brickhouse, M. Elvis, D. A. Liedahl, and S. Mathur. Toward a Self-Consistent Model of the Ionized Absorber in NGC 3783. *ApJ*, 597:832–850, November 2003.

A. Laor and W. N. Brandt. The Luminosity Dependence of Ultraviolet Absorption in Active Galactic Nuclei. *ApJ*, 569:641–654, April 2002.

J. C. Lee, A. C. Fabian, C. S. Reynolds, W. N. Brandt, and K. Iwasawa. The X-ray variability of the Seyfert 1 galaxy MCG-6-30-15 from long ASCA and RXTE observations. *MNRAS*, 318:857–874, November 2000.

J. C. Lee, P. M. Ogle, C. R. Canizares, H. L. Marshall, N. S. Schulz, R. Morales, A. C. Fabian, and K. Iwasawa. Revealing the Dusty Warm Absorber in MCG -6-30-15 with the Chandra High-Energy Transmission Grating. *ApJ*, 554:L13–L17, June 2001.

K. M. Leighly, L. E. Kay, B. J. Wills, D. Wills, and D. Grupe. The Optical Polarization and Warm Absorber in IRAS 17020+4544. *ApJ*, 489:L137+, November 1997.

K. M. Leighly and J. R. Moore. Hubble Space Telescope STIS Ultraviolet Spectral Evidence of Outflow in Extreme Narrow-Line Seyfert 1 Galaxies. I. Data and Analysis. *ApJ*, 611: 107–124, August 2004.

D. A. Liedahl. The X-Ray Spectral Properties of Photoionized Plasma and Transient Plasmas. *LNP Vol. 520: X-Ray Spectroscopy in Astrophysics*, 520:189–+, 1999.

F. J. Lockman and B. D. Savage. The Hubble Space Telescope Quasar Absorption Line Key Project. 10: Galactic H I 21 centimeter emission toward 143 quasars and active Galactic nuclei. *ApJS*, 97:1–47, March 1995.

Y. E. Lyubarskii. Flicker noise in accretion discs. *MNRAS*, 292:679–+, December 1997.

T. Maccacaro, R. della Ceca, I. M. Gioia, S. L. Morris, J. T. Stocke, and A. Wolter. The properties of X-ray-selected active galactic nuclei. I - Luminosity function, cosmological evolution, and contribution to the diffuse X-ray background. *ApJ*, 374:117–133, June 1991.

F. Macchetto, L. Colina, D. Golombek, M. A. C. Perryman, and S. di Serego Alighieri. The structure and ionization of the extended emission-line filaments surrounding the QSO MR 2251-178. *ApJ*, 356:389–398, June 1990.

A. Markowitz, R. Edelson, and S. Vaughan. Long-Term X-Ray Spectral Variability in Seyfert 1 Galaxies. *ApJ*, 598:935–955, December 2003.

H. L. Marshall, A. Tennant, C. E. Grant, A. P. Hitchcock, S. O'Dell, and P. P. Plucinsky. Composition of the Chandra ACIS contaminant. In *Proc. SPIE 5165, X-Ray and Gamma-Ray Telescopes and Instruments for Astronomy, ed. K. A. Flanagan & O. H. W. Siegmund, 497*, August 2003.

S. Mathur. Absorption in 3C 212. *ApJ*, 431:L75–L78, August 1994.

S. Mathur, M. Elvis, and B. Wilkes. Testing Unified X-Ray/Ultraviolet Absorber Models with NGC 5548. *ApJ*, 452:230–+, October 1995.

S. Mathur, B. Wilkes, and M. Elvis. Discovery of Associated Absorption LInes in an X-Ray Warm Absorber: Hubble Space Telescope Observations of PG 1114+445. *ApJ*, 503:L23+, August 1998.

S. Mathur, B. Wilkes, M. Elvis, and F. Fiore. The X-ray and ultraviolet absorbing outflow in 3C 351. *ApJ*, 434:493–502, October 1994.

I. M. McHardy, K. F. Gunn, P. Uttley, and M. R. Goad. MCG-6-30-15: long time-scale X-ray variability, black hole mass and active galactic nuclei high states. *MNRAS*, 359: 1469–1480, June 2005.

I. M. McHardy, A. Lawrence, J. P. Pye, and K. A. Pounds. The Ariel V /3 A/ catalogue of X-ray sources. II - Sources at high galactic latitude /absolute value of B greater than 10 deg/. *MNRAS*, 197:893–919, December 1981.

I. M. McHardy, I. E. Papadakis, and P. Uttley. Temporal and Spectral Variability of AGN with RXTE. In *The Active X-ray Sky: Results from BeppoSAX and RXTE*, page 509, 1998.

B. McKernan, T. Yaqoob, and C. S. Reynolds. O VII and O VIII absorption by hot gas in the vicinity of the Galaxy (astro-ph 0408506). astro-ph 0408506, August 2004.

B. R. McNamara, M. Wise, P. E. J. Nulsen, L. P. David, C. L. Sarazin, M. Bautz, M. Markevitch, A. Vikhlinin, W. R. Forman, C. Jones, and D. E. Harris. Chandra X-Ray Observations of the Hydra A Cluster: An Interaction between the Radio Source and the X-Ray-emitting Gas. *ApJ*, 534:L135–L138, May 2000a.

B. R. McNamara, M. W. Wise, L. P. David, P. E. J. Nulsen, and C. L. Sarazin. New Perspectives on Cooling Flows and Cluster Radio Sources. In *Constructing the Universe with Clusters of Galaxies*, 2000b.

A. Merloni and A. C. Fabian. Thunderclouds and accretion discs: a model for the spectral and temporal variability of Seyfert 1 galaxies. *MNRAS*, 328:958–968, December 2001.

R. Mewe and E. H. B. M. Gronenschild. Calculated X-radiation from optically thin plasmas. IV - Atomic data and rate coefficients for spectra in the range 1-270 A. *A&AS*, 45:11–52, July 1981.

C. J. Miller, R. C. Nichol, P. L. Gómez, A. M. Hopkins, and M. Bernardi. The Environment of Active Galactic Nuclei in the Sloan Digital Sky Survey. *ApJ*, 597:142–156, November 2003.

T. Mineo and G. C. Stewart. Further constraints on the warm absorber in MR2251 - 17.8 from GINGA and EXOSAT observations. *MNRAS*, 262:817–822, June 1993.

G. Miniutti and A. C. Fabian. A light bending model for the X-ray temporal and spectral properties of accreting black holes. *MNRAS*, 349:1435–1448, April 2004.

E. M. Monier, S. Mathur, B. Wilkes, and M. Elvis. Discovery of Associated Absorption Lines in an X-Ray Warm Absorber:Hubble Space Telescope Faint Object Spectrograph Observations of MR 2251-178. *ApJ*, 559:675–679, October 2001.

R. F. Mushotzky, L. L. Cowie, A. J. Barger, and K. A. Arnaud. Resolving the extragalactic hard X-ray background. *Nature*, 404:459–464, March 2000.

R. F. Mushotzky, C. Done, and K. A. Pounds. X-ray spectra and time variability of active galactic nuclei. *ARA&A*, 31:717–761, 1993.

K. Nandra, T. Le, I. M. George, R. A. Edelson, R. F. Mushotzky, B. M. Peterson, and T. J. Turner. The Origin of the X-Ray and Ultraviolet Emission in NGC 7469. *ApJ*, 544: 734–746, December 2000.

K. Nandra and K. A. Pounds. Highly ionized gas in the nucleus of the active galaxy MCG-6-30-15. *Nature*, 359:215–+, September 1992.

K. Nandra and K. A. Pounds. GINGA Observations of the X-Ray Spectra of Seyfert Galaxies. *MNRAS*, 268:405–+, May 1994.

K. Nandra, K. A. Pounds, and G. C. Stewart. The X-ray spectrum of MCG-6-30-15 and its temporal variability. *MNRAS*, 242:660–668, February 1990.

K. Nandra, K. A. Pounds, G. C. Stewart, I. M. George, K. Hayashida, F. Makino, and T. Ohashi. Compton reflection and the variable X-ray spectrum of NGC 5548. *MNRAS*, 248:760–772, February 1991.

H. Netzer, S. Kaspi, E. Behar, W. N. Brandt, D. Chelouche, I. M. George, D. M. Crenshaw, J. R. Gabel, F. W. Hamann, S. B. Kraemer, G. A. Kriss, K. Nandra, B. M. Peterson, J. C. Shields, and T. J. Turner. The Ionized Gas and Nuclear Environment in NGC 3783. IV. Variability and Modeling of the 900 Kilosecond Chandra Spectrum. *ApJ*, 599: 933–948, December 2003.

M. A. Nowak and J. Chiang. Implications of the X-Ray Variability for the Mass of MCG -6-30-15. *ApJ*, 531:L13–L16, March 2000.

P. M. Ogle, T. Brookings, C. R. Canizares, J. C. Lee, and H. L. Marshall. Testing the Seyfert unification theory: Chandra HETGS observations of NGC 1068. *A&A*, 402:849–864, May 2003.

P. M. Ogle, H. L. Marshall, J. C. Lee, and C. R. Canizares. Chandra Observations of the X-Ray Narrow-Line Region in NGC 4151. *ApJ*, 545:L81–L84, December 2000.

A. Orr, P. Barr, M. Guainazzi, A. N. Parmar, and A. J. Young. BeppoSAX spectroscopy of MR 2251-178: A test for ionized reflection in radio quiet QSOs. *A&A*, 376:413–421, September 2001.

C. Otani, T. Kii, C. S. Reynolds, A. C. Fabian, K. Iwasawa, K. Hayashida, H. Inoue, H. Kunieda, F. Makino, M. Matsuoka, and Y. Tanaka. The Variable O,VIII Warm Absorber in MCG-6-30-15. *PASJ*, 48:211–218, April 1996.

H. C. Pan, G. C. Stewart, and K. A. Pounds. The variable X-ray absorption and soft X-ray excess of the QSO MR2251 - 178. *MNRAS*, 242:177–187, January 1990.

R. A. Perley, J. W. Dreher, and J. J. Cowan. The jet and filaments in Cygnus A. *ApJ*, 285: L35–L38, October 1984.

G. C. Perola, L. Piro, A. Altamore, F. Fiore, A. Boksenberg, M. V. Penston, M. A. J. Snijders, G. E. Bromage, J. Clavel, A. Elvius, and M. H. Ulrich. New results on the X-ray emission and its correlation with the ultraviolet in NGC 4151. *ApJ*, 306:508–521, July 1986.

B. M. Peterson. Reverberation mapping of active galactic nuclei. *PASP*, 105:247–268, March 1993.

J. R. Peterson, S. M. Kahn, F. B. S. Paerels, J. S. Kaastra, T. Tamura, J. A. M. Bleeker, C. Ferrigno, and J. G. Jernigan. High-Resolution X-Ray Spectroscopic Constraints on Cooling-Flow Models for Clusters of Galaxies. *ApJ*, 590:207–224, June 2003.

M. M. Phillips. MR 2251-178 - A nearby quasi-stellar object in a cluster of galaxies. *ApJ*, 236:L45–L48, March 1980.

Plucinsky, P. P., et al. Flight spectral response of the ACIS instrument. In *Proc. SPIE 4851, X-Ray and Gamma-Ray Telescopes and Instruments for Astronomy, ed. J. E. Truemper & H. D. Tananbaum, 89*, March 2003.

D. Porquet and J. Dubau. X-ray photoionized plasma diagnostics with helium-like ions. Application to warm absorber-emitter in active galactic nuclei. *A&AS*, 143:495–514, May 2000.

K. A. Pounds, A. R. King, K. L. Page, and P. T. O'Brien. Evidence of a high-velocity ionized outflow in a second narrow-line quasar PG 0844+349. *MNRAS*, 346:1025–1030, December 2003a.

K. A. Pounds, J. N. Reeves, A. R. King, K. L. Page, P. T. O'Brien, and M. J. L. Turner. A high-velocity ionized outflow and XUV photosphere in the narrow emission line quasar PG1211+143. *MNRAS*, 345:705–713, November 2003b.

A. Ptak, T. Yaqoob, P. J. Serlemitsos, R. Mushotzky, and C. Otani. Rapid X-ray spectral variability in NGC 3227. *ApJ*, 436:L31–L34, November 1994.

J. N. Reeves, P. T. O'Brien, and M. J. Ward. A Massive X-Ray Outflow from the Quasar PDS 456. *ApJ*, 593:L65–L68, August 2003.

C. S. Reynolds. An X-ray spectral study of 24 type 1 active galactic nuclei. *MNRAS*, 286: 513–537, April 1997.

C. S. Reynolds. On the Lack of X-Ray Iron Line Reverberation in MCG -6-30-15: Implications for the Black Hole Mass and Accretion Disk Structure. *ApJ*, 533:811–820, April 2000.

C. S. Reynolds, A. C. Fabian, K. Nandra, H. Inoue, H. Kunieda, and K. Iwasawa. ASCA PV observations of the Seyfert 1 galaxy MCG-6-30-15: rapid variability of the warm absorber. *MNRAS*, 277:901–912, December 1995.

C. S. Reynolds, M. J. Ward, A. C. Fabian, and A. Celotti. A multiwavelength study of the Seyfert 1 galaxy MCG-6-30-15. *MNRAS*, 291:403–+, November 1997.

C. S. Reynolds, J. Wilms, M. C. Begelman, R. Staubert, and E. Kendziorra. On the deep minimum state in the Seyfert galaxy MCG-6-30-15. *MNRAS*, 349:1153–1166, April 2004.

G. R. Ricker, G. W. Clarke, R. E. Doxsey, R. G. Dower, J. G. Jernigan, J. P. Delvaille, G. M. MacAlpine, and R. M. Hjellming. Discovery of an X-ray QSO. *Nature*, 271:35–37, January 1978.

G. Risaliti, M. Elvis, and F. Nicastro. Ubiquitous Variability of X-Ray-absorbing Column Densities in Seyfert 2 Galaxies. *ApJ*, 571:234–246, May 2002.

R. R. Ross and A. C. Fabian. A comprehensive range of X-ray ionized-reflection models. *MNRAS*, 358:211–216, March 2005.

R. R. Ross, A. C. Fabian, and A. J. Young. X-ray reflection spectra from ionized slabs. *MNRAS*, 306:461–466, June 1999.

M. Ruszkowski, M. Brüggen, and M. C. Begelman. Cluster Heating by Viscous Dissipation of Sound Waves. *ApJ*, 611:158–163, August 2004.

M. Sako, S. M. Kahn, G. Branduardi-Raymont, J. S. Kaastra, A. C. Brinkman, M. J. Page, E. Behar, F. Paerels, A. Kinkhabwala, D. A. Liedahl, and J. W. d. Herder. Can a Dusty Warm Absorber Model Reproduce the Soft X-Ray Spectra of MCG -6-30-15 and Markarian 766? *ApJ*, 596:114–128, October 2003.

S. F. Sánchez, K. Jahnke, L. Wisotzki, D. H. McIntosh, E. F. Bell, M. Barden, S. V. W. Beckwith, A. Borch, J. A. R. Caldwell, B. Häussler, S. Jogee, K. Meisenheimer, C. Y. Peng, H.-W. Rix, R. S. Somerville, and C. Wolf. Colors of Active Galactic Nucleus Host Galaxies at $0.5 < z < 1.1$ from the GEMS Survey. *ApJ*, 614:586–606, October 2004.

R. Schödel, T. Ott, R. Genzel, R. Hofmann, M. Lehnert, A. Eckart, N. Mouawad, T. Alexander, M. J. Reid, R. Lenzen, M. Hartung, F. Lacombe, D. Rouan, E. Gendron, G. Rousset, A.-M. Lagrange, W. Brandner, N. Ageorges, C. Lidman, A. F. M. Moorwood, J. Spyromilio, N. Hubin, and K. M. Menten. A star in a 15.2-year orbit around the supermassive black hole at the centre of the Milky Way. *Nature*, 419:694–696, October 2002.

J. E. Scott, G. A. Kriss, M. Brotherton, R. F. Green, J. Hutchings, J. M. Shull, and W. Zheng. A Composite Extreme-Ultraviolet QSO Spectrum from FUSE. *ApJ*, 615: 135–149, November 2004a.

J. E. Scott, G. A. Kriss, J. C. Lee, N. Arav, P. Ogle, K. Roraback, K. Weaver, T. Alexander, M. Brotherton, R. F. Green, J. Hutchings, M. E. Kaiser, H. Marshall, W. Oegerle, and W. Zheng. Intrinsic Absorption in the Spectrum of Markarian 279: Simultaneous Chandra, FUSE, and STIS Observations. *ApJS*, 152:1–27, May 2004b.

D. C. Shih, K. Iwasawa, and A. C. Fabian. The continuum variability of MCG-6-30-15: a detailed analysis of the long 1999 ASCA observation. *MNRAS*, 333:687–696, July 2002.

P. L. Shopbell, S. Veilleux, and J. Bland-Hawthorn. The Very Extended Ionized Nebula around the Quasar MR 2251-178. *ApJ*, 524:L83–L86, October 1999.

J. M. Shull and M. van Steenberg. The ionization equilibrium of astrophysically abundant elements. *ApJS*, 48:95–107, January 1982.

J. Siebert, S. Komossa, and W. Brinkmann. The warm absorber in IRAS 13349+2438: dusty or not? *A&A*, 351:893–902, November 1999.

L. Jr. Spitzer. *Physical Processes in the Interstellar Medium.* John Wiley & Sons, New York, 1978.

C. B. Tarter and E. E. Salpeter. The Interaction of X-Ray Sources with Optically Thick Environments. *ApJ*, 156:953–+, June 1969.

C. B. Tarter, W. H. Tucker, and E. E. Salpeter. The Interaction of X-Ray Sources with Optically Thin Environments. *ApJ*, 156:943–+, June 1969.

R. D. Taylor, P. Uttley, and I. M. McHardy. The nature of X-ray spectral variability in Seyfert galaxies. *MNRAS*, 342:L31–L35, June 2003.

R. C. Telfer, W. Zheng, G. A. Kriss, and A. F. Davidsen. The Rest-Frame Extreme-Ultraviolet Spectral Properties of Quasi-stellar Objects. *ApJ*, 565:773–785, February 2002.

S. Tremaine, K. Gebhardt, R. Bender, G. Bower, A. Dressler, S. M. Faber, A. V. Filippenko, R. Green, C. Grillmair, L. C. Ho, J. Kormendy, T. R. Lauer, J. Magorrian, J. Pinkney, and D. Richstone. The Slope of the Black Hole Mass versus Velocity Dispersion Correlation. *ApJ*, 574:740–753, August 2002.

E. Triester and C. M. Urry. AGN Unification and the X-ray Background. astro-ph 0505300, 2005.

A. K. Turner, A. C. Fabian, J. C. Lee, and S. Vaughan. The soft X-ray absorption lines of the Seyfert 1 galaxy MCG-6-30-15. *MNRAS*, 353:319–328, September 2004.

A. K. Turner, A. C. Fabian, S. Vaughan, and J. C. Lee. A softer look at MCG-6-30-15 with XMM-Newton. *MNRAS*, 346:833–840, December 2003.

T. J. Turner, K. Nandra, I. M. George, A. C. Fabian, and K. A. Pounds. X-Ray Observations of the Warm Absorber in NGC 3783. *ApJ*, 419:127–+, December 1993.

Y. Ueda, T. Takahashi, H. Inoue, T. Tsuru, M. Sakano, Y. Ishisaki, Y. Ogasaka, K. Makishima, T. Yamada, K. Ohta, and M. Akiyama. A population of faint galaxies that contribute to the cosmic X-ray background. *Nature*, 391:866–+, February 1998.

M.-H. Ulrich. Far-ultraviolet absorption lines in active galaxies. *MNRAS*, 230:121–130, January 1988.

C. Urry. AGN Unification: An Update. In *ASP Conf. Ser. 311: AGN Physics with the Sloan Digital Sky Survey*, pages 49–+, 2004.

P. Uttley and I. M. McHardy. The flux-dependent amplitude of broadband noise variability in X-ray binaries and active galaxies. *MNRAS*, 323:L26–L30, May 2001.

S. Vaughan and R. Edelson. Evidence for Rapid Iron Kα Line Flux Variability in MCG -6-30-15. *ApJ*, 548:694–702, February 2001.

S. Vaughan, R. Edelson, R. S. Warwick, and P. Uttley. On characterizing the variability properties of X-ray light curves from active galaxies. *MNRAS*, 345:1271–1284, November 2003a.

S. Vaughan and A. C. Fabian. A long hard look at MCG-6-30-15 with XMM-Newton- II. Detailed EPIC analysis and modelling. *MNRAS*, 348:1415–1438, March 2004.

S. Vaughan, A. C. Fabian, and K. Nandra. X-ray continuum variability of MCG-6-30-15. *MNRAS*, 339:1237–1255, March 2003b.

D. A. Verner and G. J. Ferland. Atomic Data for Astrophysics. I. Radiative Recombination Rates for H-like, He-like, Li-like, and Na-like Ions over a Broad Range of Temperature. *ApJS*, 103:467–+, April 1996.

D. A. Verner, G. J. Ferland, K. T. Korista, and D. G. Yakovlev. Analytic FITS for photoionization cross sections of atoms and ions. *Bulletin of the American Astronomical Society*, 27:859–+, May 1995.

D. A. Verner, E. M. Verner, and G. J. Ferland. Atomic Data for Permitted Resonance Lines of Atoms and Ions from H to Si, and S, Ar, Ca, and Fe. *Atomic Data and Nuclear Data Tables*, 64:1–+, 1996.

D. A. Verner and D. G. Yakovlev. Analytic FITS for partial photoionization cross sections. *A&AS*, 109:125–133, January 1995.

G. S. Voronov. A Practical Fit Formula for Ionization Rate Coefficients of Atoms and Ions by Electron Impact: Z = 1-28. *Atomic Data and Nuclear Data Tables*, 65:1–+, 1997.

R. Walter and T. J.-L. Courvoisier. X-ray variability in a sample of Seyfert 1 type AGN. *A&A*, 266:57–64, December 1992.

M. C. Weisskopf, H. D. Tananbaum, L. P. Van Speybroeck, and S. L. O'Dell. Chandra X-ray Observatory (CXO): overview. In *Proc. SPIE 4012, X-Ray Optics, Instruments, and Missions III, ed. J. E. Truemper & B. Aschenbach, 2*, July 2000.

D. A. White, C. Jones, and W. Forman. An investigation of cooling flows and general cluster properties from an X-ray image deprojection analysis of 207 clusters of galaxies. *MNRAS*, 292:419–+, December 1997.

B. J. Wills, D. Wills, N. J. Evans, A. Natta, K. L. Thompson, M. Breger, and M. L. Sitko. Polarimetry and spectrophotometry of the QSO IRAS 13349+2438 and the unification of active galaxies. *ApJ*, 400:96–114, November 1992.

M. A. Worsley, A. C. Fabian, X. Barcons, S. Mateos, G. Hasinger, and H. Brunner. The (un)resolved X-ray background in the Lockman Hole. *MNRAS*, 352:L28–L33, August 2004.

T. Yaqoob, R. S. Warwick, and K. A. Pounds. Variable X-ray absorption in NGC 4151. *MNRAS*, 236:153–170, January 1989.

A. J. Young, J. C. Lee, A. C. Fabian, C. S. Reynolds, R. R. Gibson, and C. R. Canizares. A Chandra HETGS Spectral Study of the Iron K Bandpass in MCG -6-30-15: A Narrow View of the Broad Iron Line. *ApJ*, 631:733–740, October 2005.